ABSTRACT

Title of dissertation: HOVER AND WIND-TUNNEL TESTING
                            OF SHROUDED ROTORS FOR IMPROVED
                            MICRO AIR VEHICLE DESIGN

                            Jason L. Pereira
                            Doctor of Philosophy, 2008

Dissertation directed by: Professor Inderjit Chopra
                            Department of Aerospace Engineering

The shrouded-rotor configuration has emerged as the most popular choice for rotary-wing Micro Air Vehicles (MAVs), because of the inherent safety of the design and the potential for significant performance improvements. However, traditional design philosophies based on experience with large-scale ducted propellers may not apply to the low-Reynolds-number ($\sim$20,000) regime in which MAVs operate. An experimental investigation of the effects of varying the shroud profile shape on the performance of MAV-scale shrouded rotors has therefore been conducted. Hover tests were performed on seventeen models with a nominal rotor diameter of 16 cm (6.3 in) and various values of diffuser expansion angle, diffuser length, inlet lip radius and blade tip clearance, at various rotor collective angles. Compared to the baseline open rotor, the shrouded rotors showed increases in thrust by up to 94%, at the same power consumption, or reductions in power by up to 62% at the same thrust. These improvements surpass those predicted by momentum theory, due to the additional effect of the shrouds in reducing the non-ideal power losses of the rotor. Increasing the lip radius and decreasing the blade tip clearance caused performance to improve, while optimal values of diffuser angle and length were found to be 10° and 50% of the shroud throat diameter, respectively. With the exception of the lip radius, the

Report Documentation Page		*Form Approved* *OMB No. 0704-0188*

Public reporting burden for the collection of information is estimated to average 1 hour per response, including the time for reviewing instructions, searching existing data sources, gathering and maintaining the data needed, and completing and reviewing the collection of information. Send comments regarding this burden estimate or any other aspect of this collection of information, including suggestions for reducing this burden, to Washington Headquarters Services, Directorate for Information Operations and Reports, 1215 Jefferson Davis Highway, Suite 1204, Arlington VA 22202-4302. Respondents should be aware that notwithstanding any other provision of law, no person shall be subject to a penalty for failing to comply with a collection of information if it does not display a currently valid OMB control number.

1. REPORT DATE **2008**	2. REPORT TYPE	3. DATES COVERED **00-00-2008 to 00-00-2008**
4. TITLE AND SUBTITLE **Hover and Wind-Tunnel Testing of Shrouded Rotors for Improved Micro Air Vehicle Design**		5a. CONTRACT NUMBER
		5b. GRANT NUMBER
		5c. PROGRAM ELEMENT NUMBER
6. AUTHOR(S)		5d. PROJECT NUMBER
		5e. TASK NUMBER
		5f. WORK UNIT NUMBER
7. PERFORMING ORGANIZATION NAME(S) AND ADDRESS(ES) **University of Maryland, College Park,Department of Aerospace Engineering,College Park,MD,20742**		8. PERFORMING ORGANIZATION REPORT NUMBER
9. SPONSORING/MONITORING AGENCY NAME(S) AND ADDRESS(ES)		10. SPONSOR/MONITOR'S ACRONYM(S)
		11. SPONSOR/MONITOR'S REPORT NUMBER(S)
12. DISTRIBUTION/AVAILABILITY STATEMENT **Approved for public release; distribution unlimited**		
13. SUPPLEMENTARY NOTES		

14. ABSTRACT

The shrouded-rotor configuration has emerged as the most popular choice for rotary-wing Micro Air Vehicles (MAVs), because of the inherent safety of the design and the potential for significant performance improvements. However, traditional design philosophies based on experience with large-scale ducted propellers may not apply to the low-Reynolds-number (20,000) regime in which MAVs operate. An experimental investigation of the effects of varying the shroud profile shape on the performance of MAV-scale shrouded rotors has therefore been conducted. Hover tests were performed on seventeen models with a nominal rotor diameter of 16 cm (6.3 in) and various values of diffuser expansion angle, diffuser length, inlet lip radius and blade tip clearance, at various rotor collective angles. Compared to the baseline open rotor, the shrouded rotors showed increases in thrust by up to 94%, at the same power consumption, or reductions in power by up to 62% at the same thrust. These improvements surpass those predicted by momentum theory, due to the additional effect of the shrouds in reducing the non-ideal power losses of the rotor. Increasing the lip radius and decreasing the blade tip clearance caused performance to improve while optimal values of diffuser angle and length were found to be 10 and 50% of the shroud throat diameter, respectively. With the exception of the lip radius, the effects of changing any of the shrouded-rotor parameters on performance became more pronounced as the values of the other parameters were changed to degrade performance. Measurements were also made of the wake velocity profiles and the shroud surface pressure distributions. The uniformity of the wake was improved by the presence of the shrouds and by decreasing the blade tip clearance, resulting in lower induced power losses. For high net shroud thrust, a favorable pressure distribution over the inlet was seen to be more important than in the diffuser. Strong suction pressures were observed above the blade-passage region on the inlet surface; taking advantage of this phenomenon could enable further increases in thrust. However trade studies showed that, for a given overall aircraft size limitation, and ignoring considerations of the safety benefits of a shroud, a larger-diameter open rotor is more likely to give better performance than a smaller-diameter shrouded rotor. The open rotor and a single shrouded-rotor model were subsequently tested at a single collective in translational flight, at angles of attack from 0 (axial flow) to 90 (edgewise flow), and at various advance ratios. In axial flow, the net thrust and the power consumption of the shrouded rotor were lower than those of the open rotor. In edgewise flow, the shrouded rotor produced greater thrust than the open rotor, while

15. SUBJECT TERMS

16. SECURITY CLASSIFICATION OF:			17. LIMITATION OF ABSTRACT	18. NUMBER OF PAGES	19a. NAME OF RESPONSIBLE PERSON
a. REPORT **unclassified**	b. ABSTRACT **unclassified**	c. THIS PAGE **unclassified**	**Same as Report (SAR)**	**349**	

effects of changing any of the shrouded-rotor parameters on performance became more pronounced as the values of the other parameters were changed to degrade performance.

Measurements were also made of the wake velocity profiles and the shroud surface pressure distributions. The uniformity of the wake was improved by the presence of the shrouds and by decreasing the blade tip clearance, resulting in lower induced power losses. For high net shroud thrust, a favorable pressure distribution over the inlet was seen to be more important than in the diffuser. Strong suction pressures were observed above the blade-passage region on the inlet surface; taking advantage of this phenomenon could enable further increases in thrust. However, trade studies showed that, for a given overall aircraft size limitation, and ignoring considerations of the safety benefits of a shroud, a larger-diameter open rotor is more likely to give better performance than a smaller-diameter shrouded rotor.

The open rotor and a single shrouded-rotor model were subsequently tested at a single collective in translational flight, at angles of attack from 0° (axial flow) to 90° (edgewise flow), and at various advance ratios. In axial flow, the net thrust and the power consumption of the shrouded rotor were lower than those of the open rotor. In edgewise flow, the shrouded rotor produced greater thrust than the open rotor, while consuming less power. Measurements of the shroud surface pressure distributions illustrated the extreme longitudinal asymmetry of the flow around the shroud, with consequent pitch moments much greater than those exerted on the open rotor. Except at low airspeeds and high angles of attack, the static pressure in the wake did not reach ambient atmospheric values at the diffuser exit plane; this challenges the validity of the fundamental assumption of the simple-momentum-theory flow model for short-chord shrouds in translational flight.

HOVER AND WIND-TUNNEL TESTING OF SHROUDED ROTORS FOR IMPROVED MICRO AIR VEHICLE DESIGN

by

Jason L. Pereira

Dissertation submitted to the Faculty of the Graduate School of the
University of Maryland, College Park in partial fulfillment
of the requirements for the degree of
Doctor of Philosophy
2008

Advisory Committee:
Professor Inderjit Chopra, Chair/Advisor
Professor James D. Baeder
Professor Derek Boyd
Professor Darryll Pines
Professor Norman M. Wereley

Preface

Dedication

To my parents, Owen and Sherry, who showed the greatest understanding and restraint by never once uttering the words, "How is your thesis was coming along?", always instead leaving it to me to tell them if I so chose.

Acknowledgements

Thanks are due to several people, without whom this research, and the lessons that I have learned as a graduate student, would never have occurred. First and foremost, to my advisor, Dr. Inder Chopra, who stood by me and continued to support and guide me through all the years it took me to complete this research, despite the many, many mistakes that I made. Stern, yet also gentle and forgiving, and with uncommon patience, he has been a father-figure to me in my professional academic career. I am grateful also to the other members of my advisory committee — Dr. Darryll Pines, Dr. Norm Wereley, Dr. Jim Baeder and Dr. Derek Boyd — for their insightful comments and suggestions regarding my research. To Dr. Pines I owe special thanks for his enthusiasm, encouragement and motivational pep talks, and for many discussions about my future professional career.

To my fellow graduate students and co-workers: Andy Bernhard, the first graduate student I ever worked with, and who has been my inspiration ever since; Paul Samuel, Felipe Bohorquez, Jayant Sirohi, Beerinder Singh, Ashish Purekar and Jeanette Epps, from whom I learned the fundamentals of conducting laboratory research; Shreyas Ananthan, Manikandan Ramasamy, Sandeep Gupta and Karthikeyan Duraisamy, who patiently answered all my questions about fluid dynamics; Paul Samuel (again), Jinsong Bao, Anubhav Datta and Shaju John, for support, encouragement and general 'graduate-student-advice', especially when times were rough; Nicholas Rosenfeld, Carlos Malpica, Joseph Conroy, Brandon Bush, Brandon Fitchett, Monica Syal, Abhishek Abhishek, and Felipe, Karthik and Mani (again), for the camaraderie and 'extra-curricular', recreational bonding that helped make my graduate-school experience an enjoyable one. These people, and numerous others, too many to mention here but remembered nontheless, have given me countless happy memories of my years at the Alfred Gessow Rotorcraft Center.

Similarly, to Bernard 'Bernie' LaFrance and Howard 'Howie' Grossenbacher,

Table of Contents

List of Tables

List of Figures

Nomenclature

A	shroud throat cross-sectional area $= \pi(D_t/2)^2$
A_R	rotor disk area, corrected for blade root cut-out $= \pi(R^2 - R_0^2)$
A_e	diffuser exit area
a	airfoil lift-curve slope $= \mathrm{d}C_L/\mathrm{d}\alpha$
C_D	drag coefficient $= D/\rho A(\Omega R)^2$
C_L	lift coefficient $= L/\rho A(\Omega R)^2$
$\bar{C}_L$	mean lift coefficient of rotor $= 6C_{T_{\mathrm{rotor}}}/\sigma$
C_M	pitch moment coefficient $= C_N \times x_{cp}/R$
C_N	normal force coefficient $= N/\rho A(\Omega R)^2$
C_P	power coefficient $= P/\rho A(\Omega R)^3$
C_p	pressure coefficient $= (p - p_{\mathrm{atm}})/q_{\mathrm{tip}}$
C_T	thrust coefficient $= T/\rho A(\Omega R)^2$
c	rotor blade chord
c_{S}	shroud chord
D	drag
D_{R}	rotor diameter
D_{t}	shroud throat diameter (minimum inner diameter)
J	propeller advance ratio $= v_\infty/nD_R$
L	lift
L_{d}	shroud diffuser length
M	pitch moment (at rotor hub)
$\dot{m}$	mass flow $= \rho Av$
N	normal force
N_{b}	number of blades
n	rotor rotational speed, rev/s
P	rotor shaft power $= \kappa P_{\mathrm{i}} + P_o$
P_{i}	ideal power
P_o	profile power
p	local static pressure
p_{atm}	ambient atmospheric pressure
Q	rotor torque
q_{tip}	dynamic pressure at blade tips $= \frac{1}{2}\rho v_{tip}^2$
R	rotor radius $= D_R/2$
R_0	rotor blade root cut-out
Re	Reynolds number
r	non-dimensional radial coordinate $= y/R$
r_{lip}	shroud inlet lip radius
S	shroud diffuser slant length $= L_d/\cos(\theta_d/2)$
s	non-dimensional distance along shroud surface
T	thrust
T_{total}	total shrouded-rotor thrust $= T_{\mathrm{rotor}} + T_{\mathrm{shroud}}$
t	shroud wall thickness

v	air velocity
v_i	(ideal) induced velocity at rotor plane
v_tip	rotor tip speed $= \Omega R$
v_∞	free-stream velocity (airspeed)
w	induced velocity in far wake of rotor
x_cp	location of model center of pressure
y	radial coordinate
z	axial coordinate, positive downstream from rotor

Greek symbols

α	model angle of attack; blade element aerodynamic angle of attack
α_rotor	conventional rotor angle of attack $= 90° - \alpha$
δ_tip	blade tip clearance $= (D_\mathrm{t} - D_\mathrm{R})/2$
ϕ	induced inflow angle $= \lambda/r$
κ	induced power correction factor
λ	induced inflow ratio $= v_\mathrm{i}/(\Omega R)$
μ	rotor advance ratio $= v_\infty \cos(\alpha_\mathrm{rotor})/\Omega R$
μ'	airspeed ratio $= v_\infty/\Omega R = J/\pi$
Ω	rotor rotational speed, rad/s
ρ	air density
σ	rotor solidity $= N_b c/\pi R$
σ_d^*	shroud diffuser expansion ratio $= A_e/A$
σ_d	expansion ratio, corrected for rotor hub blockage $= A_e/A_R$
θ_0	rotor collective (blade pitch angle)
θ	blade element pitch angle $= \alpha + \phi$
θ_d	diffuser included angle
θ_lip	shroud inlet lip angular coordinate
ψ	rotor azimuth angle

Subscripts

OR	Open (unshrouded) Rotor
SR	Shrouded Rotor
c	value in the climb condition
diffuser	component due to shroud diffuser
h	value in the hover condition
inlet	component due to shroud inlet
rotor	component due to rotor
shroud	component due to shroud

Shrouded-rotor model nomenclature

LRx	model with lip radius $= x\% \; D_\mathrm{t}$
Dy	model with diffuser included angle $= y°$
δz	model with blade tip clearance $= z\% \; D_\mathrm{t}$
Lw	model with diffuser length $= w\% \; D_\mathrm{t}$

Abbreviations

AoA	Angle of Attack
BEMT	Blade-Element-Momentum Theory
CFD	Computational Fluid Dynamics
DAS	Data Acquisition System
DL	Disk Loading $= T_{\mathrm{rotor}}/A$
FM	Figure of Merit $= P_i/P$
FM*	Generalized Figure of Merit $= \mathrm{FM}\sqrt{\sigma_{\mathrm{d}}}$
ID	Inner Diameter
MAV	Micro Air Vehicle
OAV	Organic Air Vehicle
OD	Outer Diameter
PL	Power Loading $= T/P$
rpm	revolutions per minute
UAV	Unmanned Air Vehicle
V/STOL	Vertical/Short Take-Off and Landing

Chapter 1

Introduction

1.1 Background: Micro Air Vehicles

One of the hallmarks of maturing technology is the increase in complexity and capability of the devices created by that technology, and in many cases the simultaneous decrease in size of those devices. In the multi-disciplinary field of air vehicle design and development, this characteristic is evident in all aircraft components, from propulsion and power generation systems to sensors, navigation systems and flight control systems — many of these in turn dependent on the incredible degree of miniaturization achieved in the computer and microchip-fabrication industries. This miniaturization has led to the development and widespread use of Unmanned Aerial Vehicles, or 'UAV's — aircraft that do not carry a human pilot, and are therefore often much smaller in size than conventional manned aircraft. The commonly-seen radio-controlled ('RC') aircraft flown by hobbyists around the world also fall into this category; however, these aircraft are meant primarily for entertainment purposes, and seldom have the capability of carrying a significant payload or mission equipment package (MEP). The term 'UAV' is therefore typically used for aircraft that are designed for a specific mission, either civil or military, and have actual utility towards that purpose.

The UAVs that are in use today vary in size from a few feet to several tens of feet[1], where, in the case of fixed-wing aircraft, the wingspan is typically regarded as the characteristic length, while for rotating-wing aircraft like helicopters, it is

_____

[1]Ryan Aeronautical / Northrop Grumman RQ-4 Global Hawk: 116 ft wingspan; Boeing A160 Hummingbird: 36 ft rotor diameter

the main rotor diameter that is used. The natural process of continuing minia-turization led people to consider the possibility of *mission-capable* aircraft that would be even smaller, with maximum spatial dimensions of a foot or less. In 1992, a DARPA[2]/RAND Corporation workshop on "Future Technology-Driven Revolu-tions in Military Operations" investigated the concept of 'mobile microrobots' at the 1-cm/1-g scale [1]. This was followed by a series of feasibility studies at the MIT Lincoln Laboratory and the U.S. Naval Research Laboratory, and led to the creation of a DARPA Small Business Innovation Research (SBIR) program in the fall of 1996 to develop this 'new dimension in flight' [2]. According to this program, the formal definition of a *Micro* Air Vehicle, or 'MAV', was an aircraft that would have no dimension larger than 15 cm (6 in), weigh approximately 100 g — which included a payload weight of 20 g — and have an endurance of one hour. The payload would typically be some type of sensor — optical, chemical or radiological, for example — and/or a radio transmitter. The envisioned military use of such an aircraft was as man-portable, 'eye-in-the-sky' flying robot that could be carried and operated by an individual soldier, for increased situational awareness while mini-mizing exposure of him- or herself to risk. Because of their small size and weight, these aircraft would have a much smaller footprint compared to the larger UAVs, not just in terms of the aircraft itself, but also with regard to their ground station and logistical trail, and would therefore be faster and easier to deploy, and would compete minimally with the other equipment that soldiers are required to carry — armament, food, water, protective gear, and the like. The primary driver for MAV development was therefore as a reconnaissance asset for military and paramilitary applications (Figs. 1.1a–d), but civilian applications such as power-line inspection, traffic monitoring and disaster-response management were also forseen for this tech-

---

[2]U.S. Defense Advanced Research Projects Agency — called the Advanced Research Projects Agency (ARPA) before March 1972 and between February 1993 and February 1996 (http://www.darpa.mil/body/arpa_darpa.html).

(a) Urban operations   (b) Bio-chemical sensing

(c) MAV-assisted pilot rescue   (d) 'Over-the-hill' reconnaissance
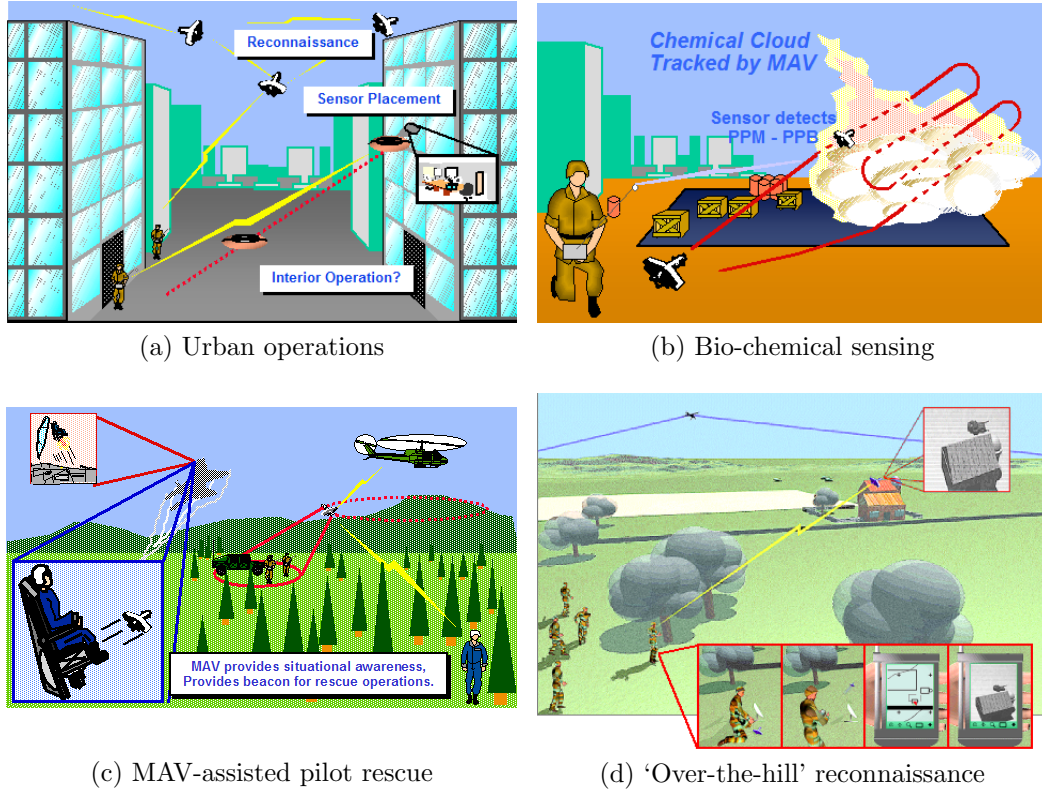
Figure 1.1: MAV missions [3]

nology.

1.2   The need for more efficient hover-capable MAVs

The early developmental work in MAVs led to the creation of highly-successful fixed-wing aircraft such as Aerovironment's *Black Widow*, which had an endurance of half an hour and a range of almost 2 km while weighing only 80 g [4]. However, such high-speed platforms — *Black Widow* had a loiter velocity of 25 mph — are restricted in operation to large, open spaces with a minimum of obstacles — outdoors, and at altitudes higher than the tops of trees and buildings. For operations in highly-congested, highly-cluttered environments like urbanized areas (the so-called 'urban canyon'), whether indoors or outdoors, aircraft are required that are capable of high maneuverability at low speeds, and even of hovering. Aircraft

3

that have these capabilities fall into three classes: rotating-wing configurations, like helicopters and tilt-rotors, flapping-wing configurations, like birds and insects — biological flyers, and fixed-wing configurations with powered-lift capability, such as the Hawker Siddeley Harrier and the Lockheed Martin Joint Strike Fighter (F-35 Lightning II). For any aircraft, low-speed flight and, if it is possible, hovering flight are inherently much more power-hungry than most other parts of the flight regime. Of the three classes of aircraft listed above, rotary-wing aircraft exhibit the highest efficiency in hover and low-speed flight. The potential for high efficiencies in flapping-wing — ornithoptic — configurations has been demonstrated for aircraft of the MAV-size and smaller [5, 6], but the mechanical and aeroelastic complexity of such mechanisms are hurdles that remain to be overcome.

Given that hovering and low-speed flight are already states of high power consumption, the situation is further exacerbated by the highly degraded performance of conventional airfoils at the MAV-scale. In fluid dynamics, the sense of scale is best quantified by a non-dimensional parameter called the Reynolds number (Re), which is proportional to the product of the size and the velocity of the object that is moving relative to the fluid. Large aircraft, such as commercial airliners, operate at Reynolds numbers in the tens of millions, whereas MAVs operate in a Reynolds-number regime of approximately 10,000 to 50,000 — three orders of magnitude lower (Figs. 1.2a–c). The Reynolds number is given by the formula:

$$Re = \frac{\rho v l}{\mu}$$

where ρ is the density of the fluid, μ is the dynamic viscosity of the fluid, v is the relative velocity between the object and the fluid, and l is a characteristic length of the object. This fluid-dynamic parameter can be considered as a ratio between

the inertial forces and the viscous forces that act on fluid elements in the flow.[3] At high Reynolds numbers the inertial forces dominate, while at low Reynolds numbers the nature of the flow is more strongly affected by the effects of viscosity. Where airfoils are concerned, this results in two immediate effects: first, a decreased ability of the fluid to withstand (or maintain) adverse pressure gradients, and therefore to separate easily from the surface of the airfoil, thereby reducing the maximum lift capability and increasing the pressure drag; and second, an increase in the skin-friction drag when the flow *does* remain attached to the airfoil (Fig. 1.3). Together, these effects result in extremely low lift-to-drag (L/D) ratios for airfoils in low-Reynolds-number flows. Certain airfoil shapes, similar to those found in bird and insect wings, are optimized for low-Re flight, and these do fare better — in this flight regime — than 'conventional' airfoils that have been designed for larger, manned aircraft; however, the highest L/D ratios achieved by even these optimized, low-Re airfoils are still substantially lower than those achieved by the conventional airfoils at higher Reynolds numbers [8].

The degraded performance of airfoils is an obstacle faced by both fixed- and rotary-wing MAVs, but it is especially critical for the latter, as they spend a large portion of their mission-profile in the power-intensive hovering and low-speed conditions. The hovering efficiency of a rotor is typically expressed in two different ways:

(i) By a non-dimensional parameter called the Figure of Merit (FM), which is the ratio of the ideal amount of power (P_i) required by the rotor to generate a certain amount of thrust, to the value of the actual amount of power (P) it requires:

$$\mathrm{FM} = \frac{P_\mathrm{i}}{P}$$

---

[3]An excellent exposition of the characteristics and significance of the Reynolds number is given by Vogel [7, Ch. 5].
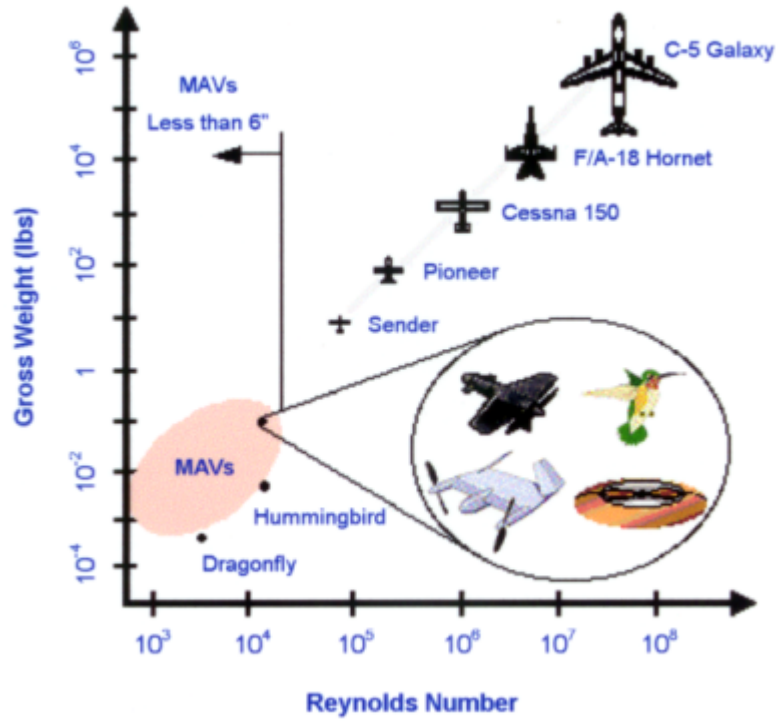
(a) From Ref. [2].
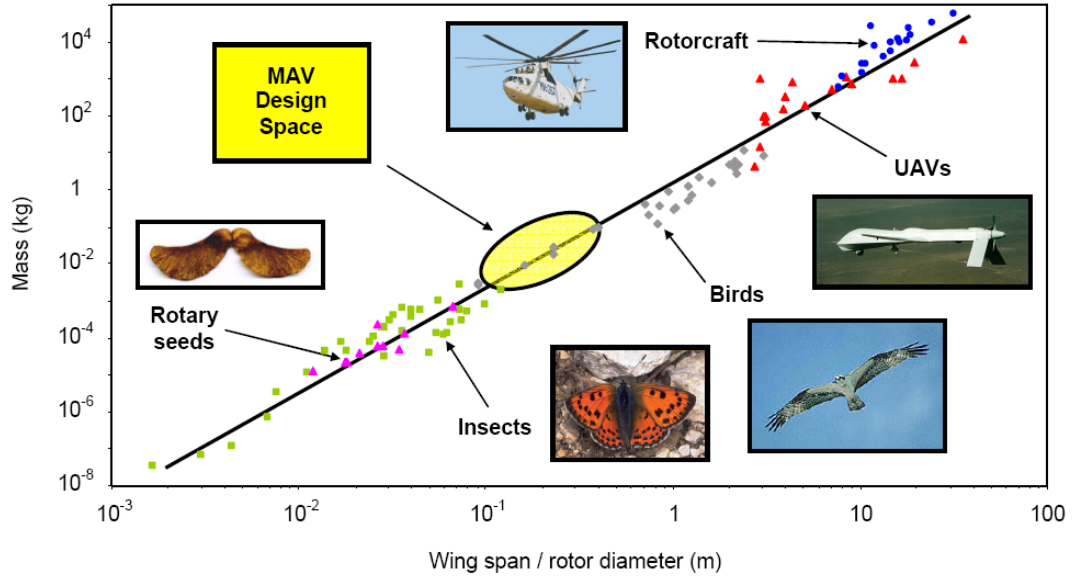
(b) From Ref. [5], from data in [9–11].

Figure 1.2: The MAV flight regime.
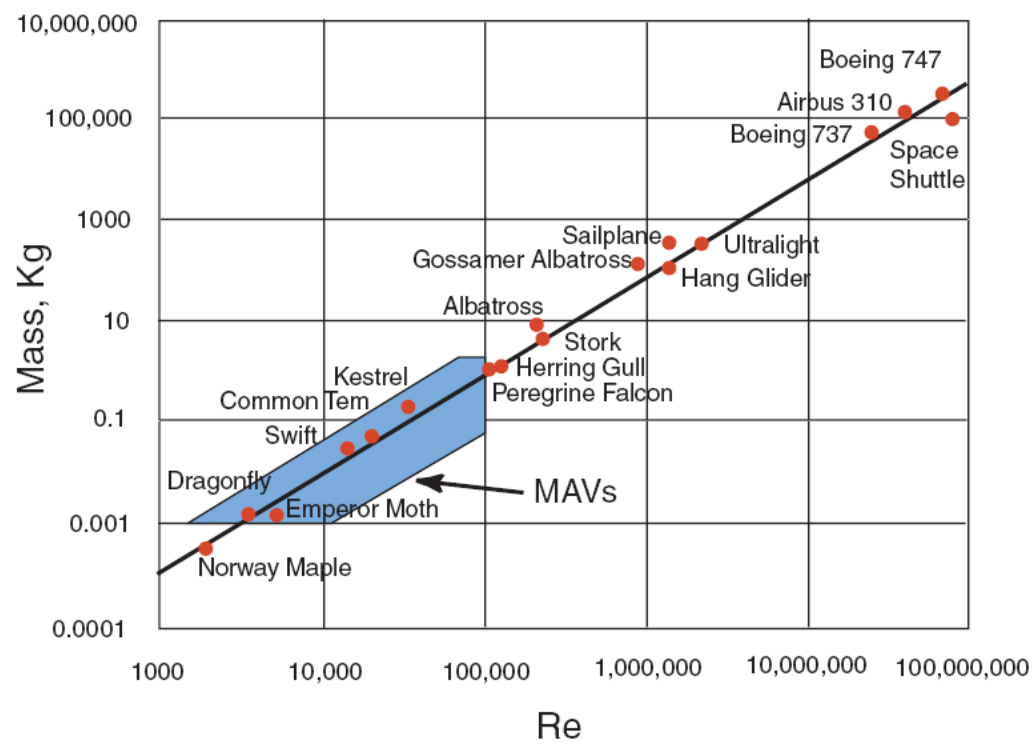
(c) From Refs. [8, 12], from data in [9].

Figure 1.2: The MAV flight regime (contd.)
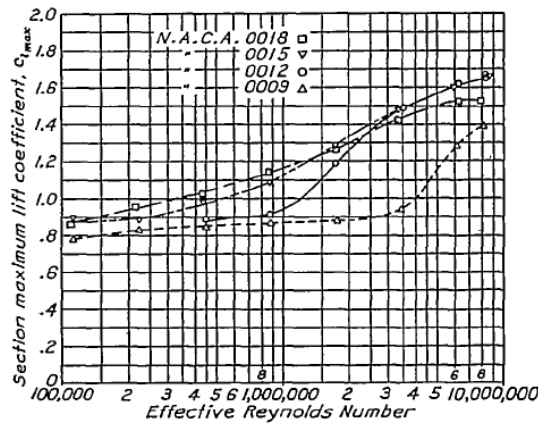
(a) Symmetric airfoils: Effect of thickness on maximum lift.
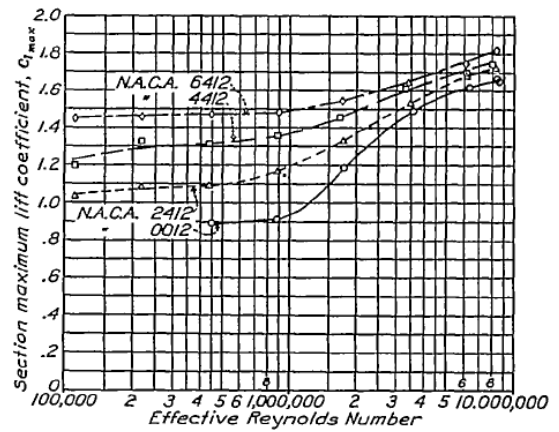
(b) Cambered airfoils: Effect of camber on maximum lift.
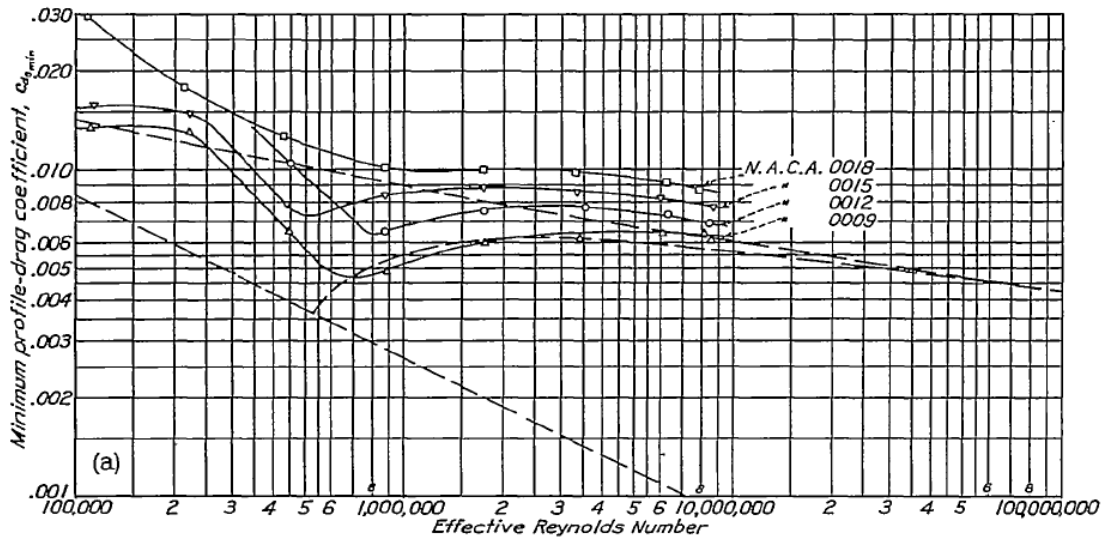
(c) Symmetric airfoils: Effect of thickness on minimum drag.
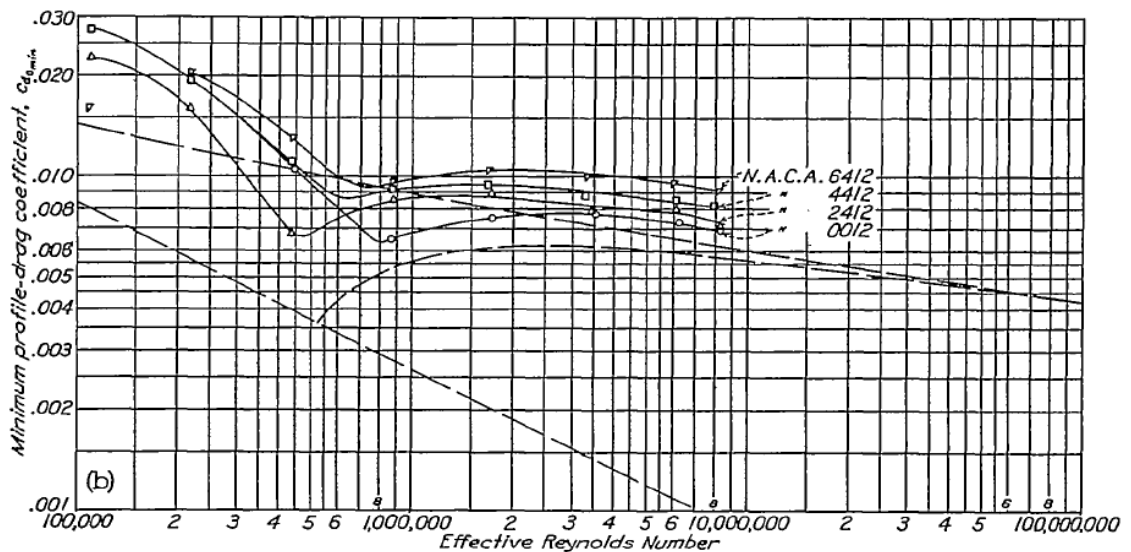
(d) Cambered airfoils: Effect of camber on minimum drag.

8

Figure 1.3: Effect of decreasing Reynolds number on the maximum lift coefficient and minimum drag coefficient of airfoil sections [13].

The maximum possible value of the figure of merit is therfore 1.0, which would imply a 'perfect' rotor.

(ii) By a dimensional parameter called the Power Loading (PL), which is the ratio of the thrust (T) produced by a rotor to the power (P) it consumes to produce that thrust:

$$\mathrm{PL} = \frac{T}{P}$$

As will be elucidated upon in Chapter 3 and in Appendix B of this dissertation, both of these formulations have their respective demerits. For example, a restriction on the former is that a comparison of the figures of merit of different rotors is only meaningful when they are operating such that they have the same rotor disk loading ($\mathrm{DL} = T/A$). The power loading, on the other hand, has the undesirable attibute of being a dimensional quantity, having units of velocity^{-1}, and is inversely proportional to the tip speed of rotor. A non-dimensional, tip-speed-independent form of this efficiency measure can, however, be obtained by taking the ratio of the coefficient forms of the rotor thrust and power ($C_T/C_P = v_\mathrm{tip} \times T/P$). For now, it suffices to state that rotors are desired to have the highest possible values of FM and power loading. Larger rotors that are used on conventional, manned helicopters have been designed that achieve figures of merit of up to 0.8 and power loadings of around 10 lb/hp [14, p. 43, p. 47]. Assuming a typical rotor tip speed of 700 ft/s (210 m/s) [15, pp. 683–701], this implies a C_T/C_P ratio of 12.6. MAV-scale rotors (Fig. 1.4) are currently capable of FM values of up to 0.65 [16], and while this is a significant improvment from the maximum values of 0.40–0.45 achieved by the early micro-rotors [17–19], the power requirements remain high: the data from investigations by Bohorquez and Pines [16] and Hein and Chopra [20], for example, indicate maximum values of C_T/C_P between 5.0 and 6.0, less than half that achieved at the larger scales. Reductions in power consumption would lead to
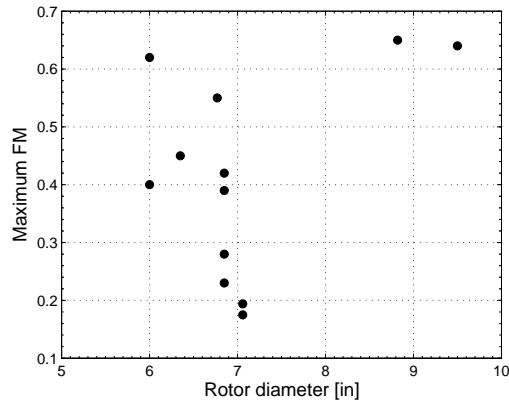
Figure 1.4: Maximum figures of merit achieved by MAV-scale rotors [16, 19–25].

increases in aircraft endurance beyond the 10–15 minutes currently achievable by rotary-wing MAVs [16], and/or reductions in the aircraft weight-fraction taken up by the energy-storage components like batteries, thereby allowing for larger payloads.

1.3 The shrouded-rotor configuration: Potential for improved performance

Improvements in airfoil and rotor design constitute one means of improving the efficiency of hover-capable MAVs. Another approach is to investigate alternative aircraft configurations that have the potential for performance better than that of conventional rotorcraft designs. One such configuration is the *shrouded rotor*, which involves surrounding the rotor with — in its most basic form — a cylindrical shroud or duct.[4] More commonly, the shroud resembles an annular airfoil or 'ring-wing', with camber and finite thickness that vary along its length, and with a rounded 'leading edge' and a smoothly tapered 'trailing' edge which form, respectively, the inlet and exit or diffuser sections of the shroud (Fig. 1.5). The shrouded-rotor configuration has been extensively investigated for over half a century and found to result

---

[4]An arbitrary convention that is sometimes adopted is that the enclosing structure is called a 'duct' if it is greater in length than the rotor diameter, and a 'shroud' or a 'short-chord duct' otherwise.

in significant gains in aerodynamic performance (increased thrust, reduced power consumption) compared to the unshrouded or 'open' rotor, and has therefore been utilized in various forms, from ducted propellers and ducted fans on powered-lift V/STOL aircraft to 'Fenestron' tail-rotors[5] on helicopters and ducted-rotor UAVs (Figs. 1.6a–p). For a shroud with a profile that is cambered inwards, like that shown in Fig. 1.5, and which therefore accelerates the flow towards the rotor, the performance gain is principally in static (hover) and near-static conditions. However, a benefit is obtained in high-speed forward flight as well: with the rotor pitched forward to provide the required thrust, the shroud, behaving as an annular wing, can provide the required lift — with potentially less than half the induced drag of a planar wing of the same aspect ratio [26, 27] — and, because of the induced flow of the rotor, can safely operate at angles of attack far greater than the stall angle of the 'unpowered' annular wing [27].

Finally, in addition to these aerodynamic benefits, shrouding the rotor conveys two other advantages over an open rotor: (1) the shroud can potentially attenuate the noise signature of the rotor, which is an advantage for MAV missions that require covert operation, and, (2) the shroud serves as a safety feature, protecting both the rotating blades from damage by other objects as well as personnel from injury by the blades. In fact, in most cases, it was this latter reason — improved safety — that the shrouded-rotor configuration was chosen for an aircraft design [28–33].

The performance benefit of shrouding the rotor derives principally from the ability of the diffuser section of the shroud to restrain the natural contraction of the flow after it passes through the rotor. For any fluid-dynamic propulsive device, the increase in velocity of the far wake over that of the free-stream fluid represents an 'induced' power expenditure that is unavoidable in the generation of thrust. Additional losses do arise due to the viscosity of the fluid, but even in the ideal case

---

[5]Also known as a 'Fan-in-fin', 'Fantail' or 'Ducted Tail Rotor', depending on the helicopter manufacturer.

11
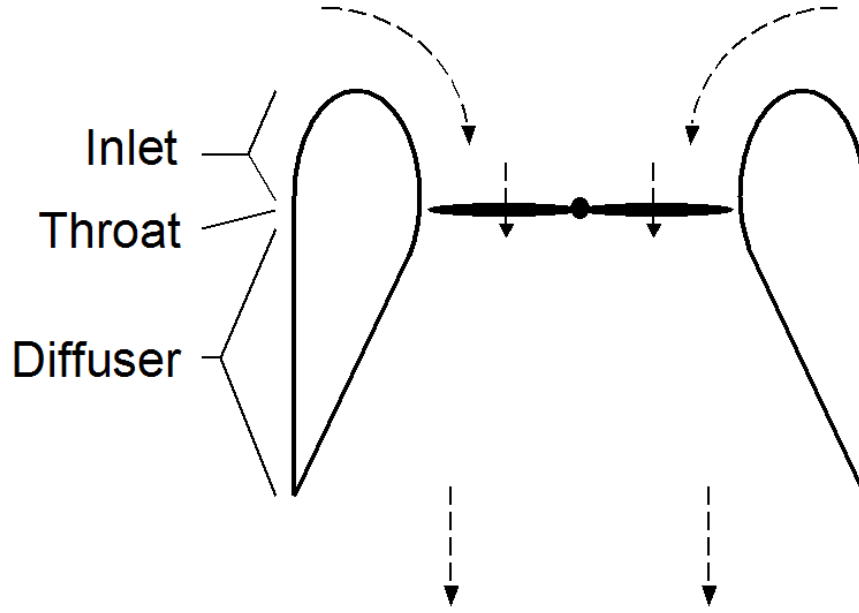
Figure 1.5: Cross-section of a shrouded rotor in hover.

of an inviscid fluid, this induced increase in the kinetic energy of the fluid constitutes the minumum possible power required to generate a given amount of thrust. For a conventional open rotor, by combining an actuator-disk model of the rotor with the conservation laws of fluid dynamics, the classical Momentum Theory is able to predict the increase in velocity at the far wake as being twice the value of the induced velocity at the plane of the rotor disk [14, Ch. 2; See also Appendix A of this dissertation]. By mass conservation, the contraction ratio of the slipstream is inversely proportional to the increase in velocity, and, in the hover condition, has a value of 1/2. In other words, the final cross-sectional area of the slipstream in the far wake is one-half that of the rotor disk area. In the case of a shrouded rotor, the change in area of the slipstream is determined by the shape of the diffuser. By using a cylindrical diffuser, or a diverging one, the slipstream can be forced to either maintain a constant cross-sectional area or to actually *increase* in area, respectively. Thus, if the flow is able to stay attached to the diffuser walls, the presence of the
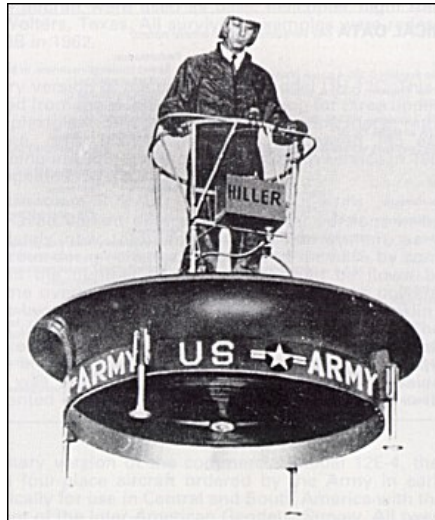
(a) Hiller VZ-1 Pawnee.
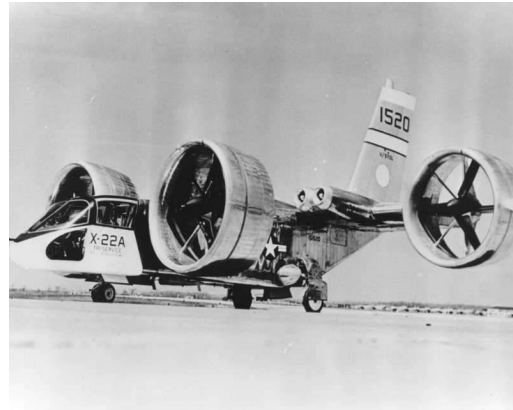
(b) Bell X-22A.

(c) Piasecki VZ-8 AirGeep.

(d) Doak VZ-4.

(e) GE/Ryan XV-5 Vertifan.

(f) Vanguard Omniplane.

Figure 1.6: Applications of shrouded rotors: Powered-lift V/STOL aircraft.

(g) Mississippi State University XAZ-1 Marvelette.

(h) Mississippi State University XV-11A Marvel.

(i) Piasecki 16H-1 Pathfinder.

(j) Piasecki 16H-1A Pathfinder II.

Figure 1.6: Applications of shrouded rotors: STOL aircraft and compound helicopters.

(k) Boeing/Sikorsky RAH-66 Comanche.

(l) Aérospatiale SA365 (HH-65) Dauphin.

Figure 1.6: Applications of shrouded rotors (contd.): Helicopter tail rotors.

(m) Sandia AROD.

(n) Sikorsky Cypher.

(o) Honeywell Kestrel.

(p) Microcraft/Allied Aerospace iSTAR.

Figure 1.6: Applications of shrouded rotors (contd.): Unmanned VTOL aircraft.

shroud is able to reduce the increase in velocity of the far wake, and thereby reduce the induced-power requirements of the rotor.

Just as for an open rotor, momentum theory can be used for a first-order prediction of the performance and characteristics of a shrouded rotor — with one difference: instead of using the actuator-disk model of the rotor, the assumption is made that the slipstream has fully expanded back to ambient atmospheric pressure at the exit plane of the diffuser. Therefore, a key parameter in determining the performance of a shrouded rotor is the diffuser expansion ratio (σ_d), which is equal to the ratio of the diffuser exit plane area (A_e) to the area of the rotor disk (A):

$$\sigma_\mathrm{d} = \frac{A_e}{A}$$

Appendix A (p. 269) contains detailed derivations of the predictions of momentum theory for a shrouded rotor, but some of the more important results are repeated here below. In the hover case, for a given total system thrust ($T_\mathrm{total} = T_\mathrm{rotor} + T_\mathrm{shroud}$), the ideal induced velocity at the rotor disk (v_i), the ideal induced power (P_i), the figure of merit (FM)[6] and the fraction of the total thrust produced by the diffuser of the shroud are given by:

$$v_\mathrm{i} = \sqrt{\frac{\sigma_\mathrm{d}\, T_{total}}{\rho A}} \tag{1.1}$$

$$P_\mathrm{i} = \frac{T_\mathrm{total}^{3/2}}{\sqrt{4\sigma_\mathrm{d}\rho A}} \tag{1.2}$$

$$\mathrm{FM} = \frac{C_{T_\mathrm{total}}^{3/2}}{2\sqrt{\sigma_\mathrm{d}}C_P} \tag{1.3}$$

$$\frac{T_\mathrm{diffuser}}{T_\mathrm{total}} = -\frac{(\sigma_\mathrm{d} - 1)^2}{2\sigma_\mathrm{d}} \tag{1.4}$$

The actuator-disk model of the rotor is used only to derive the fractions of the total

---

[6]In the shrouded-propeller/ducted-fan literature, this is often instead called the Static Efficiency (η_s).
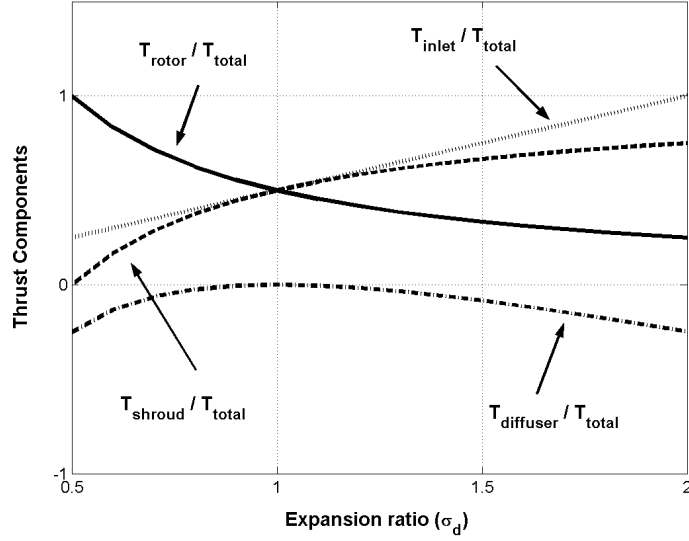
Figure 1.7: Shrouded rotor thrust components

thrust that are borne by the rotor disk itself and by the shroud inlet:

$$\frac{T_{\text{rotor}}}{T_{\text{total}}} = \frac{w}{2v_i} = \frac{A}{2A_e} = \frac{1}{2\sigma_d} \tag{1.5}$$

$$\frac{T_{\text{inlet}}}{T_{\text{total}}} = \frac{\sigma_d}{2} \tag{1.6}$$

Equations (1.4)–(1.6) are plotted as functions of the expansion ratio in Fig. 1.7. Note that these thrust fractions are functions of the expansion ratio only, and are independent of the precise shape of the shroud, and that as σ_d is increased, the rotor's contribution (T_{rotor}) to the total thrust decreases, while the shroud's contribution ($T_{\text{shroud}} = T_{\text{inlet}} + T_{\text{diffuser}}$) increases.

In the case of an open rotor, $T_{\text{rotor}} = T_{\text{total}}$, so, from Eq. (1.5), $\sigma_d = 1/2$, which is exactly the value of the 'expansion' that momentum theory predicts for an open rotor. Equations (1.1)–(1.3) therefore apply equally to both shrouded and unshrouded (open) rotors, with the effective value of 1/2 being used for the expansion ratio in the case of an open rotor.[7] In the case of a shrouded rotor with a diffuser

---

[7]Note, however, that applying the special-case formula for the figure of merit of an open rotor

expansion ratio greater than 1/2, the total thrust is clearly greater than the thrust acting on the rotor alone. The physical basis for this additional thrust is a region of low-pressure suction forces acting on the inlet of the shroud, caused by the turning of the air that the rotor ingests from around the sides of the shroud. This is directly analogous to the leading-edge suction on the nose of an airfoil. Similarly, just as the flow around an airfoil experiences a pressure-recovery region on the trailing surfaces of the airfoil, so too does the flow in the diffuser experience an adverse pressure gradient as it expands back to ambient atmospheric pressure. The inner surface of the diffuser therefore also experiences suction pressures and generates a negative thrust, as can be seen from Eq. (1.4). However, the positive thrust from the inlet is always large enough that the net shroud thrust (T_{shroud}) remains positive (for $\sigma_{\mathrm{d}} > 1/2$). A clear understanding of the preceding discussion can be obtained from Fig. 1.8, which illustrates qualitatively the variations in pressure through the flow-fields of an open and a shrouded rotor in hover. The equations used to generate these figures are also derived using the momentum theory model, and are given in Section A.1.1.4 of Appendix A (p. 279).

The momentum theory model also allows for comparison of the characteristics and performances of open and shrouded rotors, as functions of the expansion ratio of the shrouded rotor. For example, it can be shown that if an open and a shrouded rotor are compared such that both their rotor disk areas and the amount of (ideal) power they each consume are the same, then, with increasing expansion ratio, the total thrust produced by the shrouded rotor continuously increases, relative to the thrust produced by the open rotor. Simultaneously, the mass flow ($\dot{m}$) and induced velocity (v_{i}) through the shrouded rotor also increase, again relative to the corresponding values for the open rotor, while the final wake velocity (w)

— $C_T^{3/2}/\sqrt{2}C_P$ — to the case of a shrouded rotor would be incorrect, and would result in a value of FM that would be greater than the true value by a factor of $\sqrt{2\sigma_{\mathrm{d}}}$.

(a) Open rotor flow-field   (b) Shrouded rotor flow-field
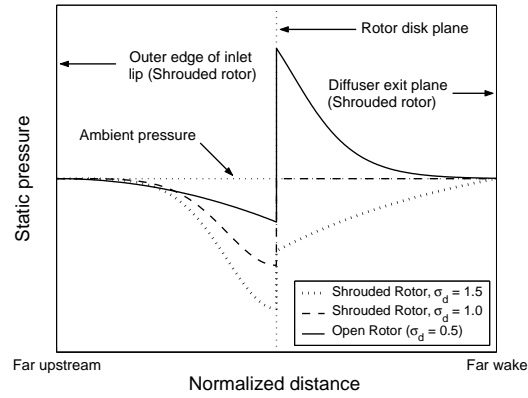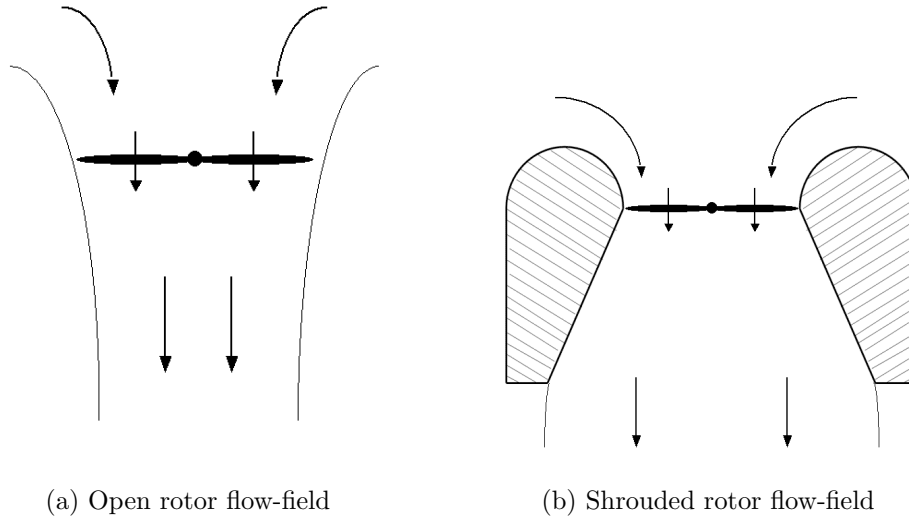
(c) Pressure variations

Figure 1.8: Variations in pressure in the hover flow-fields of open and shrouded rotors, at the same thrust coefficient

and the thrust provided by the rotor itself (T_{rotor}) decrease. These variations are described by Eqs. (A.27) in Appendix A, and have been plotted in Fig. 1.9a. In a similar manner, Fig. 1.9b illustrates the variations in these quantities when the open and shrouded rotors are compared such that their rotor disk areas and total thrust produced are held to be the same (Eqs. (A.28)). In this case, as in the previous one, the rotor thrust and wake velocity decrease with increasing expansion ratio, while the mass flow and induced velocity at the rotor disk increase, but it is also seen that the ideal power requirement also continuously decreases[8]. Thus, for example, with an expansion ratio of 1.0 — corresponding to a straight-sided, cylindrical diffuser — a shrouded rotor can theoretically produce 26% more thrust than an open rotor of the same size while consuming the same amount of power, or consume 29% less power while producing the same amount of thrust. Increasing the expansion ratio further causes the performance improvements to further increase, without limit — in theory.

In reality, upper limits on the amount of performance improvement are imposed by viscosity-dependent phenomena such as surface frictional losses and flow separation, which the 'simple' momentum theory is unable to account for. As the diffuser expansion ratio is increased, performance does improve, until at some point the flow is unable to counter the adverse pressure gradient in the diffuser and separates from the diffuser wall. Similarly, reducing the radius of the shroud inlet lip increases the turning that the air flowing into the shroud must accomplish. With increased turning, the suction pressures on the inlet increase[9]; but at some point, at a low enough lip radius, the flow will simply separate from the inlet surface before

---

[8]As will be shown in Chapter 3 and Appendix B of this dissertation, a consequence of this change in ideal power requirement with changing σ_{d} is that the figure of merit is not an appropriate way to compare the performances of an open rotor and a shrouded rotor, or, in general, shrouded rotors with different diffuser expansion ratios.

[9]Note, however, that with decreasing lip radius, the total surface area of the inlet on which those suction forces act also decreases, so it cannot be said a priori whether the resultant inlet thrust will increase, decrease, or remain the same.
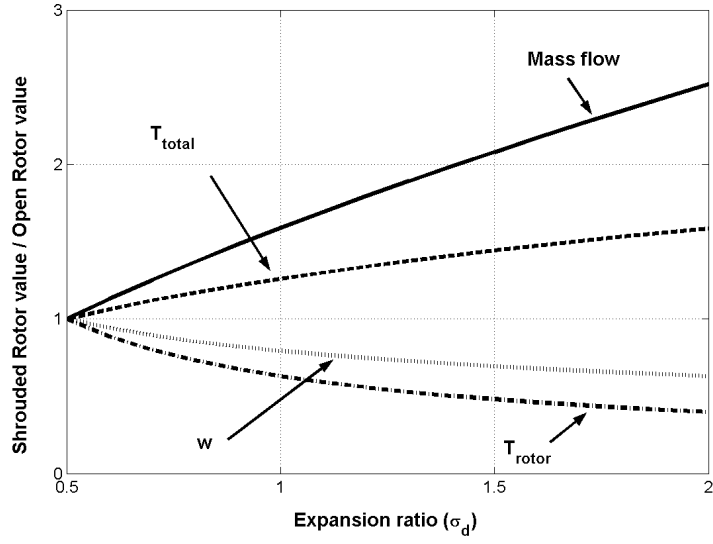
(a) Comparison at same rotor disk area and same ideal power
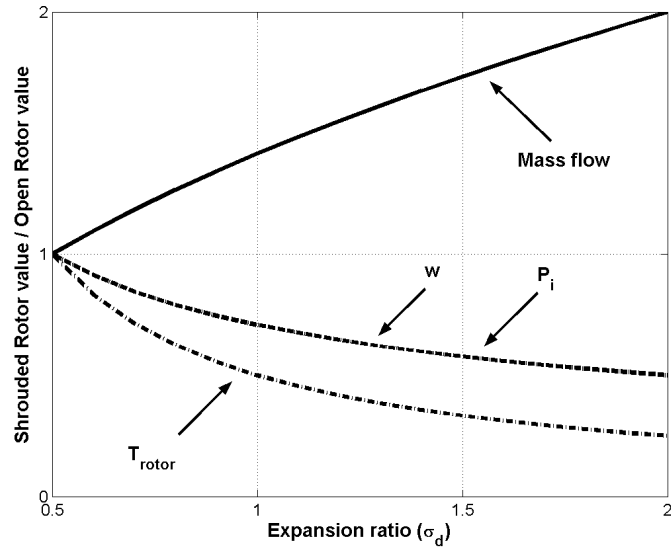
(b) Comparison at same rotor disk area and same total thrust

Figure 1.9: Comparison of characteristics of open and shrouded rotors

even reaching the rotor. This separated flow, when ingested by the rotor, causes further losses in thrust as well as increases in noise and vibration. Both of these separation phenomena are governed by viscous effects, and as such are strongly affected by the Reynolds number of the flow. Flow separation can be delayed by using a large inlet lip radius and by increasing the length of the diffuser, so that for a given expansion ratio, the expansion angle and the adverse pressure gradient in the diffuser are reduced; however, both these methods have the accompanying penalties of increasing the size and weight of the shroud, and of increasing the surface area and corresponding skin-friction losses. Careful design of the shroud is therefore of utmost importance: maximum possible performance improvement is desired while minimizing the increase in size and weight of the aircraft due to the shroud itself. For the shrouded-rotor configuration to be a viable option, the increase in thrust over that of an open rotor must be greater than the weight of the shroud, and/or a decrease in power required must be realized while producing a thrust increment equal to the weight of the shroud.

Additionally, the improvements or deterioration in performance of the shrouded rotor configuration over the baseline open rotor must be examined over the entire flight envelope and mission profile of the aircraft. In addition to the requirement for efficient hovering flight, it is important for a MAV to remain stable in gusting cross-winds, to be able to transition quickly to translational flight, and to have good forward-flight performance characteristics. In non-hovering axial-flow conditions like climbing flight, the natural contraction of an open rotor is less than in hover. Therefore, the benefits of having a diffuser that restricts this contraction become less significant, while conversely, the drag of the shroud becomes an important factor. In non-axial flow conditions (Fig. 1.10), besides the bluff-body drag of the shroud itself, the turning of the oncoming flow from the freestream direction to the axial direction results in the production of an additional momentum or 'ram' drag.

Although this is partly alleviated by the subsequent turning of the rotor wake from the axial direction back to the freestream direction, the ram drag is still "usually the largest [component of the total aircraft] drag, and ... can easily be 95% of the total drag at low velocities (< 10 knots)" [34].

The other adverse consequence of this turning of the flow from the freestream direction to the axial direction is that the turning is much sharper at the windward (forward) side of the shroud than at the leeward (aft) side. Equivalently, the windward side of the shroud effectively operates at a higher angle of attack to the flow than the leeward side, and therefore experiences greater suction on the inlet and produces more lift. For a regular, axisymmetric shroud design, this fore/aft aerodynamic dissymmetry leads to a strong nose-up pitch moment, much greater than that experienced by an open rotor[10]. This moment works in opposition to any command to pitch the vehicle nose-down into the wind and tilt the thrust vector forward, whether to maintain position while hovering in a gusty environment or to attain a forward translational flight. In a gust, for example, the resulting nose-up moment would actually tend to tilt the thrust vector towards the downwind direction, exactly the opposite as desired.[11] Reference [34] states that "robust, precise control in turbulent conditions ... including the complex, turbulent flow fields around buildings and trees ... poses one of the key technical hurdles for the successful operation of these vehicles. Current analysis shows that even in the best cases, typical position control of ducted-fan VTOL UAVs hovering in light winds (< 10 knots) is limited to about 10 feet of error." Further complicating the situation is the possibility of

---

[10]The nose-up pitch moment on an (untrimmed) open rotor is due to different reasons, depending on the type of rotor. For an articulated rotor, it is due to a *lateral* dissymmetry on the rotor — greater lift on the advancing blade than on the retreating one — and the 90° phase-lag of a harmonic system forced at its fundamental frequency, while for a rigid rotor it is due to a longitudinal variation in the rotor inflow — greater inflow and therefore lower angles of attack for the blades at the rear of the rotor.

[11]For a transient gust, the resulting motion in what was originally the downwind direction after the gust had died out could lead to a reversal of the direction of the pitch moment on the aircraft, and an ensuing oscillatory motion that might eventually damp out. The possibility — and details — of such motion can be ascertained from a dynamic stability analysis of the aircraft.
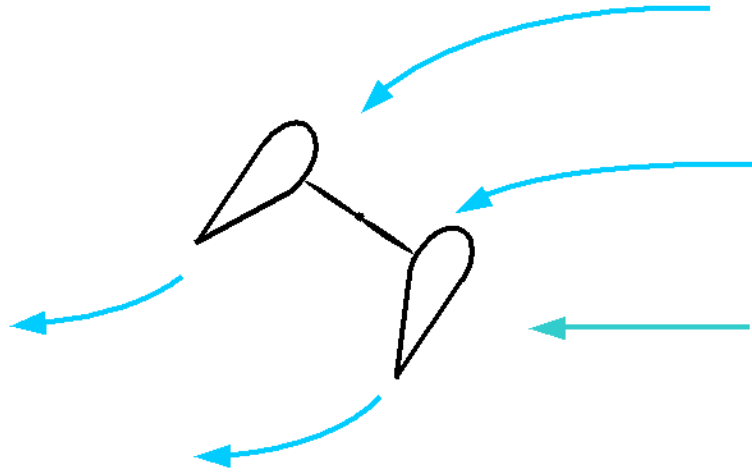
(a) Flow pattern.
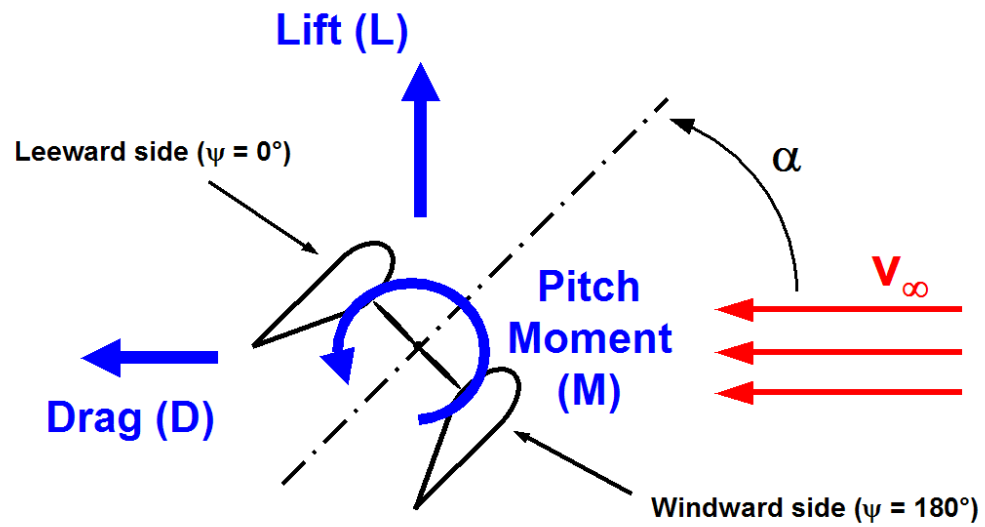
(b) Forces and moments.

Figure 1.10: Shrouded rotor in non-axial flight.

flow separation on the windward side of the inlet, which would lead to a sudden, sharp decrease in pitching moment ('moment stall'), perhaps to the point where the pitching moment reverses sign [35].

Besides the weight considerations of a shroud, it is these detrimental characteristics of a shrouded rotor that are of greatest concern to the aircraft designer. Clearly, for a shroud of fixed geometry, the design of the aircraft will be optimized for maximum performance improvement over the open rotor at a single point in the flight regime, which may be in hover or at some forward/translational speed. At all other points, the performance of the shrouded rotor will be sub-optimal, and possibly even worse than that of the open rotor. Variable-geometry inlets, diffusers and auxiliary control devices such as aft-mounted vanes may be considered, but these introduce their own associated trade-offs in weight and system complexity. Compromises such as these are therefore unavoidable in the design of the shroud. Another example of a compromise is the choice of the inlet lip radius: as mentioned earlier, a sharp inlet lip is disadvantageous in hover and in near-edgewise flight because it promotes early flow separation; on the other hand, such an inlet is beneficial in axial flight because it creates less drag [36]. Effects such as these, which depend on the detailed shape of the shroud, the design of the rotor and the Reynolds number of the flow, cannot be analyzed by the momentum theory model. More sophisticated theoretical models as well as experimental and computational-fluid-dynamic (CFD) investigations are therefore essential for the successful design of shrouded-rotor aircraft.

1.4   Previous research in ducted propellers and shrouded rotors

1.4.1   Historical overview

The idea of surrounding a rotor with an enclosing structure is not a recent one, although the reasons for doing so have been varied, and the question of who originally invented the concept remains open to debate. A US patent issued to Georges Hamel, a French citizen, in 1923 [37] describes a fixed-wing aircraft with propellers embedded in the wings, with their axes in the vertical direction, perpendicular to the wing chord: the so-called 'fan-in-wing' configuration (Fig. 1.11). The objective of the design was to "combine the principle of the aeroplane with that of the helicopter," and thus obtain an aircraft with both good performance in high-speed forward flight as well as improved safety in low-speed and vertical flight near the ground. The text of the patent makes no mention, however, of any enhancements in performance of either the wings or the embedded propellers due to their mutual interaction, so it is likely that the author was unaware of the existence of such a phenomenon. By 1933, however, as indicated by the application for another US patent filed by Ludwig Kort in Germany [38] (the patent was awarded in 1936), people had become aware of the potential for improvements in the the propulsive efficiency of *ship* propellers by surrounding them with "nozzle-shaped appendages attached to [the] ship's hull ... rings, straight or conical tubes or the like" (Fig. 1.12). However, "all of these combinations ... failed in practical use, as none of them were uniting the proper shape of the nozzle with the proper relation between the propeller, its revolutions, the areas at the narrowest cross section and at the mouth of the nozzle and the form, speed and resistance of the ship" [38]. At around the same time, in Italy, Luigi Stipa was investigating the effects of integrating an air propeller with a hollow airplane fuselage shaped like a venturi tube on the inside (Fig.1.13), and found similar increases in thrust and decreases in power consumption compared

to the open propeller [39, 40]. Credit is usually therefore given to Kort and to Stipa for the first serious, scientific, experimental work on optimizing the shape of a surrounding duct or shroud for improved thrust characteristics of marine and aeronautical propellers, respectively.[12] This was followed shortly afterwards, in the 1940s, by further systematic testing of different shroud profile shapes by Krüger at the Aerodynamics Research Institute (Aerodynamische Versuchsanstalt, or 'AVA') in Göttingen [43] and by the theoretical analyses of Küchemann and Weber, also in Germany [44–51], and then by a proliferation of studies around the world, including the United States. The objective of much of this early work was to improve the efficiency of regular airplane propellers — which were usually designed for optimal performance in high-speed cruising flight — at the low-speed and take-off flight conditions, by using the shroud to increase the inflow through the propeller [43, 52]. The increased inflow in static conditions also meant that that the *changes* in inflow with changing cruise speed would be smaller, resulting in more uniformly efficient performance of a fixed-pitch propeller over the entire aircraft mission profile, and less of a need for a mechanically-complex variable-pitch propeller. Fairchild et al. [53] provide a good historical overview of these research programs, and Sacks and Burnell [54] compiled an exhaustive survey of the experimental work and state-of-the art in ducted-propeller aerodynamics as of 1962. In the United States, in particular, the goal of developing viable V/STOL (Vertical/Short Take-Off and Landing) aircraft resulted in a considerable amount of experimental work that led (Figs. 1.6a–j, p. 13) to the design of 'flying platforms' such as the Hiller VZ-1 Pawnee and the Piasecki VZ-8 AirGeep [55], fan-in-wing aircraft such as the GE/Ryan XV-5 and the Vanguard Omniplane [56–58], tilt-duct aircraft like the Doak VZ-4 [59–68] and the Bell Aerosystems X-22A [69–76], and aircraft with non-tilting shrouded pro-

---

[12]Even today, shrouded marine propellers are frequently referred to as 'Kort nozzles', a widely-used series of which were systematically designed in the 1950s and '60s by the Maritime Research Institute Netherlands (MARIN) [41], just as the NACA did for airfoil shapes. A review of the state of the art in marine ducted propellers as of 1966 was compiled by Thurston and Amsler [42].
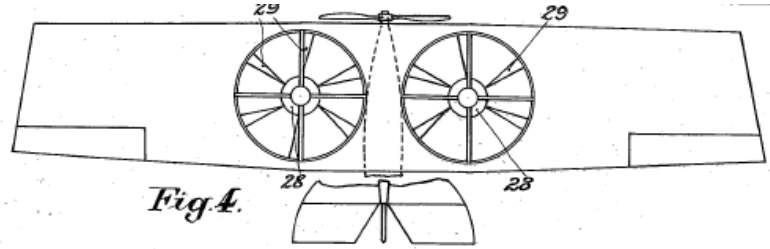
Figure 1.11: An illustration from Hamel's 1923 patent [37].
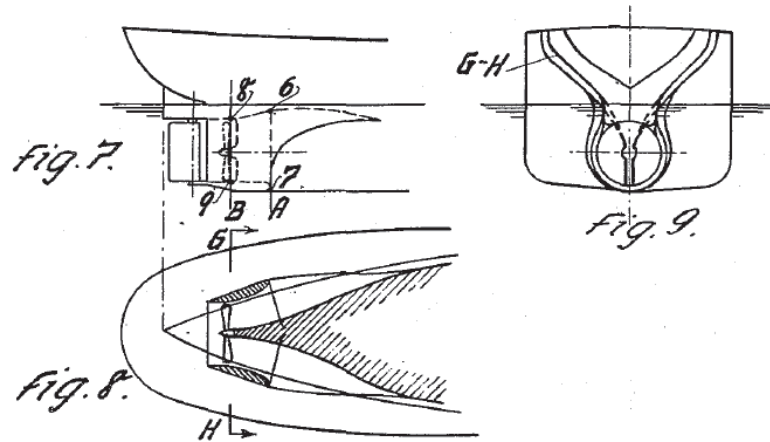
Figure 1.12: An illustration from Kort's 1936 patent [38].

pellers meant solely for forward propulsion, like the Mississippi State University's XAZ-1 Marvelette and XV-11A Marvel STOL aircraft [77] and the Piasecki 16H-1 Pathfinder and 16H-1A Pathfinder II compound helicopters. Similar work was also being carried out in Europe, such as that by the French company, Nord Aviation, in developing the tilt-duct Nord 500 Cadet aircraft [78] (Fig. 1.14).

From the 1970s onwards, the emphasis in research shifted from V/STOL aircraft to a different type of fan-in-wing application: the shrouded tail-rotor or 'fan-in-fin' on helicopters (Figs. 1.6k–l, p. 14). Originally developed by Aérospatiale in France for the SA.341 Gazelle helicopter, and termed the 'fenestron' [28, 79], the concept was then investigated and further developed by other helicopter manufacturers as well. Research at the Bell Helicopter Company [53] led to development of a 'Ducted Tail Rotor' on a modified Model 222 helicopter [80, 81]. Earlier tests
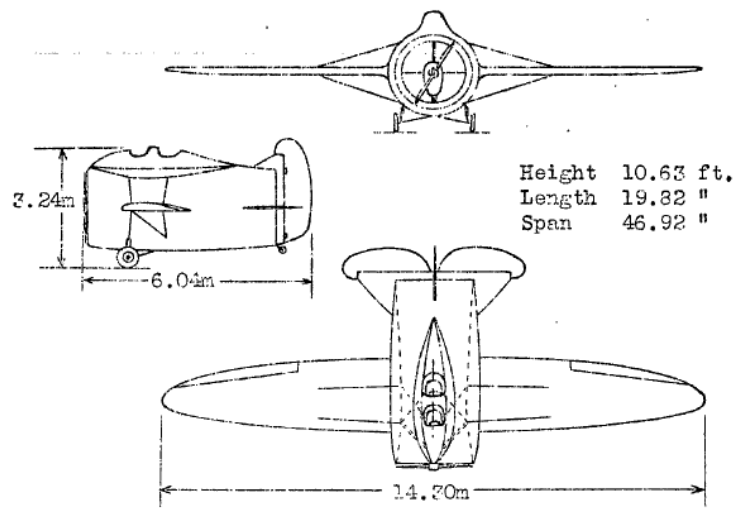
Figure 1.13: Stipa's 1933 venturi-fuselage monoplane design [40].

Figure 1.14: Nord 500 'Cadet'.

of a thin (less than 2 inches thick), protective ring called a 'Ring-Fin' around the tail rotor of a modified Model 206 JetRanger (Fig. 1.15) revealed thrust augmentation effects from even this rudimentary structure [82, 83]. The Sikorsky Division of the United Technologies Corporation tested a fan-in-fin on its S-67 Blackhawk prototype, which had originally been designed with a conventional tail rotor [84]. Based on that experience, the Boeing-Sikorsky team incorporated a 'FANTAIL^{TM}' tail rotor in its winning proposal for the US Army's Light Helicopter Experimental (LHX) program: the RAH-66 Comanche [31, 85–91]. In Japan, Kawasaki Heavy Industry, Ltd., used a fan-in-fin system for the XOH-1 observation helicopter [32], as did, in Russia, the Kamov Company in the design of the Ka-60 'Kasatka' ('Killer Whale') helicopter [92]. Meanwhile, Aérospatiale, which later (in 1992) merged with Messerschmitt-Bölkow-Blohm (MBB) of Germany to form Eurocopter, continued to develop the fenestron [29, 30, 33, 93], and incorporated it in several of its helicopter models: the SA/AS365 and EC155 Dauphin 2, the AS565 Panther, EC120 Colibri, EC130, and EC135/635.

As interest grew in *unmanned* VTOL aircraft, which would operate in cluttered environments and in close proximity to humans, the shrouded-rotor configuration was an obvious choice, given the safety benefits of the shroud [18]. Indeed, as Fleming et al. [94] succinctly state: "For survivability, operational safety, packaging and transport considerations, the ducted fan configuration has become the preferred platform for small VTOL UAV development." For cancelling the torque reaction of the rotor, these vehicles either used stator vanes in the downwash of a single rotor or a pair of coaxial, counter-rotating rotors. Examples of such aircraft (see Figs. 1.6m–p on page 15) include the 'AROD', or Airborne Remotely Operated Device, developed in the 1980s by Moller and Sandia National Laboratories for the US Marine Corps' Exploratory Development Surveillance and Ground Air Telerobotic System (GATERS) programs [35, 95, 96], the 'Cypher', developed by the Sikorsky
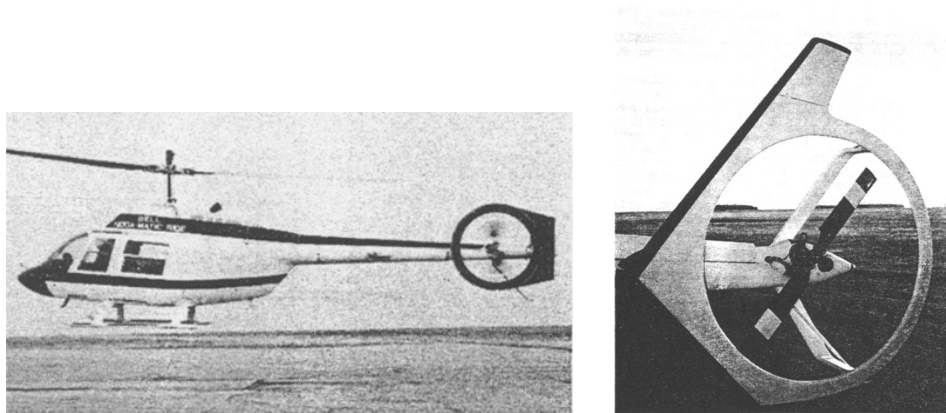
(a) Ring-Fin shapes being tested on a Bell 206.
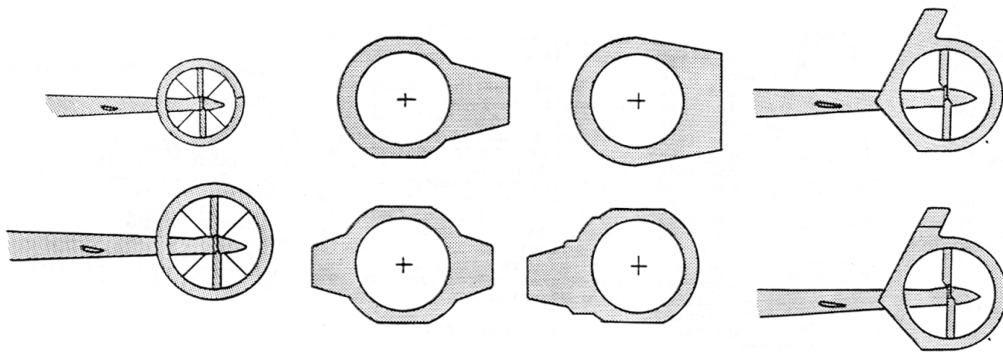
(b) Ring-Fin shapes tested.
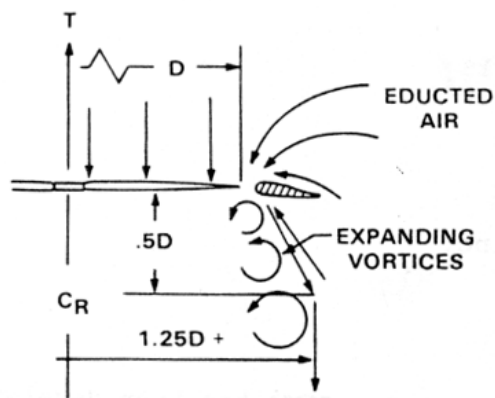
(c) Ring-Fin wake structure.

Figure 1.15: Ring-Fin tail rotors tested at the Bell Helicopter Company [82, 83].

Aircraft Corporation in the 1990s for the US military's Air-Mobile Ground Security and Surveillance System (AMGSSS) program [96–110], and, most recently, the Honeywell 'Kestrel' and Micro Craft[13] 'Lift-Augmented Ducted Fan' ('LADF')[14], both developed in the last decade in response to the DARPA MAV/OAV (Organic Air Vehicle) programs [27, 112, 113].

1.4.2   Experimental work: Effects of variations in shroud design

As can be seen from Fig. 1.5 (p. 12), the cross-sectional profile shape of a shroud closely resembles that of an annular wing, albeit with camber inwards rather than outwards. Design and optimization of the shroud for a shrouded-rotor application is therefore very similar to the design of airfoil profiles: parameters involved include chordwise thickness and camber distributions, leading-edge (inlet lip) radius, angle of attack to the freestream, and, in this special case of an annular shape, the ratio of the diameter to the chord (the 'aspect ratio', D_t/c_S). However, a number of additional parameters specific to the case of a rotor–shroud assembly need to be considered as well: these are the number and configuration of blade stages, i.e., rotors and/or non-rotating stators or guide vanes, the chord-wise locations of the blade stages within the shroud, and the size of the gap between the blade tips and the shroud wall, to say nothing of the myriad of variables involved in the detailed design of the rotor stages and blades themselves. The design space is vast, and the numerous studies conducted on shrouded rotors invariably focused on different subsets of these various parameters. Some of these studies are described below, but before doing so, it is worthwhile to note that, excluding the last aspect of the design mentioned above, i.e., the configuration and detailed design of the blade stages, it

---

[13]A division of Allied Aerospace Industry Incorporated.

[14]Also known as the 'iSTAR' vehicle — an acronym for 'Intelligence, Surveillance, Target Aquisition, Reconnaissance', and seemingly derived from a Hughes Missile Systems Company design, as suggested by a patent awarded to Ebbert et al. in 1994 [111].

was found that the performance and characteristics of shrouded rotors were most strongly dictated by a small subset of parameters: the diffuser expansion ratio and expansion angle, the inlet lip radius, and the blade tip clearance (Fig. 1.16). The importance of carefully selecting the value of the inlet lip radius and diffuser expansion angle was discussed earlier in Section 1.3, namely, the trade-offs between improving performance, avoiding flow separation and minimizing vehicle weight. The third variable — the blade tip clearance — plays a critical role because of the fact that the close proximity of the shroud wall impedes the formation of the strong blade tip vortices which otherwise reduce the thrust produced on an open rotor. Although some leakage flow from the high-pressure region below the rotor disk to the low-pressure region above it is unavoidable, minimizing the tip gap was always found to improve performance. In fact, in several studies [57, 114], the losses due to the tip vortices on an open rotor caused the performance improvements from shrouding the rotor to be *greater* than those predicted by momentum theory, which assumes ideal conditions for both the open and shrouded rotors.[15] A large tip gap allows stronger tip vortices to form and not only reduces the rotor thrust, but also reduces the shroud thrust due to suction on the inlet by reducing the inflow velocities at the shroud wall. In addition, as stated by Ahn [115], "the less energized flow in [the] blade-tip region generates [a] slower-flow region [that] . . . reduces the effectiveness of the [diffuser], by surrounding the [more-] energized flow and preventing its expansion." The minimum size of the tip gap is limited by the danger of the blades striking the shroud wall, either during 'normal' operation or because of excessive

---

[15] Another possible reason for this phenomenon is the off-loading of the rotor by the shroud: At the same total thrust, the greater induced velocity at the rotor causes the blades to operate at a lower angle of attack, compared to the open rotor, and therefore to not only produce lower thrust (T_{rotor}) than the open rotor (Fig. 1.9b), but also consume less profile power. If the factor of reduction in the profile power is greater than that for the reduction in the ideal induced power, as predicted by momentum theory, then the net improvement in performance will be better than that predicted. This, of course, requires consideration of the additional power input required to offset the losses due to friction from the shroud wall, and requires a more detailed analytical model. Whichever the reason, several investigations have found that shrouded rotors come closer to achieving their ideal predicted performance than do their unshrouded counterparts [52, 114].
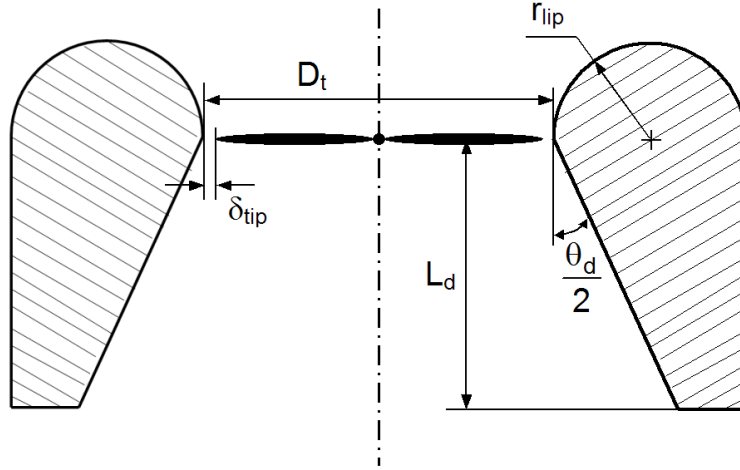
Figure 1.16: Principal shroud parameters affecting shrouded-rotor performance: diffuser included angle (θ_d), diffuser length (L_d), inlet lip radius (r_lip) and blade tip clearance (δ_tip).

vibrations or blade flapping amplitudes. In many applications, though, such as in some gas turbine engines and also in the Comanche FANTAIL[TM] design [31], the gap is closed off near-completely by lining the shroud wall with a brush or some sort of expendable, easily-abradable material at the blade-passage region.

The details of the shrouded-rotor configurations tested in the studies described in the following pages are tabulated for easy comparison in Table 1.1. Parameters for which values were not available are marked with a dash (" – "). Where possible, values for some parameters have been approximated from the shroud coordinates and other information given in the literature, and have been noted as such. For example, where the precise value of the inlet lip radius was not available, this was approximated, as an upper bound, as half of the maximum thickness of the shroud wall. For some shroud models, such as those used on the VZ-4 and the X-22A [68, 72, 116], and those tested by Martin and Tung [117], values of both the true leading-edge radius and the wall thickness were given. Assuming these cases to be typical, the lip radii of the other models can be expected to be about one-half of this upper-bound value. For the diffuser, two values for the expansion ratio are listed: σ_d^*, which is

the geometric value of the shroud alone (A_e/A), and σ_d, which is the effective value after correction for the blockage by the rotor hub (A_e/A_R):

$$\sigma_d = \sigma_d^* \times \frac{A}{A_R} = \frac{\sigma_d^*}{1 - \left(\frac{R_0}{R}\right)^2}$$

In cases where the diffuser internal surface was very nearly conical, i.e., with straight sides, and the value of one of the three diffuser variables — expansion ratio, expansion angle or length — was not given, it has been calculated using the relation:

$$\sigma_d^* = \left[1 + 2\frac{L_d}{D_t} \tan\left(\frac{\theta_d}{2}\right)\right]^2$$

Where the diffuser length was not explicitly given, and the exact chordwise position of the rotor within the shroud also indeterminable, the total length of the shroud (c_S) has been listed, and has been noted as such.

In addition to the shroud parameters, the table also lists some of the rotor parameters of the test items: the blade root-cutout (R_0), the blade tip speed (v_{tip}), the number of blades (N_b), the amount of blade twist (θ_{tw}), as measured from the blade tip to the blade root, i.e., the attachment point to the hub, and the rotor collective angles (θ_{75}), measured at the 75% radial station, for which test data were presented in the literature. Finally, unless otherwise specified, the 'diameter' of a shroud refers to its throat or minimum inner diameter, D_t.

Table 1.1: Previous experimental work: Shrouded-rotor configurations

Test gram	Pro-	D_t [in]	θ_d [°]	σ_d^*	σ_d	R_0	L_d [%D_t]	r_{lip} [%D_t]	δ_{tip} [%D_t]	v_{tip} [ft/s]	N_b	θ_{tw} [°]	θ_{75} [°]	Other notes
Stipa, [39]	1931	20.5 (inlet)	–	1.0	–	–	300	–	–	160–440	2	–	17°, 14°	3 shrouds, 2 propellers
Bell, [118]	1941	21	–	–	–	0.69R	–	–	–	330	24 (c'vanes: 37)	6 (c'vanes: 9)	5–40 (c'vanes: 40–70)	Upstream con-travanes
Kruger, [43]	1944	9.5 (24 cm)	–	0.88, 1.14 (0.66–1.49)	1.0, 1.3 (0.75–1.70)	0.35R	34, 22	–	–	500	8	45, 37.5	25–65	15 shroud shapes
Platt, [52]	1948	48	7, 14.4, 22.4	1.1, 1.3	1.24, 1.46	0.33R	33.6, 50.2	4.1 ($\frac{1}{2}$ t_{max})	0.13 (1/16")	420–630	Upper: 5, Lower: 7	33	OR: 15–50, SR: 35–45	Coaxial
Hubbard, [119]	1950	48	–	~1.1, 1.19, 1.25	1.21, 1.31, 1.37	0.3R	12, 24, 36	1.07, 1.43, 1.49	0.2 (3/32") – 4.4	690	2	27	21.5	Shroud shapes = NACA 4312, 4315, 4318 with enlarged nose radii
Parlett, [55]	1955	18	0	1.0	–	–	34	1.4–8.3 (fwd. flight: 1.4 only)	0.33 (0.06")	470–825 (fwd. flight: 470 only)	2	–	8	Shroud shape = cylindrical shell

Table 1.1: (contd.)

Test Program	D_t [in]	θ_d [°]	σ_d^*	σ_d	R_0	L_d [%D_t]	r_{tip} [%D_t]	δ_{tip} [%D_t]	v_{tip} [ft/s]	N_b	θ_{tw} [°]	θ_{75} [°]	Other notes
Taylor, 1958	16	0, 7, 14	1.0–1.5	1.07–1.60	0.25R	3, 28, 53, 78, 103	0, 1.56, 3.13, 6.25, 12.5	0.4 (1/16")	–	3	18	12–37	Fan-in-wing config
Doak VZ–4 [68, 72, 116]	48	22	1.28	1.33	0.33R	34.4	2.5 (2.45 for NACA xx18 ($\frac{1}{2}$ t_{max} = 5.43)	0.06 (0.03")	380–1000	8 (inlet guide vanes: 7, stators: 9)	33 (inlet vanes: 0, stators: 15)	18–50	Thickness distribution approx. that of a NACA 0018 airfoil.
Bell X-22A [72, 75, 116]	84	~17 (calc.)	1.21	1.27 (1.17, acc. for blockage by exit vane)	0.18R	~33	2.36 (2.07 for NACA xx18 ($\frac{1}{2}$ t_{max} = 4.98)	0.45 (3/8") (0.3–2.0 tested)	–	3 (stators: 6)	41	14–49	Thickness distribution approx. that of a NACA 0018 airfoil.
Black et al., 1968 [114]	30	7 (base), 14, 20, 9.3 (short-chord)	1.1 (base), 1.2, 1.3	1.17 (base), 1.28, 1.39	0.25R	30 (short chord), 40 (base), 50 (prop moved up-stream)	5 ($\frac{1}{2}$ t_{max})	0.12 (base), 0.26, 0.56	600–1050	3 (base), 4	–	20–55	12 shrouded-propeller models

Table 1.1: (contd.)

Test Program	D_t [in]	θ_d [°]	σ_d^*	σ_d	R_0	L_d [%D_t]	r_{tip} [%D_t]	δ_{tip} [%D_t]	v_{tip} [ft/s]	N_b	θ_{tw} [°]	θ_{75} [°]	Other notes
Fairchild et al., 1973 [53]	12	0, 5, 10, 15, 20	–	–	–	20, 40, 60 (cs). Rotor at 16%, 31%, 45%, 71%cs.	–	0.52 (1/16")	220	–	19	10–30	σ = 7.3%, 14.5%, 21.8%, 29.0%
Sikorsky S-67 Blackhawk fan-in-fin testbed [84, 85]	56	0	1.0	–	0.39R	–	10	–	–	–		25, 35	–
Aérospatiale Gazelle; early Dauphins [15, 28, 79, 93]	28 (70 cm); 35 (90 cm)	7	~1.0	–	~0.46R	–	–	0.3 (2 mm)	690; 745	13	12.5, later 7; 8	1–49	σ = 0.46; 0.4
Later Aérospatiale Dauphins, Panther [29, 93]	43 (110 cm)	10 (7–25 tested)	~1.0	–	–	–	–	–	–	11	7	–	–
Boeing/Sikorsky H-76 FANTAIL™ demonstrator [85, 86]	47	10	1.0	–	–	–	7.5 (0.9–7.5 tested)	–	605	8	7	-20 – +50	σ = 0.64
Boeing/Sikorsky RAH-66 Comanche [87, 120]	54	10	–	–	–	–	–	–	–	8	7	-2 – 30	σ = 0.62 [88]

38

Table 1.1: (contd.)

Test Program	D_t [in]	θ_d [°]	σ_d^*	σ_d	R_0	L_d [%D_t]	r_{tip} [%D_t]	δ_{tip} [%D_t]	v_{tip} [ft/s]	N_b	θ_{tw} [°]	θ_{75} [°]	Other notes
Bell Ducted Tail Rotor [80, 81]	51.5	–	–	–	–	10, 20 (cs)	–	0.9 (3/8 in = 0.73%?)	600, 640, 680, 720	4, 5	–	–	Even and uneven blade spacing, σ = 0.284–0.422
Kawasaki XOH-1 [32]	43.3 (110 cm)	–	–	–	–	–	–	–	662	8	11	–	σ = 0.556.
Kamov Ka-60 [92, 121]	23.6 (60 cm)	8	1.1	1.25	0.35R	35	10	0.5 (3 mm)	245	11	12	−12 – +47	σ = 0.495
AROD [35]	16 (full-scale: 24)	7, 14	–	–	–	–	–	–	460	–	–	–	Full-scale thrust = 85 lbs
Sikorsky Cypher proof-of-concept vehicle [97]	60	–	~1.0	–	–	–	–	–	–	3 (ea.)	–	–	Coax. Wt. = 44 lbs. 3.8 hp engine.
Sikorsky Cypher baseline experimental model [97]	69 (ID/OD?)	–	~1.0	–	–	18 in (cs)	–	–	–	4 (ea.)	–	–	Coax. Wt. = 350 lbs. 65 hp engine.
Sikorsky Cypher technology demonstrator [98–100]	48	–	~1.0	–	–	40 (cs)	15.6 ($\frac{1}{2}t_{max}$)	–	650	4 (ea.)	–	–	Coax. Wt. = 170 lbs (empty), 300 lbs (MTOW). 45–58 hp engine.

Table 1.1: (contd.)

Test Program	D_t [in]	θ_d [°]	σ_d^*	σ_d	R_0	L_d [%D_t]	r_{tip} [%D_t]	δ_{tip} [%D_t]	v_{tip} [ft/s]	N_b	θ_{tw} [°]	θ_{75} [°]	Other notes
MIT PUAV [122]	10	–	–	–	–	60 (cs)	–	2.5 (0.25")		2 (ea.)	–	–	Coax. Shroud = NACA 0012. Wt. = 2.7 lbs.
Dyer, 2002 [123]	8.66 (22 cm)	0, 12, 23	1.00, 1.40, 1.82	–	–	86	1.4, 5.7, 11.5	0.23, 0.46 (0.5, 1.0 mm)	Up to 230	2 (ea.)	–	0–35	Coax. σ = 0.17 (ea.) Wt. = 12 lbs.
Fleming et al., 2003 [34, 94]	10	–	–	–	–	60 (cs)	5.7 ($\frac{1}{2} t_{max}$)	1.0 (0.1 in)	220–570 ft/s	2	–	–	Shroud cambered outwards. Max thrust: 7.6 lbs. 1.6-hp motor.
Martin & Tung, 2004; Martin & Boxwell, 2005 [117, 124]	10	~0	~1.0	~1.12	0.33R	58 (cs)	1.7, 2.9 ($\frac{1}{2} t_{max}$ = 5.5, 5.8)	0.5, 0.75, 1.0, 1.25, 1.5, 2.0 (0.05–0.2 in)	85–415 ft/s	2	–	–	Shroud cambered outwards. Also tested notched and stepped shroud profiles with extended-diameter rotor.

Table 1.1: (contd.)

Test Program	D_t [in]	θ_d [°]	σ_d^*	σ_d	R_0	L_d [%D_t]	r_{lip} [%D_t]	δ_{tip} [%D_t]	v_{tip} [ft/s]	N_b	θ_{tw} [°]	θ_{75} [°]	Other notes
Graf et al., 2005 [125]	–	–	–	–	–	~50 (cs)	~0.8, 1.8, 1.9, 2.2, 3.0 ($\frac{1}{2} t_{max} \approx 3.1, 3.9$)	–	–	–	–	–	Different lip shapes, not just diff. lip radii.
Microcraft LADF [27]	9 (OD)	–	–	–	–	–	–	–	Up to 18000 rpm	2 (8 flapped stators)	–	–	Shroud weight: 117 gm (1/4 lb). GTOW: 3.1–3.5 lb. Max thrust: 4.3 lb. 1.2-hp engine.
Honeywell MAV	–	–	–	–	–	–	–	–	–	–	–	–	GTOW: 12.5 lb.
GTRI 'Bagel' (Active Flow Control testbed) [126–128]	11	–	–	–	–	31.8	9.1	0.1 (0.01 in)	170–500	3 (4 stators)	–	–	Thrust: 12 lb. Power: 2.4 hp (1.8 kW). $\sigma = 0.17$
Sirohi et al., 2005 [23, personal communication]	6.52	10	1.14	1.20	0.22R	40	12	1.27 (2.1 mm)	55–110	3 (4 stators)	0	18	$\sigma = 0.15$
Hrishikeshavan & Chopra, 2008 [25]	9.6 (24.4 cm)	0	1.0	–	–	24	15	0.6 (1.5 mm)	105–126	2	0	–	$\sigma = 0.115$

1.4.2.1 The early work

Stipa's 1931 experiments [39] consisted of static and wind-tunnel tests of two different conventional airplane propellers, approximately 20 inches in diameter, in isolation and coupled with three different duct shapes (Fig. 1.17). The ducts, in length approximately three times the diameter of the propellers, had the inner shape of a venturi and the outer shape of a wing profile. The propellers were located at the inlet plane of the ducts — not, as later became the convention, at the point of minimum inner diameter, or 'throat'. Since both the inlet and exit planes of the ducts had the same diameter, the effective expansion ratio for all three 'venturi-tubes' was equal to 1.0. Although the differences in the profile shapes of the three ducts involved changes in more than one parameter, the general changes were a decrease in thickness — corresponding to an increase in throat diameter, i.e., less constriction at the throat, a decrease in the expansion angle, and a decrease in the inlet lip radius — and a movement of the chordwise location of throat further back from approximately $0.25c_S$ to $0.45c_S$. In all cases tested, the 'intubed' propellers exhibited higher thrusts, static power loadings and propulsive efficiencies than the open propellers. Of the ducted configurations, the model with the thinner profile exhibited lower drag, higher propulsive efficiency and higher static shroud thrust.

In 1941, Bell [118] tested a 21-inch-diameter, 24-bladed, high-solidity fan (σ = 0.86) in a duct with and without contravanes upstream of the fan, at different fan-blade and contravane angles. When the contravanes were removed, the swirl angle in the flow increased from approximately 5–10° to approximately 24°, and
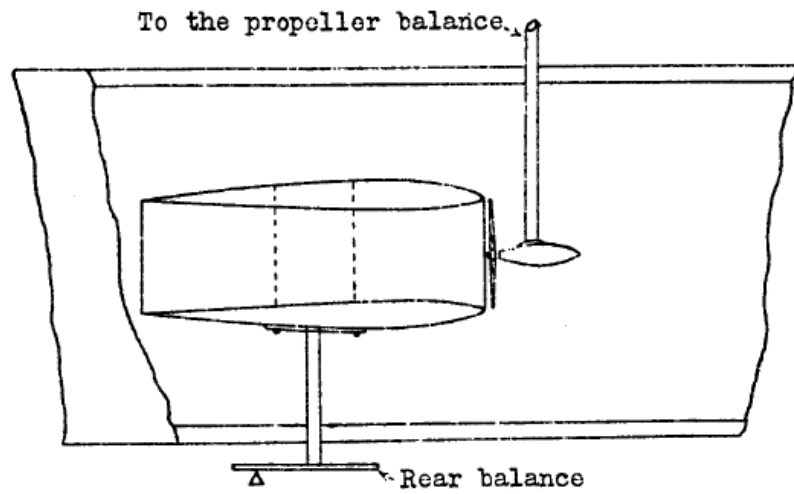
(a) Wind-tunnel set-up.
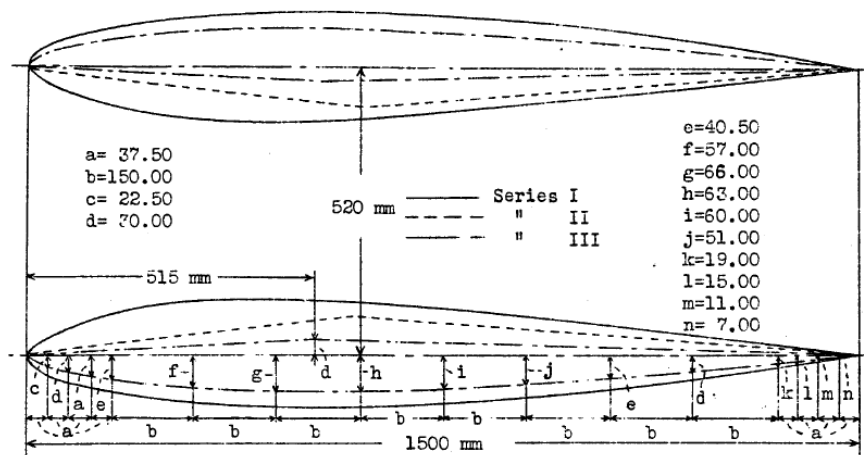
Fig. 1 Tube having inside shape of venturi tube and outside shape of wing profile. Scale 1.5 of the model. Longitudinal section.

(b) Models tested.

Figure 1.17: Stipa's 1931 venturi-tube wind-tunnel tests [39].

43

maximum figure of merit dropped from 0.88 to 0.80, indicating that "the rotational losses without contravanes were greater than the profile drag of the contravanes."

In the early 1940s, Krüger [43] conducted tests on fifteen different annular-airfoil shrouds with a 9.5-inch-diameter propeller (Fig. 1.18). The parameters varied between the shroud profile shapes were the chord, thickness, camber, and angle of incidence between the profile chordline and the propeller axis. Shrouds with both expanding and contracting 'diffusers' were tested: effective diffuser expansion ratios varied from 0.75 to 1.70. The report that was translated into English and published by the NACA contained data on two of the fifteen shrouds: the baseline shroud (the right-most profile in Fig. 1.18b), which had an expansion ratio of 1.0 and a diffuser length of approximately $34\%D_\text{t}$, and a much shorter, thinner shroud (the fourth profile from the left in Fig. 1.18b) with a sharper inlet lip radius, $\sigma_\text{d} = 1.3$ and $L_\text{d} = 22\%D_\text{t}$. The models were tested at rest and in axial flow up to airspeed ratios ($\mu' = v_\infty/\Omega R$) up to 1.4, and at different blade pitch angles. In static and near-static conditions, the sharper lip caused the flow to separate on the second shroud, so that although the propeller thrust (T_rotor) was about the same, the shroud thrust and total thrust were substantially lower than those of the baseline shroud. In forward flight, at the higher airspeed ratios, the thinner profile had lower drag and therefore higher shroud thrust than the baseline shroud. However, the propeller thrust decreased faster with increasing airspeed ratio than it did for the baseline shroud, so, for the same blade angle, the total thrust was actually about the same or slightly less than that of the baseline shroud. Attaching an external split ring (Fig. 1.18c) to the leading edge of the thinner shroud helped to improve its

static characteristics, but worsened performance at airspeed ratios (μ') above 0.3. Both the baseline shroud and the thinner shroud with the split-ring attachment achieved static thrust coefficients more than twice as high as the open propeller, but also stalled much more sharply with increasing collective compared to the open propeller. The maximum figure of merit achieved for the open propeller was 0.62. For the baseline shroud, this increased to 0.69, while for the thinner shroud with the split-ring attachment it decreased to 0.47. Adding stator vanes to the baseline shroud caused C_T and FM to increase further, while the power coefficient remained about the same. Due to the increased inflow, both shrouded propellers achieved their maximum FM at a blade pitch angle 10° higher then that at which the open propeller achieved its maximum FM.

Measurments of the flow velocity at the diffuser exit plane of the baseline shroud and at another station inside the shroud indicated that the actual expansion ratio of that model was 1.07, i.e., further expansion took place downstream of the shroud exit. Furthermore, flow visualization using smoke showed that the cross-sectional area of the slipstream did not change with varying loading (thrust coefficient), indicating that the expansion ratio depends only on the shape of the shroud. The use of smoke for flow visualization was only possible when the model was equipped with stator guide vanes. Without stators, the extreme rotation of the flow in the wake made it impossible to obtain good photographs of the smoke. Measurements of total (stagnation) pressure upstream and downstream of the empty shrouds, that is, without the propeller present, showed that both the shrouds had about the same, negligible amount of pressure loss in the the internal flow due to
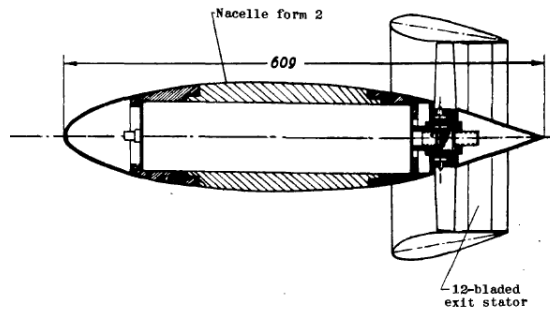
(a) Model configuration.
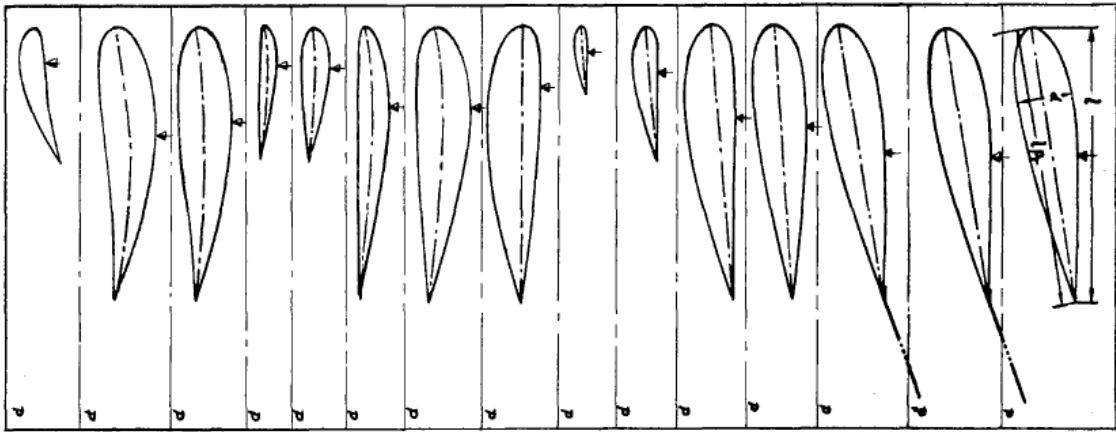
(b) Shroud shapes tested. The arrow marks the location of the propeller.
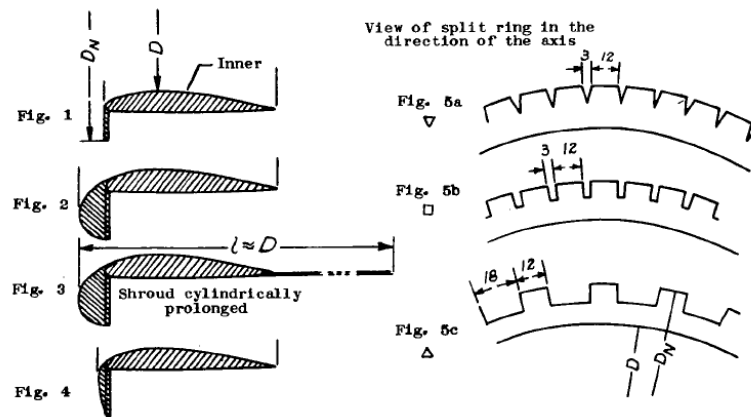
(c) Leading-edge split-ring configurations tested.

Figure 1.18: Shroud shapes tested by Krüger [43].

shroud wall friction and viscous effects. However, the report mentions that another shroud, which had the largest expansion ratio tested (1.7), had pressure losses about twenty times higher. This translates directly to greater power input requirements and lower efficiencies. Krüger noted that "since the [diffuser efficiency] will hardly increase beyond 0.9 unless special steps are taken, ... an attempt to increase the slipstream cross-section ratio essentially beyond $[\sigma_d^*] = 1$ would be useless."

In addition to the baseline, 8-bladed propeller used in these tests, two other propellers were also tested. Reducing the number of blades from eight to four resulted in C_T, C_P and FM decreasing at any given blade angle, because of the reduced inflow, while using blades with a reduced amount of twist (-37.5° vs. the baseline -45°), so as to take advantage of the tendency for the inflow velocity to increase towards the shroud wall, resulted in a negligible change in performance.

In 1948, Platt [52] tested contra-rotating, 48-inch-diameter propellers with three different shrouds (Fig. 1.19) which had two different values of expansion ratio (1.1 and 1.3), resulting from three different diffuser angles (7°, 14.4°and 22.4°) and two different diffuser lengths (33.6% and 50.2%D_t). At the same expansion ratio, the shroud with the longer diffuser (smaller θ_d) resulted in a higher value of C_T/C_P, when compared at the same C_P. At the same diffuser length, the shroud with smaller expansion (smaller θ_d) resulted in lower C_T/C_P, but also came slightly closer to producing the ideal amount of thrust for any given power. At all propeller blade angles, increasing σ_d caused a reduction in power consumption, but the decrease, which was most pronounced at the highest blade angles, was never more than 10%. In general, the differences in performance between the three shrouded propellers was
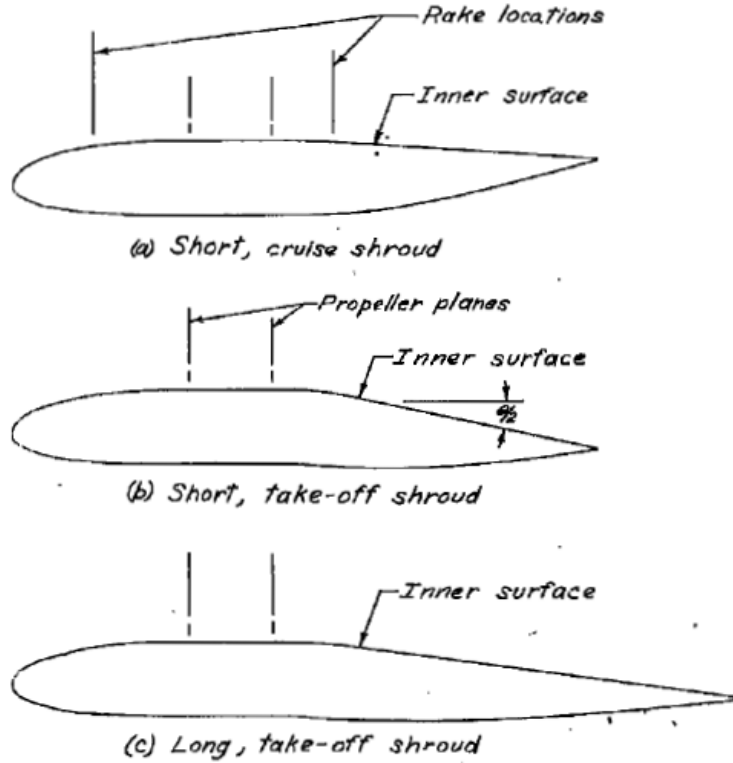
Figure 1.19: Shroud shapes tested by Platt [52].

found to be very marginal, within the limited range of blade angles tested (35°, 40° and 45°). On the other hand, all the shrouded propellers produced C_T/C_P ratios that were more than twice as high as the open propeller, at the same C_P, and came much closer to producing the ideal amount of thrust; then again, these results were obtained at the higher collectives at which the open propeller had already stalled.

In 1950, Hubbard [119] tested a fixed-pitch, 48-inch-diameter propeller with four shrouds (Fig. 1.20) that had three different diffuser lengths, from 12% to 36%D_t, and three different inlet lip radii (1.07–1.49%D_t). Shroud thrust, which was measured by integrating the measured static pressure variation over the shroud surfaces, was found to increase with increasing L_d. By shortening the propeller blades, tip clearances of 0.2% to 4.4%D_t were tested with the shroud that had $r_{lip} = 1.49\%D_t$
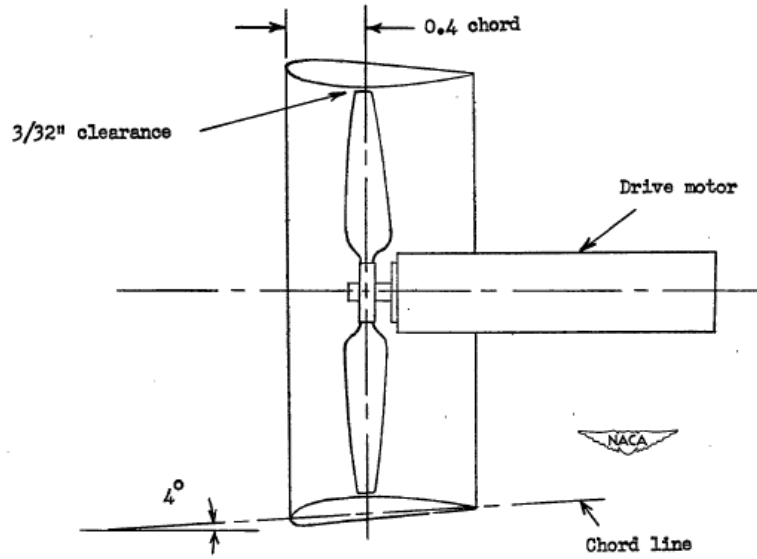
Figure 1.20: Hubbard's test arrangement [119].

and $L_d = 24\% D_t$. The increase in tip clearance resulted in approximately an 84%
reduction in total thrust, mostly due to a drop in shroud thrust, and a 15% reduc-
tion in power. In both Hubbard's and Platt's experiments, the incoming flow was
found to separate at the shroud leading edge at low propeller rotational speeds —
leading to loss of the inlet suction and large reductions in shroud thrust — but then
re-attach as the speed was increased.

In 1955, Parlett [55] investigated the effect of changing lip radius on the static
thrust of a fixed-pitch, 18-inch-diameter shrouded propeller (Fig. 1.21). The shroud
was a simple cylindrical shell, with an expansion ratio of 1.0, and was tested with
lip radii varying from 1.4% to 8.3%D_t. The increase in r_{lip} caused a near-linear
increase in figure of merit (at the same collective) from 0.72 to 0.89.

In 1958, Taylor [57] tested configurations with five different inlet lip radii (0–
12.5%D_t), three diffuser angles (0°, 7°, 14°) and four diffuser lengths (3–103%D_t),

49
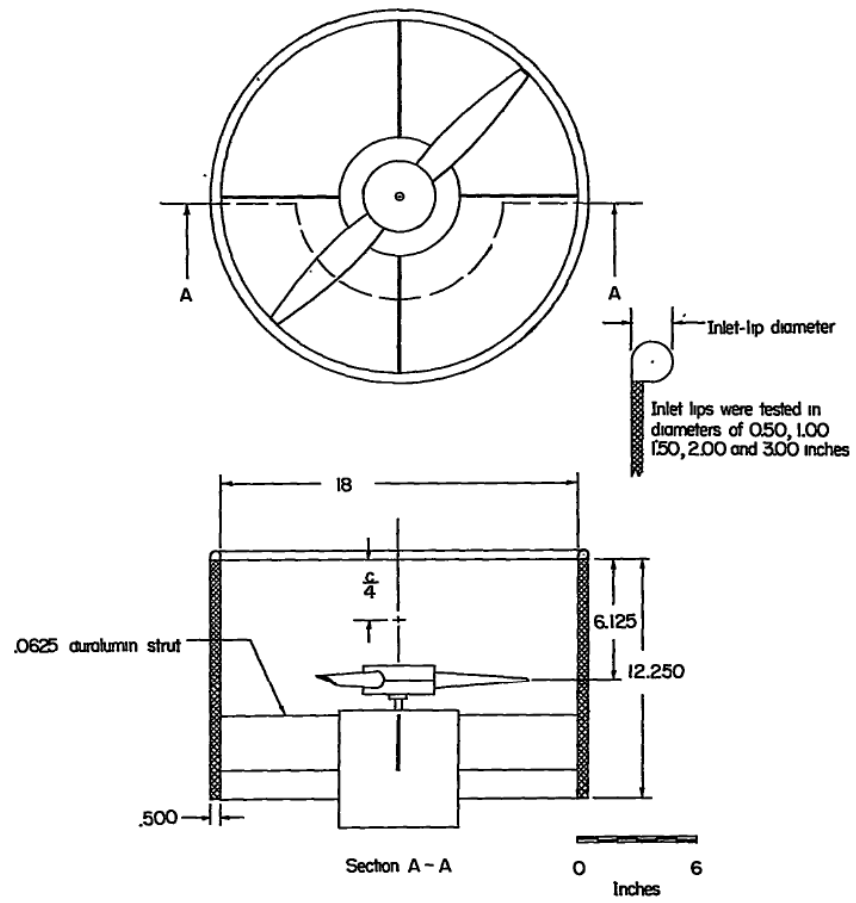
Figure 1.21: Shrouded propeller tested by Parlett [55].

thereby creating expansion ratios from 1.0 to 1.5 and allowing for examination of the same expansion ratio with different diffuser angles (Fig. 1.22). Although the test set-up was a propeller embedded in a wall, to simulate the 'upper' surface of a fan-in-wing configuration, the results are nevertheless also applicable to a shrouded-rotor configuration in the static (hovering) condition. The maximum figure of merit of the open propeller was 0.64, at a collective (θ_{75}) of 13°. In comparison, for the model with an expansion ratio of 1.0 and the longest diffuser, the maximum FM occured at a higher collective angle of 25°. The highest values of FM were achieved by the models with the inlet lip radii of 12.5% and 6.25%D_t, with a maximum value of 0.75. For the smaller lip radii, the flow was found to have separated from the inlet surface, and reducing r_lip caused FM to decrease. For r_lip less than 3%D_t, the FM was lower than that of the open propeller, with values around 0.5 for the smallest lip radius. The decrease in FM with reduction in lip radius coincided with simultaneous decrease in the shroud thrust fraction ($T_\text{shroud}/T_\text{total}$), from 50% (in agreement with momentum theory predictions) with the larger lip radii to 30% at the smallest lip radius.

At a fixed diffuser angle of 0° ($\sigma_\text{d} = 1.0$) and with the larger lip radii, decreasing the diffuser length from 1.03D_t to 0.03D_t resulted in a decrease in FM from about 0.75 to 0.68. A similar decrease was seen when, with the largest lip radius, σ_d was *increased* from 1.0 to 1.5, whether by increasing the diffuser angle or its length. However, even though the FM decreased, the total thrust was found to increase with increasing expansion ratio. The shroud thrust fraction ($T_\text{shroud}/T_\text{total}$) increased exactly in accordance with the momentum theory prediction, and, when compared
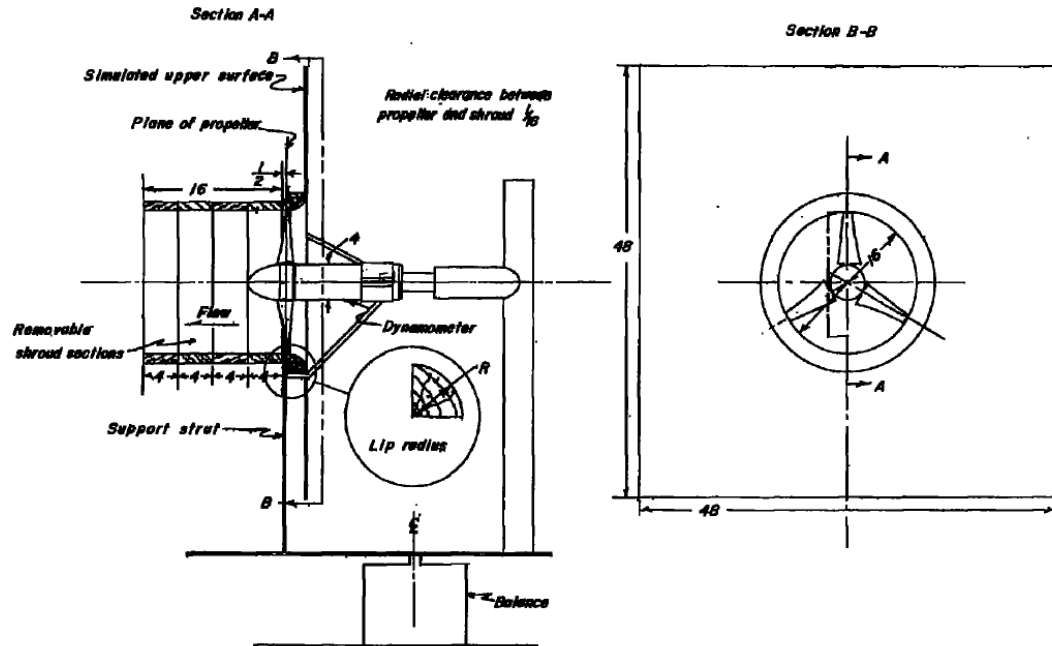
(a) Test arrangement.
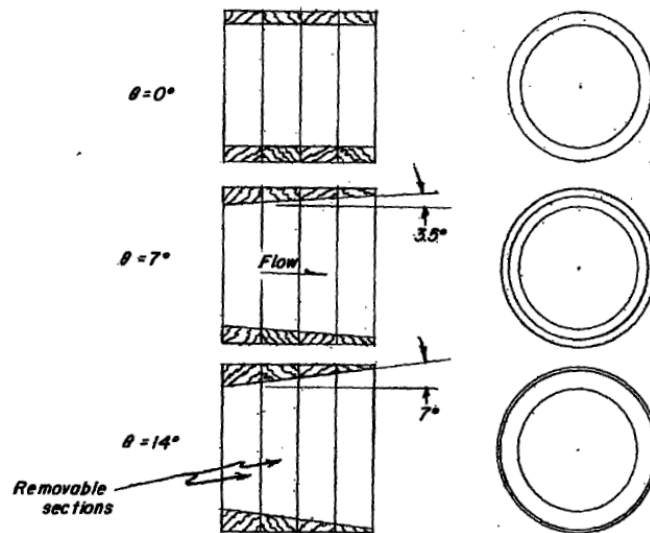
(b) Shroud shapes tested.

Figure 1.22: Shrouded-propeller tests conducted by Taylor [57].

at the same power input, the increase in thrust over the open propeller ($T_{\text{SR}}/T_{\text{OR}}$) also increased as predicted, but with values 15–20% greater than the momentum theory prediction. (This, as was mentioned earlier, was attributed to the tip losses on the open propeller.) In this set of experiments, these results were found to be virtually independent of the expansion *angle* of the diffuser, and depended only on the value of the expansion ratio.

In 1966, during the development of the 7-foot-diameter ducted fans for the Bell X-22A, Mort reported [72] that an increase in tip clearance from 0.3% to 2.0%D_{t} resulted in approximately a 20% drop in static thrust coefficient on a full-scale model. This was principally due to a reduction in shroud thrust rather than in propeller thrust. The power consumed also decreased, but by a lesser amount, so that the ratio of shroud thrust to power consumed also decreased. A comparison of these results with those obtained by Hubbard [119] on a smaller, 4-foot-diameter model revealed that for the smaller model, $C_{T_{\text{shroud}}}$ and C_P were individually less affected by changes in δ_{tip}, compared to Mort's 7-foot model, but the $C_{T_{\text{shroud}}}/C_P$ *ratio* decreased much more rapidly with increasing δ_{tip} than for the larger model. In axial flow (forward flight), the reductions in the thrust and power coefficients because of the larger tip clearance became smaller with increasing advance ratio.

At around the same time, a comprehensive, three-year investigation of the effects of various shroud parameters was conducted at Hamilton Standard by Black, Wainauski and Rohrbach [114] under a contract for the US Navy. Twelve different shrouded-propeller models, with a propeller diameter of 30 inches, were tested (Fig. 1.23). The parameters investigated included the exit area ratio, lip shape,
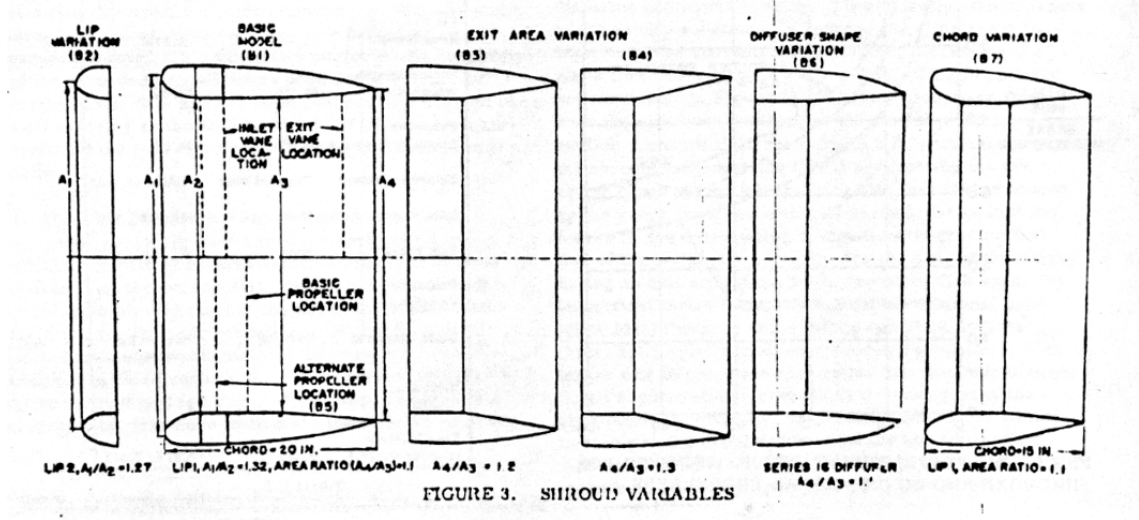
Figure 1.23: Shroud models tested by Black et al. [114].

shroud chord, propeller location within the shroud, effect of inlet and exit vanes, propeller blade shape, number of blades, blade tip clearance, and shroud external shape. Of all these, "results showed that the most powerful shrouded propeller variable [was the] shroud exit area ratio." The models were tested in static conditions and in axial flight up to a Mach number of 0.6. For the baseline model ($\sigma_\mathrm{d}^* = 1.1$), the increase in static thrust over the open propeller, at the same power consumption, was greater than that predicted by momentum theory. Compared to the predicted value of 1.3 for $T_\mathrm{SR}/T_\mathrm{OR}$ (for the same ideal power), an experimental sweep of different rotational speeds at fixed collective angle resulted in $T_\mathrm{SR}/T_\mathrm{OR}$ values from 1.67 at lower rotational speeds (power inputs) to 1.90 at the higher speeds. This greater-than-predicted improvement was attributed to the increased efficiencies due to off-loading of the rotor by the shroud, but could also have been due to lower blade tip-vortex losses, as has been explained earlier.

The thrust on the shroud was measured by a separate force balance, as well

as from measurements of surface pressure distributions. The difference between the two methods yielded an estimate of the drag on the shroud due to skin friction. In static conditions, the baseline shroud model came very close to achieving the theoretical $T_{\text{total}}/T_{\text{rotor}}$ ratio (Eq. (1.5)) of 2.2. In axial flight, with increasing freestream velocity, the drag on the shroud caused T_{shroud} to reduce and eventually become negative, resulting in progressively lower values of $T_{\text{total}}/T_{\text{rotor}}$ and $T_{\text{SR}}/T_{\text{OR}}$. In all cases, though, increasing the input power, either by increasing rotational speed or by increasing collective, caused T_{shroud} and T_{total} to increase, by increasing the suction forces on the shroud inlet. In fact, the report explicitly states that "throughout the program, increasing power [input] was found to be a very influential factor whereby the effectiveness of the shroud generally was increased." The authors therefore concluded that greater benefit from shrouding would probably be seen by using high-solidity propellers that are capable of absorbing greater amounts of power. In static conditions, while power loading (T/P) did decrease with increasing collective, this was probably because the propeller was being operated past its collective for maximum efficiency. In axial flight, as the freestream velocity was increased, the variation in power loading changed to increasing with increasing collective. In general, with increasing axial velocity, the power input and collective for maximum power loading also increased.

The effects of changing the various shroud parameters were expressed in terms of the change in total thrust from that of the baseline shrouded propeller, at the same power consumption. Increasing the area ratio from 1.1 to 1.2 and 1.3, while keeping the diffuser length constant (i.e., increasing the diffuser angle from 7° to

14° and 20°) caused the total static thrust to increase significantly, then level off and decrease. Compared to the baseline shroud, up to a 15% further increase in static thrust was obtained at σ_d^* between 1.2 and 1.3. Considering that the baseline shrouded propeller produced up to 90% more thrust than the open propeller at the same power input, this means that thrusts up to 2.2 times that of the open propeller, at the same power, were achieved with these higher area ratios. Here too, the thrust increments were greater than those predicted by the simple momentum theory. Based on results from an associated experimental program in which "a long-chord, 1.4 area ratio shroud was tested with extremely favourable results," the authors surmised that the performance levelling-off was "more likely due to a diffusion rate limitation," i.e., an expansion-angle limitation, rather than to an area-ratio limitation. In axial flight, as freestream velocity was increased, increasing the area ratio caused performance to deteriorate severely, and, in the same associated experimental program mentioned above, "area ratios of 0.9 and 1.0 were tested and shown to be beneficial" at the higher speeds. Shortening the shroud chord — effectively, reducing the diffuser length from the baseline $40\%D_\mathrm{t}$ to $30\%D_\mathrm{t}$ — while maintaining the area ratio at 1.1, and thereby increasing θ_d from 7° to 9.3°, caused little to no effect in static conditions, but resulted in degradations in thrust at the higher axial velocities. This was attributed to the higher thickness ratio of the shorter shroud. Two propeller positions within the shroud were tested: the baseline, with the propeller 40% of the chord-length back from the shroud inlet plane, and a second case with the the propeller moved forward to the $0.25c_\mathrm{S}$ station. Having the propeller further forward gives the wake more axial length to achieve

the desired diffusion, whereas having it further rearward helps to even out any asymmetries in the inflow. Since the models were only tested in axial flow, the effects of inflow asymmetries due to operation at an angle of attack to the freestream were not evaluated; however, it was found that the forward propeller location gave better results in axial forward flight, while the rearward location performed better in static conditions. A significant result of these tests was that, from the shroud surface pressure measurements, it was seen that on almost all the models tested, the pressure at diffuser exit was greater than atmospheric, and that "only on rare occasions did the pressure there equal the ambient value." This indicated that the wake had over-expanded and would have to re-contract downstream of the exit plane. No estimates were given of the true final area of the wake in this study.

The effects of changing the other shrouded-propeller parameters were much smaller compared to those of changing the diffuser parameters. Three different propeller blade planforms were tested: rectangular blades, blades with wider tips which were designed for higher tip loadings, and blades with narrower tips, which were designed for higher shank loadings. The results varied with input power and with freestream Mach number, but the differences in total thrust were never more than 5%. Notably, these variations were more so due to changes in the propeller thrust rather than the shroud thrust. With narrow-tipped blades, a three-bladed model fared better in static and near-static conditions, while a four-bladed model produced more thrust at the higher Mach numbers. For this parameter — blade number — too, though, the variations were within 5% of the baseline. Both inlet and exit vanes, in the form of untwisted, uncambered, constant-chord airfoils, set

at up to $\pm 10°$ from the axial direction, caused performance to either deteriorate slightly or hardly change at all. Increasing the blade tip clearance from the baseline $0.12\%D_\mathrm{t}$ up to $0.56\%D_\mathrm{t}$ caused performance to consistently deteriorate only in static and near-static conditions, and even there the degradations were by less than 5% of the baseline thrust. At higher axial velocities, thrust first decreased when δ_tip was increased to $0.26\%D_\mathrm{t}$, and then increased again when the clearance was further increased to $0.56\%D_\mathrm{t}$.

1.4.2.2   Helicopter tail rotors

For helicopter tail-rotor applications, the shrouded rotor has typically only been used on small- and medium-sized helicopters. For larger helicopters, the size and weight of the fan-in-fin assembly grow disproportionately large; also, safety considerations in ground handling become less critical because a conventional tail rotor is typically mounted at the top of a pylon, and lateral tilt angles for equilibrium in hover with a low-mounted fan-in-fin become uncomfortably large [29, 79]. An important constraint on the application of the shrouded-rotor concept to helicopter tail rotors is that the length of the shroud is limited by the maximum allowable thickness of the tailboom and empennage structure. In the ideal case, a uniform inflow distribution is desired at the plane of the rotor. Therefore, a large shroud length is desirable, with the rotor placed as far back from the inlet as possible, so that in forward flight for the helicopter — which is a sideways-flow condition for the tail rotor, a long length of shroud is available for the the flow to return

to a nearly-uniform profile after turning from the freestream direction to the rotor axial direction. This requirement is less important in low-speed flight or high-thrust conditions, when the inflow distribution tends to be fairly uniform already, but it does become critical in high-speed/low-thrust conditions. A long shroud length, i.e., a low shroud thickness-to-chord ratio, also allows for smooth fairing of the trailing edge of the shroud, for low drag in axial-flow conditions (sideways flight for the helicopter). On the other hand, in sideways flight for the tail rotor (forward flight for the helicopter), a long shroud length also results in a larger bluff body being presented to the oncoming flow, and consequently higher drag.

In 1975, Clark [84] reported on an innovative solution to this problem that was developed at Sikorsky, in designing the fan-in-fin that was tested on the S-67 Blackhawk helicopter. This solution was a shroud design (Fig. 1.24) that was not radially symmetric: On the forward half of the shroud, towards the tailboom, the inlet of the shroud was swollen to increase its chord length, before gradually fairing into the lesser thickness of the tailboom, while on the opposite half, the shroud was allowed to taper towards the rear of the empennage. This was possible because, in sideward flow (helicopter forward flight), the stagnation point that is formed on the aft side of the inlet "washes out the sensitivity to duct length seen on the [forward side]," and so the aft side of the shroud need not be as deep as the forward side. Additionally, the cross-sectional profile shape of the aft side of the shroud was changed from an ovoid shape to a cusped shape, with a concave cut-out on the exit side of the external profile. This cusp design helped reduce weight by doing away with a long aft fairing, reduced the strength of the separated flow on the aft surface in sideways

59

flight, compared to the otherwise convex surface of a 'doughnut'-shaped shroud, and reduced the area around the diffuser exhaust, minimizing negative thrust due to separated flows in that region.

As has been described already, the quality of the inflow distribution of the rotor is also affected by the shape of the inlet lip. Based on a survey of experimental fan-in-wing data, an inlet lip radius of $10\%D_t$ was selected for the S-67's fan-in-fin, in order to achieve a uniform inflow distribution as closely as possible, "while maintaining fully attached flow in all phases of flight" [84]. Later, during 1/3- and 1/4-scale tests of the FANTAIL™ for the Boeing/Sikorsky LH (Comanche) helicopter, tests with different lip radii showed that reducing r_{lip} from $6.5\%D_t$ to $0.9\%D_t$ resulted in separation of the flow from the inlet surface and approximately a 7% decrease in maximum figure of merit [85]. According to this reference, "it was found that to obtain maximum hover performance," r_{lip} values greater than 6.5–$7.5\%D_t$ were required. A lip radius of $7.5\%D_t$ was finally selected for the LH. It was also found that a sharp diffuser exit radius was required "for best static performance," but negative thrust — for helicopter directional control — and helicopter forward flight performance "were compromised." Based on additional test results, the radius of the aft 1/3 of the FANTAIL exit lip was increased to that of the inlet, as this was found to provide "a measurable drag reduction ... [and] improve reverse thrust performance."

In 1973, in investigating the same problem — the applicability of the shrouded-rotor configuration to helicopter tail rotors — Fairchild et al. [53] conducted experiments on short-chord shrouded rotors, with total shroud lengths (c_S) varying from
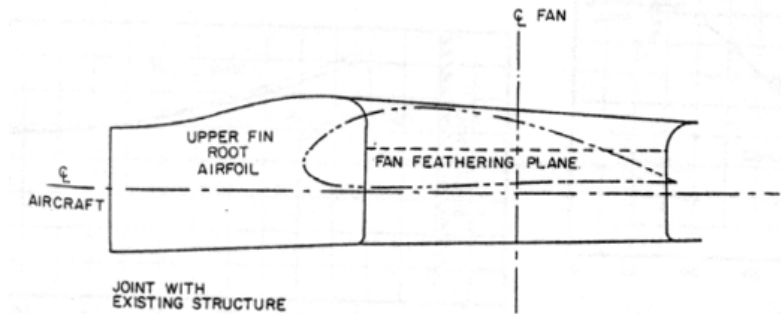
(a) Fore-aft taper of shroud length, with swelling at the tailboom joint.
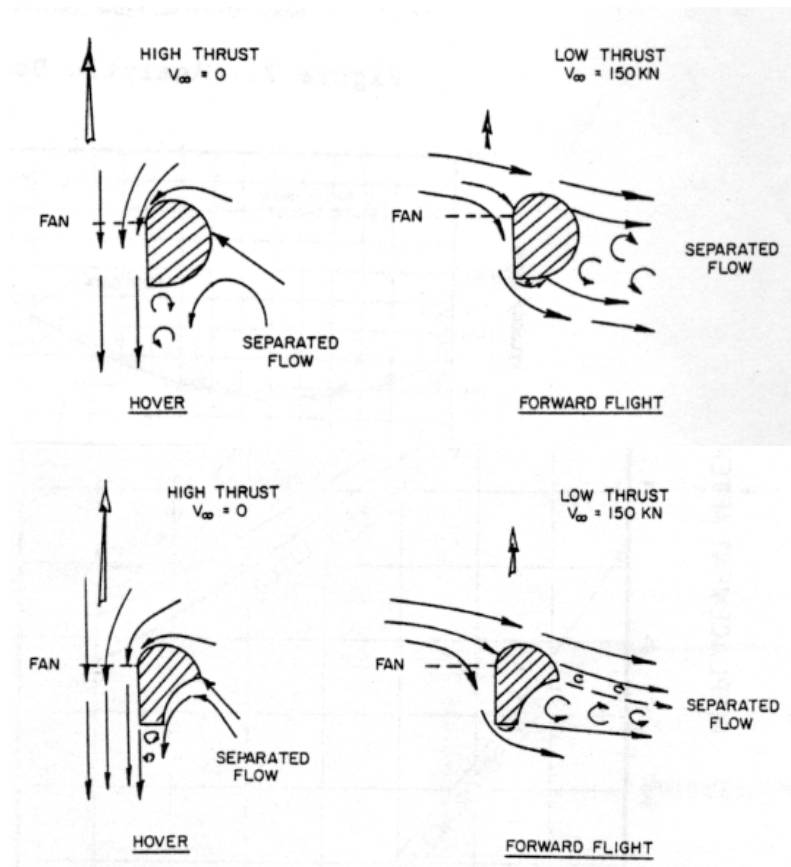
(b) Streamlines around ovoid ('doughnut-shaped') vs. cusped aft sections of the shroud.

Figure 1.24: Shroud design of the Sikorsky S-67 Blackhawk's fan-in-fin: cross-sectional top views [84].

$20\%D_t$ to $60\%D_t$ and diffuser included angles from $0°$ to $20°$. With the longest shroud and $\theta_d = 15°$, the maximum thrust achieved was twice as much as the maximum thrust from the open rotor. Power measurements were made but not presented since excessive scatter in those data rendered them inconclusive. In general, increasing the length of the shroud was found to increase the total thrust and the shroud thrust fraction, T_{shroud}/T_{total}. At fixed diffuser angle, the increase in shroud length from $0.2D_t$ to $0.6D_t$ caused T_{shroud}/T_{total} to increase from approximately 36% to 53%. At low expansion angles, the effect of changing c_S/D_t was greater at the lower values of c_S/D_t, while at the higher expansion angles, the effect was more uniform. At fixed shroud length, increasing the diffuser angle from $0°$ to $20°$ was predicted to cause T_{shroud}/T_{total} to increase. However, the experimental data showed this parameter (θ_d) to not have a strong effect: at $c_S/D_t = 0.6$, the shroud thrust fraction increased very slightly, while for the shorter shrouds it decreased slightly. This was attributed to flow separation in the diffuser, due to the low disk loading of the test model (5–7 lb/ft^2).

From the data for the shrouds with $\theta_d = 15°$, it was seen that, at the lowest collective angle of $10°$, there was little difference between the total thrust of the open rotor and the shrouded rotors, while at the higher collectives, the shrouded rotors produced greater thrust than the open rotor. With increasing collective, the effects of shrouding and of increasing the length of the shroud became more pronounced, with the initial increase in thrust due to adding a shroud being greater than the further increase from increasing the length of the shroud. This was due to the fact that the open rotor stalled at a collective of around $20°$, while the shrouded rotors

"did not indicate a stall up to the maximum angles tested" (30°). Increasing the length of the shroud seemed to increase the linearity of the thrust–collective curve, and postpone stall to higher collectives.

Tests were also conducted on the effects of rotor solidity and the location of the rotor within the shroud. At fixed diffuser angle (15°) and fixed shroud length, increasing the solidity of the rotor from 7% to 30% caused $T_{\mathrm{shroud}}/T_{\mathrm{total}}$ to decrease. For $c_{\mathrm{S}}/D_{\mathrm{t}} = 0.6$, the decrease occurred uniformly over the range of solidities tested, whereas for the shorter shrouds, the decrease occurred mostly between $\sigma = 7\%$ and 15%, after which it remained mostly constant. The highest shroud thrust fraction was therefore achieved with the longest shroud, the largest expansion angle (although not significantly so), and the lowest solidity rotor. The effect of rotor location was tested in the shroud with $\theta_{\mathrm{d}} = 0°$ and $c_{\mathrm{S}}/D_{\mathrm{t}} = 0.6$. Moving the rotor from the $0.16c_{\mathrm{S}}$ location back to the $0.71c_{\mathrm{S}}$ location resulted in the thrust measurements showing a slight maximum when the rotor was at the mid-chord location ($0.5c_{\mathrm{S}}$). However, these data were taken with the rotor at a collective of 10°, at which the shroud had minimal effect on the rotor performance.

In the mid-1990s, tests at Bell Helicopter Textron on Ducted Tail Rotor (DTR) models (Fig. 1.25) with different shroud lengths (called the 'thickness ratio' in the reports) — 10% and 20%D_{t} — showed greater reductions in power from the baseline open rotor and greater 'duct thrust sharing' in hover for the longer ('thicker') shroud [80]. Tests of rotor blades with tapered tips showed "a slight performance degradation compared to the [baseline] square tip rotor." Part of the reason for this was that "by reducing the blade loading at the tip, the suction on the duct
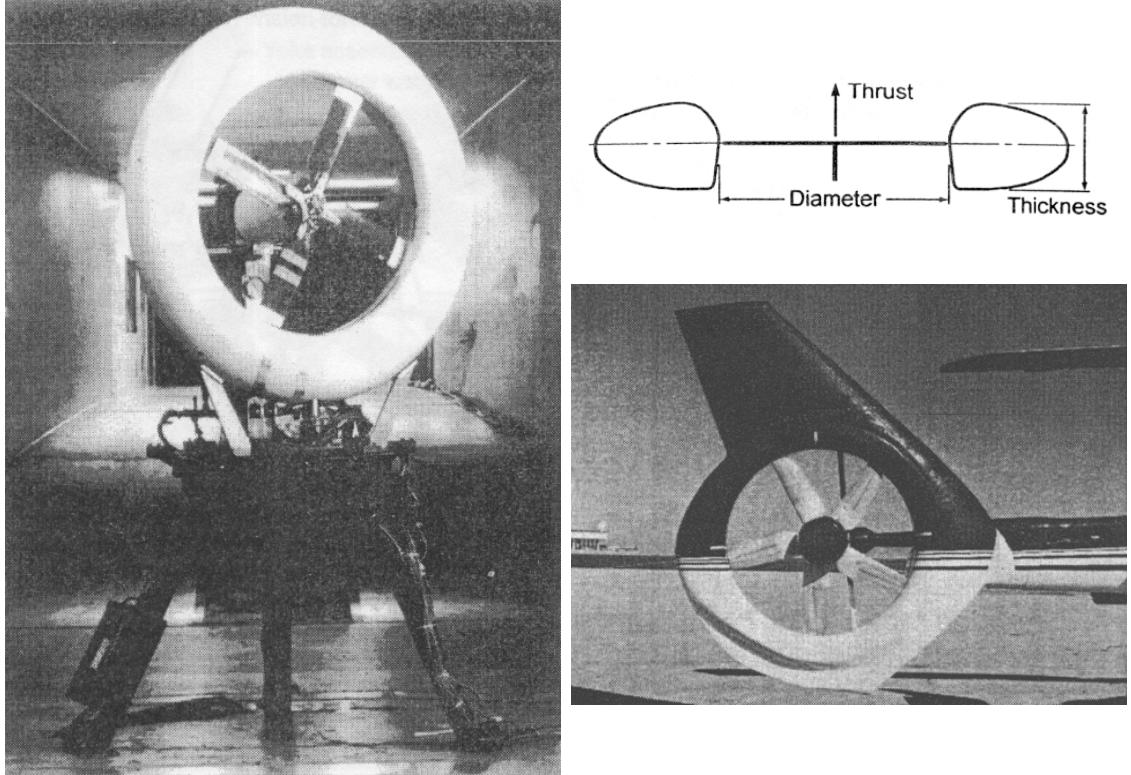
Figure 1.25: Ducted Tail Rotor tested by Bell Helicopter Textron [80, 81].

decreased, resulting in a 6% reduction in thrust produced by the duct." Other rotor parameters were also varied, as part of a simultaneous investigation of the acoustic characteristics of the DTR, but full-scale tests on a Bell Model 222U helicopter showed "no measurable difference" in performance between the baseline, 4-bladed rotor with equally-spaced blades and a quieter, 5-bladed rotor with unevenly-spaced blades, increased solidity and reduced tip speed.

With the shroud length limited by the width of the tailboom, helicopter fan-in-fan tail rotors have typically had expansion ratios of little more than 1.0. Reporting on the development of the FANTAIL™ shroud for the Boeing/Sikorsky LH design, and its testing on an H-76 demonstrator aircraft, Keys et al. [85] stated that the shroud was designed with a 'divergence angle' (half the included angle) of 5° to

"prevent premature flow separation from the duct walls while maximizing performance." They also state that thrust augmentation ($T_{\text{total}}/T_{\text{rotor}}$) values of 1.8 to almost 2.0 were achieved, compared to the "theoretical maximum of 2.0," and this, along with other analyses presented in this reference and in Ref. [86], indicates an expansion ratio of 1.0. Tests on the Kamov Ka-60's fan-in-fin ($\theta_d = 8°$, $\sigma_d^* = 1.1$) [92] also showed a rotor thrust fraction ($T_{\text{rotor}}/T_{\text{total}}$) of 0.55, or an augmentation factor of 1.82. Aérospatiale helicopter fenestrons also had shroud expansion ratios of approximately 1.0 [93], although tests on fenestron models with diffuser included angles varying from 7° up to 25° resulted in maximum thrust occurring at $\theta_d = 20°$ [29, 93]. On the production helicopters such as the later Dauphins, however, this angle was limited to 10° due to "flow instabilities" arising from interactions with the main rotor wake [93]. Adverse interactions with the main rotor wake, leading to a dead-band in the yaw control authority (the problem did not occur with isolated fenestron test models), were also the reason for a reduction in blade twist from $-12.5°$ on the early Gazelle fenestrons to $-7°$ on the later aircraft [28, 29, 79, 93]. Similar reasoning, based also on experience with $-32°$ of twist on the fan-in-fin of the modified Sikorsky S-67 Blackhawk, led to the adoption of -7° of twist on the Boeing/Sikorsky FANTAIL$^{\text{TM}}$ [85].

As in other shrouded-rotor applications, the presence of the shroud caused the stall of the fan-in-fin rotors to be postponed to extremely high blade collective angles. In tests of the Ka-60's fan-in-fin [92], it was found that, up to the collective at which the open rotor stalled, the shrouded rotor produced only slightly more thrust than the open rotor, at the same power. However, because the shrouded rotor didn't

stall until a much higher collective of around 55°, its maximum achieved thrust was twice as high as that for the open rotor. Similarly, a 3/4-scale model of the LH FANTAIL stalled at a collective (θ_{75}) of 48° [86], and, in half-scale model tests of a Gazelle fenestron with $\theta_{\mathrm{d}} = 7°$ and with a rotor with $-7°$ of twist, stall occurred at a collective (θ_{70}) of 45° [93]. In this Aérospatiale test, stall first occurred at the blade tips and then proceeded radially inwards, as evidenced by measurements of the flow velocities in the wake, which showed a widening zone of substantially decreased axial velocities near the shroud wall. Later design iterations of the fenestron incorporated radial variations in blade thickness and airfoil geometry intended to increase the load at the blade tip, "so as to get the maximum depressure level on the shroud and delay as far as possible the blade tip stall" [93]. Prior to stall, at $\theta_{70} = 35°$, the average flow swirl (rotational) angle was about 10°, while at $\theta_{70} = 47°$, post-stall, the mean swirl angle was 18° in the core of the wake, increasingly sharply to up to more than 60° near the shroud wall. Surprisingly, the measurements of the shroud surface pressure distributions show that even after stalling, the rotor continued to maintain strong suction pressures on the shroud inlet; indeed, the suction on the inlet at $\theta_{70} = 47°$ (post-stall) was greater than that at 35° (pre-stall). The pressure-jump through the rotor remained approximately the same between the two conditions, so that the suction pressures on the diffuser were also greater at the higher, post-stall collective. These pressures, of course, are due to to the total velocity at the shroud surface, which includes both the axial and the tangential (swirl) components of the velocity, so it is quite likely that while the axial velocites at the wall decrease after the rotor blades have stalled, it is the increased swirl velocities that maintain the

high suction pressures on the shroud.[16]

Stator guide vanes can be used to recover this rotational energy and produce additional thrust, while also functioning as structural support struts for the rotor centerbody. However, these were only incorporated on the most recent versions of Aérospatiale's fenestrons — on the later Dauphins and subsequent aircraft. Even the design of the LH FANTAIL only used elliptical cross-sections for the supporting struts and the driveshaft cover, for the sole purpose of minimizing their drag [85]. With stators, almost complete straightening of the flow was achieved in tests at Aérospatiale [93], as well as increases in thrust and the ability to reduce the length of the diffuser required for pressure recovery, and thereby the thickness of the helicopter empennage. In half-scale model tests with $\theta_d = 10°$, the use of stator guide vanes caused thrust to increase by 11%; in full-scale ground tests of Dauphin fenestrons, the addition of guide vanes caused thrust to increase by 26%, and maximum FM by 4.2% up to a value of 0.74 (the use of blades with newly-developed OAF airfoil sections led to a further 11% increase in thrust and 3% increase in FM, up to 0.76) [29, 93]. 3/4-scale tests of the LH FANTAIL resulted in a maximum figure of merit of 0.69 [85, 86], which is slightly lower compared to the Aérospatiale data presented in Ref. [93], but also a slightly higher maximum loading coefficient, C_T/σ[17], in hover of 0.31, which is about twice as high as that typically achieved by

---

[16]The same pressure measurements also showed that the flow pressure at the diffuser exit plane was still slightly less than ambient, indicating that further expansion of the wake took place downstream of the diffuser exit [29, 93].

[17]For a shrouded rotor, because $C_T = C_{T_\text{total}}$ and not C_{T_rotor}, this quantity cannot be considered as a 'blade-loading' coefficient, as is done for an open rotor. The equivalent quantity would be obtained by multiplying this coefficient by the factor $\frac{1}{2\sigma_d}$, which requires knowledge of the true value of the expansion ratio of the wake.

an open rotor [86].

1.4.2.3 Unmanned aircraft

During the design of the AROD UAV (Fig. 1.6m, p. 15) for the US Marine Corps, Weir reported in 1988 [35] on tests conducted at Sandia National Laboratories on six different shrouded-propeller configurations (Fig. 1.26). The full-size vehicle had a propeller diameter of 2 feet and was required to produce 85 lbs of thrust, whereas these tests were conducted on 2/3-scale models (16-inch diameter). The tests were to investigate the designs of the inlet, diffuser, and stator control vanes. The baseline shroud had an annular airfoil profile with a diffuser included angle of 14° and four all-moving vanes attached below the diffuser exit plane in a cross configuration. The principal changes that were made to this configuration in creating the other shrouds were (a) to reduce θ_d to 7°, (b) to reduce θ_d to 7° and extend the diffuser so that the vanes were shielded from the freestream, (c) to replace the annular airfoil with a torus, thereby increasing the inlet lip radius, and a conical diffuser with $\theta_d = 14°$, and (d) to remove the conical diffuser, thereby leaving a shroud that consisted of the torus only. For comparing the different configurations, only translational-flight data were presented in this reference, and these data were taken with the models in an "equilibrium" condition with no net drag. Therefore, since the models were tested at a fixed blade pitch angle and a fixed rotational speed, the data at low angles of attack (axial flow) were taken at the higher tunnel speeds (μ' up to 0.27), while the data at high angles of attack (edgewise flow) were taken

(a) Annular shroud.   (b) Toroidal shroud.
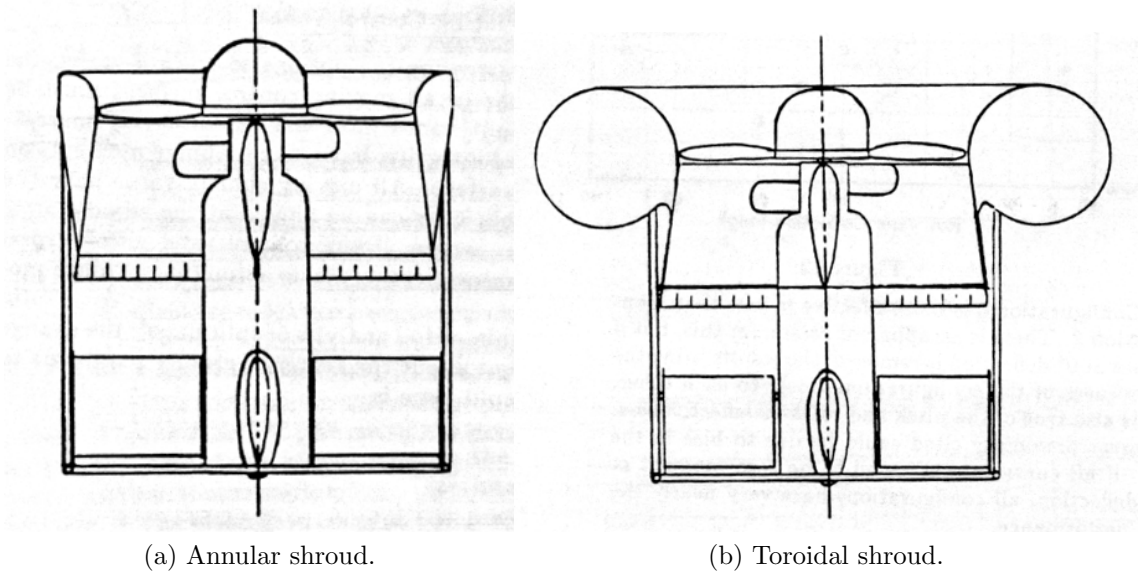
Figure 1.26: Shroud configurations tested for the AROD by Weir [35].

at the lower tunnel speeds. Additionally, high-speed (low-α) data were only taken

for two of the configurations: the annular airfoil shroud with the diffuser extension,

and the toroidal shroud with no diffuser.

For all the shrouds, the general trend was for the lift (C_L) and pitch moment

(C_M) coefficients (as normalized by v_{tip}, not v_∞) to increase with increasing airspeed

(and simultaneously decreasing angle of attack), reach a maximum around $\mu' \approx$

0.125 ($\alpha \approx$ 45–50°), and then decrease — as would be expected. In all cases,

the differences in C_L due to the configuration changes were much smaller than the

differences in C_M — almost smaller than the limits of experimental error, even.

Between the annular-airfoil shrouds, decreasing θ_{d} from 14° to 7° led to an increase

in C_M but almost no change in C_L. Extending the 7° diffuser to shield the vanes

caused a slight decrease in C_L, but a large increase in C_M. This was because, when

the vanes were exposed, the freestream air caused the exhaust jet to bend away from

the propeller axis, increasing the angle of attack at the control vanes and creating a larger nose-down (negative) pitch moment that opposed the natural nose-up moment of the shroud. With the vanes shielded from the freestream, the shroud's pitch moment is unopposed, and increases to that of a shroud with no vanes. The toroidal shrouds had higher C_M and slightly higher C_L than the annular-airfoil shrouds at low-μ'/high-α — this was attributed to their larger lip radius; however, the toroidal shrouds also changed, with increasing μ'/decreasing α, to decreasing values earlier and more abruptly than did the annular shrouds. Surface flow visualization using tufts showed that this sudden change was not due to any sort of flow separation. At high-μ'/low-α (near-axial flow conditions), the extended-diffuser/annular-airfoil shroud had higher C_L and C_M than the no-diffuser/toroidal-inlet shroud. Between the two toroidal shrouds, the one with the diffuser had higher values of C_L and C_M than the one without — again, with the differences in C_M being much larger than those in C_L.

The Cypher (Fig. 1.6n, p. 15) was a larger, 4-foot-rotor-diameter UAV developed by Sikorsky from 1986 to 1998 [96–110]. Unlike previous shrouded-rotor UAV designs, which utilized a single rotor with vanes in the downwash for anti-torque and yaw as well as pitch and roll control, the Cypher instead used a pair of counter-rotating, coaxial, bearingless rotors, with each rotor having independent cyclic and collective controls.[18] Use of a coaxial rotor system eliminated gyroscopic coupling in pitch and roll that would have occurred with a single-rotor system [97, 103]. Also,

---

[18]The Hiller VZ-1 flying platform (Fig. 1.6a, p. 13) also used a coaxial rotor system, but the propellers were of fixed pitch. Yaw and thrust were controlled by varying the propeller rotational speeds, and pitch and roll by kinesthetic control from the human pilot [103].

these six control degrees of freedom provided complete control of the aircraft along all three axes, "thereby eliminating the requirement for additional [control] surfaces or equipment" [103].[19] The azimuthal variations in inflow over the shroud inlet caused by the cyclic variation in blade angle resulted in pitching moments induced on the shroud that were more than six time higher than those on the rotor alone, thereby greatly increasing their control authority. For example, in forward flight, at an airspeed of 70 knots and with the 300-lb aircraft at a 5-degree nose-down attitude, only 11° of forward cyclic was required to trim the aircraft and neutralize the 1650 ft-lbs of nose-up pitch moment that was being otherwise produced by the shroud [103]. In addition, the external shape of the shroud of the final Technology Demonstrator (TD) was tailored to itself produce a nose-down pitch moment in translational flight, so as to reduce the cyclic trim requirements [98]. With this shaping, the shroud moment — and rotor cyclic requirement — increased to a maximum at an airspeed of 40 kts and decreased thereafter. As of 1998, the TD aircraft had achieved a flight endurance of 2–3 hours and a range of 30–50 miles, depending on the mission profile, a maximum speed of 60 mph (52 kts) and a maximum altitude of 8000 feet [100]. Table 1.1 shows the evolution of the final TD aircraft from the initial proof-of-concept vehicle, and Ref. [103], a patent filed in 1990, gives an indication of some of the experimental work performed in designing the shroud:

---

[19]Weir [35], on the other hand, argued for using vanes in the downwash for UAV control, stating that "reaction control jets and a cyclic pitch propeller are too complex. Control surfaces or vanes in the propeller jet stream offer the best solution as they are relatively simple and take advantage of the high dynamic pressure in the jet under all conditions." Similar sentiments were expressed by Lipera [27] in describing the design of the Allied Aerospace iSTAR UAV (Fig. 1.6p): "Because of the absence of complex mechanisms common with other VTOL aircraft (counter-rotating propellers, gearboxes, articulating blades, etc. ...) the iSTAR also benefits from a reduced part count contributing to improved reliability, low structural weight and low cost."

Two separate sets of figure-of-merit data show that decreasing the inlet lip radius caused FM to either steadily decrease from about 0.88 to 0.72 when r_{lip} was reduced from 17% to 3%D_{t}, or to remain constant at approximately 0.74 as r_{lip} was reduced from 14%D_{t} to 5%D_{t}, and then sharply decrease to 0.50 at a lip radius of zero. Another noteworthy result shown was that, for two different values of lip radius tested (6.25% and 12.5%D_{t}), reducing the shroud length from 100%D_{t} to less than 5%D_{t} caused the thrust to decrease by less than 10%, in contrast to what appears to be an analytical result that predicted a decrease of more than 30%, and also that there was very little difference in thrust between these two lip radii.

Another shrouded-rotor UAV design that used a coaxial rotor system was the 10-inch-diameter Perching UAV, or PUAV, developed at MIT's Charles Stark Draper Laboratory during 2000–2002 [122, 123, 129] (Fig. 1.27). Unlike the Cypher, though, the PUAV only had collective control of the rotors, and therefore also used vanes for pitch and roll control. The unique feature of the PUAV design was that the direction of rotor thrust was reversed between the hover and forward-flight conditions (Fig. 1.27b), by changing the blade pitch to negative angles of attack. The shroud profile shape was that of a NACA 0012 airfoil, arranged so that the leading edge was the inlet during forward (axial) flight, with the vanes upstream of the shroud, acting as canard control surfaces. In hover, with the direction of thrust reversed, the sharper trailing edge of the annular airfoil became the inlet, and the vanes operated in the rotor downwash. Not surprisingly, in static tests of the prototype vehicle, the maximum thrust of the shrouded-rotor model was 25% lower than that of the open-rotor model [122]. These initial tests were followed by

an investigation of the various shroud parameters by Dyer [123], who tested models with three different lip radii (1.4–11.5%D_t), three different diffuser angles (0–23°, $\sigma_d^* = 1.00$–1.82) and two different blade tip clearances (0.23% and 0.46%D_t). The reduction in tip gap caused the power consumption to decrease, but not significantly so. Increasing the lip radius caused thrust and power loading (T/P) to increase, as expected. On the other hand, increasing the diffuser angle caused thrust and power loading to decrease, contrary to predictions. Surveys of the wake with a pitot probe and with a tufted wand revealed a large reversed-flow region in the core of the wake. This was due to separation of the flow from the rotor centerbody, and was probably what prevented the larger diffusers from producing the desired expansion and the corresponding performance improvements.

In 2003, Fleming et al. [34, 94] investigated the effectivness of seven different auxiliary control devices (Fig. 1.28), in addition to conventional aft-mounted vanes, for controlling ducted-fan VTOL UAVs in crosswind turbulence. The devices, some of which were inspired by the patents related to Paul Moller's "Aerobot" line of ducted-propeller UAVs [130, 131], were tested separately, and included (1) an internal duct vane, mounted immediately below the rotor on the windward side of the duct, (2) a retractable "duct deflector" on the windward side of the internal duct wall, with and without bleeding of air to the outside of the duct, (3) a trailing edge (diffuser exit) flap on the leeward side of the duct, to increase the effective camber of the duct profile, (4) a deflector trough or "thrust reverser" on the windward side of the diffuser exit, (5) a spoiler on the windward side of the inlet lip, (6) a lip extension or "leading edge slat" on the leeward side of the inlet, and (7) tangential and normal

73
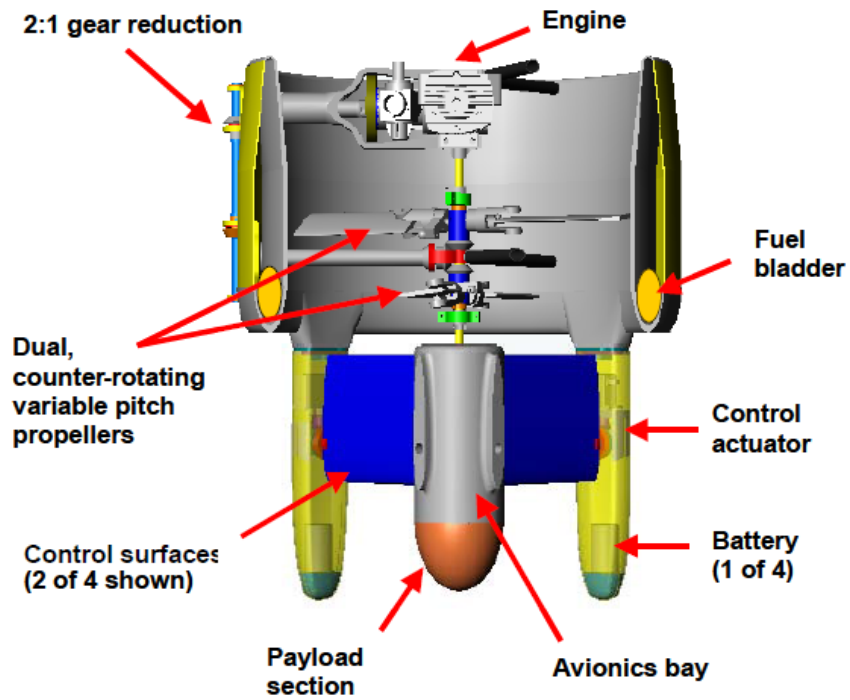
(a) Vehicle cutaway view.
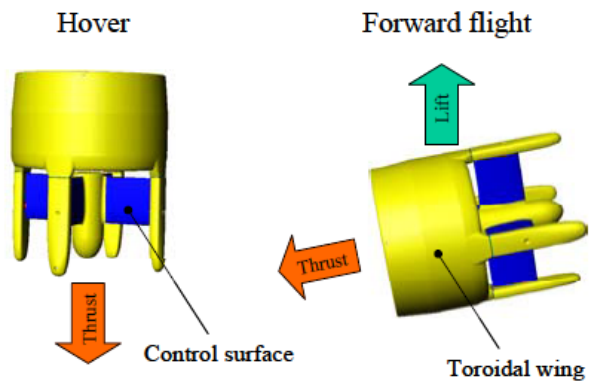
(b) Vehicle flight modes.

Figure 1.27: MIT/Draper Perching UAV (PUAV) [122].

blowing of pressurized air on both windward and leeward sides of the inlet. The goal of the investigation was a device that would augment, not replace, the conventional aft-mounted vanes, and which would provide as close to a pure pitch moment as possible, without generating any side-force or additional drag.[20] The test model was similar in form to the 10-inch-diameter Honeywell Kestrel (Fig. 1.6o, p. 15), although without the two side pods present on that aircraft, and was tested with a fixed-pitch propeller in hover and in crosswinds (edgewise flow) of speeds up to 30 knots (50 ft/s). In hover, the models were tested at different rotational speeds, with tip speeds from 200 to 500 ft/s. Above a tip speed of about 300 ft/s, the baseline shrouded propeller (no vanes, no auxiliary control devices) averaged a 20% increase in thrust coefficient above the open propeller (0.0205 vs. 0.017). At these higher tip speeds, C_T remained fairly constant, while at the lower tip speeds, C_T decreased near-linearly with decreasing v_{tip}. In the cross-wind tests, it was stated that the models were maintained at a constant disk loading[21] of 12 psf[22], which would imply that the rotational speed was varied with changing airspeed.

In edgewise flow, the total drag of the baseline shrouded rotor was almost identically equal to the prediction for the momentum drag of the system, clearly showing how large this component of the drag is, compared to the profile drag of the shroud. Unlike the drag, which increased as would be expected with increasing airspeed, the pitch moment data showed an increase in nose-up pitch moment up

---

[20]Conventional aft-mounted vanes generate a corrective, nose-down pitching moment by creating a force that acts in the same direction as the vehicle drag, further exacerbating the situation.

[21]The authors seem to use the term "disk loading" to mean the ratio T_{total}/A, not T_{rotor}/A.

[22]"For comparison to actual flying vehicles, ducted-fan VTOL UAVs of comparable size have disk loadings ranging from approximately 11 to 25 psf." [34]
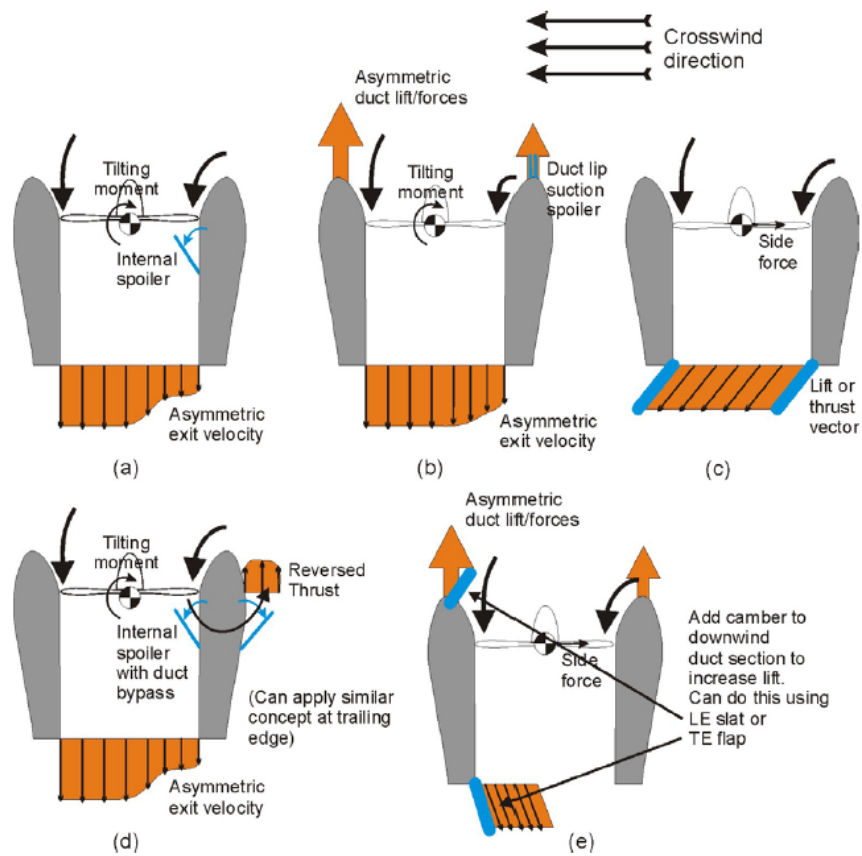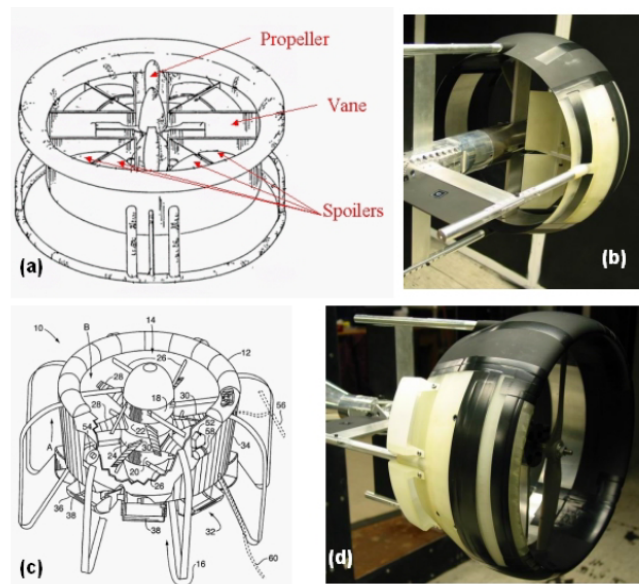
Figure 1.28: Auxiliary control devices tested by Fleming et al. [34].

to an airspeed of 17 ft/s, and then an unexpected decrease to nose-down pitch moments. The authors surmised that this was possibly due to separation of the flow from the windward side of the "relatively sharp leading edge" (r_{lip} was less than $6\%D_{\text{t}}$). However, from the illustrations of the model, it seems that the shroud profile was cambered *outwards*, rather than inwards, as is the norm for shrouded rotor systems that are optimized for low-speed flight, and this may have also been a factor in causing this phenomenon.

The vanes were tested at deflection angles from $-30°$ to $+30°$, and caused the expected increases in drag and changes in pitch moment. At airspeeds above 15–20 kts (25–34 ft/s), though, the results due to different vane deflection angles were nearly identical, indicating that the deflection of the jet (the rotor downwash) by the freestream had increased the angle of attack of the flow at the vanes to large enough values that they had stalled. This was confirmed by a CFD simulation of the bending of the jet by the crosswind.

Of the various auxiliary control devices tested, the best performing were the internal duct deflector with bleed, the flow control at the inlet by blowing, and the internal duct vane, although flow control by blowing would probably not be a feasible option on a MAV because of the high plenum air pressures that were required in these tests to have any significant effect. In general, the various devices were able to produce the desired nose-down pitch moments, although their effectiveness varied at different airspeeds. At low speeds, the best performing devices augmented the control authority of the primary control vanes by up to about 50%, while at higher speeds, where the vanes had stalled, the auxiliary devices were able to provide

changes in pitch moment that the control vanes alone could not.

In 2004, Martin and Tung [117] tested two 10-inch-diameter shrouded-rotor models (Fig. 1.29) in hover and in forward flight, at angles of attack from $0°$ (axial flow) to $110°$ and airspeed ratios (μ') up to 0.18 (41 knots, 70 ft/s). The two shrouds had different inlet lip radii – $1.7\%D_t$ and $2.9\%D_t$ – as well as different camber and thickness distributions. In the following discussion, these will be referred to as the 'LR1.7' and 'LR2.9' shrouds, respectively. Both shrouds were cambered outwards, like the models tested by Fleming et al. [34, 94], and "were constant internal diameter along the length, except for a very small region near the trailing edge," i.e., they had expansion ratios of approximately 1.0. As can be seen from the profile shapes shown in Fig. 1.29, this approximation is more accurate for the LR2.9 model; σ_d for the LR1.7 model would have been slightly greater than 1.0. Both models were tested with fixed-pitch propellers of varying diameters, to test tip clearances from 0.5% to $2\%D_t$.

In hover, the shrouded and open rotors were tested at tip speeds from 87 to 415 ft/s. The open rotor produced a thrust coefficient of 0.019, which was fairly constant down to a tip speed of 214 ft/s, below which it decreased to $\sim$0.017 at v_{tip} = 87 ft/s. The shrouded rotors also displayed a reduction in C_T with decreasing tip speed, but at a rate more severe than that for the open rotor, to the extent that for tip speeds below about 130–170 ft/s, the thrust coefficients of the shrouded rotors were lower than that of the open rotor. This was attributed by the authors "either to loss of the suction peak on the duct lip from laminar separation, or more likely due to the viscous losses inside the duct."

(a) Shroud profiles. Red = 'LR1.7', blue = 'LR2.9'.   (b) Test model.
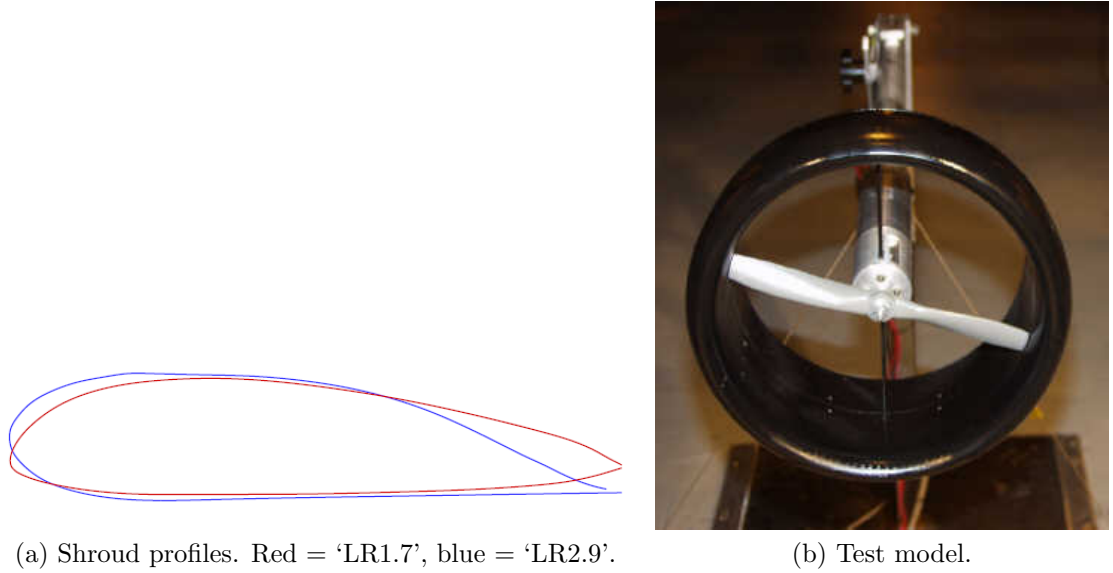
Figure 1.29: Shrouded rotors tested by Martin and Tung [117].

The shrouded-rotor model with the larger, $2.9\%D_\mathrm{t}$ lip radius ('LR2.9') achieved

a maximum thrust coefficient of 0.026 — 37% higher than that of the open rotor —

at the smallest tip gap of $0.5\%D_\mathrm{t}$. When δ_tip was increased to $2\%D_\mathrm{t}$, the maximum

C_T fell by 12% to 0.023, which was still 21% higher than that of the open rotor.

Decreasing the lip radius to $1.7\%D_\mathrm{t}$ caused C_T to decrease by about 15%: from

0.026 to 0.022 at a tip gap of $0.5\%D_\mathrm{t}$, and from 0.025 to 0.021 at a tip gap of $1\%D_\mathrm{t}$.

With the sharper inlet-lip ('LR1.7') model, thus, the highest thrust coefficients were,

respectively, 16% and 10% higher than that of the open rotor. A potential flow anal-

ysis showed that a decrease in inlet suction would have been the most likely reason

for the reductions in thrust due to increasing tip gap and decreased lip radius. On

the other hand, the LR1.7 model did display, experimentally, a slightly less-severe

reduction in thrust with decreasing tip speed than did the LR2.9 model.

As with the thrust coefficient, the increase in blade tip clearance also caused a

reduction in the figure of merit, as seen from the data given for the LR2.9 model at the highest tip speed tested. The open rotor achieved a FM of 0.44. The reported FM for the LR2.9 shrouded rotor was 0.67 at the smallest tip gap $(0.5\%D_\mathrm{t})$, which was 52% higher than that of the open rotor. Doubling the tip gap to $1\%D_\mathrm{t}$ caused FM to drop rapidly by 24% to 0.51, after which a further doubling of δ_tip to $2\%D_\mathrm{t}$ caused FM to decrease more slowly, by 7%, to 0.46. However, the authors used the formula for an *open* rotor in calculating the figure of merit for the shrouded rotors as well; hence, for a shrouded rotor with $\sigma_\mathrm{d} \approx 1.0$, their reported values would be 40% higher than the actual values. The correct values of FM for the LR2.9 model would therefore be 0.47 for the smallest tip gap $(\delta 0.5)$, which is only 7% higher than that of the open rotor, and 0.33 at the largest tip gap $(\delta 2.0)$, which is 25% *lower* than that of the open rotor.

Given FM and C_T, the power coefficients for the open rotor and the LR2.9 shrouded rotor can be calculated, and the values of C_T/C_P obtained as follows: 4.52 for the open rotor, 5.91 for LR2.9 at the smallest tip gap $(\delta 0.5)$, which is 30% higher than for the open rotor, a 23% decrease to 4.55 for $\delta 1.0$, and a further 5% decrease to 4.26 for $\delta 2.0$, which is 6% lower than that for the open rotor. The variation in C_T/C_P with changing tip clearance is thus similar to that of the figure of merit. However, even these values are not entirely accurate, because even though a six-component balance was used to measure the forces and moments on the models in this investigation, the values of power used in the analysis by the authors were the measurements of electrical power supplied to the motor, and so include electrical and transmission losses in addition to the pure aerodynamic torque on the rotors.

Although the measurements were taken at the same rotational speed, the motor efficiency also depends on the loading conditions, and is therefore different at different rotor torques. Therefore, not only would the true values of FM and C_T/C_P have been higher than those presented above, for both the open and shrouded rotors, but their indicated variations also be questionable.

In forward flight, in the low angle-of-attack range (0–45°), the various shrouded rotors exhibited very similar lift (C_L-vs.-α) characteristics: an initial slope 75% greater than that of the "unpowered" shroud (annular wing) alone, a slight kink in the curve at an angle of attack between 16° and 23°, and then a further increase with almost the same slope before stalling at around $\alpha = 40°$. The unpowered LR2.9 shroud, in comparison, stalled at $\alpha = 14°$, and had a maximum C_L that was 3.75 times lower than that of the powered model (LR2.9-δ1.0). Decreasing either the tip gap or the lip radius caused the kink in the curve to be postponed to a slightly higher angle of attack. The pitch moment (C_M) characteristics, on the other hand, were quite different for the two shroud models. From axial flow ($\alpha = 0°$) up to an angle of attack of 12°, the two models had nearly identical pitch moment coefficients. Beyond $\alpha = 12°$, C_M for the sharper-inlet model (LR1.7) remained roughly constant, exhibiting some scatter, while C_M for the LR2.9 model increased dramatically to values roughly ten times higher than those of LR1.7. At $\alpha = 40°$, coincident with the lift stall, both models displayed a sudden, sharp drop in pitch moment. For the LR1.7 model, for which C_M was already fairly low, this resulted in negative, nose-*down* pitch moment between $\alpha = 40°$ and 45°. These preceding measurements were taken at an airspeed ratio of 0.15 (60 ft/s). At a

81

slightly lower airspeed — $\mu' = 0.1$ (40 ft/s) — and in the higher angle-of-attack range (60°–110°), the pitch moments were once again positive (nose-up) for both models, with C_M for the LR2.9 model being 37% higher than that for the LR1.7 model at angles of attack near 90° (edgewise flow). The lower pitch moments of the sharper-inlet model was attributed to separation of the flow from the inlet, and this is also suggested by the greater scatter in the C_M data for this model, in comparison with the much smoother variations in the data for the LR2.9 model. However, since the two shroud profiles also had different thickness and camber distributions, in addition to different leading-edge radii, it is quite possible that those factors also affected the C_M characteristics. The effect of changing airspeed on the pitch moment was investigated by a sweep from 12 to 54 ft/s ($\mu' = 0.03$–0.14) for the LR2.9-δ1.0 model in edgewise flow ($\alpha = 90°$). The C_M data increased to a maximum value at $\mu' = 0.125$ before starting to decrease again, although the "decrease" may have been an artifact of possible scatter in the measurements and the curve-fit that was applied to them.

Following up on the results obtained in this investigation on the beneficial effects of minimizing the blade tip clearance, Martin and Boxwell [124] tested two other shrouded-rotor models that were designed to effectively eliminate the tip clearance completely (Fig. 1.30). Both models were derived from the baseline, 10-inch inner-diameter LR2.9 shroud of the earlier investigation, and were tested with a 10.35-inch-diameter propeller. In one shroud, the extended-diameter propeller fit into a notch that was cut into the inner shroud surface at the propeller tip-path plane. In the second shroud, a rearward-facing step was cut into the inner shroud

82
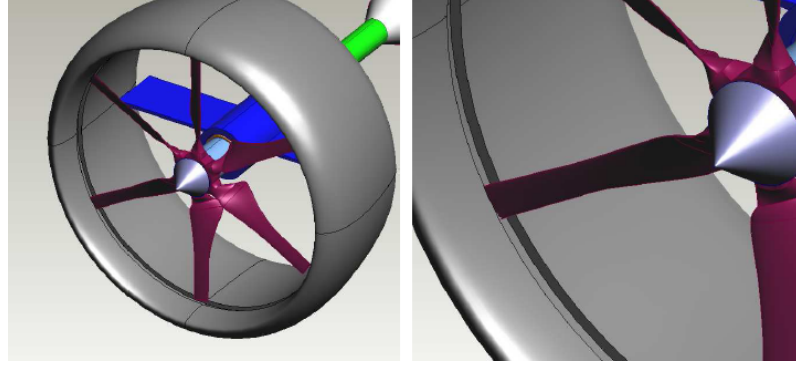
(a) Notched shroud.
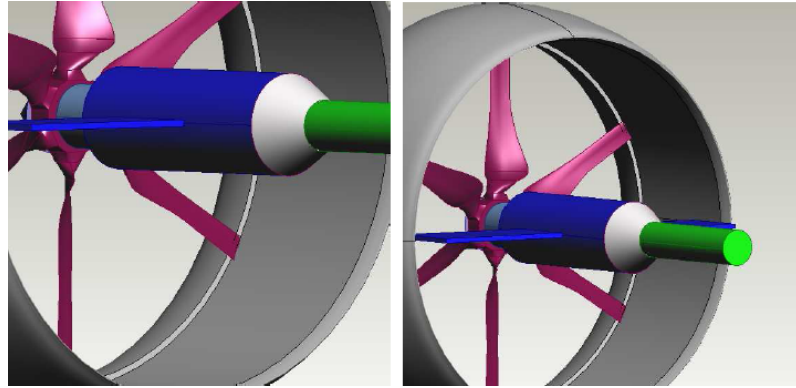
(b) Stepped shroud.

Figure 1.30: Shrouded rotors tested by Martin and Boxwell [124].

profile just above the tip-path plane to accomodate the propeller. The potential-flow

analysis predicted increased inlet suction and a "dramatically increased performance

increment" for the stepped shroud. However, the experimental (hover) thrust and

power data showed no difference between the performance of the baseline model and

the notched-shroud model, and degraded performance for the stepped shroud. The

failure of the analytic model was attributed by the authors to "viscous dominated

flow in the area of the [blade] tip along the duct wall."

During the same time period, Graf et al. [125] tested the effects of five different

lip geometries (Fig. 1.31) on the hover and forward-flight performance of a similarly-

scaled shrouded-rotor UAV model, the goal being to obtain "a duct lip design that

provides good static thrust performance while also avoiding the generation of adverse moments as much as possible." Three lip geometries were extensively tested: a "baseline1" lip with $r_{\mathrm{lip}} \approx 1.8\% D_{\mathrm{t}}$ and a shroud profile thickness of $12.5\% c_{\mathrm{S}}$; a "step" lip with a rearward-facing step above the rotor plane, similar to that tested by Martin and Boxwell [124], and with slightly increased shroud profile thickness $(15.8\% c_{\mathrm{S}})$ and lip radius $(\sim 2.2\% D_{\mathrm{t}})$; and a "baseline2" lip, which was a blending of the designs of the other two shapes — similar in shape to the stepped lip, but without the step, and with reduced thickness $(12.5\% c_{\mathrm{S}})$ and lip radius $(\sim 1.9\% D_{\mathrm{t}})$. The baseline2 lip was tested on a shroud model that was 15% larger than that for the other models, and also had stator vanes of a different design. Two additional lip shapes were initially also tested — an elliptical lip, with a reduced lip radius of $\sim 0.8\% D_{\mathrm{t}}$, and a circular-arc lip, with an increased lip radius of $\sim 3.0\% D_{\mathrm{t}}$ — but these were not tested further because they produced less static thrust than the other three models. The circular-arc lip produced slightly more thrust than the elliptical lip, and the baseline1, baseline2 and step lips produced almost the same amount of thrust, with the values for the baseline2 and step being only very slightly higher than those of baseline1. The test set-up allowed for separate measurement of the axial load on the shroud only, and it was found that, although their total static thrust values were nearly the same, the baseline2 model achieved a higher shroud thrust fraction $(T_{\mathrm{shroud}}/T_{\mathrm{total}})$ of about 0.53, compared to about 0.35 for the baseline1 model.

In forward flight, the baseline1 and step-lip models were tested in edgewise flow $(\alpha = 90°)$ at airspeeds from 10 to 40 ft/s. In these conditions, the step lip

84
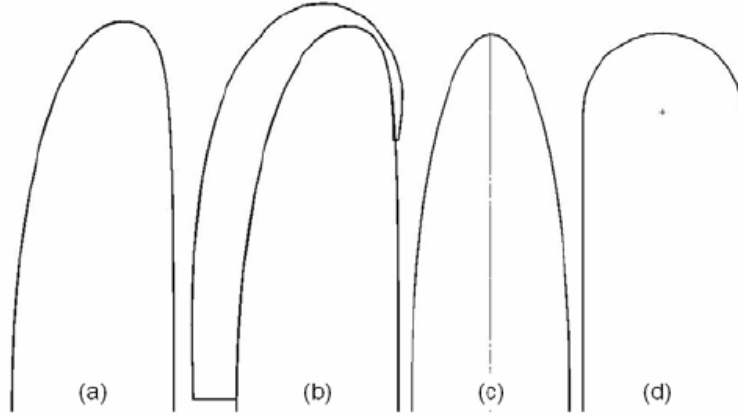
Figure 1.31: Inlet lip shapes tested by Graf et al. [125]: (a) baseline1, (b) step, (c) elliptical, and (d) circular arc. The left side of each lip corresponds to the interior of the shroud. The last shape tested (baseline2) was not shown.

produced slightly higher lift, slightly lower drag, and significantly higher nose-up pitch moments than the baseline1 lip. For both models, increasing the airspeed caused lift to remain approximately constant or decrease very slightly, drag to increase significantly, and the pitch moment to initially increase before starting to level off at the higher airspeeds. For both models, the ram drag averaged 80% of the total drag, with the ratio slowly decreasing as airspeed increased, indicating the increasing contribution of the shroud profile drag to the total.[23]

The baseline2 model was tested at airspeeds from 30 to 85 ft/s, and at angles of attack from axial flow (0°) to edgewise flow (90°). At all airspeeds, lift and drag both increased with angle of attack, although the lift data did show a maximum value near $\alpha = 70°$, beyond which it slowly decreased. With increasing airspeed, the angle of attack at which this maximum occurred slowly decreased. Both lift and drag increased slowly with increasing airspeed. On the other hand, the pitch moment

---

[23]The ram drag is proportional to the airspeed, while the profile drag scales with the square of the airspeed.

was seen to decrease with increasing airspeed, showing nose-down (negative) values at 85 ft/s, and to also exhibit increasing scatter in the data. At the lower airspeeds, the pitch moment increased steadily with increasing angle of attack, while at the highest airspeed it showed a gradually decreasing trend. Both of these phenomena point to separation of the flow on the windward side of the inlet with increasing airspeed.

1.4.3   Experimental work: Tests of a single shrouded-rotor model

This section lists experimental investigations in which a single shrouded-rotor configuration was tested, without changing any of the shroud parameters described above. Typically, these investigations were for the purpose of determining the effects of changing the freestream velocity and angle of attack on a shrouded rotor. These included the work of Krüger [43], Parlett [55], Moser [58], Kelly [132], Milla and Blick [133], Abrego and Bulaga [134], the tests in support of the development of the Doak VZ-4 aircraft by Parlett, Yaggy, Goodson, Mort, Grunwald, Kelley and Champine [60–68], and of the Bell X-22A aircraft by Newsom, Maki, Giulianetti, Mort, Spreemann, Biggers, and Gamse [69, 71–75].

In 2005, Sirohi et al. [23] investigated the effects of adding a shroud with an expansion ratio (σ_d^*) of 1.14 and anti-torque stator vanes to a 6-inch-diameter rotor (Fig. 1.32). The open rotor achieved its maximum figure of merit of 0.45 at a thrust coefficient of 0.029. Testing the open and shrouded rotors at the corresponding collective angle, and over a range of rotational speeds, resulted in increases in thrust
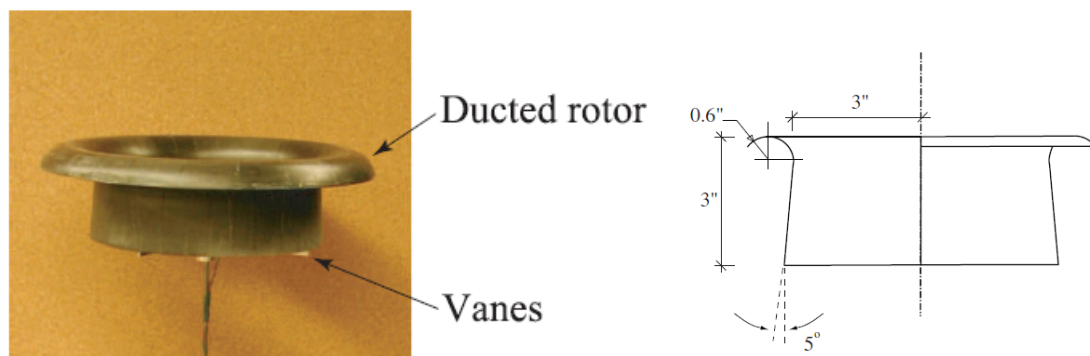
Figure 1.32: Shrouded rotor tested by Sirohi et al. [23].

over the open rotor, at the same *electrical* input power to the motor, of up to 35%, or reductions in electrical power at the same thrust by up to 44%. More recently, tests by Hrishikeshavan and Chopra [25] in 2008 on a 9.5-inch-diameter (24 cm) rotor, with a maximum open-rotor figure of merit of 0.64, showed increases in thrust from shrouding ($\sigma_{\mathrm{d}}^* = 1.0$) of around 30% at the same mechanical input power.

1.4.4   Analytical methods for performance prediction

Analytical methods for predicting the performance of shrouded rotors have ranged from the elementary momentum-theory, blade-element-momentum-theory (BEMT) and blade-element-vortex-theory (BEVT) models to more sophisticated potential-flow models (the classical 'method of singularities' [54]), sometimes coupled with a separate boundary-layer code in order to provide some modeling capability for viscous effects, and, in recent years, computational-fluid-dynamics (CFD) methods using the Euler equations and various other simplifications of the full Navier-Stokes equations. An excellent account of each of these approaches, along with comparisons of their relative merits and demerits, was provided by Sacks and Burnell in 1962 [54]

— except for the CFD methods, which were developed after their time.

1.4.4.1   Blade-Element and Potential-flow methods

The seminal work in this area is considered to be that of Küchemann and Weber [44–51], who, in the 1950s, developed potential-flow solutions for annular airfoils ('ring-shaped cowlings') in a uniform flow, by modeling the bodies with distributions of vortex rings over their surfaces, and also performed wind-tunnel experiments with which to compare their predictions. In the 1960s, using the same method, Kriebel [135] derived expressions for the force and pitching moment coefficients of a ducted propeller in steady flight at an angle of attack as well as the longitudinal stability derivatives in pitching motion, incorporating the effects of duct length, thickness, camber and taper ratio, but modeling the propeller as a uniformly loaded actuator disk. Kriebel and Mendenhall [116] developed methods for predicting the forces and moments on a duct in terms of the propeller thrust, as well as the duct surface pressure distributions and boundary-layer separation, and compared their predictions with measurements made on the Bell X-22A and Doak VZ-4 aircraft models. In 1970, Mendenhall and Spangler [136, 137] consolidated the earlier work and presented a computer program for predicting the forces and moments on a ducted fan at a specified advance ratio and angle of attack, as well as the radial inflow variations and duct surface pressure distributions. The program algorithm consisted of an iterative application of a blade-element-vortex-theory model and the superposition of two solutions: "an axial flow solution for the fan-duct-centerbody

combination and an angle of attack solution for the duct." Sheehy [138] presented a computer algorithm for the inverse task: that of designing the propeller and stator vanes when the shroud geometry and performance requirements are specified. This algorithm was later used in 1988 by Weir in designing the AROD UAV [35]. Earlier, also in 1970, Gray and Wright [139] developed a vortex wake model for heavily loaded ducted fans, in which the "inner vortex sheets [shed from the blades] move at a different rate from that of the boundary sheet [shed from the trailing edge of the duct]", thereby removing the restriction of light loading — in which the two sheets move downstream at the same rate — inherent in previous analyses. A simpler method, compared to that of modeling the shroud as chordwise distribution of vortex rings, was suggested by McCormick in 1967 [140], and involved concentrating the entire circulation of the shroud as a single vortex ring at the shroud quarter-chord location. This formulation was used by Fairchild et al. in 1973 [53] to show that even for a diffuser angle of $0°$, in axial flow, increasing the shroud chord causes greater reductions in ideal power compared to an open rotor.

An early attempt at modeling the effect of the finite tip clearance was performed by Goodman [141], who, in 1956, formulated a correction factor for thrust and efficiency measurements in wind-tunnel tests of propellers. This formulation was essentially a "re-working [of] the Prandtl solution ... [which accounts] for a finite number of blades by considering the radial flow near the blade tips ... taking into account the presence of a nearby wall." As the size of the gap approaches infinity, i.e., the case of an open rotor, the Goodman correction factor reduces to the standard Prantl tip-loss correction factor for an open rotor [14, pp.102–105]. The

analysis shows that "the circulation at any [blade] station is larger when there is a wall present than when there is not. ... Because of the constraint of the wall, less air is able to flow *around* the propeller disc and more air must flow *through* it." The gain in thrust is achieved at the cost of a loss in efficiency, however, if a blade design is used that has been optimized for use on an open rotor, indicating that blades designed for shrouded rotors should have a different twist schedule than those designed for open rotors.

In 1974, Gibson [142] conducted theoretical studies of the effects of the tip clearance and of radial variations in blade loading on the performance of shrouded rotors, with the shroud modeled using continuous surface distributions of ring vorticity. Decreasing the tip clearance from 5% to 1%D_t showed the expected increases in thrust and efficiency. However, below 1%D_t, further reducing the clearance caused the predicted thrust and efficiency to decrease; this was attributed to failure of the inviscid flow model to accurately model the interaction between the blade tips and the shroud boundary layer. The highest thrusts and efficiencies were also predicted with uniform and with tip-biased loading distributions.

In designing the fan-in-fin for the Sikorksy S-67 helicopter in the early 1970s, Clark [84] used a potential-flow method originally developed for fan-in-wing applications, combined with a boundary-layer analysis to check for the existence of separation. The potential-flow method involved a superposition of three basic solutions — those of (1) a 'closed' or blocked duct in axial flow, (2) an 'open' duct in axial flow, and (3) an open duct in cross (edgewise) flow — to simulate the flow at any thrust level and angle of attack. The predictions of power consumption, sur-

face pressure distributions and inflow velocity distributions from this model agreed extremely well with experimental measurements.

In 1991, Wright et al. [86] described a model "based on a momentum approach" used in the design of the H-76 FANTAIL, which seems to essentially consist of a fixed augmentation factor ($T_{\text{total}}/T_{\text{rotor}}$, set equal to 2.0) multiplying the predictions of the GenHel code for rotor thrust as a function of collective. The same year, DeCampos [143] gave a review of the analytical methods used in the design of marine ducted propellers, and presented a three-dimensional theoretical analysis of the steady interaction between a ducted propeller and a radially and circumferentially sheared axial inflow. In 1996, Page [144] presented a blade-element-based algorithm for designing and analyzing contra-rotating or single-rotor/single-stator ducted fans. However, the algorithm does not account for the effects of the blade tip gap, requiring an empirical correction factor, nor does it include any predictions of the force (thrust) on the duct itself.

In 1998, as part of the aeroservoelastic model developed for handling qualities analysis of the RAH-66 Comanche, Kothmann and Ingle [88] presented an "analytic model for the dynamic thrust response of a ducted rotor, which captures the effects of high-speed edgewise flight and high-frequency blade pitch inputs". The model is of the BEMT-type, developed for axial flow as well as flow at an angle of attack, and with additional terms to account for unsteady inflow effects. The formulation of the model is for the special case of a constant area duct ($\sigma_{\text{d}} = 1.0$), and so the expansion ratio does not appear explicitly in it. This correction, as well as other improvements and enhancements, were made in a similar model developed

by Basset and Brocard [33] in 2004 for the flight dynamics analysis of fenestron-equipped helicopters like the Dauphin.

In 2000, Bourtsev and Selemenev [92] presented a computational method developed at the Kamov company during the development of the fan-in-fin of the Ka-60 helicopter. Their method used momentum theory for modeling the global effect of the shroud on the system, and blade-element-vortex theory for calculation of the blade loads. Empirical correction factors were used for the pressure losses due to flow through the shroud, as well as for the effects of the shroud geometric parameters — lip radius, blade tip clearance, diffuser angle, diffuser length — in both positive and reverse thrust conditions. The effect of the blade tip gap on the blade loads is accounted for via a 'Prandtl-Shaidakov factor', which, like the Goodman correction factor [141], reduces to the regular Prandtl tip-loss correction factor for an open rotor when the tip 'gap' becomes infinitely large. Extremely good agreement was achieved between the predictions of this method and experimental test data.

In 2003, Guerrero et al. [145] developed a code called AVID-OAV for "the design and analysis of ducted-fan VTOL UAVs". In this model, the shroud and rotor aerodynamics are considered separately, and their solutions superimposed. The shroud is modeled as an annular airfoil, and its characteristics in a freestream flow derived by interpolation from the wind-tunnel measurements made by Fletcher in 1957 [26]. The rotor is modeled as either an actuator disk, or with thrust/power/efficiency data from a "propulsive performance map" that is obtained using a separate blade-element-vortex analysis. As in the case of Wright et al. [86], it is unclear, however, how the influence of the shroud on the performance of the rotor is modeled, espe-

cially since even the expression presented in this reference for the induced velocity in the shroud is actually the special-case formula for an open rotor, with no mention of the expansion-ratio factor. Nonetheless, the predictions for the forward flight performance of the Allied Aerospace 29-inch iSTAR vehicle match fairly well with the wind-tunnel data for that aircraft.

In 2004, Quackenbush et al. [146] used the CHARM (Comprehensive Hierarchical Aeromechanics Rotorcraft Model) code, which uses a free-wake, potential-flow model for the rotor and lifting panel model for fuselages and other bodies, to analyze shrouded-rotor configurations for UAV applications. Good agreement was achieved between their predictions and previously published experimental data on both annular airfoils (shroud-only) [26] and the X-22A shrouded propellers [75], but only in the pre-stall region. For capturing viscous effects and modeling post-stall behavior, the RSA3D code was used, which showed varying agreement with the experimental data.

1.4.4.2   Computational-Fluid-Dynamics methods

Blade element and momentum methods are useful for approximate comparisons with experiments and for predicting upper limits of performance, but cannot represent the geometric characteristics of the shroud, unless empirical correction factors are used. Potential flow methods can address this issue, but because of their inherent assumptions — inviscid, irrotational and incompressible flow — cannot predict friction drag and stall characteristics [147]. For these reasons, and with the

advances in computing power, CFD-based approaches have assumed a prominent role in the design and analysis of shrouded rotors.

At Aérospatiale [93], early performance estimations and initial sizing of fenestrons were obtained by BEMT methods, while detailed analysis of the effects of the shape of the shroud was conducted using a code called METRAFLU which combined CFD with table look-ups for blade airfoil characteristics. This reference shows comparisons of the predictions of this code and those of the BEMT method with fenestron test measurements of thrust, power, inflow velocity distributions and shroud surface pressure distributions.

In 1989, Rajagopalan and Zhaoxing [147] performed a CFD analysis to compare the performances and flow-fields of a shrouded and an open propeller in axial flow, in which the propeller was modeled by time-averaged momentum sources. Their code was also used later in the detailed design of the RAH-66 Comanche's FANTAIL [87]. A coupled CFD analysis of the entire Comanche fuselage, with the FANTAIL rotor modeled either as an actuator disk or with a blade-element model, was described in 2003 by Alpman, Long and Kothmann [89–91, 148]. An improved momentum source model, coupled with the OVERFLOW-D mesh solver, was used by Nygaard et al. [120] in 2004 for modeling the FANTAIL. This reference provides detailed comparisons with experimental data and with a more accurate, but also more computationally-intensive, discrete-blade CFD model used earlier by Ruzicka, Strawn and Meadowcroft [149, 150]. The analysis shows how reducing the blade tip clearance reduces the leakage flow and the size of the reversed-flow zone at the shroud wall, resulting in increased system thrust and figure of merit, and also demonstrates

the sensitivity of the predicted shroud thrust to accurate modeling of the effect of the blade tip clearance. In this region, the flow is three-dimensional, and the applicability of 2-D airfoil tables "becomes questionable." Both the momentum-source and discrete-blade models show the flow separating at the shroud wall slightly upstream of the rotor, due to the tip vortices lifting the flow away from the wall, and the prevention of the flow from re-attaching downstream of the rotor due to the adverse pressure gradient in the diffuser. The importance of realistic 3-D tip modeling was also demonstrated in 2003 by Lee, Kwon and Joo [121], who performed a CFD analysis of the Kamov Ka-60 fan-in-fin, and showed closer agreement with the experimental results than did the analytical model of Bourtsev and Selemenev [92] described earlier.

In 2004, Ahn and Lee [115, 151] used a CFD model of a representative fan-in-fin tail rotor in axial flow to parametrically investigate the effects of varying the inlet lip radius, diffuser angle and rotor radial 'strength' distribution. The CFD methodology was an extension of the ISES code developed in the 1980s by Drela and Giles [152], and the rotor was modeled as an axisymmetric actuator disk, but with radially varying strength distributions. At fixed thrust and freestream velocity (sideways flight for the helicopter), increasing θ_d from 8° to 12° caused a 1% reduction in power; increasing r_lip from 4.75%D_t to 7.5%D_t caused the power required to decrease by less than 0.1%; and changing the rotor strength distribution from a uniform one to one that has increasing strength towards the blade tips — corresponding to less blade twist and greater blade pitch angles at the tip than would be obtained with an ideal twist distribution — caused a 7% reduction in

power, "by facilitating the expansion of the fan duct flow," and also less sensitivity to losses due to the blade tip gap.

Aeroelastic stability and blade-flutter analyses for ducted fans, as used in aircraft engine and turbomachinery applications, were developed in the late 1990s by Srivastava et al. [153], Keith and Srivastava [154] and Srivastava and Reddy [155]. In these analyses, which used the unsteady Euler equations for modeling the flow, only the blades were considered elastic, while the hub and the duct were considered rigid. In that same time period, Elena and Schiestel [156] and Randriamampianina et al. [157] presented models for the prediction of transitional and turbulent flow inside shrouded rotor-stator systems, taking into account the effects of rotation on turbulence.

1.4.5   Other shrouded-rotor research

This section briefly describes some of the work that has been performed on aspects of shrouded-rotor operation that were not addressed in this investigation, but are of significant importance in the design of MAVs of this configuration: noise considerations, detailed analysis of the physics of tip-clearance flow, aircraft stability and control considerations, and the aerodynamics of annular wings.

1.4.5.1   Noise considerations

In 1950, Hubbard [119] took sound measurements on five shrouded propellers in static conditions, as well as on the unshrouded (open) propeller. The maximum

total sound pressure produced by the shrouded propellers varied from approximately one-half to two times as much as that for the open propeller, depending on whether the flow at the shroud surface was attached or separated, respectively, at the inner surface of the shroud inlet. The models were tested on an outdoor setup, and although nominally static conditions were tested, it was found that crosswinds and tailwinds caused the flow to separate more easily, whereas headwinds helped the flow stay attached. Low propeller rotational speeds also led to the flow separating. In attached flow conditions, noise levels increased with increasing tip speed, just as for an unshrouded propeller, and with increasing blade tip clearance. Increasing the number of blades decreased the noise levels, also as for an unshrouded propeller, because of the increase in the fundamental frequency (at the same rotational speed). Increasing the length of the shrouds had no significant effect on the noise levels.

In 1971, Drischler [158] performed analytic studies of sound pressures *inside* the shroud of a shrouded propeller in axial flight, by modeling the propeller disk as a distribution of rotating acoustic pressure doublets, and the shroud and centerbody as infinite coaxial circular cylinders. The purpose of this study was "to develop criteria for light-weight structures of sufficient acoustic-fatigue life, particularly in the critical region near the propeller disk." The effects of varying the propeller loading, loading distribution, tip clearance, tip speed, freestream velocity and hub-tip ratio were analyzed. The analysis showed that for a fixed torque and total thrust, increasing the freestream Mach number or decreasing the tip gap by "only a few percent" caused up to 6-dB increases in sound pressures in the vicinity of the blade tips, but "insignificant variations at distances greater than about one duct radius

from the propeller disk," while "increasing the hub-tip ratio from 0.2 to 0.5 results in an increase in sound-pressure level of approximately 2 dB to 3 dB throughout the duct." The increase in sound pressures with decreasing tip gap agreed with the earlier experimental results of Fricke et al. [159], who had tested gap sizes of 0.375 and 1.5 inches on a modified, full-scale model of the X-22A shrouded propeller.

At Aérospatiale, tests on fenestron tail rotors [29] in the mid-1980s showed increases in noise levels with increasing blade collective, and also faster attenuation of noise with distance compared to that for a conventional tail rotor. This occurred because the fundamental frequencies of the fenestron noise were higher by approximately an entire order of magnitude, and was due partly to the higher number of blades in the fenestron, and partly to the interaction between the rotating blades and the non-rotating support struts. This blade-strut interaction was found to be the main origin of fan-in-fin noise. An increase in the spacing between the rotor and the support struts by 6 cm (approximately $5.5\%D_\mathrm{t}$) caused a rapid reduction in the noise levels — by up to 10 dB for the 40°-collective case — to the same level as the case with no support struts at all. The masking effect of the shroud itself resulted in a 5–6-dB reduction in in-plane noise. Reference [29] also stated that "a simple theoretical model has been established which provides good acccount of the general trend of fan-in-fin rotational noise evolution with rotor speed, blade pitch setting, blade/support spacing and support shapes," but provided no further information about this model.

Riley [81] and Andrews et al. [80] reported on tests, conducted at Bell Helicopter Textron in the mid-1990s, of the effects of uneven blade spacing on shrouded

98

tail rotor acoustics. Tests were conducted on a 4-bladed evenly-spaced rotor, two 4-bladed scissors rotors with 70°110° and 55°125° spacings, a 5-bladed evenly-spaced rotor, and three 5-bladed rotors with different amounts of sinusoidally-modulated spacings. This last concept "re-distributes the energy of a single tone over a number of discrete frequencies, ... reducing the amplitude of each blade passage frequency harmonic and producing a more broadband-like spectrum," which reduces the perceived annoyance, and had been previously used with success in radiator fan designs and by Eurocopter in the design of the EC135's fenestron. Also tested were different rotor solidities, airfoils, tip shapes, tip speeds, and "a number of duct treatments and modifications which included inflow turbulence, simulated driveshaft and support struts, two spinners and two centerbody fairings, uneven rotor-to-duct gap, unequal blade collective pitch, and reduced duct diffuser exit angle." The quietest configuration — one of the 5-bladed rotors with sinusoidally-modulated blade spacing, reduced tip speed and increased solidity, and an aft-tapered blade tip — achieved an 11.3 dBA reduction in harmonic noise compared with the baseline rotor. Of this reduction, the sinusoidal spacing accounted for 5.4 dBA, the aft-tapered blade tip for 0.3 dBA, and the reduced tip speed and increased solidity together for 5.6 dBA. Similarly, the use of unequal blade spacing resulted in a reduction in sound pressure levels by approximately 4.5 dB, compared to an equally-spaced blade arrangement, in tests at the Japan Defense Agency's Technical Research and Development Institute (TRDI); this led to the adoption of a 55°/35° blade-spacing scheme for the XOH-1 helicopter's ducted tail rotor [32].

In 2004, Martin and Boxwell [124] measured the noise produced by a 10-inch-

diameter shrouded-rotor UAV model. Adding the shroud to the open propeller did not change the 'rotational noise' — the harmonics of blade passage frequency, which are strongest in the plane of the rotor — but increased the level of the 'broadband noise', which is strongest in the axial direction (called 'vortex noise' by Hubbard [119]). Increasing the blade tip clearance from 0.5% to 2.0%D_t caused no measurable difference in the acoustic signatures. However, separated flow caused by sharper inlet lip radius, and by a rearward-facing step above the rotor disk in one of the models, caused broadband noise levels to increase.

1.4.5.2 Tip-gap flow physics

In 1966, Gearhart [160] reported on a study of the mechanics of tip clearance flow in turbomachinery in an effort to reduce tip clearance cavitation losses in marine shrouded propulsors. The study characterized the flow patterns associated with variously-shaped gap configurations, and experimentally examined the effects on the tip clearance flow due to variations in the size of the clearance, the wall boundary layer and the blade tip loading.

More recently, in 2005, Oweis and Ceccio [161] used particle image velocimetry (PIV) to examine the flow-field in the tip region of a marine ducted propulsor, and revealed significant vortical phenomena in the instantaneous flow-fields that get masked in the more-common time-averaged measurements of such flows. In further investigations, both PIV and LDV (laser-doppler velocimetry) were used to determine how the tip-leakage flow varied with Reynolds number [162], and to

compare this flow with the tip vortices formed on an unducted (open) rotor [163]. The presence of the duct was found to reduce the strength of the primary tip vortex, relative to the other, secondary vortices in the tip-flow region, but the radius of its core did not vary substantially between the ducted and open cases. The strength and core size were only weakly dependent on the Reynolds number — within the range tested in this study (0.7×10^6–9.2×10^6) — and the core size was found to be on the same order as the tip clearance (0.26 in, $0.77\% D_t$).

1.4.5.3 Shrouded-rotor UAV stability and control

A number of investigations have addressed the topic of the stability and control of shrouded-rotor UAVs. In 1988, Weir [35] presented a sizing analysis for traditional, aft-mounted control vanes, compared the relative merits of split vanes (flapped stators) versus all-moving vanes, and presented experimental data showing the effectivness of the vanes in hover. In 2003, Fleming et al. [34, 94], as described earlier, tested a UAV model with control vanes as well as with seven other auxiliary control devices, and presented data comparing their effectiveness in hover and in crosswind conditions. In 2004, Sirohi et al. [23] tested flat-plate and circular-arc vanes on a 6-inch-diameter rotor, in both the shrouded and unshrouded conditions, and found that the vanes produced more anti-torque moment when the shroud was present than when it was not. As would be expected, the curved vanes produced more anti-torque than the flat ones, and were able to completely neutralize the torque produced by the rotor. The power penalty due to the need to overcome the

download on the vanes was approximately 10% for both the open and shrouded rotors.

In 2001, as an alternative to the mechanical complexity of cyclic rotor control mechanisms, Kondor and Heiges, Kondor et al., and Fung and Amitay [126–128] advocated using active flow control devices for vehicle control, citing mechanical simplicity, a minimum of moving parts and a potential reduction in weight as advantages of this approach. In tests on an 11-inch-diameter model, combinations of tangential and normal blowing on the inner diffuser wall, near the exit, resulted in the ability to generate pure sideforces in hover, without any pitching/rolling moment [126]. Such pneumatic circulation control requires an on-board source of compressed air, which is not feasible for a small UAV. Therefore, the use of synthetic jets, which require only small amounts of fluid momentum flux for their operation, was investigated, with a series of such devices embedded in the fixed stator vanes of the model [127, 128] . The operation of these devices is binary in nature, causing the flow to be completely attached or completely separated, resulting not only in a much simpler on/off control scheme, but also a means for avoiding the "unpredictable flow separation and attachment tendencies of thick laminar boundary layers at low Reynolds numbers." With these devices, successful yaw control was achieved, but significant coupling occurred between the pitch and roll control moments.

Finally, mathematical models of the dynamics of shrouded-rotor UAVs have been developed in recent years by Avanzini et al. [164–166] and Salluce [167].

1.4.5.4 Behavior of annular wings

The aerodynamic characteristics of annular wings ('unpowered shrouds') have been studied by Fletcher [26], who measured the lift, drag and pitch moment on five different annular airfoils, and Lipera [27], who experimentally compared the lift characteristics of powered and unpowered shrouds.

1.5 Low-Reynolds-number rotor aerodynamics

While this investigation has focused on the design of the shroud for a shrouded-rotor MAV, an awareness of the aerodynamics of the rotor itself in this Reynolds-number regime is of obvious importance. The influence on MAV performance of rotor parameters such as blade aspect ratio, twist and taper distributions, tip shape, airfoil shape, solidity, number of blades, collective angle and rotational speed have been investigated by, among others, Samuel et al. [17], Bohorquez and Pines [12, 16, 19, 22, 168, 169], Hein and Chopra [20, 170] and Ramasamy et al. [24]. Flow-visualization studies using particle image velocimetry (PIV) have also been conducted by Ramasamy et al. [24, 171] with a view to obtaining a better understanding of the physics of the flow around rotating wings at these small scales. 2-D and 3-D CFD studies of airfoils at low Reynolds numbers, using the OVER-FLOW and TURNS codes with a low-Mach pre-conditioner, have been conducted by Schroeder and Baeder [172, 173].

1.6 Objectives and approach of current research

As can be seen from the preceding survey of the literature on the subject of shrouded rotors, a considerable amount of work, both experimental and theoretical, has been performed in this area. However, the data that are available from these investigations are predominantly from tests of rotors with diameters from one to seven feet, typically operating at blade tip Reynolds numbers on the order of 10^5 to 10^6 and higher. Rotary-wing MAVs, on the other hand, operate in the laminar flow regime, with tip Reynolds numbers on the order of 10^4, where viscous effects become dominant and the flow separates much more readily in the face of adverse pressure gradients. Traditional design philosophies — rules-of-thumb for the optimal values of different shroud parameters — based on experience with larger-scale ducted propellers, while instructive in terms of indicating possible starting points for design, may or may not apply to MAVs as well. Although this flight regime has, in recent years, become a burgeoning area of aerodynamics research, and some testing has been done on smaller, near-MAV-scale models, yet, the data are not comprehensive, and compared to the collective experience with aerodynamic phenomena at both much higher (and also much lower) Reynolds numbers, there is still much that is not known about the physics of the flow at this particular scale. In many of the research programs conducted, at both MAV- and larger scales, vital pieces of information are lacking, such as the power consumption of the shrouded rotors, or direct comparisons between the shrouded and unshrouded ('open') versions of the same rotor, or the effects of rotor tip speed and blade pitch angle. In many

cases, more than one parameter value was changed between the different models tested, and so it is not possible to say with certainty which particular parameter was primarily responsible for the differences in the test results obtained. Even in the cases where strictly a single parameter value was changed, the results obtained varied between the different test programs conducted. This indicates that the changes in the performance characteristics also depended on the values of the other, *unchanged* parameters — which includes the size of the model itself, as well. And finally, predictive, computational tools, while immensely useful in reducing the amount of experimental testing that must be performed in designing an aircraft, are themselves hampered by difficulties in modeling flow separation phenomena, which is of critical importance in this low-Re regime.

All of these factors point to the need for an extensive, systematic investigation, at low Reynolds numbers, of the effects of varying the different shrouded-rotor design parameters on the hover and translational-flight characteristics of aircraft of this configuration. Such an investigation has been carried out, and is described in the following chapters of this dissertation. The goal of this research program was two-fold: first, to investigate the improvements in performance that are achievable from using the shrouded-rotor configuration for micro air vehicles; and second, to acquire a body of experimental data that could be used for the validation of analytical, predictive tools, and as guidelines in the design of more efficient, more capable MAVs. Chapter 2 describes the experimental setup used in conducting this investigation, and gives the details of the various shrouded-rotor models tested. Chapter 3 presents the results obtained from the tests of these models in the hover condition, wherein

measurements were made of the performance variables (thrust produced, power consumed) as well as of the pressure distributions over the shroud surfaces and the axial velocity distributions in the wakes of the models. Chapter 4 presents the results obtained from the wind-tunnel tests of the open rotor and one of the shrouded-rotor models, at angles of attack from axial flow to edgewise flow, and at various freestream velocities. In those tests, measurements were made of thrust, power, pitch moment, normal force, and shroud surface pressure distributions. Chapter 5 presents trade studies, based on the results obtained in this research, to determine whether it is worthwhile to choose the shrouded-rotor configuration for the design of a hover-capable micro air vehicle. Chapter 6 summarizes the work and presents concluding remarks and suggestions for future work. Appendix A contains detailed derivations of the momentum-theory and combined blade-element-momentum-theory models for a shrouded rotor, and Appendix B presents a discussion of the different measures used to describe the efficiency of hovering rotors, including reasons why the traditional formulation of the figure of merit is unsuitable for shrouded rotors, and proposes a new, generalized form of the figure of merit that overcomes this limitation and is applicable to both open and shrouded rotors.

Chapter 2

Experimental Setup

2.1 Shrouded-rotor models

For this test program, the parameters chosen for investigation were those that were found, from the literature on previous research, to have the greatest influence on shrouded-rotor performance. These were — see Fig. 2.1 — the blade tip clearance (δ_{tip}), the inlet lip radius (r_{lip}), the diffuser angle (θ_{d}), the diffuser length (L_{d}) and the diffuser expansion ratio (σ_{d}). In cross-section, the profile shape chosen for the shrouds consisted of a simple semi-circular inlet joined to a conical diffuser.[1] While advanced shroud designs would have profiles with smoothly and possibly non-linearly varying camber and thickness distributions, this elementary profile was chosen for this investigation because it involved a finite number of discrete and easily changeable parameters, yet would offer universal insight into the behavior of most shroud shapes.

The nominal inner, or 'throat', diameter of the shrouds (D_{t}) was chosen to be 16.0 cm (6.3 in), to match the diameters of the MAV-scale rotors being tested in other investigations at the Alfred Gessow Rotorcraft Center, which ranged from 15.2 cm to 17.4 cm [12, 16, 17, 19, 20, 22, 23, 168–170], to facilitate comparisons with the results of these other research efforts. The outer dimensions of the shrouds, upon

---

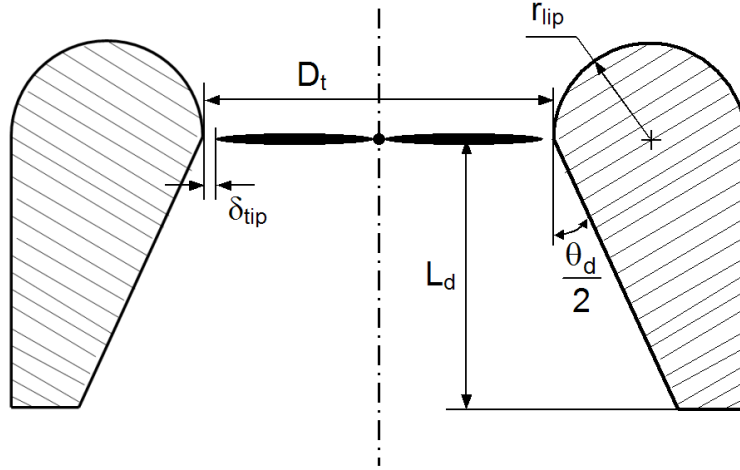[1] For these shrouds, therefore, the shroud chord $c_{\text{S}} = r_{\text{lip}} + L_{\text{d}}$.

Figure 2.1: Principal shroud parameters affecting shrouded-rotor performance: diffuser included angle (θ_d), diffuser length (L_d), inlet lip radius (r_lip), blade tip clearance (δ_tip)

which depend the maximum values of lip radius, diffuser length and diffuser angle, were constrained by the size of the equipment used to manufacture the shrouds and by the available sizes of the raw material from which the shrouds were made. Since a large number of differently-shaped shrouds were to be built and tested, the fabrication of the shrouds from composite materials was not an option, as this would require the manufacture of multiple tooling molds and was therefore prohibitive from time and cost standpoints. Instead, a machineable, low-density, polyurethane prototyping foam[2] was used. The shrouds (Figs. 2.2, 2.3) were machined on a lathe, coated with a latex-based filler to seal their surfaces, and then coated with several layers of spray-on polycrylic and extensively sanded to a smooth finish. Attachment to the rotor centerbody structure was accomplished by two sets of four support struts and a center support bracket. The struts were brass tubes with a diameter

---

[2]LAST-A-FOAM® FR-6704, produced by the General Plastics Manufacturing Company (http://www.generalplastics.com/).

Figure 2.2: Shrouded-rotor models

of 3/32 in (2.34 mm), and were attached to the shroud by delrin inserts placed in the shroud wall. The inserts had a collar which rested against the external shroud surface, and were held in place by the tension between diametrically opposite struts. Set-screws were used to make the majority of the connections between the various components of the models.

The objective of this study was to systematically investigate each of the shrouded-rotor parameters, along with their mutual 'interference' or coupling effects on each other, instead of focusing on a single parameter. Consequently, in order to limit the test matrix to a manageable size, only a few, broadly-spaced values of each parameter could be tested. Three shrouds were fabricated, each with a different inlet lip radius and a different diffuser angle. By separating the inlet

Figure 2.3: Close-up view of shrouded-rotor model LR13-D20

and diffuser sections, and 'mixing and matching' them, nine different shroud models were obtained. The values chosen for the lip radii and diffuser included angles were $6\%D_t$, $9\%D_t$ and $13\%D_t$, and $0°$, $10°$ and $20°$, respectively. These values were chosen to span the ranges tested by previous investigations of shrouded rotors, and subject to the constraints described above. The values of lip radius were biased to the upper end of the range, based on the reasoning that rotary-wing MAVs would be optimized more for efficient hover performance than for high cruise speeds. Owing to variability in the manufacturing process, the actual dimensions of the finished models were $D_t = 15.9$ cm, $r_{lip} = 6.48\%D_t$, $8.99\%D_t$ and $13.1\%D_t$ (1.03 cm, 1.43 cm and 2.08 cm, respectively), and $\theta_d = 0°$, $9.70°$ and $20.22°$. All nine shrouds had diffuser sections with a length of $72\%D_t$ (11.5 cm, 4.5 in). To test the effect of

varying diffuser length, the 10-degree diffuser was cut into three sections to obtain shorter diffusers with lengths of 31% and 50%D_t, and these were tested with the 13%D_t-lip-radius inlet. The final parameter, blade tip clearance, was tested by using rotors of different diameters to obtain clearances of 0.1%–1.6%D_t (0.15–2.50 mm, 0.006–0.100 in). The reductions in the rotor radius — by up to 2.85 mm (3.6%R) — were small enough that there was insignificant difference between the performances of the (open) rotors.

Thus, in addition to the open rotor itself, a total of seventeen different shrouded-rotor models were tested, using eleven different shroud profiles. For ease of reference in the following discussions, the models are identified with labels of the form 'LRx-Dy-δz-Lw', where 'x' is the nominal inlet lip radius, expressed as a percentage of the shroud throat diameter (D_t), 'y' is the nominal diffuser included angle, expressed in degrees, 'z' is the blade tip clearance, expressed in %D_t, and 'w' is the diffuser length, also in units of %D_t. An absence of the 'L' suffix in the model name indicates that the shroud had the default diffuser length of 72%D_t. The complete matrix of test models is shown in Table 2.1. Table 2.2 lists, for each of the diffuser profiles tested, the values of the corresponding expansion ratio and the values predicted by momentum theory for T_{rotor}/T_{total}, T_{SR}/T_{OR} and $P_{i(SR)}/P_{i(OR)}$, calculated using Equations 1.5 (A.17), A.27 and A.28, after correction for the blockage by the rotor hub. This matrix of models enabled comparison of data from multiple series of models for each of the shroud parameters. For example, for testing the effect of changing lip radius, data were available from a series of models with a diffuser angle of 0°, from another series of models with $\theta_d = 10°$, and yet another with $\theta_d =$

111

Table 2.1: Matrix of shrouded-rotor models tested in hover, indicating models for which surface-pressure measurements (P) and wake measurements (W) were also made.

Lip Radius	Diffuser Included Angle		
	D00	D10	D20
Models with the default diffuser length (L72)			
LR06	δ0.6 (P)	δ0.1	δ0.1 (P)
LR09	δ0.6 (P)	δ0.6	δ0.1 (P)
			δ0.5
LR13	δ0.6	δ0.1 (P,W)	δ0.1 (P)
		δ0.6 (P,W)	δ0.6 (P)
			δ0.8 (P)
Models with reduced diffuser lengths			
LR13	δ0.1-L50 (P,W)		
	δ0.1-L31 (P,W)		
	δ0.8-L31 (P,W)		
	δ1.6-L31 (P,W)		

20°. In each series, all variables are held constant except for the shroud parameter of interest. However, as mentioned previously, because the values of these other parameters do change from one series to the other, their interference or coupling effects cause the effects of the parameter of interest to be seen to different degrees in each of the different series.

Of the seventeen models, thirteen were instrumented with pressure taps — up to nine over the inlet lip and up to nine over the diffuser inner surface — to measure the pressure variation along the shroud surface. The tubing used for the

Table 2.2: Momentum theory predictions

Diffuser model	Expansion ratio (σ_d^*)	Expansion ratio, corrected (σ_d)	$T_{\text{rotor}}/T_{\text{total}}$	$T_{\text{SR}}/T_{\text{OR}}$ (at same A, P_i)	$P_{i,\text{SR}}/P_{i,\text{OR}}$ (at same A, T)
D00	1.000	1.033	0.48	1.27	0.70
D10-L31	1.113	1.150	0.43	1.32	0.66
D10-L50	1.184	1.224	0.41	1.35	0.64
D10	1.269	1.311	0.38	1.38	0.62
D20	1.575	1.628	0.31	1.48	0.55

pressure taps had an inner diameter of 0.0650 in (AWG16) and an outer diameter of 0.0875 in. The taps were staggered in azimuth, i.e., around the circumference of the shroud, over a range of approximately 90°, to prevent contamination of the flow at each tap by the presence of the upstream taps. This azimuthal distribution was possible because of the axial symmetry of the flow-field for a hovering rotor. In the 'axial' direction, the taps were concentrated more closely together in regions of the greatest change in pressure: on the inner portion of the inlet surface and near the blade passage region.

For the translational-flight tests, only the open rotor and a single shrouded-rotor model were tested — again, due to the prohibitive size of the test matrix that would have otherwise resulted. This model was one of those that was found to exhibit the best performance in hover, and was the model with an inlet lip radius of $13\%D_t$, a blade tip clearance of $0.1\%D_t$, a diffuser angle of 10° and a diffuser length of $31\%D_t$ ('LR13-D10-δ0.1-L31'). A model with the shortest diffuser length was chosen so as to minimize the weight and inertia of the model, to prevent overloading

of the wind-tunnel balance.

The rotor used for all the models was a three-bladed, variable-collective, rigid (hingeless) rotor with untwisted, flat-plate, rectangular, aluminum blades, and driven by a 6-volt/8.5-watt electric motor[3] attached to the rotor support structure . The values of the important rotor parameters are given in Table 2.3. This blade/airfoil geometry was chosen on the basis of its simplicity, since multiple rotors had to be fabricated to create different tip clearance values, and the emphasis of this research was on investigating the effects of different shroud geometries rather than optimizing the rotor itself. However, in order to test the effects of shrouding on a more-efficient rotor that is better suited to the low-Reynolds number flight regime, a single hover test was also conducted of the LR13-D10-L31 shroud with a second rotor with slightly higher solidity ($c = 1.27$ cm, $\sigma = 0.15$) and cambered, circular-arc airfoils (maximum camber $= 13.4\%c$). The other parameters of this rotor were the same as those of the baseline rotor, as given in Table 2.3. The blade tip clearance between this 'cambered' rotor and the LR13-D10-L31 shroud was 0.45 mm, or $0.28\%D_{\mathrm{t}}$.

2.2   Hover test setup

The setup for the hover tests is shown in Fig. 2.4. The tests were conducted with a custom-built test-stand, specially designed to measure the low values of thrust

---

[3]WES-Technik Model Micro DC 1331 (DC6-8.5) (http://www.wes-technik.de/English/motors.htm).

Table 2.3: Rotor parameters

Nominal rotor radius (R)	8.0 cm
Number of blades (N_b)	3
Rotor solidity (σ)	12%
Blade root cut-out (R_0)	18%R
Blade planform	Rectangular (no taper)
Blade twist (θ_{tw})	0°
Blade chord (c)	1.0 cm
Blade airfoil	Flat-plate (uncambered), rectangular profile (blunt leading, trailing edges), 5% thick

and torque of MAV-scale rotors.[4] The models were mounted inverted (thrusting downwards) to avoid the effects of a ground plane on their performance. The models were tested at collective angles from 5° to 40°, in steps of either 5° or 10°, and rotational speeds of 2000 to 4000 rpm, corresponding to blade tip speeds of 55 to 110 ft/s, tip Reynolds numbers of approximately 11,500 to 23,000, and tip Mach numbers of 0.05 to 0.10. A few initial tests were conducted at rotational speeds from 500 to 5000 rpm, to determine the effects of Reynolds number on the performance. The atypically high — for a conventional rotor — collective values tested are in accordance with the blade angles used in other shrouded-rotor applications and test programs, as described in the previous chapter. For the shrouded rotor, these

---

[4]The test-stand was designed by Dr. Jayant Sirohi, also of the Alfred Gessow Rotorcraft Center. The sensing elements were commercial, off-the-shelf (COTS) precision strain-gauge load cells. Thrust was measured by a Honeywell Sensotec Model 31 Precision Miniature Tension/Compression Load Cell (http://www.sensotec.com/). Torque was measured by a Transducer Techniques RTS-Series Reaction Torque Sensor (http://www.transducertechniques.com/). The sensing elements used for these tests had full-scale ranges of 1000 g (2.2 lb) and 10 oz-in (0.07 N-m, 0.05 ft-lb), respectively, but other sensors of the same form factor and with different capacities are available from these vendors and can also be used in this test-stand.

high collectives compensate for the greater inflow seen at the plane of the rotor disk, compared to the case of an open rotor. The open rotors were also tested at these high collectives to obtain a comparison of the performances of the open and shrouded rotors at the same collective angles. The rotational speed was measured by an arrangement involving a Hall Effect sensor[5] mounted to the rotor support structure and two magnets mounted diametrically opposite each other on the rotor hub. The passage of the magnets past the sensor produced electric pulses that were counted by the data acquisition program. Two magnets were used instead of one so as to keep the rotor balanced and to improve the accuracy of the measurements. The speed measurements were verified with an optical tachometer[6], which emitted a laser beam and counted the pulses reflected from a reflective-tape target positioned on the rotor hub. The mechanical shaft power of the rotors was then calculated as the product of the torque and rotational speed.

The shroud thrust (T_{shroud}) was calculated by integration of the measured pressure distributions over the shroud surface. The integrated shroud thrust was then subtracted from the total thrust to arrive at the rotor thrust (T_{rotor}). The models for which pressure data were not collected — and for which, therefore, the division of thrust between the rotor and shroud could not be calculated — were the LR06-D10-δ0.1, LR09-D10-δ0.6, LR09-D20-δ0.5 and LR13-D00-δ0.6 models. It was recognized that the measurement of shroud thrust by this method results in an upper-bound value for the actual shroud thrust, since it does not account for

---

[5]Sypris/F. W. Bell Model FH-301 (http://www.fwbell.com/).
[6]Monarch Instruments Phasar-Tach series Phaser-Laser (http://www.monarchinstrument.com/).
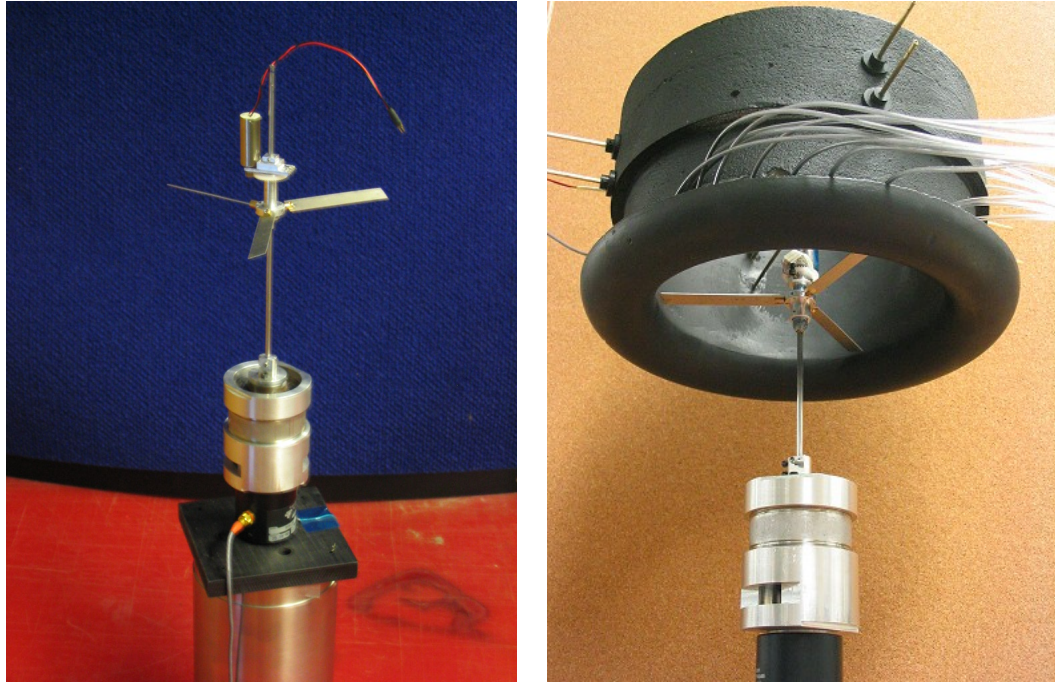
Figure 2.4: Hover test setup

drag due to surface friction on the shroud and download on the shroud support struts. An external frame was therefore constructed to support the shrouds while the rotor inside was separately mounted on the test-stand, unattached to the shroud. Difficulties were experienced, however, in accurately positioning the shroud relative to the rotor, resulting in frequent impacts between the rotor blades and the shroud; this meaurement procedure were therefore abandoned.

Measurements were also made of the axial velocity (dynamic pressure) distributions in the wakes of the open rotor and of six of the shrouded rotors — the LR13-D10 models — using a pitot-static probe. For the open rotor, the measurements were made at a collective of 20°, and at 89 locations in the wake: at radial stations r/R from 0.125 to 1.0, in steps of either $R/8$ (1 cm) or $R/16$, and at axial stations z/R from 0.04 to 1.60, in steps of $R/5$ (1.6 cm). The density of sampling

locations was increased for the regions of large gradients in the measured velocities, which corresponded to the trajectory of the blade tip vortices. A similar set of measurements was also made at 60 locations in the wake of shrouded-rotor model LR13-D10-δ0.6, also at a rotor collective of 20°. A third set of tests consisted of measurements at different radial stations at the diffuser exit plane only, for the five other LR13-D10 models, at rotor collectives of 10°, 20°, 30° and 40°. Both the shroud surface pressure distribution and the wake velocity measurements were made with a variable-capacitance, very-low-pressure transducer[7], with a full-scale range of 0–50 Pa (0–0.007 psi).

2.3   Wind-tunnel test setup

The translational-flight tests were performed in a open-jet wind tunnel with a 22 in x 22 in test section and a turbulence level of 0.3% (Fig. 2.5). A four-component sting balance (Figs. 2.6, 2.7) was designed and constructed to measure the normal force, N, pitch moment, M, roll moment (rotor torque, Q), and axial force (rotor thrust, T) (Fig. 2.8). The lift, L, and drag, D, were determined from the measured thrust and normal force by a coordinate transformation from the body axes to the wind axes:

$$L = N\cos(\alpha) + T\sin(\alpha) \tag{2.1}$$

$$D = N\sin(\alpha) - T\cos(\alpha) \tag{2.2}$$

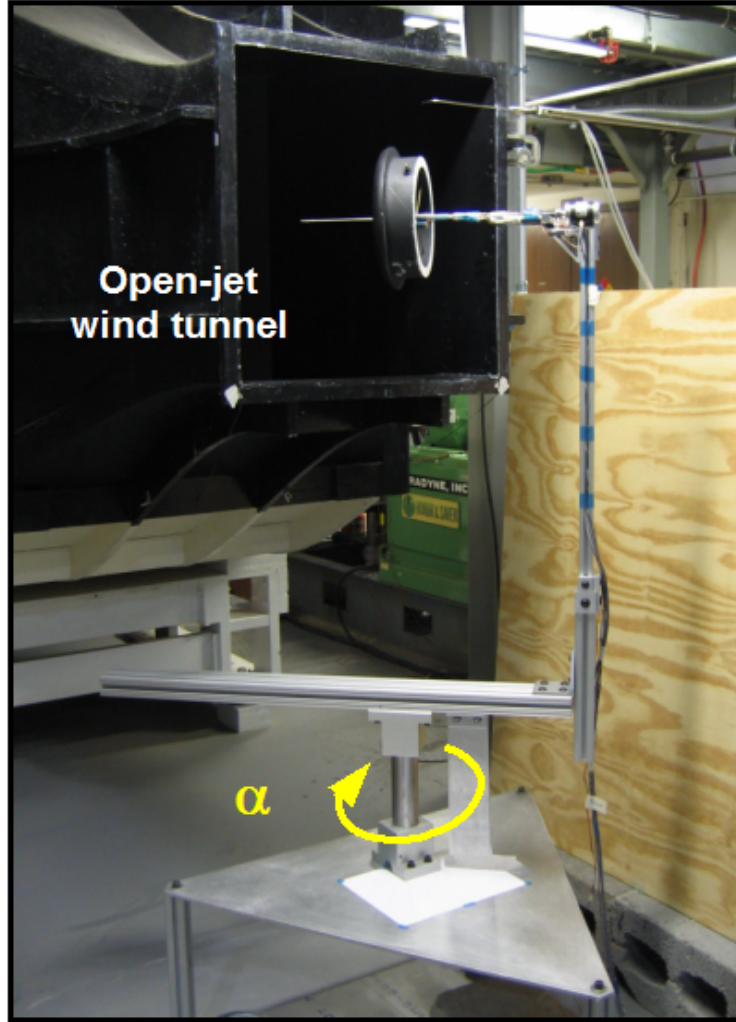[7]Setra Systems Model 267 HVAC/R-series (Heating, Ventilation, Air-Conditioning and Refrigeration) Very Low Differential Pressure sensor (http://www.setra.com/).

Figure 2.5: Wind tunnel test setup

In this study, the angle of attack, α, is defined as the angle made by the axis of rotation of the rotor with the freestream velocity vector, and is therefore the complement of the angle α_{rotor} which is considered to be the angle of attack in conventional rotor analysis (Fig. 2.9).

Note that the pitch moment at the rotor hub can be considered as equivalent to the normal force, which is perpendicular to the rotor axis, acting at a point on the axis henceforth referred to as the 'center of pressure' and located at a distance x_{cp} above the plane of the rotor disk (Fig. 2.10). x_{cp} is therefore positive for points
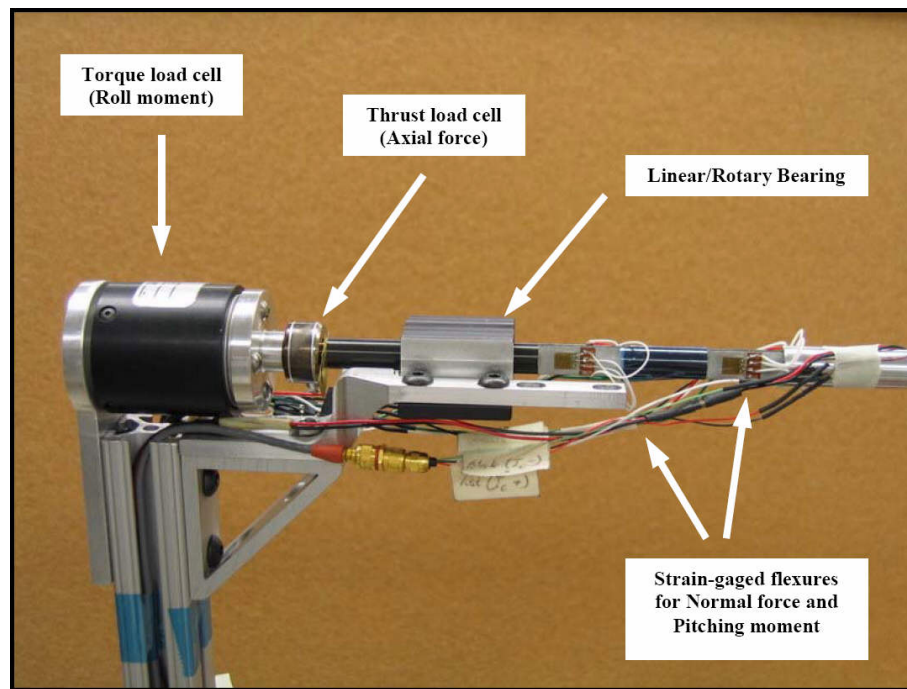
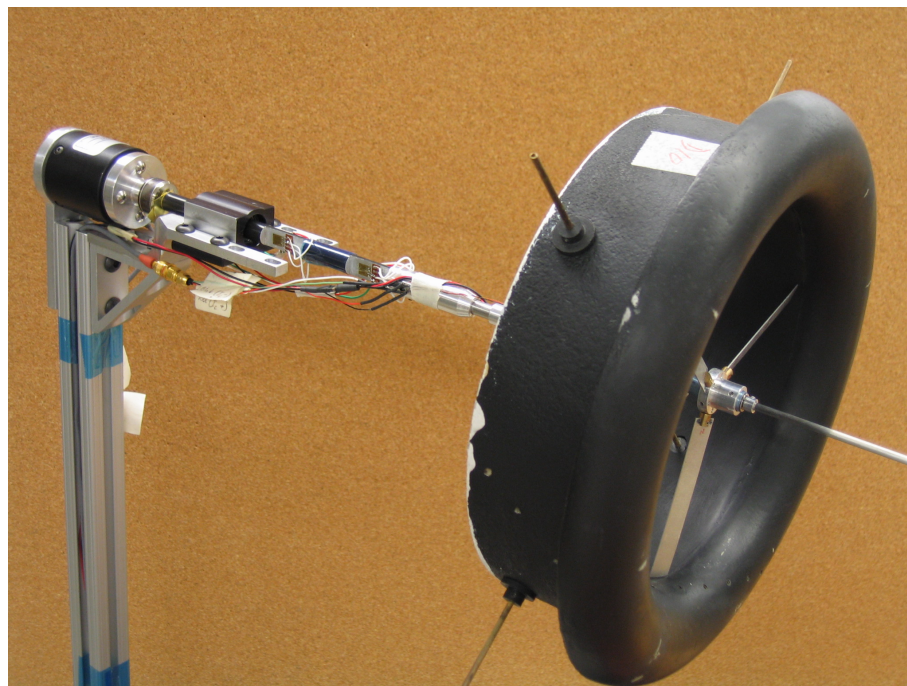Figure 2.6: Four-component wind-tunnel sting balance

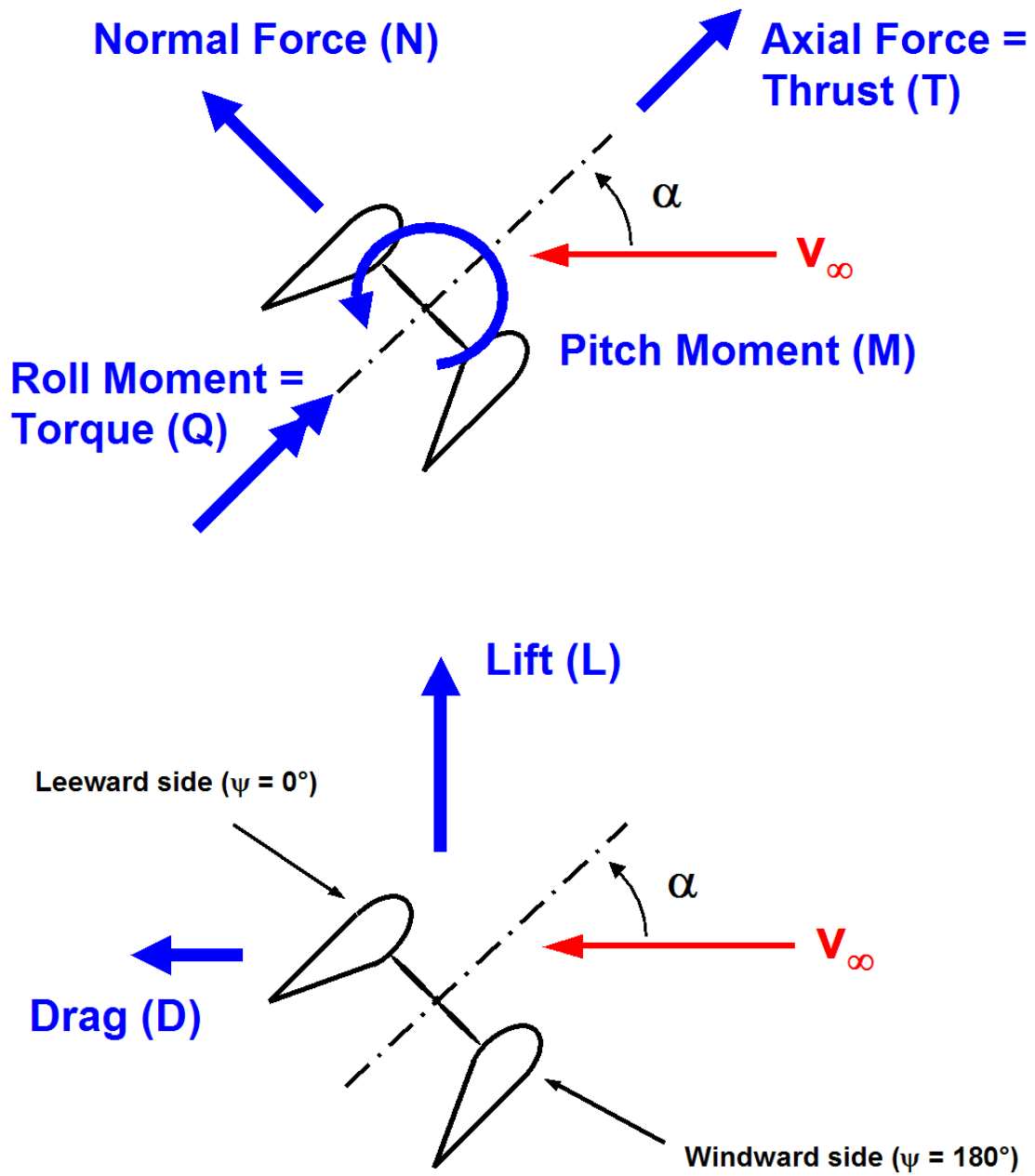Figure 2.7: Sting balance with shrouded-rotor model mounted

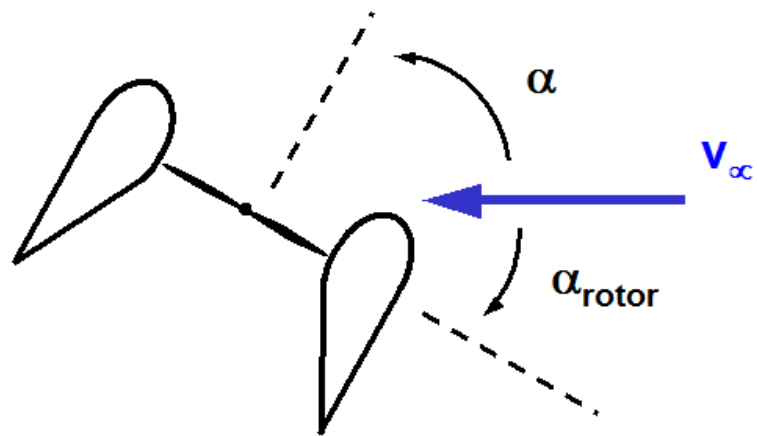Figure 2.8: Forces and moments acting on model in translational flight

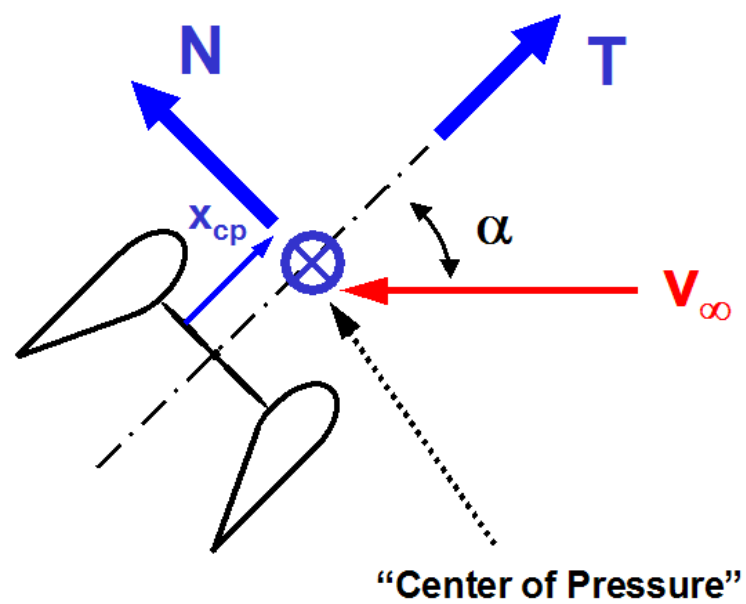Figure 2.9: Angle of attack definition

Figure 2.10: Center of pressure

above (upstream of) the rotor, and negative for points below (downstream of) the rotor.

The rotational speed and shaft power of the models was measured in the same way as in the hover tests. Like the hover-stand, the balance was designed to measure the very low forces and moments generated on MAV-scale models. The roll moment and axial force were measured using the same torque and force sensors that were used in the hover-stand, while the normal force and pitch moment were measured using a beam with two sets of strain-gauged flexures (Fig. 2.6). The full-scale ranges of the roll-moment and axial-force sensors were 0.6 in-lb and 2.2 lb, respectively, while the normal-force/pitch-moment sensing element was calibrated up to 0.7 lb and 4.0 in-lb. To avoid the normal-force sensing element having to bear the weight of the model, the test setup was designed so that the model would 'pitch' in a horizontal plane instead of a vertical one (Fig. 2.5), so the normal force and pitch moment are actually the side-force and yaw moment in the 'earth' frame of reference. The model support structure was designed so that any point on the model longitudinal axis could be positioned directly above the angle-of-attack pivot axis. For the tests described in this paper, this point was chosen to be the location of the rotor hub.

The shroud was instrumented with twenty-four pressure taps, as shown schematically in Fig. 2.11. Twelve of the taps were at the $\psi = 180°$ rotor azimuth, corresponding to the windward side of the shroud when the model is pitched forward into the wind, and twelve were at the $\psi = 0°$ azimuth, corresponding to the leeward or downwind side (Fig. 2.8). Within each set of twelve taps, eight were distributed
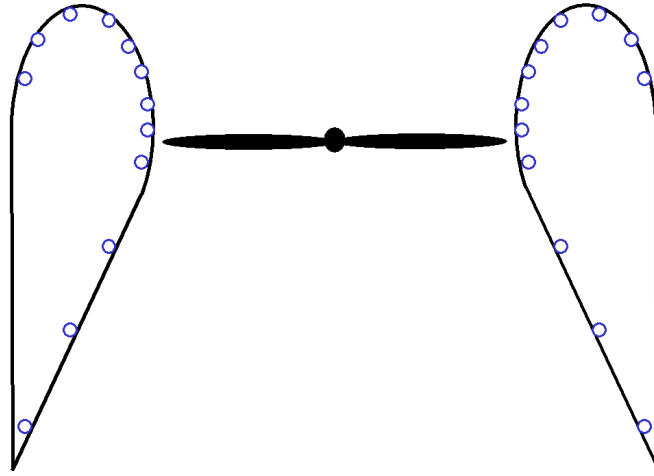
Figure 2.11: Pressure tap locations (wind-tunnel model)

over the shroud inlet and four along the inner surface of the diffuser, with a greater concentration of taps near the plane of the rotor disk. Figure 2.12 shows the test setup after the model had been instrumented with the pressure taps. The bundles of pressure tubing were adjusted to remain out of the rotor wake and to exert minimal force on the model due to their own weight. Although it was desired to have a complete picture of the flow-field around the entire model, the small size of the model resulted in limited room for additional tubing, and therefore it was not possible to intrument the outer surface of the shroud with pressure taps as well.

For both the open and shrouded rotors, the test matrix consisted of free-stream velocities of 0, 10, 15 and 20 ft/s, and angles of attack from -45° to +90°, in steps of either 5° or 15°, where $\alpha = 0°$ corresponds to axial flow (vertical climb or 'propeller mode'), and $\alpha = 90°$ corresponds to hover in edgewise flow. The performance measurements were made at rotational speeds of 2000, 3000 and 4000 rpm, while the surface pressure measurements were made at a rotational speed of 3000 rpm
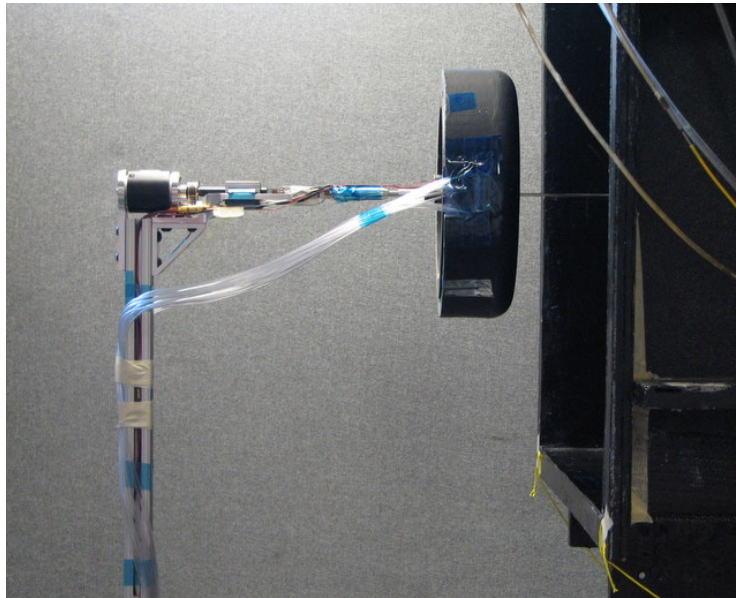
(a) Side view
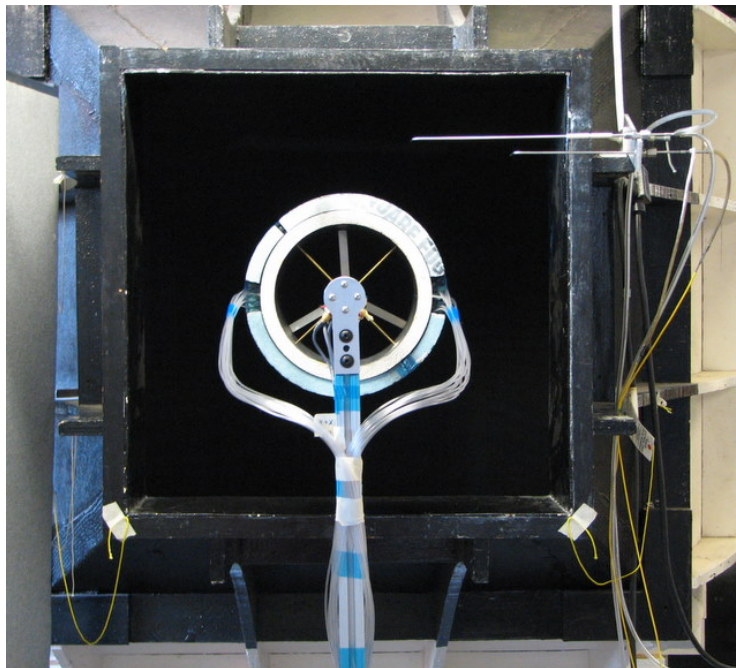
(b) Rear view

Figure 2.12: Wind tunnel model instrumented with pressure taps

only. All tests were performed at a fixed rotor collective of 20°, which was the collective at which the rotor exhibited optimal performance in hover. Note that the rotor was not trimmed in any way.

2.4   Test procedure and uncertainty analysis

For all tests, the data were acquired and analyzed using the MATLAB® programming environment[8] and a National Instruments data-acquisition system ('DAS')[9] with 12-bit resolution, or a least count of $1/2^{12}$ times the full-scale input range of the individual data channels. For the hover tests, the input ranges were set to ± 5 V for all the channels, resulting in a resolution (least count) of 2 g for the thrust measurements, 0.02 oz-in (0.14×10^{-3} N-m) for the torque and 0.025 Pa for the pressure. For the wind-tunnel tests, depending on the values of the forces, moments or pressures being produced, the input ranges were reduced so as to obtain even smaller resolutions in the measurements.

The procedure that was used to acquire the data in both the hover and the wind-tunnel tests is described below. For each point in the test matrices:

1. The rotor rotational speed was adjusted to within ± 10 rpm of the nominally desired speed.

2. With the rotor running [and the wind tunnel on], four [five] seconds of data were acquired from the transducers at a rate of 1000 [2000] samples/second

---

[8]http://www.mathworks.com/products/matlab/

[9]National Instruments DAQCard-6062E, 12-bit resolution (http://www.ni.com/). Some of the earliest tests were conducted with a National Instruments model PCI-6031E DAS which had 16-bit resolution.

from each transducer, and the values averaged to eliminate unsteady effects. A higher sampling rate and a longer time period were found necessary for the wind-tunnel tests to compensate for the higher vibration levels in the models in those conditions.

The sampling rate — at 1000 Hz, more than ten times higher than the highest rotational speed at which the models were tested (5000 rpm, 83.3 Hz) — and the lengths of time were chosen so as to be able to average out the electrical noise in the computerized data-acquisition system and any other random or periodic fluctuations in the operation of the rotor. Although this investigation was only concerned with the steady values of test variables, the setup allowed for detection of vibrations of frequencies up to the Nyquist frequency of 500 Hz, corresponding to a rotor harmonic of 6/rev or more, with a resolution of 0.25 Hz[10].

3. The rotor [and tunnel] were then stopped, and, after all transients were allowed to die out, the transducer outputs were recorded again for a period of one second and averaged. In the hover tests, the time required for to allow the model to come to rest varied from five to fifteen seconds, depending on the inertia of the specific model being tested. For the wind-tunnel tests, this duration was increased to 20–30 s.

4. The difference between the two averaged values — rotor-on[/wind-on] and rotor-off[/wind-off] — was recorded as the measurement for that particular

---

[10]The frequency resolution Δf is equal to $1/T$, where T is the length of time for which data were acquired.

run. This procedure was used for each run to avoid errors from drifting of the transducers.

5. Each measurement run was repeated from four to ten times, until the scatter in the measurements fell to acceptable levels.

The uncertainties in the measurements, and in the 'final' reported values that are discussed in the subsequent chapters, were estimated by the following procedure. For each test variable (thrust, torque, pressure):

1. The uncertainty in the measurement value from each run — the difference between the two averages, rotor-on[/wind-on] and rotor-off[/wind-off] — was considered to be equal to the 'reading error' for the test variable. For these digitally-acquired data, this would be the discretization or quantization error as set by the resolution of the DAS, and equal to plus/minus one-half of the least count for each variable.

Although this was not done, a more rigorous estimate would have been obtained by the following procedure:

   (a) For each of the 4000/5000/1000 measurement samples acquired during the rotor-on[/wind-on] and rotor-off[/wind-off] phases, estimate the statistical error, due to random variations, in the individual sample value by the standard deviation of the 4000/5000/1000 values.

   (b) Compare the value of this statistical error to the value of the reading (discretization) error, and choose the larger of the two values as the measurement error for each individual sample.

(c) Propagate the measurement error through the averaging and differencing operations to obtain the estimate for the uncertainty in the final measurement value for that run.

Since a very large number of samples (4000/5000/1000) were acquired, the final propagated value of the uncertainty, obtained by this more rigorous method, would have been much lower than the uncertainty in each individual sample value. Therefore, the value of the uncertainty that was actually used for the final measurement from the run — i.e., the reading error — is quite likely to have been very conservative.

2. Using this procedure, multiple measurement runs were conducted until the scatter in the values from each run, as quantified by the standard deviation of these values over all runs, fell to about the same magnitude as that of the reading error, or lower. Because of fluctuations in the output of the power supply controlling the drive motor and other unsteady factors in the operation of the rotors, the average rotational speed in any given measurement run typically varied by up to 10–15 rpm between different runs; hence, the values of the measurements from each run would be *expected* to be slightly different from one run to another. Even so, the reduction in the spread — the standard deviation — of the values gave a good estimate for the improvement in the precision of the measurements. Typically, only about 4–5 runs were required to obtain satisfactory precision, but in some cases up to 10–12 runs were required.

3. The measurement values of the test variables from each run were converted

into their non-dimensional coefficient forms. The uncertainties in the measurements of the rotational speed (± 1 rpm), the rotor radius (± 0.001 cm), the air density (± 0.05 kg/m³) and the (dimensional) values of the test variables were propagated through these calculations to obtain the uncertainty in the value of the coefficient for that run.

4. The final value of the coefficient for that point in the test matrix was obtained by averaging over the values of the coefficients from all runs. The uncertainties in the values from each run were propagated through the averaging operation to obtain the uncertainty in the mean value. Note, however, that this uncertainty is still due only to the reading errors in the different measurements.

5. The statistical (random) error in the coefficient values for each run was estimated by the standard deviation of the values over all runs. This is a valid operation because, even though the dimensional values of the test variables would be expected to vary from one run to another, the coefficient values would be expected to be the same. This statistical uncertainty, which gives a measure of the spread of the measurements from different runs (the precision, or, rather, the lack thereof), was similarly propagated through the averaging operation over all runs.

6. The larger of the two propagated uncertainty values — the one due to reading errors and the other due to random effects — was selected as the estimate of the uncertainty in the 'final' mean value of the coefficient.

Chapter 3

Experimental Results: Hover Tests

3.1 Introduction

This chapter presents the performance and flow-field measurements made in the hover tests of the open and shrouded rotors, and the comparisons of the different shrouded-rotor models based upon those measurements. The data — and the associated analyses — are presented in three sections: first, the performance characteristics (thrust, power, efficiency) and comparisons with the predictions of momentum theory; second, the shroud surface pressure distributions; and third, the wake velocity distributions. Within each section, the effects of varying each of the shroud geometric parameters (blade tip clearance, inlet lip radius, diffuser angle, diffuser length, diffuser expansion ratio) are discussed. In all cases, the data are presented in non-dimensional form — as force, power and pressure coefficients and as normalized distances and velocities. For obtaining the coefficients of the open rotors, the tip speed and disk area of the individual rotors were used as the reference velocity and reference area; for the shrouded rotors, since rotors with different blade tip clearances were tested, the reference velocity was the tip speed of the actual rotor used for the individual model, while the reference area was that of the shroud throat.

3.2 Simplifying assumptions

Two simplifying assumptions were made prior to performing the analyses presented in this chapter. The first was that the values of the coefficient/normalized forms of the various quantities did not vary significantly between the tested rotational speeds of 2000 and 4000 rpm, and that the values used in the analyses comparing the various shrouded-rotor models could therefore be those obtained by averaging over all the measurements made at all rotational speeds within this range. The second assumption was that the reduction in diameter of the rotor, which was required in order to test models with different blade tip clearances, did not significantly change the performance of the (open) rotor itself, and that, for the purpose of comparison with the shrouded rotors, the different open rotors could therefore be represented by a single 'representative' open rotor, the diameter and performance of which were obtained by averaging over the values of all the rotors. The reasoning and justification for these assumptions are given below.

3.2.1 Assumption regarding rotational speed

For the first open rotor and shrouded-rotor model tested (LR09-D20-δ0.5), the hover tests were conducted at rotational speeds from 500 rpm up to 5000 rpm, to determine the effects of Reynolds number on the data. The thrust and power coefficients for these two cases are shown in Figs. 3.1a–d, plotted for the different blade collective angles as functions of the rotational speed. It can be seen that the mean values of the coefficients, calculated as described above, remain fairly

constant over the range of speeds tested, although some variation is seen at the lower speeds. More significant, though, is the fact that the uncertainties in the mean values — estimated by the method described in Section 2.4 (p. 126), and shown by the errobars in the figures — increase significantly as the speed is decreased. This is due to two reasons: first, the increased sensitivity of the flow, and hence of the rotor performance, to small random disturbances at lower Reynolds numbers [8]; and second, the decrease in the relative magnitude of the absolute, dimensional values of the various measured quantities (thrust, torque, rotational speed) to the uncertainties in their measurement — effectively, a reduction in the signal-to-noise ratio. The first increases the uncertainty due to the statistical spread of the values from different measurement runs — the 'random error', while the second increases the uncertainty due to the inherent limits on the precision in measuring a physical quantity — the 'reading error' (see Section 2.4, p. 126). Figures 3.1e–f show a comparison of these two sources of uncertainty, along with their variations with changing rotational speed. It can be seen that, in these tests, the uncertainties due to the reading errors were typically greater than those due to the random errors, and especially so at the lower rotational speeds. As mentioned in Section 2.4, the final estimates of the uncertainties shown in the presentation of the data in this chapter were the greater of the two values for each individual point in the test matrix.
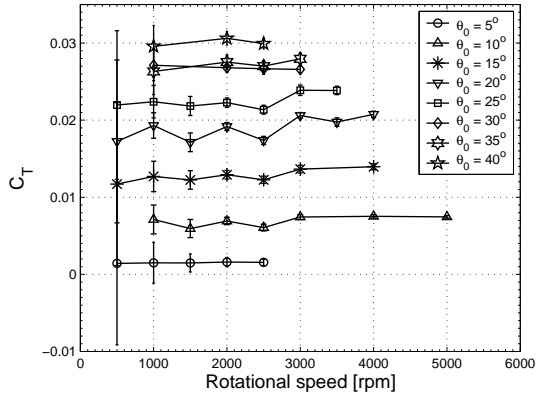
It is thus clear that, to obtain results with good confidence levels, the tests should be conducted at the higher rotational speeds. However, at the higher blade collective angles, the increased drag on the blades and the power limitation of the
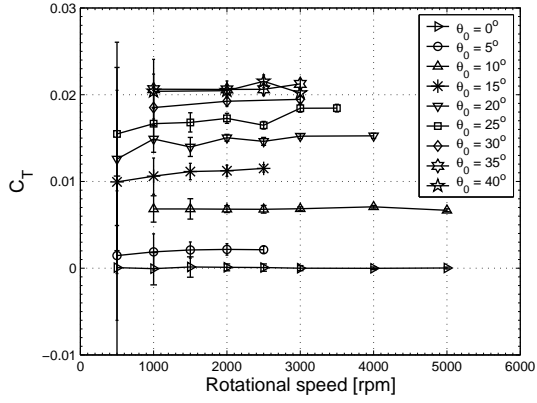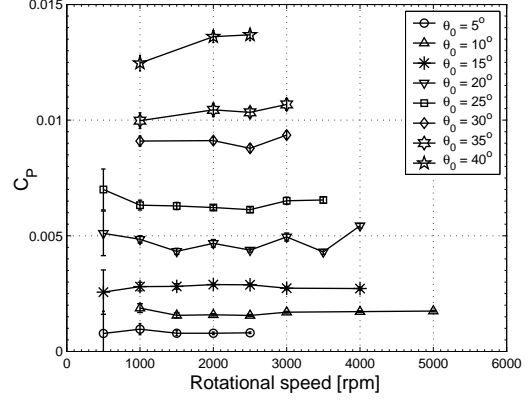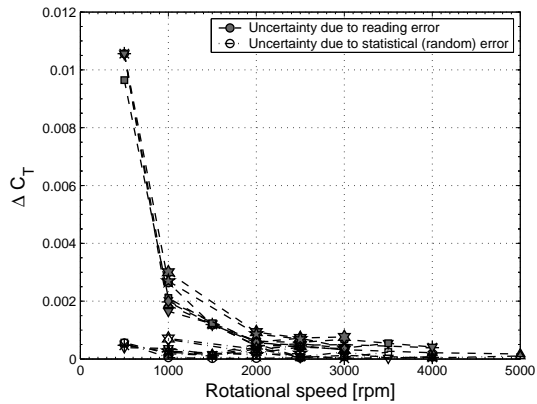
(a) Open rotor: thrust coefficient.
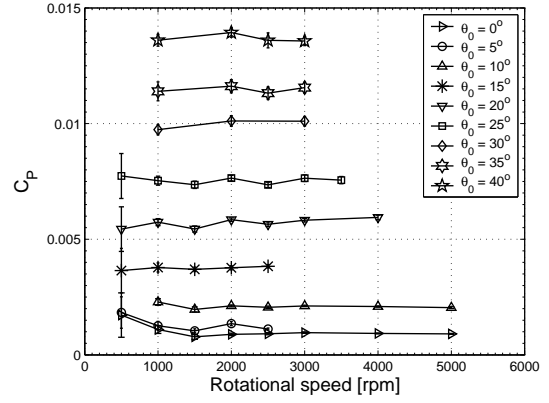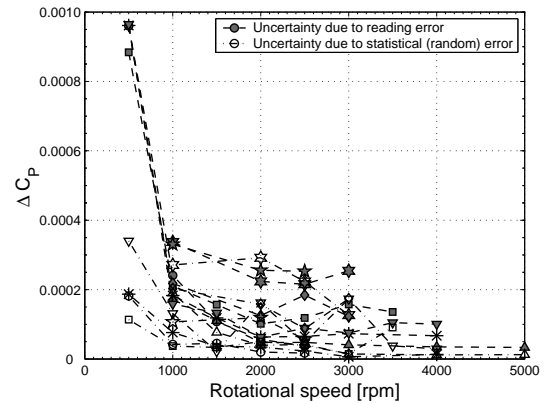
(b) Open rotor: power coefficient.

(c) LR09-D20-δ0.5: thrust coefficient.

(d) LR09-D20-δ0.5: power coefficient.

(e) LR09-D20-δ0.5: uncertainty in C_T.

(f) LR09-D20-δ0.5: uncertainty in C_P.

Figure 3.1: Effects of changing rotational speed on performance

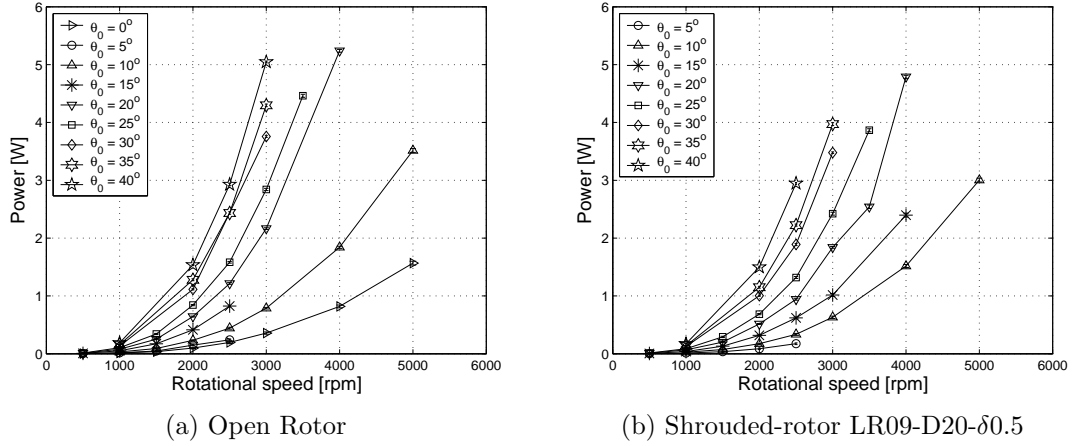| (a) Open Rotor | (b) Shrouded-rotor LR09-D20-δ0.5 |

Figure 3.2: Effect of increasing rotational speed on power consumption

drive motor[1] meant that speeds of only up to 2000 or 3000 rpm could be tested (Figure 3.2). Therefore, for the subsequent models, the tests were conducted at rotational speeds from 2000 to 4000 rpm only; and since the mean values of the coefficients at the different speeds within this range were not significantly different, the values of the coefficients were therefore averaged over all rotational speeds tested (between 2000 and 4000 rpm) for the analyses that are presented in the following sections.

3.2.2 Assumption regarding rotor radius

As mentioned earlier, the different blade tip clearances in the shrouded-rotor models were created by using rotors with blades of different lengths. Seven different rotors were used, with diameters varying from 154.0 mm to 159.7 mm — a range of 3.6%D_t. Figures 3.3a–b compare the performance of six of the rotors at four different

---

[1]The electric drive motor had a maximum 'safe' rating of 8.5 watts. Accounting for the motor efficiency — which, for these motors, is typically around 50% — and for transmission losses, the power available at the rotor would therefore be much lower.

collective angles, showing the thrust and power coefficients plotted as functions of rotor diameter, along with the average of the values of all the rotors at each collective. In these figures, the uncertainty bounds for the individual rotors are shown by the errorbars, while those for the mean values are shown by the bands enclosed by the dashed lines. It can be clearly seen that the variations in C_T and C_P with changing diameter are quite random, i.e., the reduction in diameter had no generalizable effect on the performance of the rotor. Therefore, for the purpose of comparisons with performance of the shrouded rotors, it was justifiable that, within the limits of experimental uncertainty, all seven rotors could be represented by a single 'representative' open rotor, the performance of which — in non-dimensional coefficient terms — was taken to be equal to the averages of the values of the individual rotors. This is further illustrated by Figure 3.3c, which shows the rotor polar — C_T vs. C_P — of the resulting representative open rotor, along with the measurements of the individual open rotors and those of one of the shrouded-rotor models.

3.3   Performance measurements

In this section, the general performance characteristics of the open and shrouded rotors are first discussed, followed by more detailed analysis of the effects of varying the individual shroud geometric parameters.
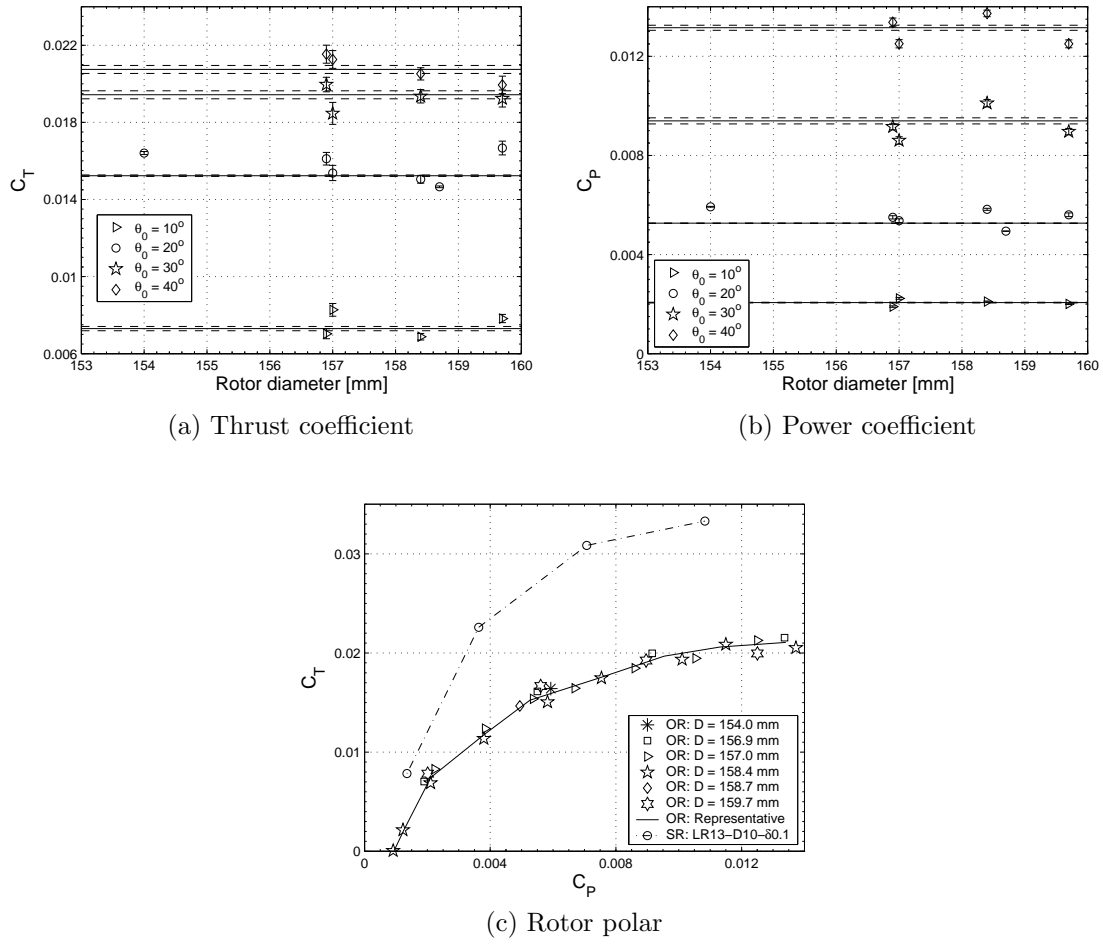
(a) Thrust coefficient

(b) Power coefficient

(c) Rotor polar

Figure 3.3: Effect of changing diameter on the performance of open rotors

3.3.1 General characteristics

The performance data for all seventeen shrouded rotors, as well as for the representative open rotor, are shown in Figs. 3.4–3.12. In these figures, the measured values are shown by the symbols and are connected by straight line-segments to reveal the trends more clearly. Figures 3.4 and 3.5 show the 'raw' thrust (C_T) and power (C_P) data plotted as functions of blade collective angle (θ_0). The maximum values of the thrust and power coefficients obtained in these tests — 0.02–0.03 for C_T, 0.010–0.014 for C_P — are substantially higher than those typically seen for larger-scale rotors. This is partly attributable to the higher collective angles at which these micro-scale rotors have been tested, but more so due to their much lower tip speeds: at a typical rotational speed of 3000 rpm, these rotors had a tip speed of around 80 ft/s, which is almost nine times lower than the typical values of 700 ft/s and higher seen for full-scale manned helicopters [15, pp. 683–701]. Even though the disk loadings of these micro-rotors (up to 0.5 lb/ft^2) are also much lower than those for large-scale helicopters (typically up to 10 lb/ft^2 [14, p. 487]), the inverse scaling of the thrust coefficient with the square of the tip speed results in much higher values of C_T; similar reasoning applies to the values of C_P.

Figures 3.4 and 3.5 also show that, for collectives above 10°–15°, the shrouded rotors all produce higher thrust than the open rotor, at the same collective angle, while consuming less power at all collectives. The increase in thrust coefficient — up to 50% more — is greatest at the higher collectives, while the decrease in power — also by up to 50% — is greatest at the lower collectives. The reduced power is
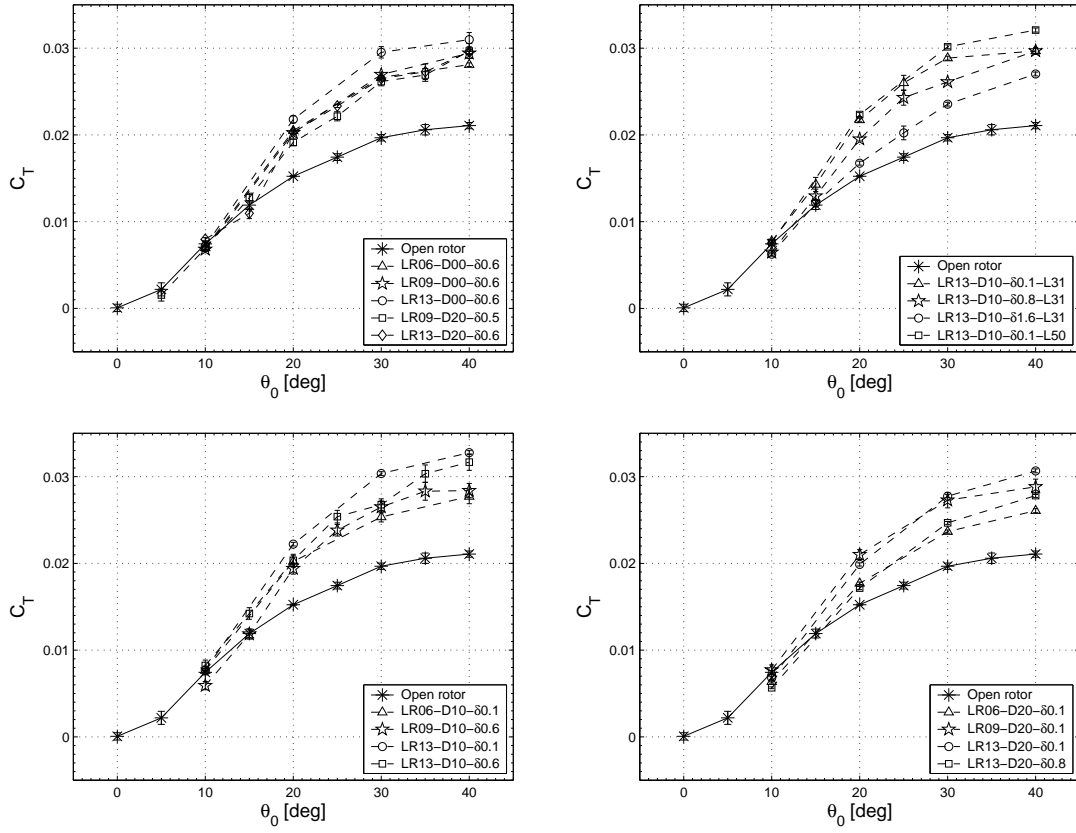
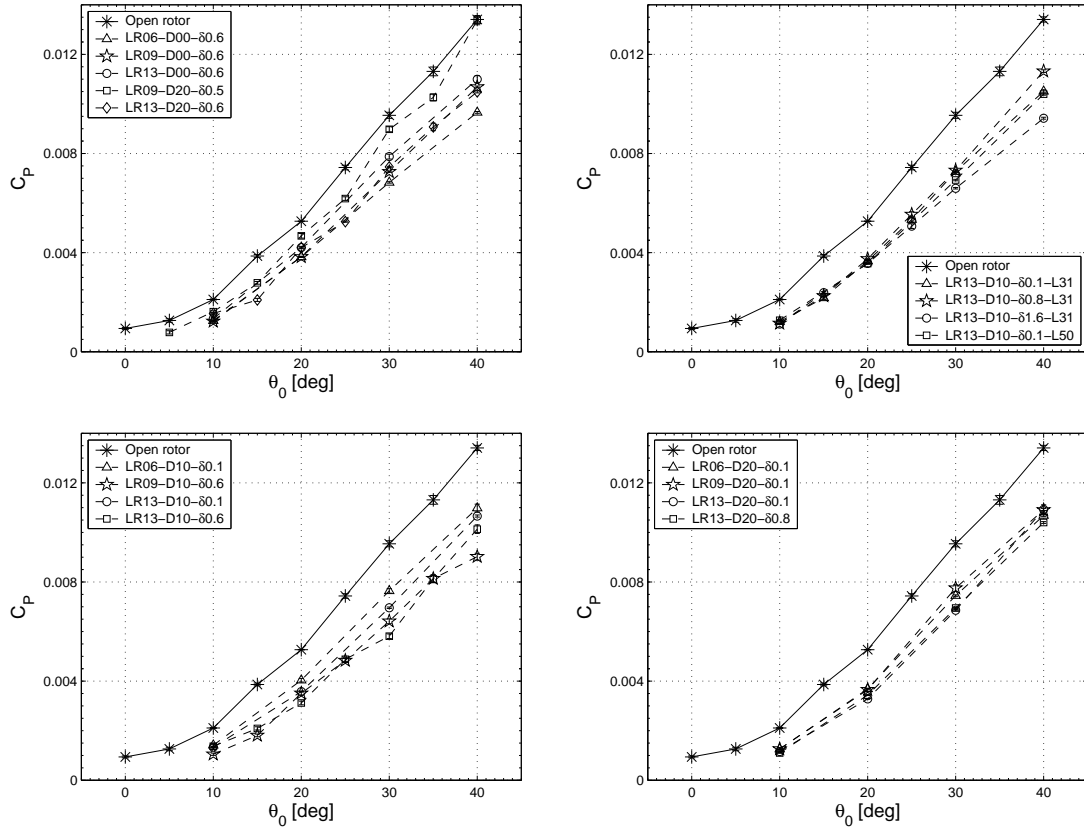Figure 3.4: Thrust coefficient vs. collective angle

Figure 3.5: Power coefficient vs. collective angle

due both to the reduction in the induced power because of the increased expansion ratio and the consequent lower velocity of the wake, as well as to the reduction in profile power because of the off-loading of the rotor by the shroud, causing the rotor blade elements to operate at lower angles of attack. The reason for the reduced thrust of the shrouded rotors at lower collectives, compared to the open rotor, can be understood by considering an approximate blade-element-momentum-theory (BEMT) model of the hovering rotor, in which it is assumed that the induced inflow (λ) is constant over the entire rotor disk and that all blade elements operate at the same angle of attack, derived from the mean lift coefficient of the rotor ($\bar{C}_L$) [14, p. 113]. The pitch angle, θ, of a blade element at any radial station along the blade is then given by the sum of the aerodynamic angle of attack (α) and the induced inflow angle (ϕ):

$$
\begin{aligned}
\theta(r) &= \alpha(r) + \phi(r) \\
&= \frac{\bar{C}_L}{a} + \frac{\lambda}{r} \\
&= \left(\frac{1}{a}\right) \frac{6C_{T_{\text{rotor}}}}{\sigma} + \frac{\sqrt{\sigma_{\text{d}} C_T}}{r} \\
&= \left(\frac{6}{\sigma a}\right) \frac{C_T}{2\sigma_{\text{d}}} + \frac{\sqrt{\sigma_{\text{d}} C_T}}{r}
\end{aligned}
\tag{3.1}
$$

Thus, for the same thrust coefficient, increasing the expansion ratio causes a reduction in the aerodynamic angle of attack of a blade element but an increase in the induced inflow angle. The corresponding change in the required rotor collective depends on the relative magnitudes of the two terms in Eq. (3.1). At very low thrust coefficients, the induced-inflow term (proportional to $\sqrt{\sigma_{\text{d}}}$) dominates, so that in-

creasing σ_{d} results in a net increase in the pitch angle required for a given C_T, or, equivalently, a lower C_T at the same rotor collective. At higher thrust coefficients, the angle-of-attack term (proportional to $1/\sigma_{\mathrm{d}}$) dominates, so that increasing σ_{d} results in a net decrease in the pitch angle required for a given C_T, or, equivalently, a higher C_T at the same θ_0. Equation (3.1) has been plotted in Fig. 3.6 for an open rotor[2] and for different values of σ_{d} for a shrouded rotor, and the cross-over seen in the experimental data in Fig. 3.4 can be clearly seen in these theoretical predictions as well, occurring between blade tip angles of 3° and 5°. A reduction in either the expansion ratio or the lift-slope (a) of the blade airfoils causes the first term in Eq. (3.1) to dominate and the cross-over to occur earlier, i.e., at a lower collective. The higher values of θ_0 at which the cross-overs are seen in the experimental data are probably due to factors that are not accounted for in this simplified model.

The improved performance of the shrouded rotors is more evident when the thrusts of the two configurations are compared at the same power (Fig. 3.7). At the same power coefficient, some of the shrouded rotors — models LR13-D10-δ0.1-L72 and -L50, specifically — have thrust coefficients up to 94% higher than that of the open rotor, with the greatest improvements occurring around $C_P = 0.004$. Conversely, at the same thrust coefficient, the shrouded rotors have power coefficients up to 70% lower than that of the open rotor, with the greatest reductions occur-

---

[2] For the special case of an open rotor, Eq. (3.1) becomes:

$$\theta_{OR}(r) = \left(\frac{6}{\sigma a}\right) C_T + \frac{\sqrt{C_T/2}}{r}$$

Thus, for comparing the aerodynamic angles of attack and the induced inflow angles of the blade elements of a shrouded rotor and an open rotor at the same thrust coefficient, this yields the relations $\alpha_{\mathrm{SR}} = \frac{1}{2\sigma_{\mathrm{d}}}\alpha_{\mathrm{OR}}$ and $\phi_{\mathrm{SR}} = \sqrt{2\sigma_{\mathrm{d}}}\phi_{\mathrm{OR}}$.

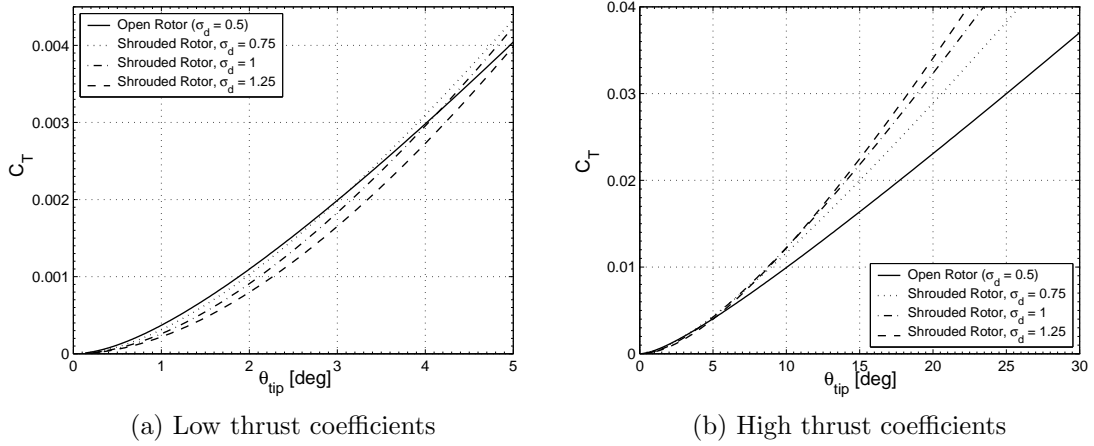(a) Low thrust coefficients

(b) High thrust coefficients

Figure 3.6: Theoretical prediction of thrust coefficient as a function of blade tip angle, for different values of expansion ratio (Equation (3.1), $\sigma = 0.1$, $a = 5.73\tilde{\text{p}}$er radian, $r = 1$.)

ring near $C_T = 0.02$, which is approximately the highest value of C_T achieved by the open rotor. Note that these comparisons are made while considering the actual power, not the ideal power, and therefore would be expected to be different from the predictions from momentum theory that were given in Table 2.2 (p. 113).

The power loading, $\text{PL} = T/P$, is the quantity that the designer of an aircraft is ultimately interested in, because it directly gives the obtainable increase in thrust at the same power, or, conversely, the decrease in power at the same thrust. While the rotor polars — the graphs of C_T versus C_P — are useful means of comparing the performances of the open and shrouded rotors, they are only good for comparisons when the different configurations are forced to operate at the same thrust or power coefficient. This is not a realistic circumstance in the design of an aircraft, since any rotor design would typically be operated as near as possible to its collective for maximum efficiency (power loading). Since the rotor polar does not directly indicate the value of this collective, it does not easily enable comparisons of the
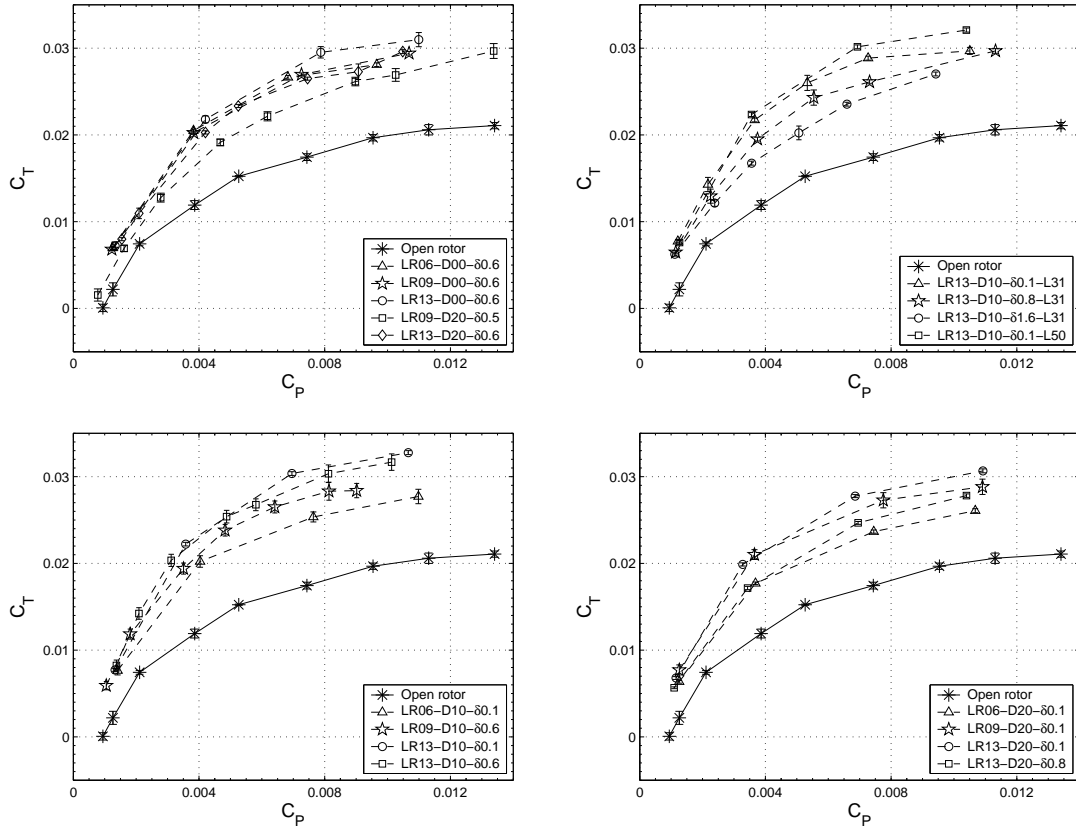
Figure 3.7: Thrust coefficient vs. power coefficient

different configurations at their respective points of maximum efficiency. Figures 3.8 through 3.12 therefore show three different measures of efficiency which do enable such a comparison, plotted as functions of collective angle and of thrust coefficient. Two of these measures are familiar to rotor aerodynamicists: the ratio of thrust coefficient to power coefficient, C_T/C_P (Figs. 3.8, 3.9), which is maximum at the point of maximum power loading when the tip speed of the rotor is constrained to a fixed value:

$$\frac{T}{P} = \frac{1}{v_{tip}} \times \frac{C_T}{C_P} \tag{3.2}$$

and the figure of merit, FM (Figs. 3.10, 3.11), which shows a maximum at the point for optimal operation when the tip speed is allowed to vary but the disk area is constrained:

$$\frac{T}{P} = \sqrt{\frac{2\rho}{\mathrm{DL}}} \times \mathrm{FM} = \sqrt{\frac{4\sigma_\mathrm{d}\rho A}{T}} \times \mathrm{FM} \tag{3.3}$$

where now, in the general case of a shrouded rotor, the disk loading (DL) is equal to $T_{\mathrm{rotor}}/\mathrm{A} = T/2\sigma_\mathrm{d}A$. These two measures are appropriate for determining the optimal operating collective of a given rotor, open or shrouded, and can be used for comparing the performances of different open-rotor designs or of different shrouded rotors with the same diffuser expansion ratio. However, when comparing designs with *different* expansion ratios, use of the traditional formulation of the figure of merit (Eq. (1.3)) can lead to incorrect conclusions. This can be seen from Eqs. (1.2) and (1.3): at the same total thrust, increasing the σ_d causes the ideal power — and hence the figure of merit — to decrease, even though the total power requirement has actually decreased, and the power loading (efficiency) increased. However,

Eq. (3.3) suggests a different efficiency measure that would overcome this limitation — a 'generalized' figure of merit, $\mathrm{FM}^* = \mathrm{FM}\sqrt{\sigma_\mathrm{d}}$, which is nothing but $C_T^{3/2}/2C_P$. This measure can be used for comparing both open and shrouded rotors, whether at the same or different value of expansion ratio, as well as for determining the optimal operating point for a given rotor, open or shrouded, since the maximum FM and maximum FM^* both occur at the same point (collective). Comparisons of the traditional FM are still permissible when the different designs have the same *rotor* thrust (disk loading); however, this is of little practical use, since it is the total thrust that a designer is interested in. At a desired total thrust and disk area, the required power is inversely proportional to FM^*, while at a given power and disk area, the thrust that would be produced is directly proportional to $(\mathrm{FM}^*)^{2/3}$. Thus, a graph of $\mathrm{FM}\sqrt{\sigma_\mathrm{d}}$ versus C_T (Fig. 3.12) would perform the same role as that of the traditional FM-vs.-C_T graph for an open rotor, while also allowing for valid comparisons of the performances of configurations with different expansion ratios. The only disadvantage of this measure is that, unlike the traditional figure of merit, it does not have a maximum possible value of unity, having instead a maximum possible value of $\sqrt{\sigma_\mathrm{d}}$, and therefore does not give as immediate an idea of how close a given design is to 'perfection.' For this purpose, the traditional figure of merit remains the better efficiency measure. Further discussion about these different measures of rotor efficiency is given in Appendix B (p. 297) of this dissertation.

Figures 3.8 and 3.9 show that, for the open rotor, the maximum value of C_T/C_P occurs at a collective angle of 10° ($C_T = 0.0075$), while for the shrouded rotors it occurs between collectives of 10° and 20° ($C_T = 0.0075$–0.0225), depending on the

specific model. Although measurements were made for only a few of the shrouded rotors at $\theta_0 = 15°$, the trends in the data suggest that the maximum C_T/C_P may occur at this collective angle for all the shrouded-rotor models (when used with this specific rotor). The greatest improvement in performance, therefore, according to this measure of efficiency, is by around 94%, comparing the maximum value of 3.5 for the open rotor with that of 6.8 for shrouded-rotor model LR13-D10-δ0.6. This corresponds to either a 94% increase in thrust at the same power, or a 49% reduction in power at the same thrust, compared to the open rotor, if the tip speeds are held the same (Eq. 3.2). Although data were not taken with this shroud and a smaller tip clearance $(0.1\%D_t)$ at $\theta_0 = 15°$, it is quite probable that the smaller tip gap would have resulted in even greater improvements in performance.

In terms of the figure of merit (Figures 3.10 and 3.11), the shrouded rotors show maximum values of up to 0.42 (model LR13-D10-δ0.1-L50), which is a 68% improvement over the maximum value of 0.25 for the open rotor, and these maxima universally occur at a collective angle of 20°, for both the open and shrouded rotors. The thrust coefficients at which these maxima occured were 0.015 for the open rotor and 0.020 or slightly higher for the shrouded rotors. As expected, the FM values for the models with the largest expansion ratio — the D20 models — are in some cases lower than those for the open rotor, which would imply a seemingly reduced efficiency for these models. The generalized form of the figure of merit eliminates this misleading effect of the conventional form of FM, and clearly shows (Figure 3.12) that *all* of the shrouded rotors are indeed much more efficient than the open rotor — up to 160% more efficient in the case of some of the LR13-D10 models, which
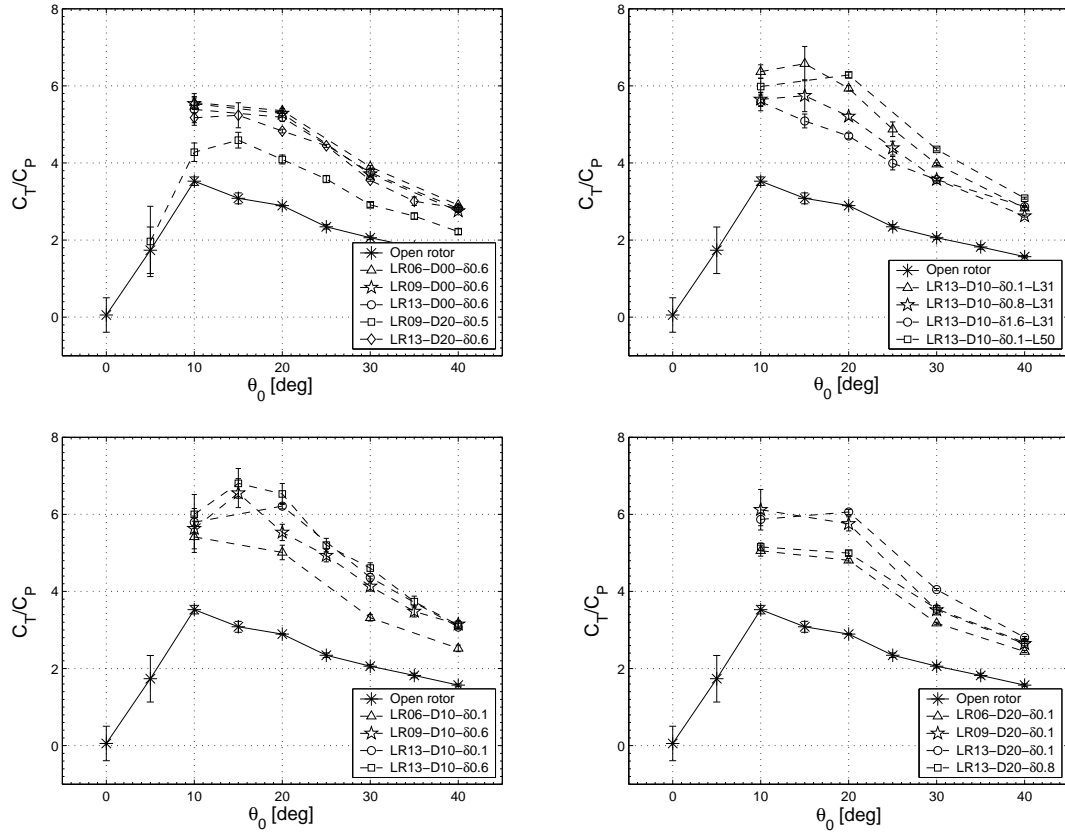
147

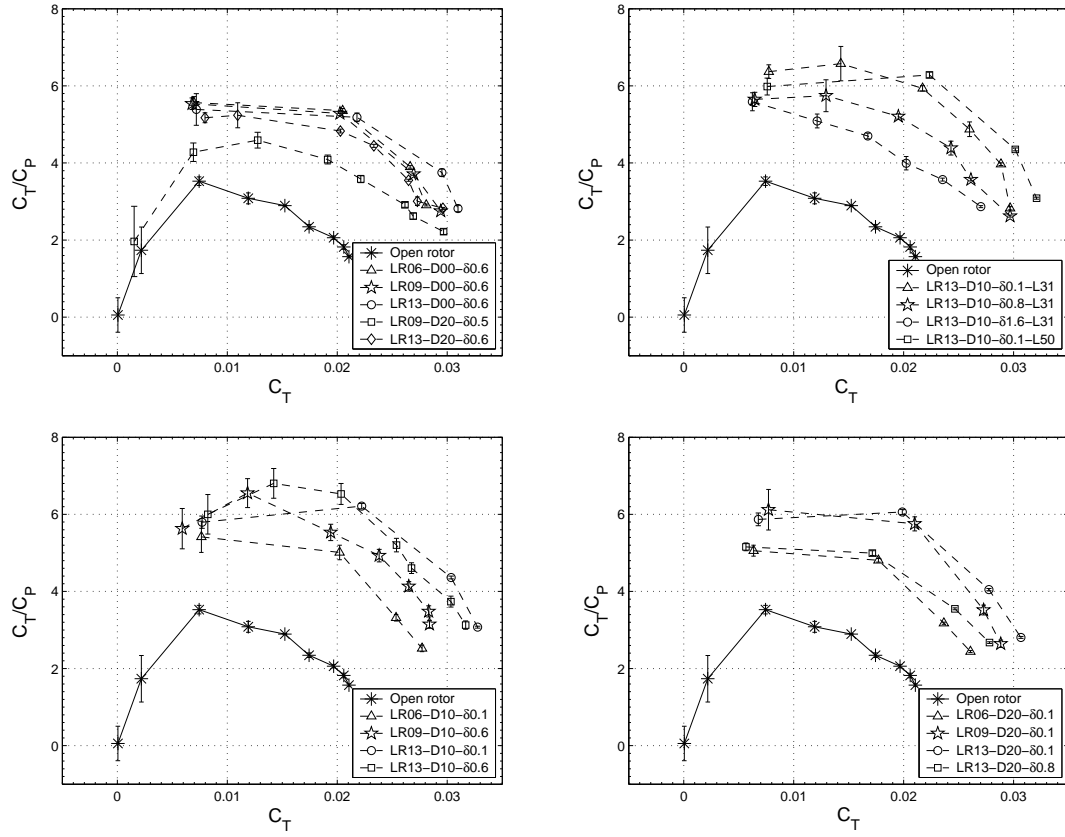Figure 3.8: Ratio of thrust coefficient to power coefficient vs. collective angle

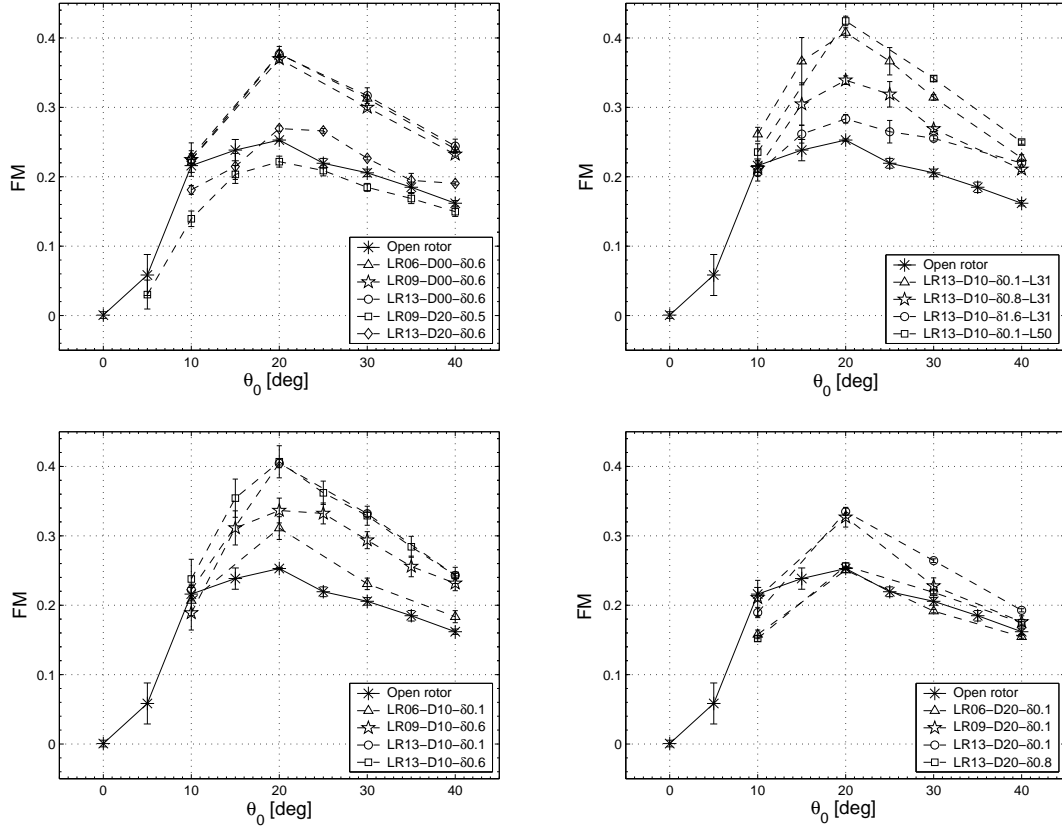Figure 3.9: Ratio of thrust coefficient to power coefficient vs. thrust coefficient

Figure 3.10: Figure of merit vs. collective angle

have maximum values of $FM\sqrt{\sigma_d}$ of 0.47 compared to 0.18 for the open rotor. This

corresponds to a 62% reduction in power for the same thrust, or a 90% increase in

thrust at the same power, when the rotor disk areas are held the same (Eq. 3.3).

These results, which take into account the *real* power consumption of the rotors,

show improvements in performance that are even better that those predicted by

momentum theory (see Table 2.2 on page 113), and clearly indicate the benefits of

shrouding a rotor at the MAV scale.

To determine whether similar improvements in performance would be obtained

with a more efficient rotor, which is better suited to the low-Reynolds number flight

regime, the LR13-D10-L31 shroud was tested with a rotor with cambered blades, as
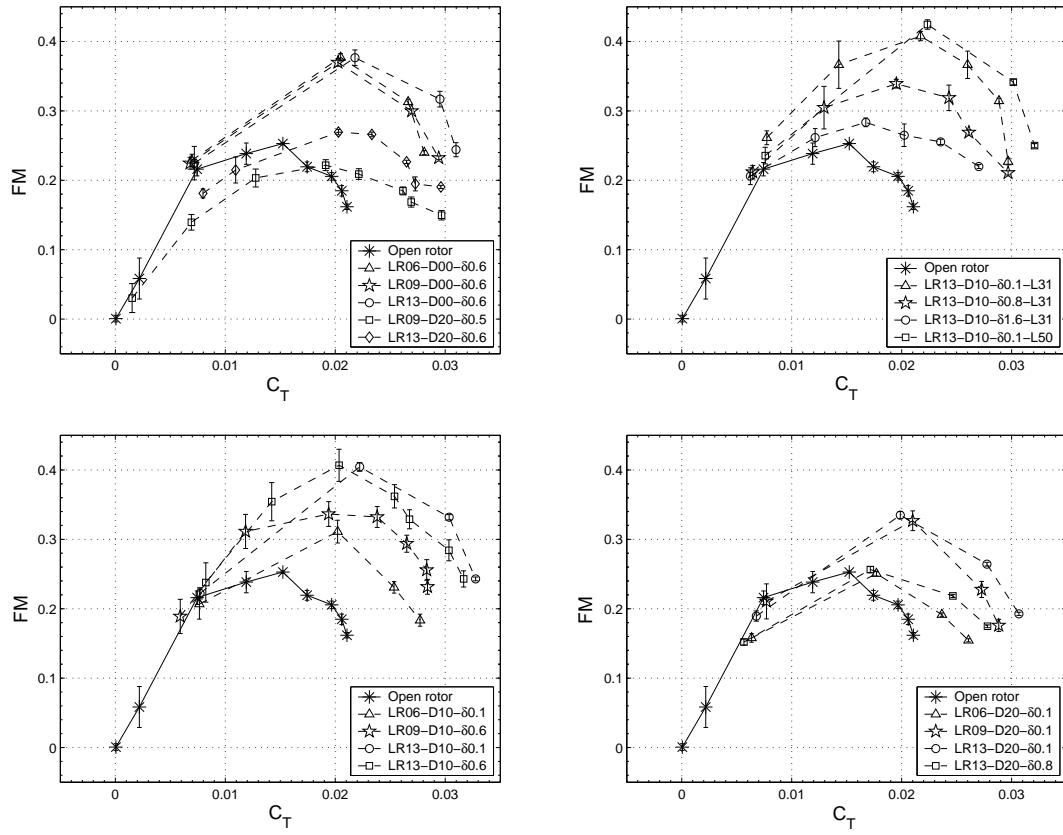
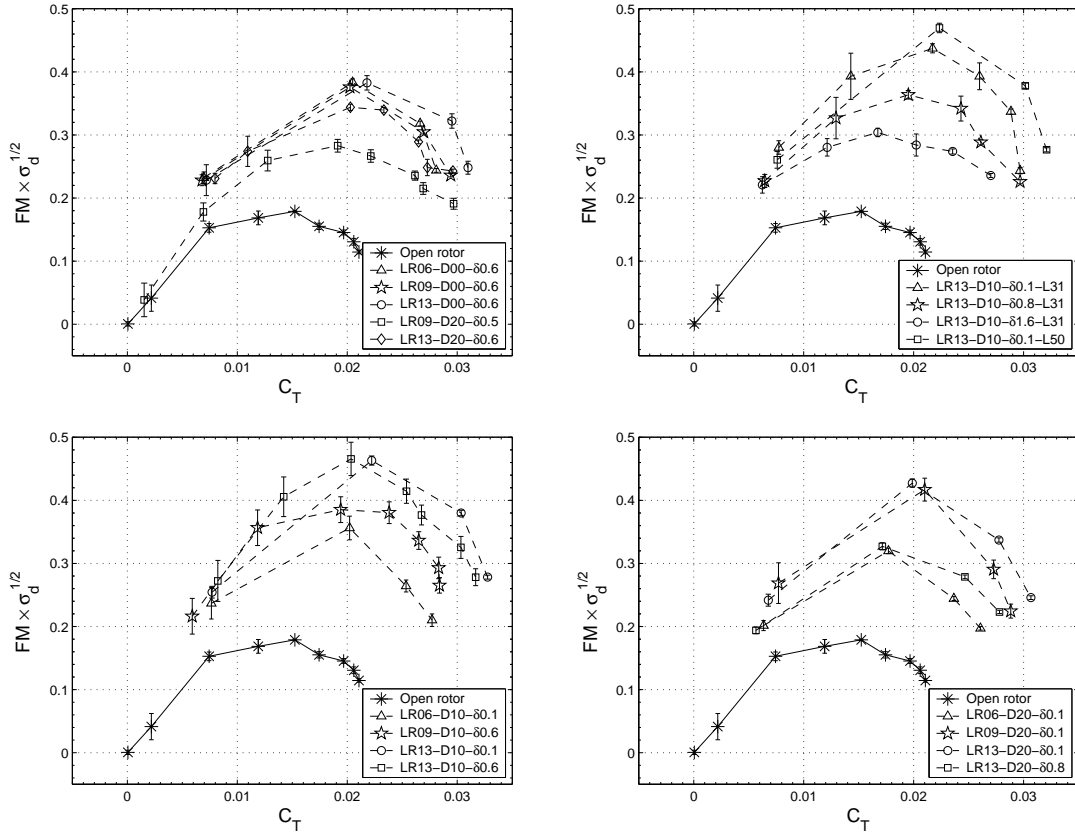Figure 3.11: Figure of merit vs. thrust coefficient

Figure 3.12: Generalized figure of merit vs. thrust coefficient

described in Chapter 2. This 'cambered' shrouded-rotor model was tested at a single collective of 20°, and, with a tip clearance of $0.3\%D_t$, produced a thrust coefficient of 0.040 and a power coefficient of 0.0075. This is equivalent to a figure of merit of 0.507, and a generalized figure of merit of 0.543. These cambered blades were the same blades used on the rotor that was tested by Sirohi et al. [23] during the design of their 'TiFlyer' MAV. In those tests, the open rotor achieved a maximum figure of merit of 0.45, equivalent to $FM^* = 0.32$, at a collective of 18°. Although the rotor hub, and hence the root cut-out, for the rotor in those tests was different from that used for this shrouded rotor ($R_0 = 0.22R$ vs. $0.18R$), the rotor diameters were almost the same (6.35 in vs. 6.3 in), and the two sets of performance data can therefore be justifiably compared. The ratio of the generalized figures of merit thus indicates that, for this 'cambered' rotor, use of a LR13-D10-δ0.3-L31 shroud can result in a 42% increase in thrust at the same power, or a 41% reduction in power at the same thrust. These performance improvements are not as great as those achieved with the baseline rotor's uncambered blades, which suggests that as the design of the rotor itself is improved[3], less of a performance benefit would be obtained from shrouding the rotor. However, further tests would be necessary to determine whether this is true.

The thrust coefficients referred to in the preceding discussions have been the 'total' thrust coefficient, as measured by the thrust transducer of the hover test-stand. The shroud surface pressure measurements, described in greater detail in

---

[3]Figures of merit as high as 0.622 have been achived by MAV-scale open rotors that incorporated taper, twist, camber and sharpened leading edges in their design [20].

Section 3.4 of this chapter, were integrated to obtain the thrust produced by the shrouds themselves, and these were subtracted from the total thrust measurements to obtain the thrust of the rotor alone. The variations in $C_{T_{\text{rotor}}}$ and $C_{T_{\text{shroud}}}$ thus obtained are shown in Figures 3.13–3.15, plotted as functions of blade collective angle. Figure 3.13 indicates that, at a given collective, the rotor does generate less thrust when it is placed inside a shroud, compared to when it is in open air. This would be due to the increased inflow through the rotor, which reduces the blade section angles of attack at a fixed collective. At higher collectives, however, the difference between $C_{T_{\text{rotor}}}$ and $C_{T_{\text{OR}}}$ becomes smaller, with the two quantities becoming almost equal in some cases. Note that the shrouded-rotor coefficients plotted in this figure were obtained by normalizing the rotor thrust by the shroud throat cross-sectional area, while the open rotor thrust coefficients were obtained by normalizing by the smaller area of the actual rotor disk. For a more fair comparison, Figure 3.14 shows the values of $C_{T_{\text{rotor}}}$ obtained when the shrouded-rotor thrusts are normalized by the actual rotor disk area, too. As expected, the coefficient values obtained are now slightly higher than those in Figure 3.13 — more so for the configurations with the larger tip gaps — but are still mostly lower than those for the open rotor. The highest thrust coefficients achieved by the rotors, whether open or shrouded, are around 0.02; this corresponds to a blade loading coefficient (C_T/σ) of 0.167, or a mean rotor lift coefficient $(\bar{C}_L = 6C_T/\sigma)$ of 1.0, which would be at the upper stall limits of the blunt, uncambered, flat-plate airfoils (Table 2.3, p. 115) at these low Reynolds numbers, and is clearly evidenced by the the flattening-out of the curves at the highest collectives. Figure 3.15 shows that most of the shroud
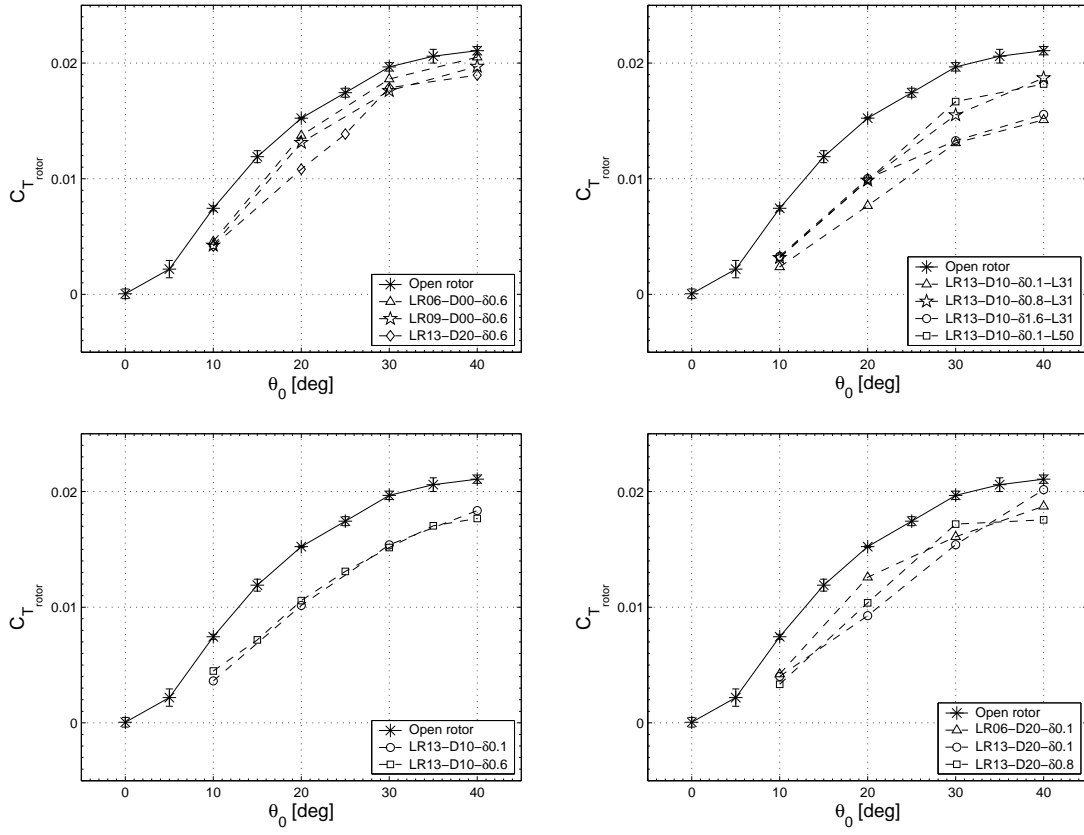
Figure 3.13: Rotor thrust coefficient, as normalized by shroud thoat area $(\pi D_t^2/4)$, vs. collective angle

models achieve their maximum thrust at a collective angle between 25° and 30°, and exhibit a gentle stall-like characteristic at higher collectives, while some — the LR13 models with tip clearances of 0.6% and 0.8%D_t — initially level off or decrease in that particular collective range, but then increase to higher values at $\theta_0 = 40°$.

3.3.2 Effects of changing shroud parameter values

The effects of varying each of the shroud geometric parameters — blade tip clearance, inlet lip radius, diffuser included angle, diffuser length and diffuser expansion ratio (Figure 3.16) — on the performance of the shrouded rotors are shown
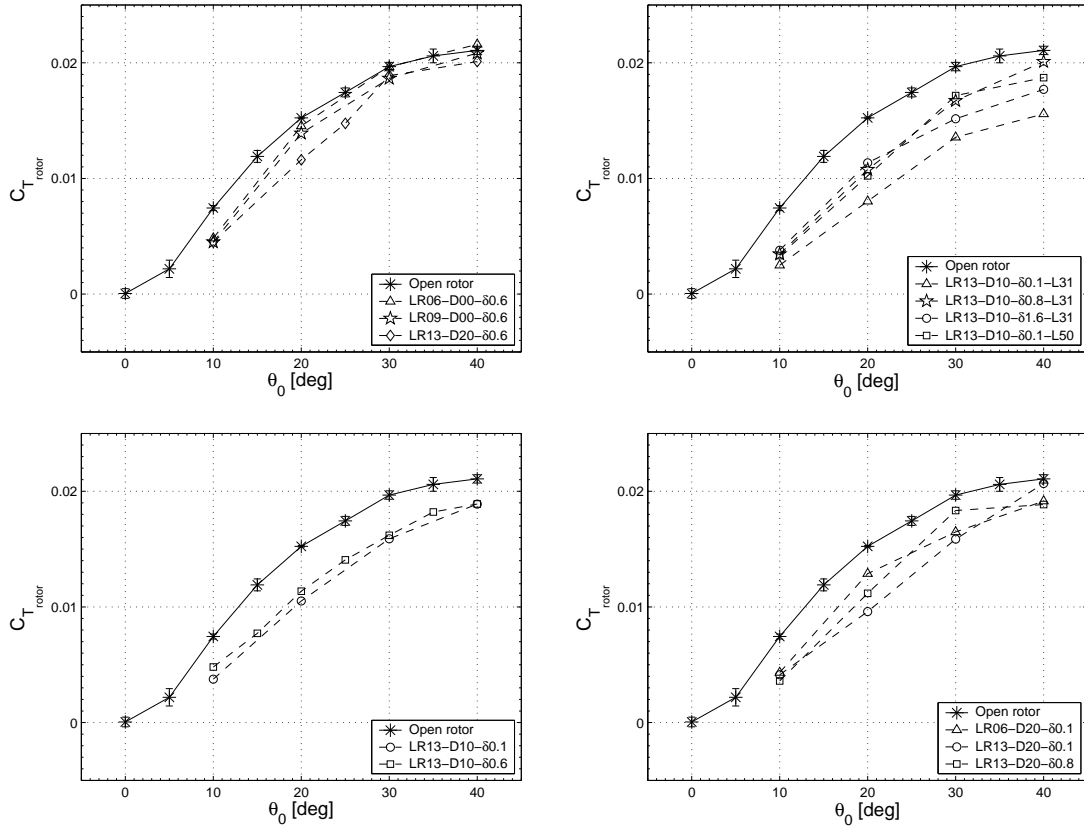
Figure 3.14: Rotor thrust coefficient, as normalized by rotor disk area $(\pi D^2/4)$, vs. collective angle
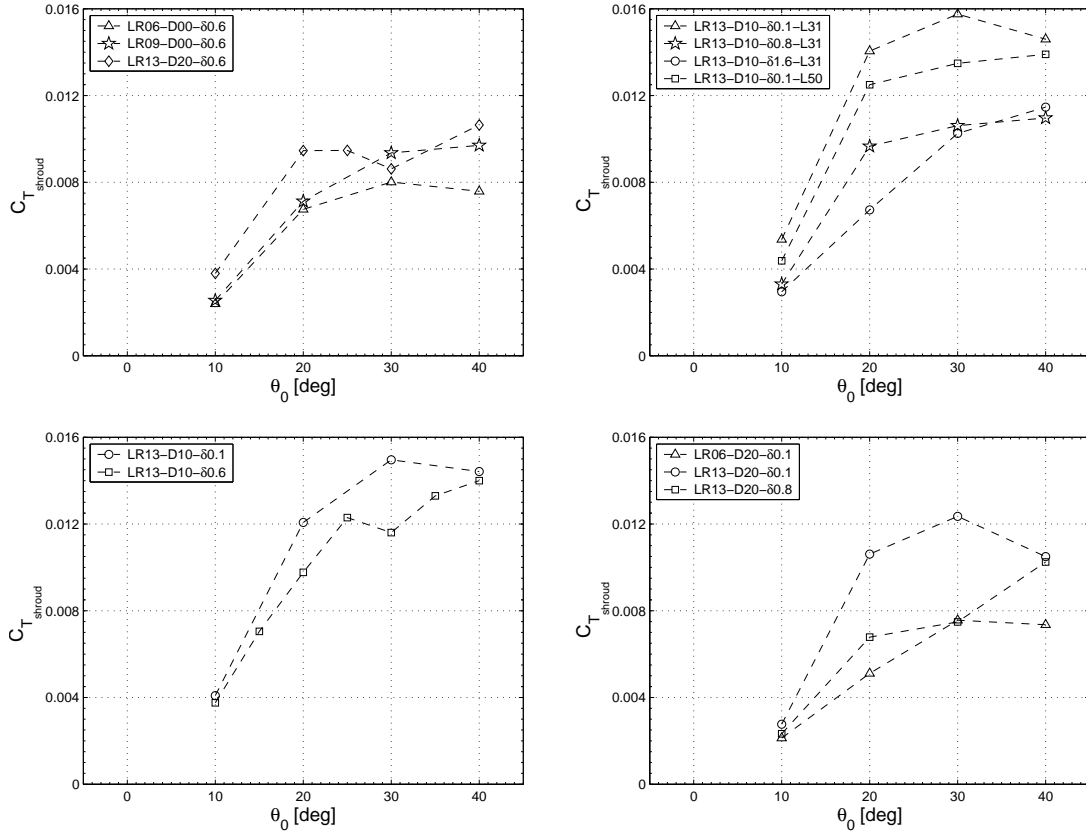
Figure 3.15: Shroud thrust coefficient vs. collective angle

in Figures 3.17–3.20. As mentioned earlier in Chapter 2, the matrix of shrouded-rotor models (Table 2.1, p. 112) enabled comparisons of data from multiple series of models for each of the shroud parameters. These series are listed below in Table 3.1. For each parameter, four different metrics have been used to illustrate the improvement in performance of the shrouded rotors over the open rotor, and to compare the performances of the different shrouded rotors. These are:

1. The ratio of the maximum value of C_T/C_P of the shrouded rotor to that of the open rotor.

2. The ratio of the maximum value of the generalized figure of merit, $\text{FM}^* = \text{FM}\sqrt{\sigma_\text{d}}$, of the shrouded rotor to that of the open rotor.

3. The ratio of the shrouded rotor's thrust coefficient (C_{T_SR}) to that of the open rotor (C_{T_OR}), with the two configurations at the same power coefficient, and evaluated at four different values of C_P: 0.002, 0.004, 0.007 and 0.010.

4. The ratio of the shrouded rotor's power coefficient (C_{P_SR}) to that of the open rotor (C_{P_OR}), at the same thrust coefficient, and evaluated at three different values of C_T: 0.010, 0.015 and 0.020.

The figures show the values of each of these metrics plotted as functions of the shroud parameters, for each of the different comparison series. The values of C_P and C_T at which the ratios of the thrust and power coefficients, respectively, were evaluated were chosen such that they spanned the range of measured power and thrust for all of the models. Although thrust coefficients higher than 0.020 were measured for the
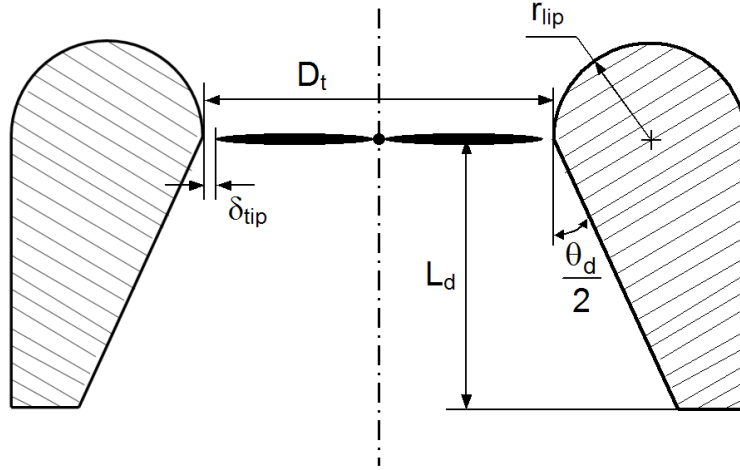
Figure 3.16: Principal shroud parameters affecting shrouded-rotor performance: diffuser included angle (θ_{d}), diffuser length (L_{d}), inlet lip radius (r_{lip}), blade tip clearance (δ_{tip})

shrouded rotors, this was the highest value of C_T achieved by the open rotor, and hence the highest value at which a comparison of the power consumption could be made.

Additionally, to illustrate the physics of the operation of the shrouded rotors, the effects of the shroud parameters on the ratios $C_{T_{\mathrm{SR}}}/C_{T_{\mathrm{OR}}}$, $C_{P_{\mathrm{SR}}}/C_{P_{\mathrm{OR}}}$, $C_{T_{\mathrm{rotor}}}/C_{T_{\mathrm{OR}}}$ (rotor thrust) and $C_{T_{\mathrm{rotor}}}/C_{T_{\mathrm{total}}}$ (rotor thrust fraction) have been shown, with the quantities for the open and shrouded rotors compared at the same collective angle and evaluated at four different values of θ_0: 10°, 20°, 30° and 40°. Since the performance measurements were made at these specific collective angles, calculation of the corresponding ratios was straightforward. For comparisons at the same power or thrust coefficients, however, interpolation between the measured values was required; this was performed using piecewise-cubic Hermite interpolating polynomials. Note that, unlike the ratios comparing the open and shrouded rotors,

Table 3.1: Shrouded-rotor model comparison series for analyzing effects of the shroud geometric parameters on performance characteristics

Model series for blade tip clearance	δ_{tip} values [$\%D_{\text{t}}$]
LR09-D20	0.09, 0.50
LR13-D20	0.09, 0.63, 0.82
LR13-D10	0.09, 0.63
LR13-D10-L31	0.09, 0.82, 1.57
Model series for inlet lip radius	r_{lip} values [$\%D_{\text{t}}$]
D10-δ0.1	6.48, 13.1
D20-δ0.1	6.48, 8.99, 13.1
D00-δ0.6	6.48, 8.99, 13.1
D10-δ0.6	8.99, 13.1
D20-δ0.6	8.99, 13.1
Model series for diffuser included angle	θ_{d} values [°]
LR06-δ0.1	9.70, 20.22
LR13-δ0.1	9.70, 20.22
LR09-δ0.6	0, 9.70, 20.22
LR13-δ0.6	0, 9.70, 20.22
Model series for diffuser length	L_{d} values [$\%D_{\text{t}}$]
LR13-D10-δ0.1	31, 50, 72

Table 3.1: Shrouded-rotor model comparison series (contd.)

Model series for diffuser expansion ratio	σ_{d} values
LR06-δ0.1-L72	1.31, 1.63
LR13-δ0.1-L72	1.31, 1.63
LR13-δ0.1-D10	1.14, 1.22, 1.31
LR09-δ0.6-L72	1.03, 1.31, 1.63
LR13-δ0.6-L72	1.03, 1.31, 1.63
LR13-δ0.8	1.15, 1.63

the rotor thrust fraction of a shrouded rotor, $T_{\mathrm{rotor}}/T_{\mathrm{total}}$, is, according to the momentum theory/actuator disk model, independent of thrust or power level — or, equivalently, of rotor collective angle — and depends only on the wake expansion ratio (Equation 1.5 on page 17).

Some of the observations that can be made from these figures are the same, no matter which shroud parameter is being considered, and these are therefore described first, before discussing the specific effects of changing the shroud parameter values. When compared at the same power coefficient, the ratio of total thrust, $C_{T_{\mathrm{SR}}}/C_{T_{\mathrm{OR}}}$, shows values between 1.3 and almost 2.0, with the ratio increasing slightly from $C_P = 0.002$ to 0.004 and then decreasing as C_P is further increased to 0.010 (Figs. 3.17c, 3.18c, 3.19c and 3.20c). For all of the shrouded rotors, the C_P value of 0.004 corresponds most closely to a collective angle of 20°, which is the collective at which they all achieved their highest value of [generalized] figure of merit. It is therefore not entirely surprising that highest values of $C_{T_{\mathrm{SR}}}/C_{T_{\mathrm{OR}}}$ are also achieved at this value of power coefficient. When compared at the same collec-

tive angle, the ratio increases with increasing collective, with most of the increase occurring between $\theta_0 = 10°$ and $20°$ (Figs. 3.17e, 3.18e, 3.19e and 3.20e). At $\theta_0 = 10°$, the ratio has values of 0.8–1.0, while at the higher collectives, this increases to between 1.2 and 1.6.

Similarly, when compared at the same thrust coefficient, the ratio of the power coefficients, $C_{P_{\mathrm{SR}}}/C_{P_{\mathrm{OR}}}$, steadily decreases with increasing C_T, with values between 0.3 and 0.7 (Figs. 3.17d, 3.18d, 3.19d and 3.20d), but, when compared at the same collective (Figs. 3.17f, 3.18f, 3.19f and 3.20f), steadily increases with increasing θ_0, showing values between 0.5 and 1.0. The reason for these opposite trends, seen in both $C_{T_{\mathrm{SR}}}/C_{T_{\mathrm{OR}}}$ and $C_{P_{\mathrm{SR}}}/C_{P_{\mathrm{OR}}}$, is simply due to the differences in the ways that C_T and C_P increase with increasing collective for the open and shrouded rotors (Figures 3.4 and 3.5). Considering, for example, the behavior of $C_{T_{\mathrm{SR}}}/C_{T_{\mathrm{OR}}}$: at low collectives, the shrouded-rotor thrust is higher than that of the open rotor, while the power consumed is lower, thereby exaggerating the differences in thrust when compared at the same power. At higher collectives, the difference between the shrouded-rotor thrust and the open-rotor thrust becomes much larger, so $C_{T_{\mathrm{SR}}}/C_{T_{\mathrm{OR}}}$ at the same collective increases, but the relative difference in power consumption becomes smaller, so $C_{T_{\mathrm{SR}}}/C_{T_{\mathrm{OR}}}$ at the same power level decreases. The behavior of the ratio of power coefficients can be explained similarly.

Looking at the thrust produced by the rotor itself, in the shrouded condition versus in the open condition, $C_{T_{\mathrm{rotor}}}/C_{T_{\mathrm{OR}}}$ — when compared at the same collective — is seen to steadily increase with increasing collective, with values between 0.3 and 1.0 (Figs. 3.17g, 3.18g, 3.19g and 3.20g). The rotor thrust fraction, $T_{\mathrm{rotor}}/T_{\mathrm{total}}$, also

mostly increases with increasing θ_0, with values between 0.3 and 0.75, depending on the shroud model (Figs. 3.17h, 3.18h, 3.19h and 3.20h). Both of these results suggest that at the higher collectives, the shroud is not able to off-load the rotor as much as at lower collectives, and the rotor is, so to speak, 'left to fend for itself.' This conclusion is supported by the stall-like behavior seen in $C_{T_{\mathrm{shroud}}}$ for many of the shroud models (Figure 3.15), while $C_{T_{\mathrm{rotor}}}$ continues to increase at the higher collectives, albeit at a decreased rate (Figure 3.13).

3.3.2.1   Blade tip clearance

The effects of varying the blade tip clearance, δ_{tip}, on the shrouded-rotor performance are shown in Figures 3.17a–h. For this parameter, data were available from four series of shrouded-rotor models, LR09-D20, LR13-D20, LR13-D10 and LR13-D10-L31, in each of which lip radius, diffuser angle and diffuser length were held constant, and the tip clearance allowed to change from one model to the next (Table 3.1).

Increasing the tip clearance is clearly seen to have adverse effects on performance, causing decreases in maximum C_T/C_P, maximum FM* and $C_{T_{\mathrm{SR}}}/C_{T_{\mathrm{OR}}}$ at the same C_P, and increases in $C_{P_{\mathrm{SR}}}/C_{P_{\mathrm{OR}}}$ at the same C_T. Of the four series, the LR09-D20 models show the most rapid degradations. The LR13-D10 models, while exhibiting the best overall performance, show the least change in performance with changing tip clearance. In fact, maximum C_T/C_P increases in this series, as δ_{tip} is increased from 0.1 to 0.6%D_{t}; however, this is because measurements were made

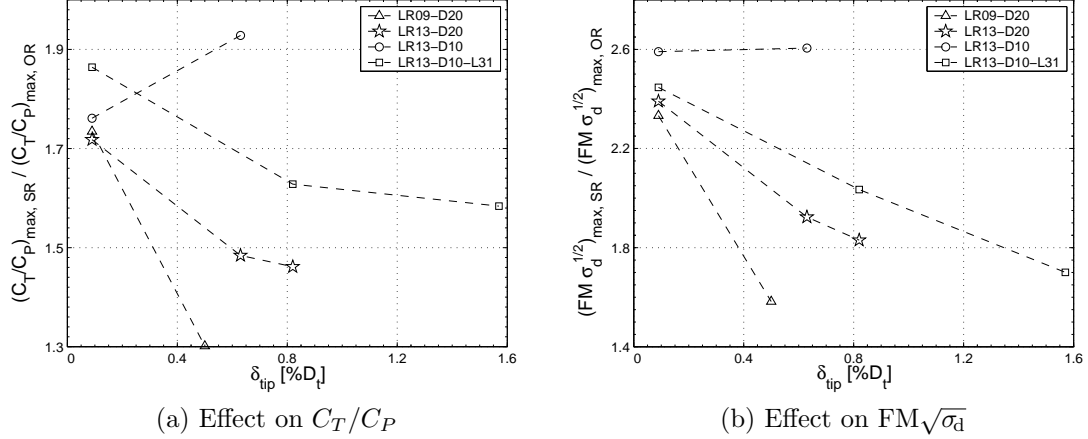(a) Effect on C_T/C_P (b) Effect on $\mathrm{FM}\sqrt{\sigma_{\mathrm{d}}}$

Figure 3.17: Effect of blade tip clearance

at $\theta_0 = 15°$ for the $\delta0.6$ model but not for the $\delta0.1$ model, as explained earlier. Comparing the LR09-D20 series and the LR13-D20 series shows that changing δ_{tip} has a stronger effect on the shroud with the smaller lip radius. Similarly, comparing the LR13-D10 and LR13-D20 series shows more pronounced changes for the D20 models, and comparing the LR13-D10 and LR13-D10-L31 series shows stronger effects for the shorter diffuser. As will be shown in subsequent sections, these are the cases in which the shrouded rotors generally show the worst performance, and it is in these that changing the tip clearance seems to have the greatest effect.
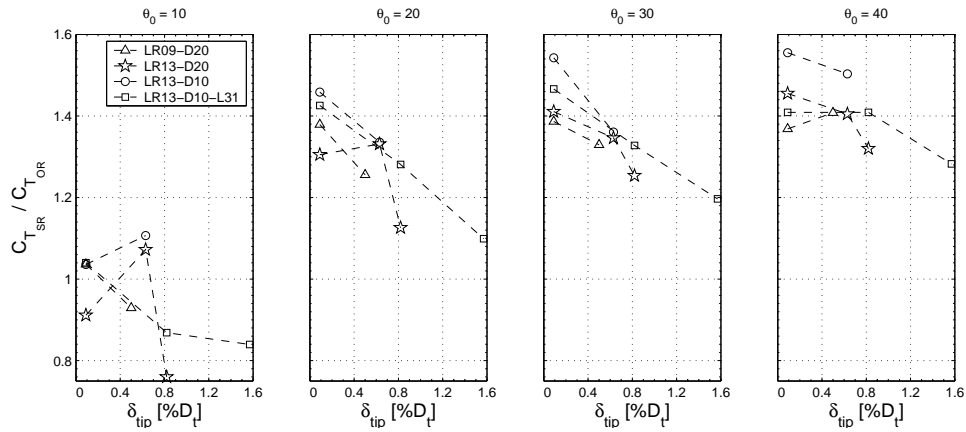
When compared at the same collective, $C_{T_{\mathrm{SR}}}/C_{T_{\mathrm{OR}}}$ is seen to decrease with increasing tip clearance, but the LR13-D20 series of models shows anomalous behavior. No consistent trends can be seen in the behavior of $C_{P_{\mathrm{SR}}}/C_{P_{\mathrm{OR}}}$ or of $C_{T_{\mathrm{rotor}}}/C_{T_{\mathrm{OR}}}$. The rotor thrust fraction, $T_{\mathrm{rotor}}/T_{\mathrm{total}}$, generally seems to increase with increasing tip clearance, but here, too, some of the data go against this trend.
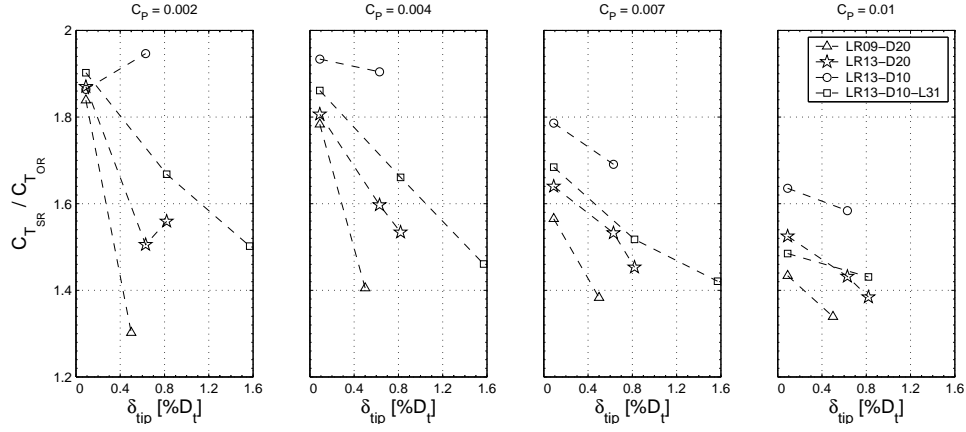
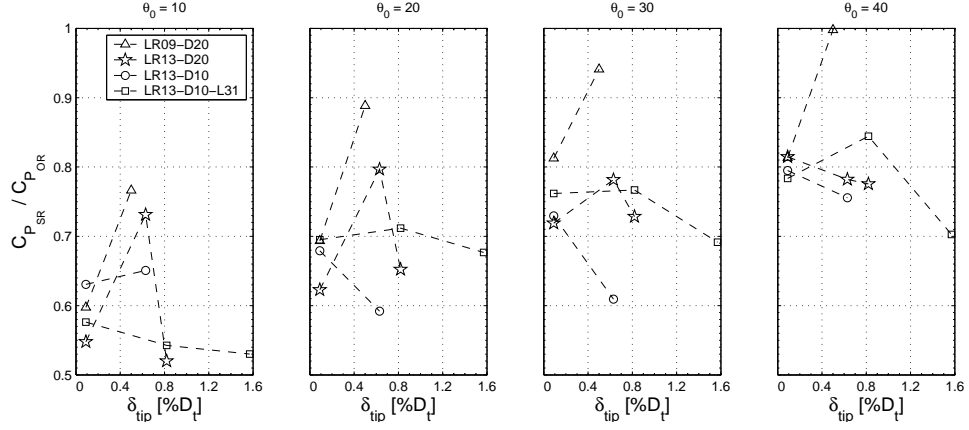(c) Effect on total thrust, compared at the same power
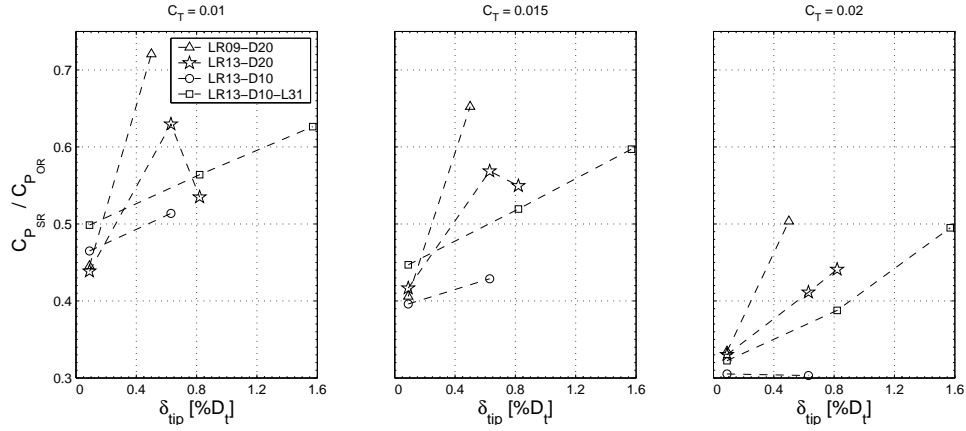
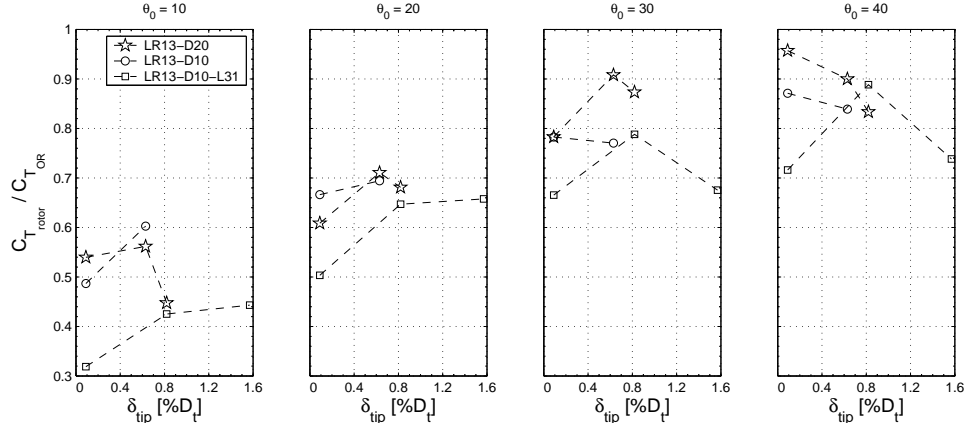(d) Effect on power, compared at the same total thrust

(e) Effect on total thrust, compared at the same collective angle
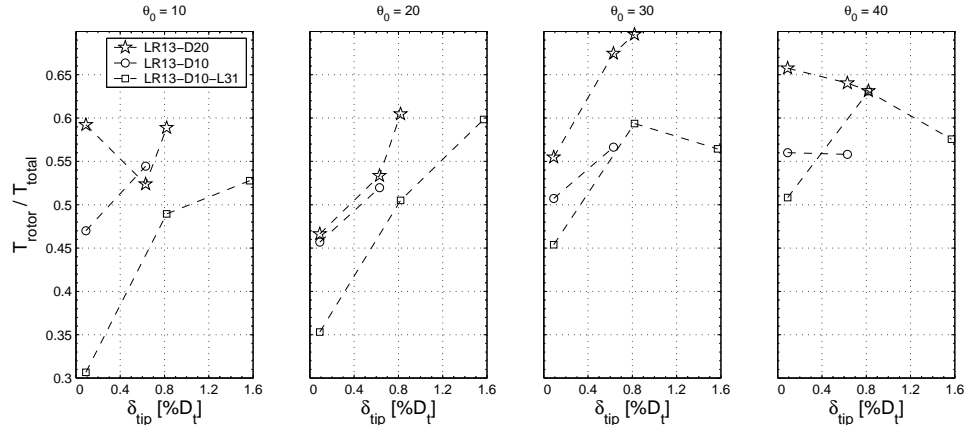
Figure 3.17: Effect of blade tip clearance (contd.)

(f) Effect on power, compared at the same collective angle

(g) Effect on rotor thrust, compared at the same collective angle

(h) Effect on rotor thrust fraction, compared at the same collective angle
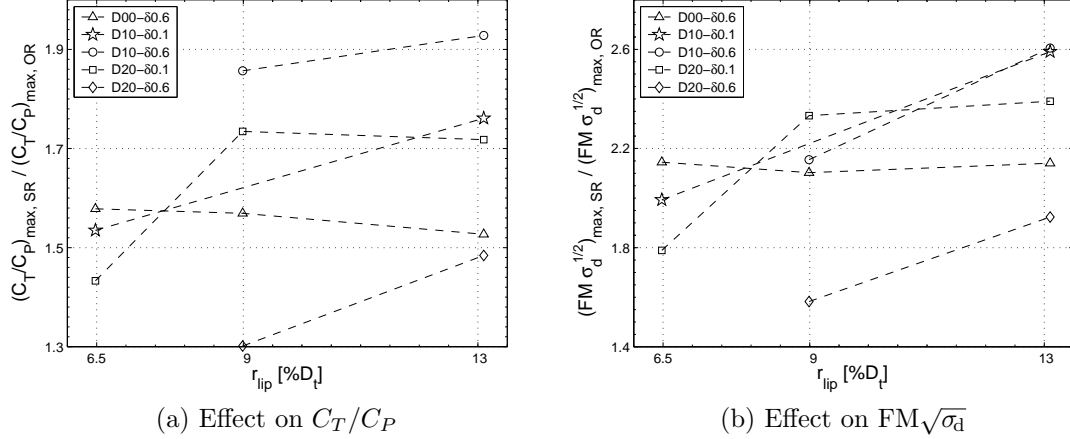
Figure 3.17: Effect of blade tip clearance (contd.)

(a) Effect on C_T/C_P (b) Effect on $\mathrm{FM}\sqrt{\sigma_\mathrm{d}}$
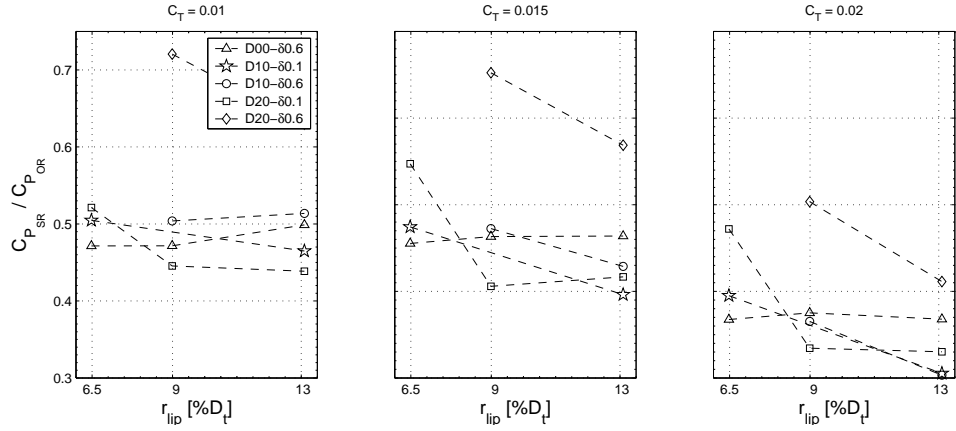
Figure 3.18: Effect of lip radius

3.3.2.2   Inlet lip radius

The effects of varying the inlet lip radius, r_lip, on the shrouded-rotor performance are shown in Figures 3.18a–h. For this parameter, data were available from five series of shrouded-rotor models: D10-δ0.1, D20-δ0.1, D00-δ0.6, D10-δ0.6 and D20-δ0.6 (Table 3.1).

As lip radius is increased, all five series of models show increases in maximum C_T/C_P, maximum FM* and $C_{T_\mathrm{SR}}/C_{T_\mathrm{OR}}$ at the same C_P. $C_{T_\mathrm{SR}}/C_{T_\mathrm{OR}}$ when compared at the same collective, also shows increases with increasing r_lip at collectives of 20° and higher, but these are not as pronounced as those seen when compared at the same power. Except for the D00-δ06 series of models, and anomalous data points corresponding to the LR09-D20-δ0.1 model, the rates of increase with increasing lip radius are about the same for all the series. The ratio of power coefficients, $C_{P_\mathrm{SR}}/C_{P_\mathrm{OR}}$ at the same C_T, decreases with increasing lip radius, with the effects being seen more clearly at the two higher thrust coefficient values than at the lowest
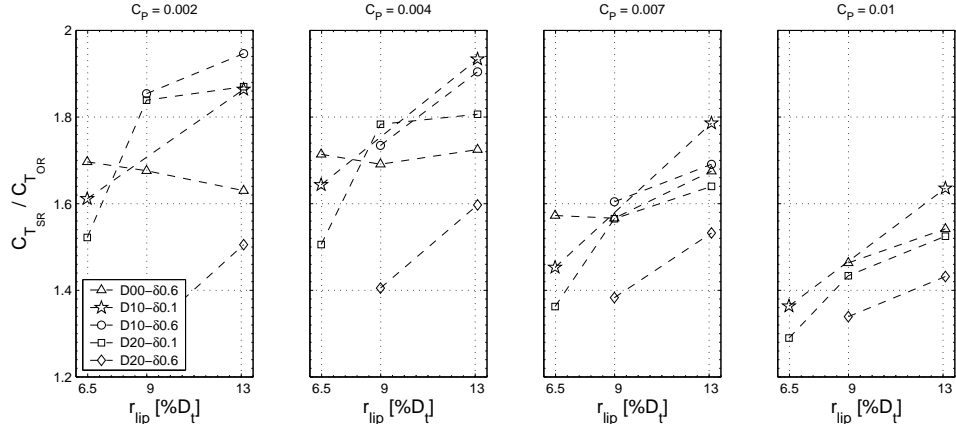
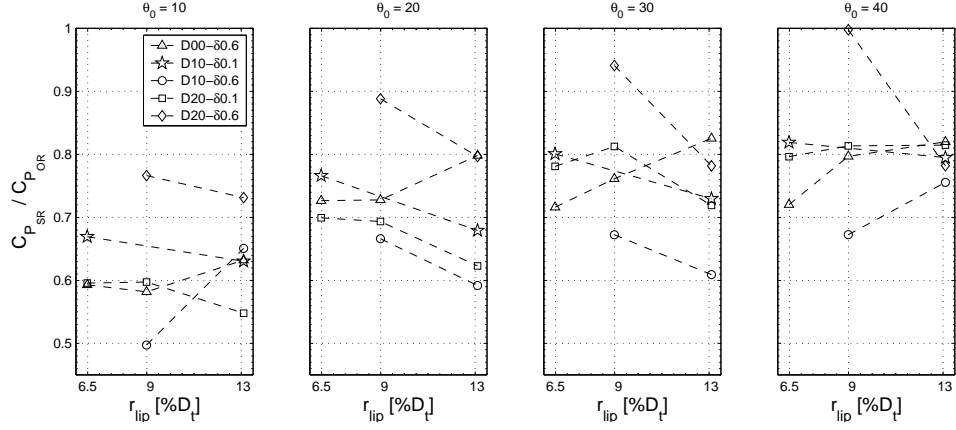(c) Effect on total thrust, compared at the same power

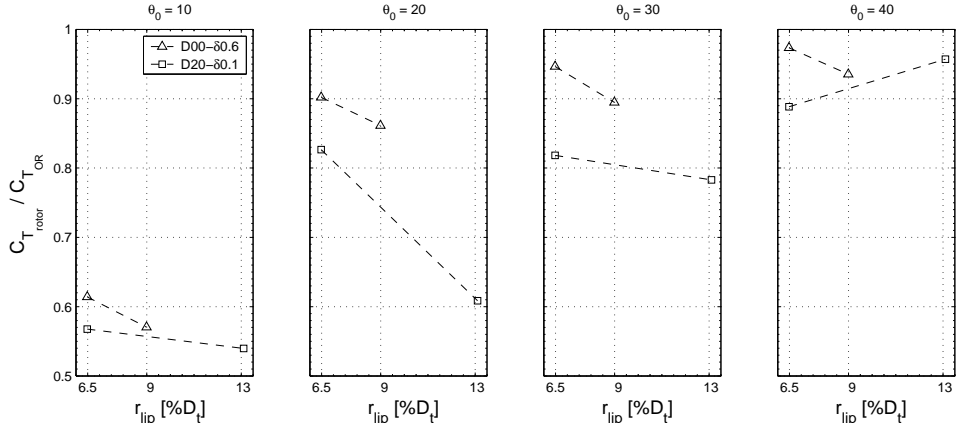(d) Effect on power, compared at the same total thrust

(e) Effect on total thrust, compared at the same collective angle

Figure 3.18: Effect of lip radius (contd.)

168
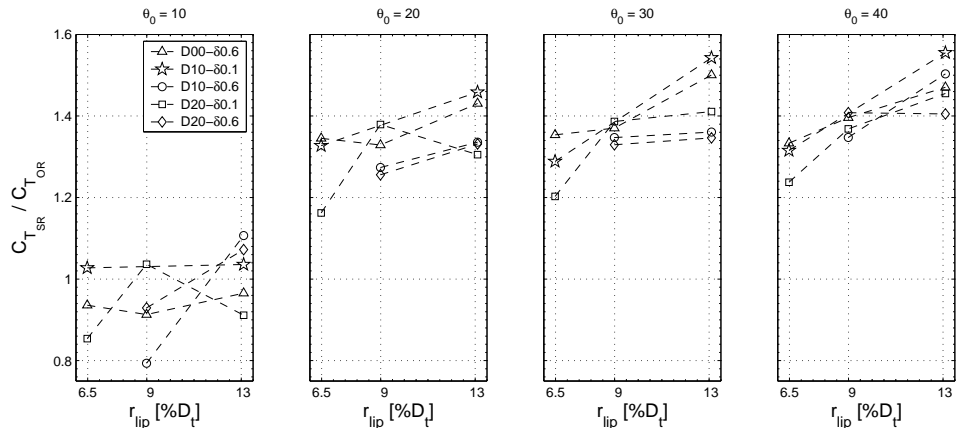
(f) Effect on power, compared at the same collective angle

(g) Effect on rotor thrust, compared at the same collective angle

(h) Effect on rotor thrust fraction, compared at the same collective angle

Figure 3.18: Effect of lip radius (contd.)

(a) Effect on C_T/C_P (b) Effect on $\mathrm{FM}\sqrt{\sigma_\mathrm{d}}$
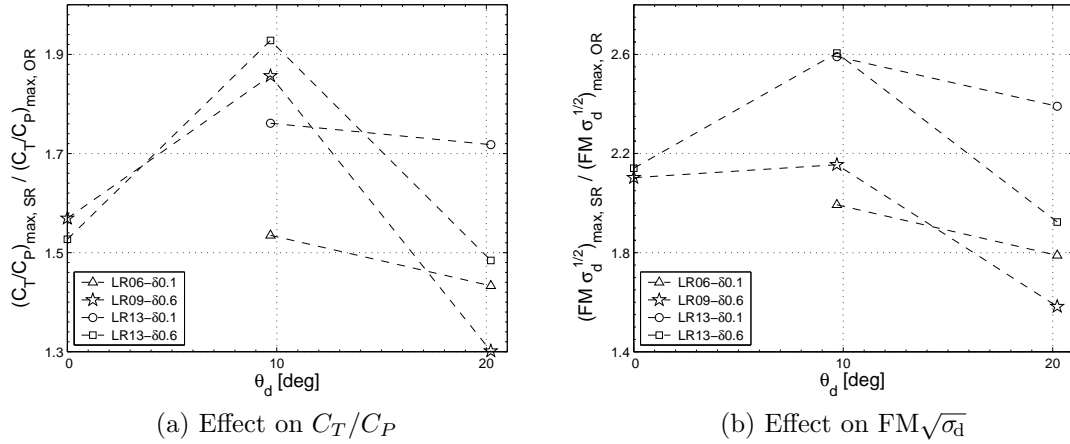
Figure 3.19: Effect of diffuser angle

one.

Increasing r_lip also causes sharp reductions in the rotor thrust fraction, $T_\mathrm{rotor}/T_\mathrm{total}$, and generally decreasing trends in $C_{T_\mathrm{rotor}}/C_{T_\mathrm{OR}}$ indicating increasing off-loading of the rotor by the shroud. As with the blade tip clearance, changing the lip radius does not appear to have a consistent effect on $C_{P_\mathrm{SR}}/C_{P_\mathrm{OR}}$ when compared at the same collective.

3.3.2.3   Diffuser angle

The effects of varying the diffuser included angle, θ_d, are shown in Figures 3.19a–h. For this parameter, data were available from four series of shrouded-rotor models: LR06-δ0.1, LR13-δ0.1, LR09-δ0.6 and LR13-δ0.6 (Table 3.1).

The figures show that, of the three diffuser angles tested, the ten-degree diffusers showed the best performance, whether the measure of performance improvement over the open rotor is maximum C_T/C_P, maximum FM^* or $C_{T_\mathrm{SR}}/C_{T_\mathrm{OR}}$ at the
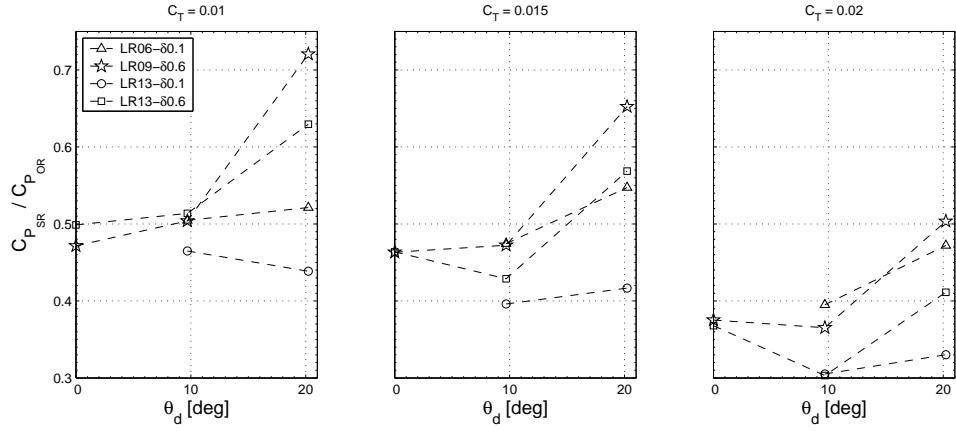
170

(c) Effect on total thrust, compared at the same power

(d) Effect on power, compared at the same total thrust

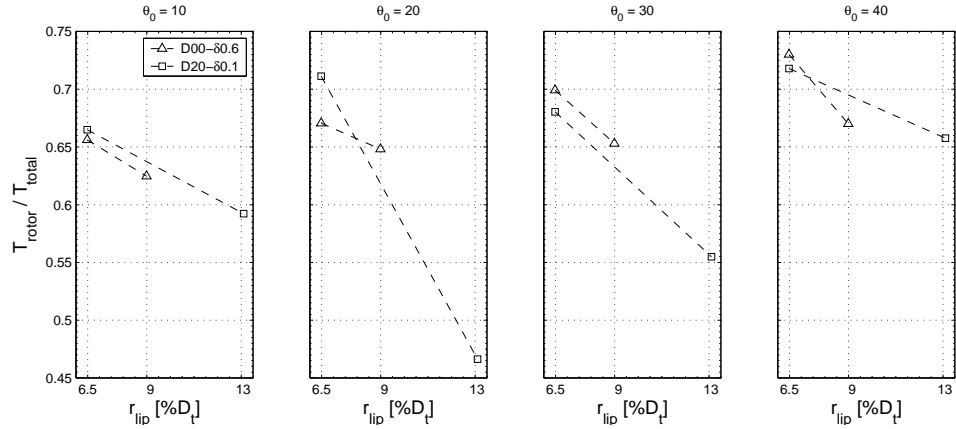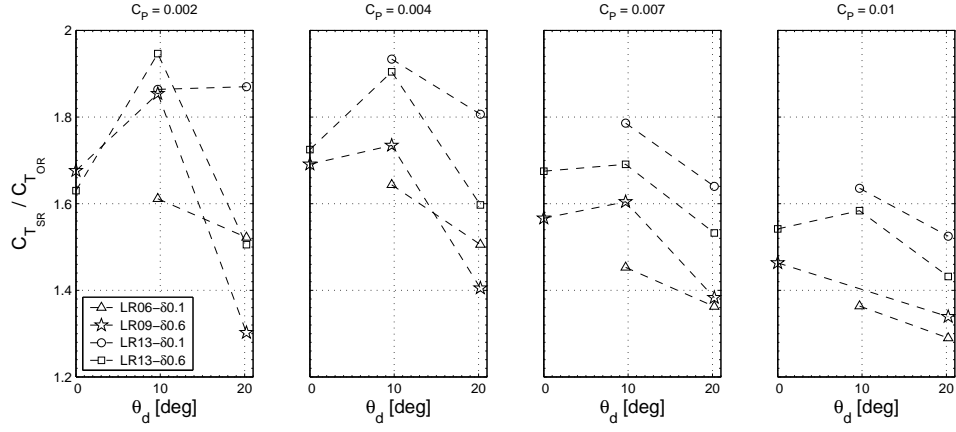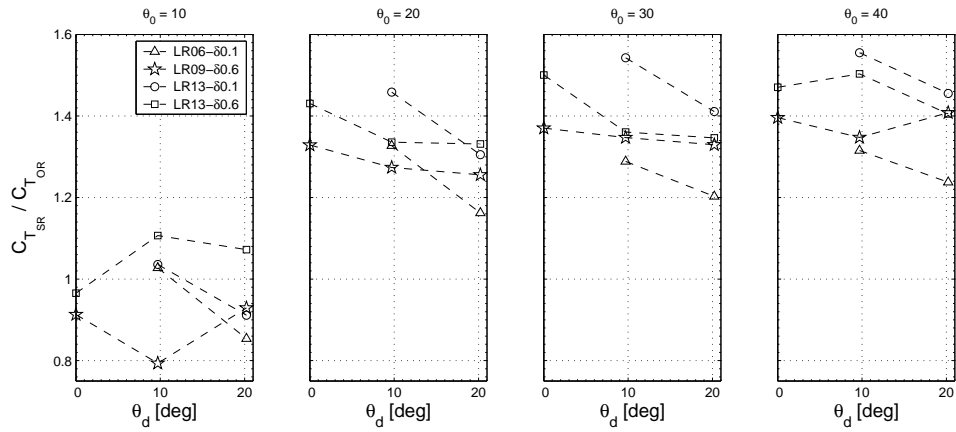(e) Effect on total thrust, compared at the same collective angle

Figure 3.19: Effect of diffuser angle (contd.)

(f) Effect on power, compared at the same collective angle

(g) Effect on rotor thrust, compared at the same collective angle

(h) Effect on rotor thrust fraction, compared at the same collective angle

Figure 3.19: Effect of diffuser angle (contd.)

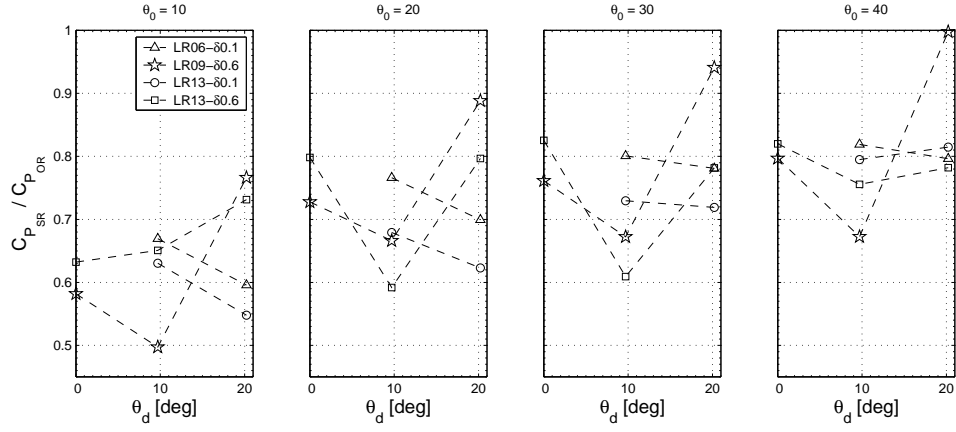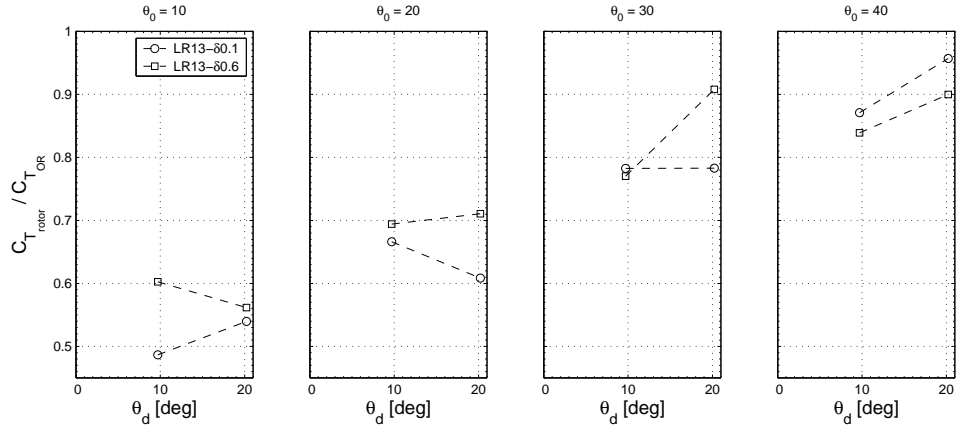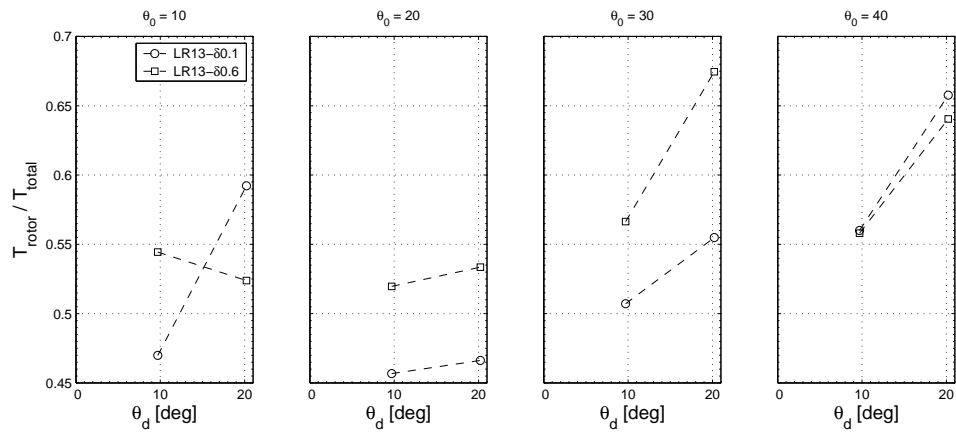same C_P. Reducing the diffuser angle to 0° causes a deterioration in performance, while increasing it to 20° causes an even greater deterioration. The same conclusions can be drawn from the variations seen in $C_{P_{\text{SR}}}/C_{P_{\text{OR}}}$ at the same C_T, which show a minimum at $\theta_\text{d} = 10°$; here too, as in the case with changing lip radius, the effect is seen more clearly at the higher thrust coefficients.

Compared at the same collective angle, the $\delta 0.6$ models again show minimum power consumption at $\theta_\text{d} = 10°$, while the $\delta 0.1$ models show slightly decreasing or unchanging power consumption when θ_d is increased from 10° to 20°. On the other hand, the $\delta 0.1$ models show a decrease in $C_{T_{\text{SR}}}/C_{T_{\text{OR}}}$ (at the same θ_0) when θ_d is increased from 10° to 20°, while the $\delta 0.6$ models show erratic behavior for this quantity. Increasing θ_d from 10° to 20° also causes $C_{T_{\text{rotor}}}/C_{T_{\text{OR}}}$ and $T_{\text{rotor}}/T_{\text{total}}$ to generally increase, indicating a decrease in off-loading by the shroud.

3.3.2.4 Diffuser length

The effects of varying the diffuser length, L_d, are shown in Figures 3.20a–h. For this parameter, data were available from one series of shrouded-rotor models: the LR13-D10-$\delta 0.1$ models, with diffuser lengths of 31%, 50% and 72% of the shroud throat diameter.

The data for this parameter show fairly clear improvements in performance — increases in thrust or decreases in power consumption — when diffuser length is increased from 31%D_t to 50%D_t, but less clear results with the further increase to 72%D_t: power consumption either stays roughly the same or increases slightly,

(a) Effect on C_T/C_P
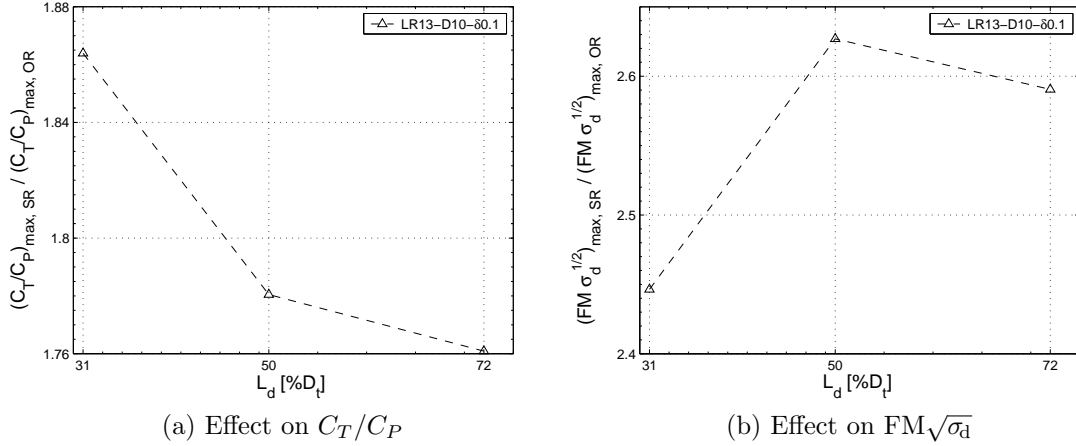
(b) Effect on $\mathrm{FM}\sqrt{\sigma_\mathrm{d}}$

Figure 3.20: Effect of diffuser length

while the thrust produced stays about the same, increases slightly, or even decreases slightly in some cases. The behavior of maximum C_T/C_P seems anomalous, showing a steady decrease as L_d is increased from $31\%D_\mathrm{t}$ to $72\%D_\mathrm{t}$; however, this is only because the L31 model had measurements made at $\theta_0 = 15°$ while the the L50 and L72 models did not. If, instead, the value of C_T/C_P at a collective of $10°$ is used for the L31 model in the comparison (Figure 3.8), as is the case for the other two models, then the variation obtained in 'maximum' C_T/C_P with increasing diffuser length is similar to that seen for maximum FM*. On the other hand, performance improvments are generally accompanied by an increase in off-loading of the rotor by the shroud; for this shroud parameter, $C_{T_\mathrm{rotor}}/C_{T_\mathrm{OR}}$ and $T_\mathrm{rotor}/T_\mathrm{total}$ are seen to generally increase with increasing diffuser length, indicating a *decrease* in the off-loading. The reasons for this behavior is unknown.
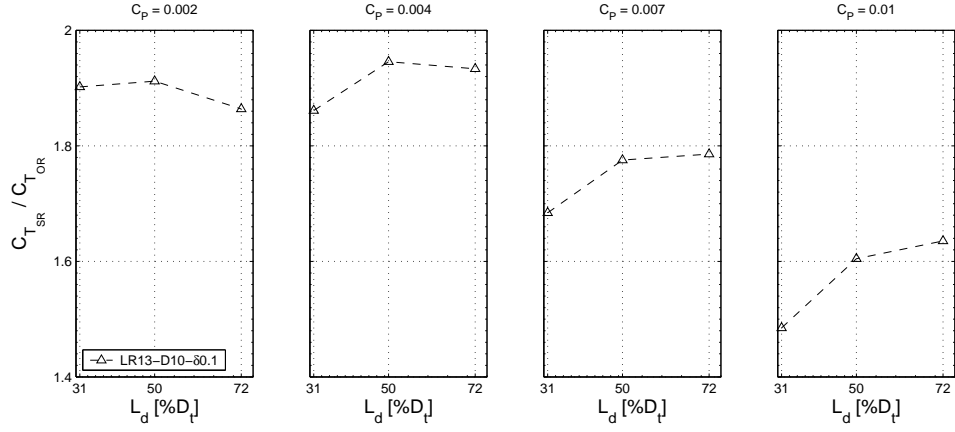
(c) Effect on total thrust, compared at the same power
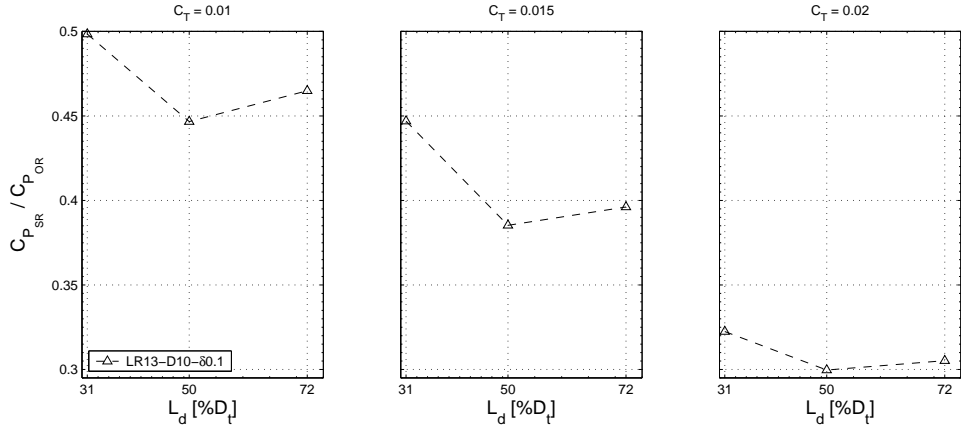
(d) Effect on power, compared at the same total thrust
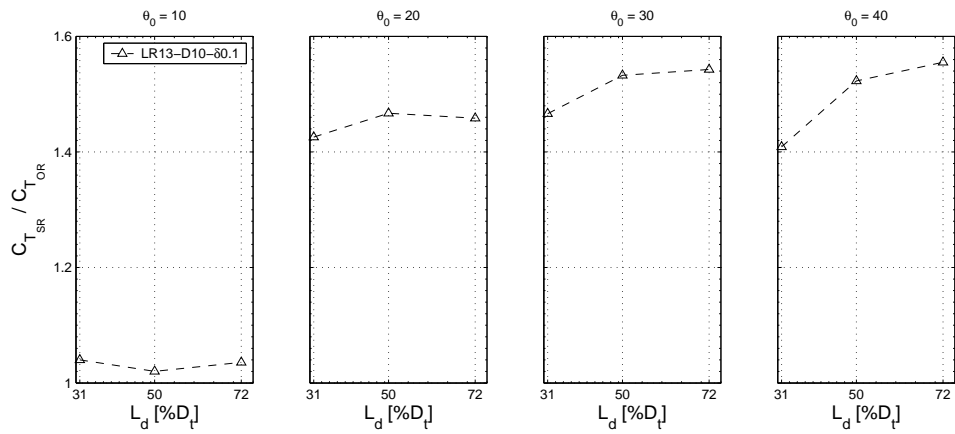
(e) Effect on total thrust, compared at the same collective angle

Figure 3.20: Effect of diffuser length (contd.)

(f) Effect on power, compared at the same collective angle

(g) Effect on rotor thrust, compared at the same collective angle

(h) Effect on rotor thrust fraction, compared at the same collective angle

Figure 3.20: Effect of diffuser length (contd.)

(a) Effect on C_T/C_P (b) Effect on $\mathrm{FM}\sqrt{\sigma_\mathrm{d}}$

Figure 3.21: Effect of diffuser expansion ratio

3.3.2.5 Diffuser expansion ratio

The diffuser expansion ratio, σ_d, is a function of both the diffuser length and the included angle — $\sigma_\mathrm{d}^* = \left[1 + 2\frac{L_d}{D_t}\tan\left(\frac{\theta_d}{2}\right)\right]^2$ — and its effects have therefore been described in the previous two sections devoted to these two parameters. However, in order to compare the relative effects of L_d and θ_d, the data from those two sections are shown together in Figures 3.21a–h, this time explicitly plotted as functions of σ_d. The data shown are therefore from four series of models in which the diffuser angle is varied, one series in which the diffuser length is varied, and one additional series — the LR13-δ0.8 models — in which both angle and length change (Table 3.1).

The superior performance of the 10-degree diffusers, compared to the 0-degree and 20-degree diffusers of the same length, is seen in these figures as well, at the corresponding expansion ratio of 1.31. However, by now considering the effect of changing σ_d by changing the diffuser length, it appears that better performance may be obtained at the slightly lower ratio of 1.22. Further reductions in σ_d caused

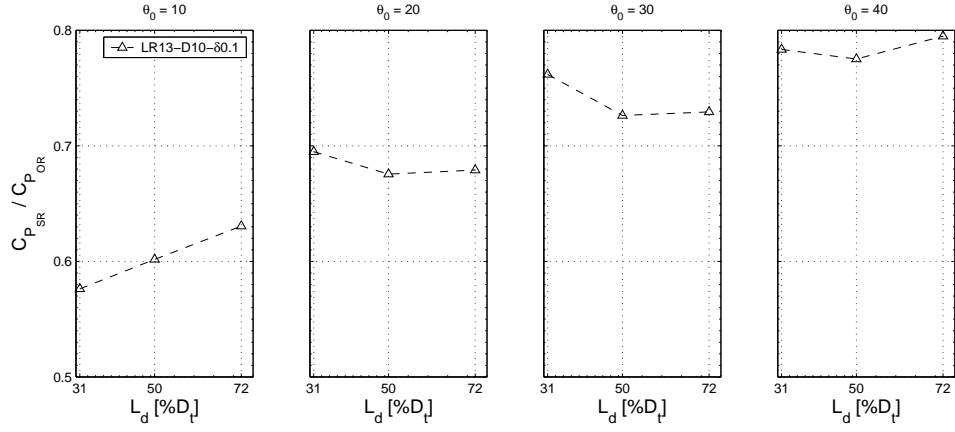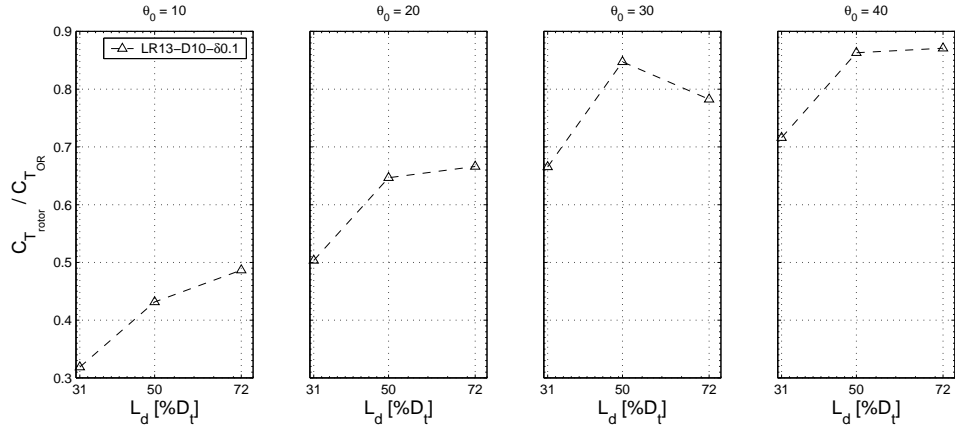(c) Effect on total thrust, compared at the same power
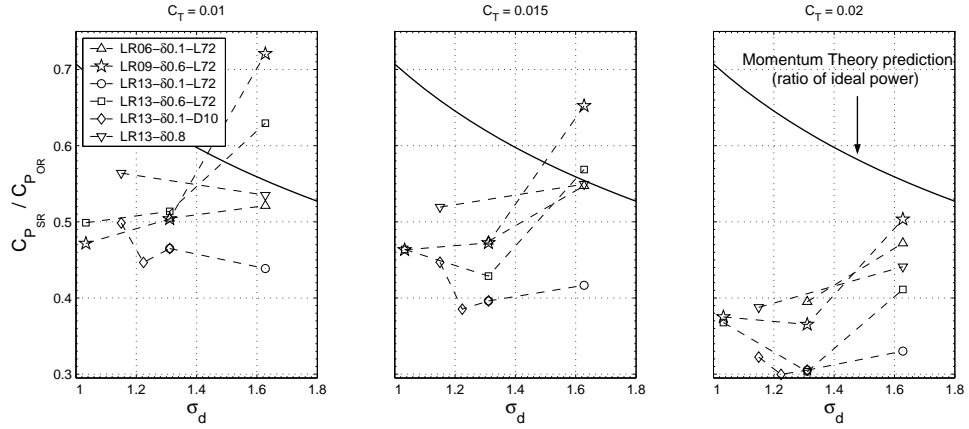
(d) Effect on power, compared at the same total thrust
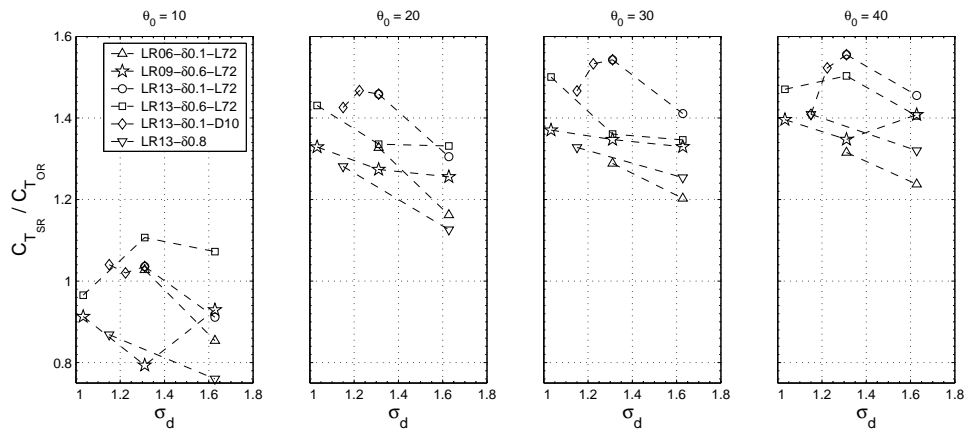
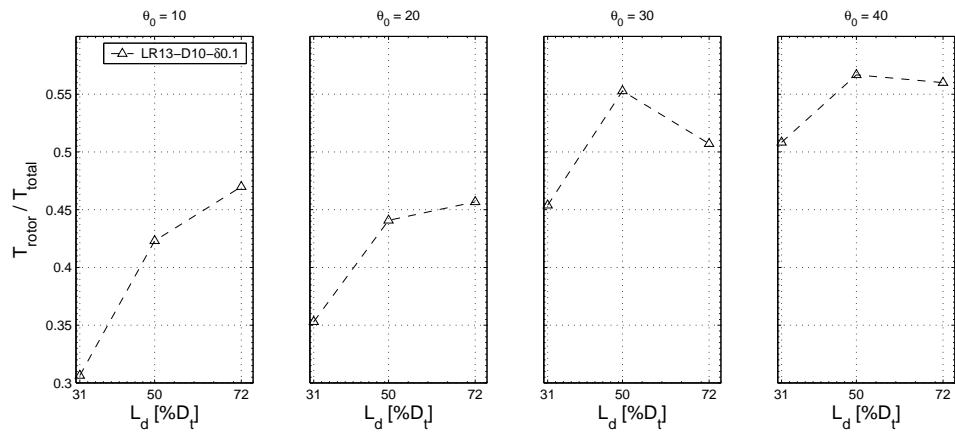(e) Effect on total thrust, compared at the same collective angle

Figure 3.21: Effect of diffuser expansion ratio (contd.)
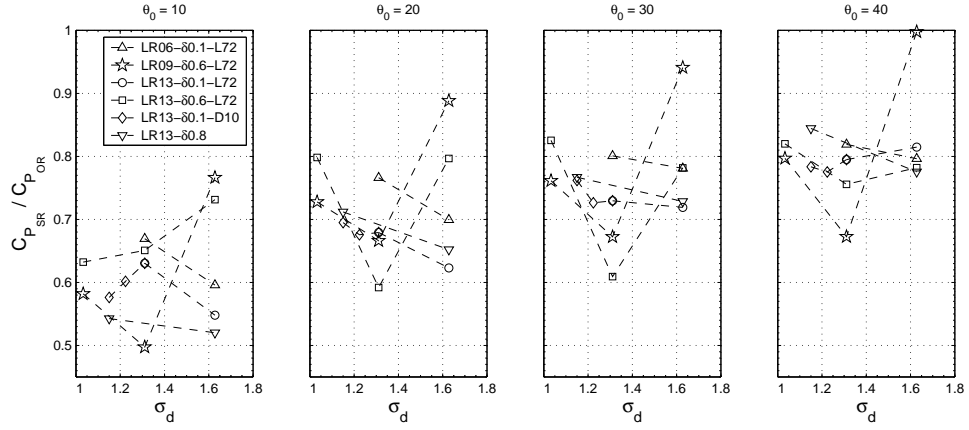
(f) Effect on power, compared at the same collective angle
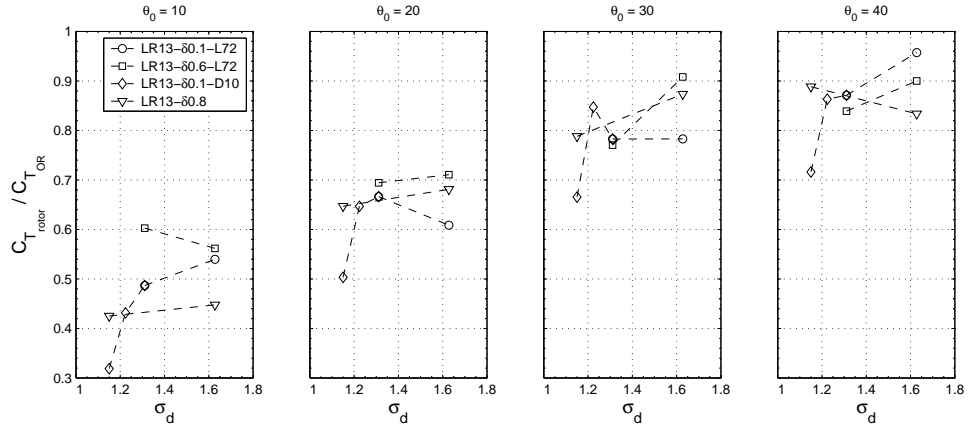
(g) Effect on rotor thrust, compared at the same collective angle
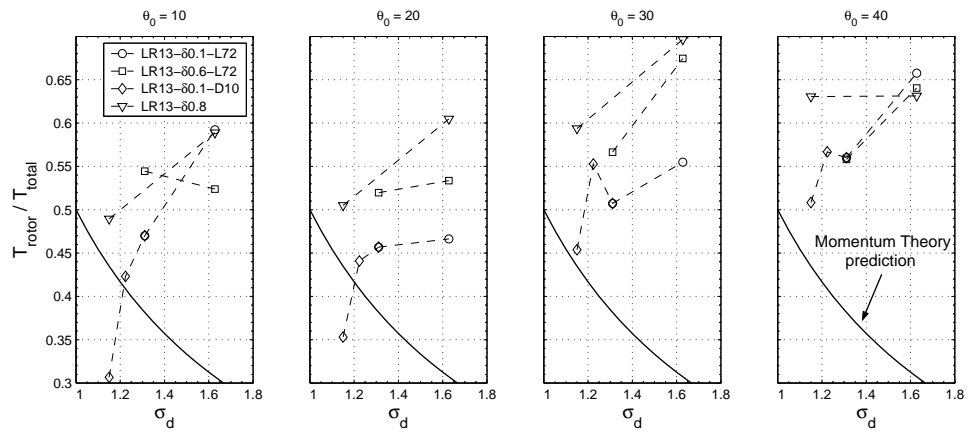
(h) Effect on rotor thrust fraction, compared at the same collective angle
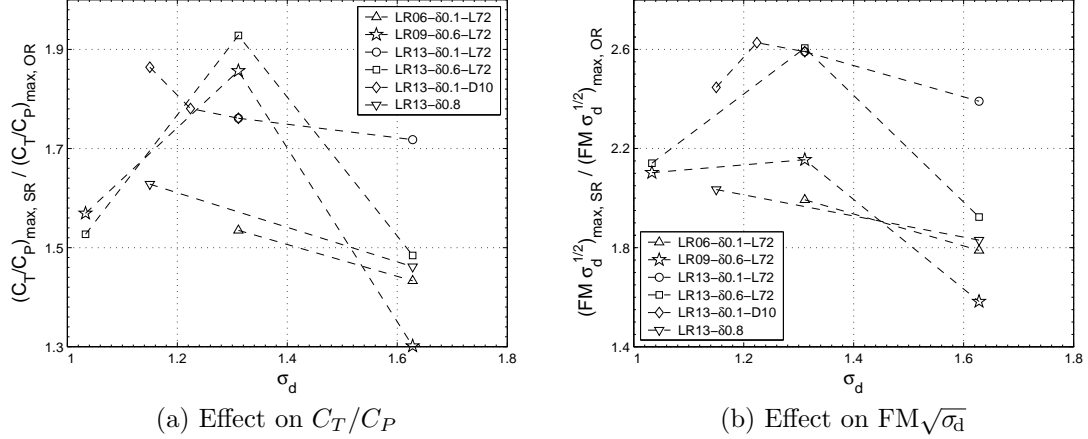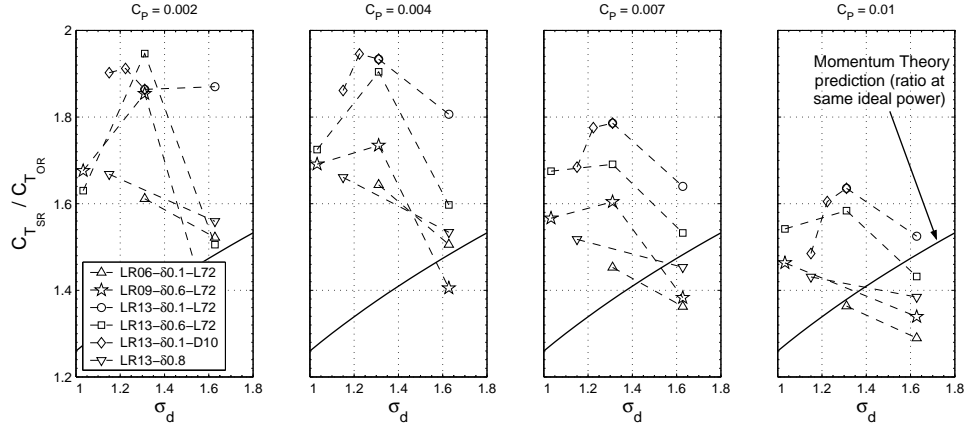
Figure 3.21: Effect of diffuser expansion ratio (contd.)

performance to degrade, with the deterioration due to reducing L_d occuring at the greater rate than that due to reducing θ_d. At higher power coefficients, the shrouds appear to be slightly better able to further expand the flow to higher σ_d; however, the improvement is marginal, and occurs at collectives higher than those at which maximum power loading is achieved.

Superimposed on Figures 3.21c and 3.21d are the predictions of momentum theory for the thrust and power ratios as functions of σ_d (Equations A.27 and A.28), but considering only the ideal power consumption. It is clearly seen that, by considering the *actual* power requirements of the open and shrouded rotors, the improvements obtained by shrouding are substantially greater than those predicted by the theory. Only at the highest expansion ratios tested, at which the diffusers were not able to fully explan the flow, did the performance deteriorate to worse than that predicted by the theory.

Figure3.21h shows the observed variations with expansion ratio of the rotor thrust fraction, T_{rotor}/T_{total}, also compared with the momentum-theory prediction. Unlike the total thrust and power, which, at low values of σ_d, do initially show the same increasing or decreasing trends with increasing expansion ratio that the theory predicts, the observed thrust fraction always increases with increasing σ_d, over the entire range of expansion ratios tested, in complete contrast to the prediction that it should decrease with increasing σ_d (Equation A.17). The reason for this behavior is not known. Of the two diffuser parameters, changing the length seems to have a stronger effect on T_{rotor}/T_{total} than does changing the diffuser angle.

3.3.2.6   Relative effects of the different parameters

The preceding discussions have shown that, in general, the shrouded-rotor models showed deteriorating performance when the inlet lip radius was decreased, the blade tip clearance increased, or the diffuser expansion ratio increased or decreased from a certain optimum value. It is of interest to the MAV designer to know, *quantitatively*, how much the performance of a shrouded rotor will be affected by changing the value of one or more of these shroud parameters, and which of the parameters have the strongest influence on the performance. Therefore, linear fits were applied to the variations in three of the four performance-improvement metrics — the shrouded-rotor-to-open-rotor ratios of maximum C_T/C_P, of maximum FM*, and of thrust coefficient at a power coefficient of 0.004, which was the C_P at which the greatest gains in thrust over the open rotor were seen — for each of the four shrouded-rotor parameters. The results are tabulated in Table 3.2, in the form of the amount of increase ('+') or decrease ('−') in each of the metrics per unit change in the value of each shroud parameter.

The numbers show that the effect of changing blade tip clearance becomes more pronounced as the other parameters are changed to degrade the shrouded-rotor's performance, i.e., decreasing diffuser length, increasing diffuser angle (from 10° to 20°) or decreasing inlet lip radius. The worsening effect of increasing θ_d from 10° to 20° is exacerbated by larger tip clearances, but is less affected by changing the lip radius. On the other hand, decreasing θ_d from 10° to 0° has a more pronounced effect on the LR13 models than on the LR09 models. Changing L_d seems to have a stronger

effect than that of changing θ_d for decreasing σ_d, but a weaker effect for increasing σ_d. In contrast to the trends seen for δ_tip and σ_d, the effect of changing the inlet lip radius seems to be fairly independent of the influence of the other shroud parameters — with the sole exception of the D00-δ0.6 models. Thus, these data suggest that, as the shroud geometry is changed from some optimal configuration, the effects of changing any one of the geometric parameters becomes more pronounced. In other words, it is not possible to categorically state that any one particular parameter has a greater effect on performance than any other, since the amount of influence of any parameter depends on the values of the other parameters. The exception to this seems to be the lip radius, changes in which have the almost same effect no matter what the values of the other parameters are.

Table 3.2: Quantitative evaluation of sensitivity of shrouded-rotor performance to changes in parameter values

Parameter	Series	$\Delta\,(C_{T_\text{SR}}/C_{T_\text{OR}})_{C_P=0.004}$	$\Delta\,(C_T/C_P)_{\text{max,SR}}/(C_T/C_P)_{\text{max,OR}}$	$\Delta\,(\text{FM}^*)_{\text{max,SR}}/(\text{FM}^*)_{\text{max,OR}}$
		Change per 1%D_t increase in δ_tip		
Blade tip clearance	LR13-D10	-0.01	+0.31	+0.03
	LR13-D10-L31	-0.25	-0.19	-0.50
	LR13-D20	-0.35	-0.35	-0.77
	LR09-D20	-0.92	-1.06	-1.83
		Change per 1%D_t increase in r_lip, $\times 10$		
Inlet lip radius	D00-δ0.6	+0.005	-0.08	-0.01
	D10-δ0.1	+0.455	+0.34	+0.90
	D10-δ0.6	+0.456	+0.17	+1.09
	D20-δ0.1	+0.458	+0.43	+0.91
	D20-δ0.6	+0.485	+0.45	+0.83

Change per unit change in σ_d away from optimum

| Parameter	Series	Decr. σ_d	Incr. σ_d	Decr. σ_d	Incr. σ_d	Decr. σ_d	Incr. σ_d
Diffuser angle	LR09-δ0.6-L72	-0.13	-1.12	-1.03	-1.74	-0.19	-1.79
	LR13-δ0.6-L72	-0.73	-1.08	-1.49	-1.39	-1.60	-2.13
	LR06-δ0.1-L72	–	-0.42	–	-0.32	–	-0.64
	LR13-δ0.1-L72	–	-0.42	–	-0.13	–	-0.63
Diffuser length	LR13-δ0.1-D10	-1.20	-0.15	–	-0.21	-2.59	-0.24

3.4 Shroud surface pressure measurements

This section presents the measurements of the static pressure distributions over the shroud surfaces. The general characteristics of the pressure distributions, common to all the shroud models, and of the consequent forces exerted on the inlet, the diffuser, and the shroud as a whole, are discussed first, followed by more detailed analyses of the effects of varying the individual shroud geometric parameters.

3.4.1 General characteristics

The pressure distributions for the individual shroud models, for each of four different rotor collective angles, $\theta_0 = 10°$, $20°$, $30°$ and $40°$, are shown in Figures 3.22b–n, with the (suction) pressure coefficient, $-C_p = (p_{\mathrm{atm}} - p)/q_{\mathrm{tip}}$, plotted as a function of non-dimensional distance along the shroud surface. The coordinate system for the normalized surface distance coordinate, s, is shown in Figure 3.22a. For points downstream of the rotor, i.e., the shroud diffuser, s is equal to the actual surface distance divided by the diffuser slant length, $S = L_d/\cos(\theta_d/2)$, while for points upstream of the rotor, i.e., the shroud inlet, the distances are normalized by the inlet lip circumference, $\pi \cdot r_{\mathrm{lip}}$. Therefore, s is equal to 0 at the rotor plane, $+1$ at the diffuser exit plane, and -1 at the outer edge of the inlet lip. An angular coordinate, θ_{lip}, is also convenient for discussion of the pressure distribution over the shroud inlet, where $\theta_{\mathrm{lip}} = 0°$ corresponds to the rotor plane ($s = 0$) and $\theta_{\mathrm{lip}} = 180°$ corresponds to the outer edge of the inlet lip ($s = -1$).

To better depict the actual, two-dimensional shape of the pressure distribution,
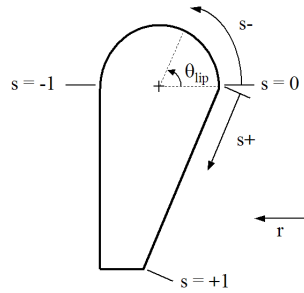
(a) Coordinate system for pressure distribution plots
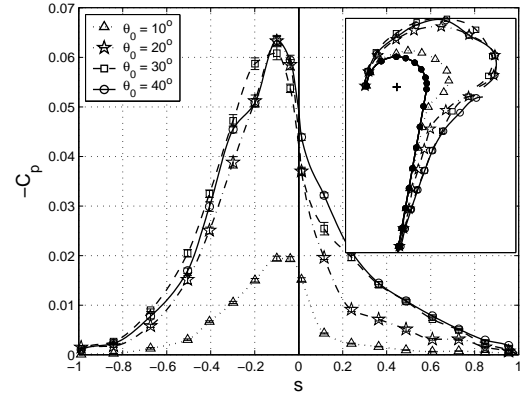
(b) Model LR13-D20-δ0.1
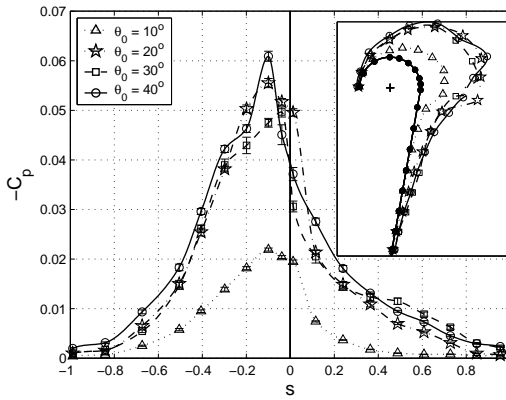
(c) Model LR13-D20-δ0.6
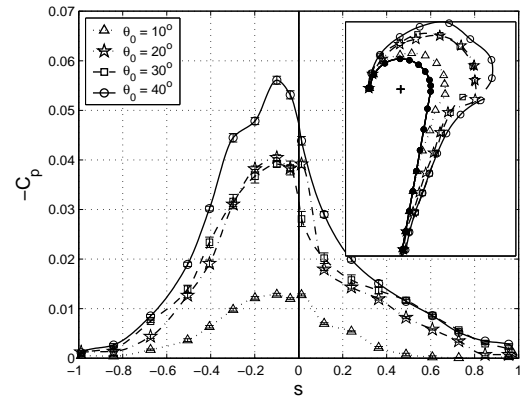
(d) Model LR13-D20-δ0.8

Figure 3.22: Shroud surface pressure distributions in hover: LR13-D20 models
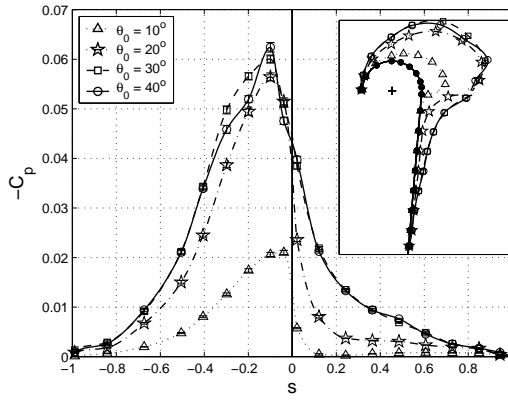
(e) Model LR13-D10-δ0.1
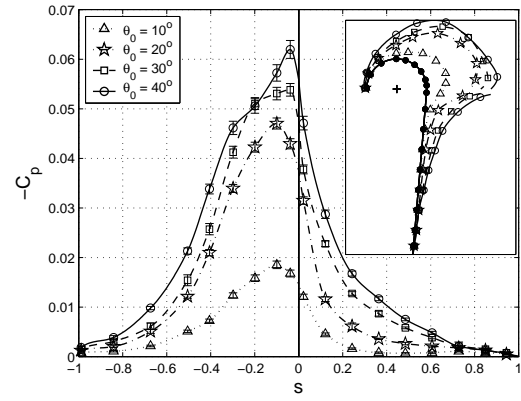
(f) Model LR13-D10-δ0.6
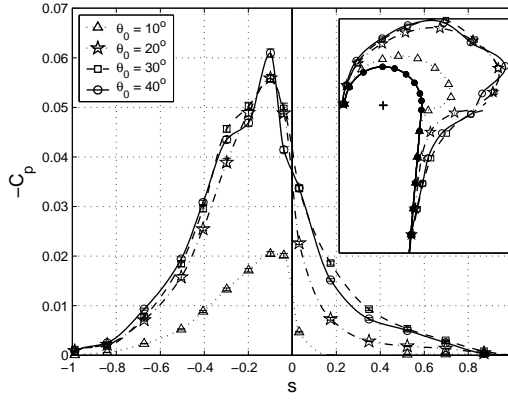
(g) Model LR13-D10-δ0.1-L50
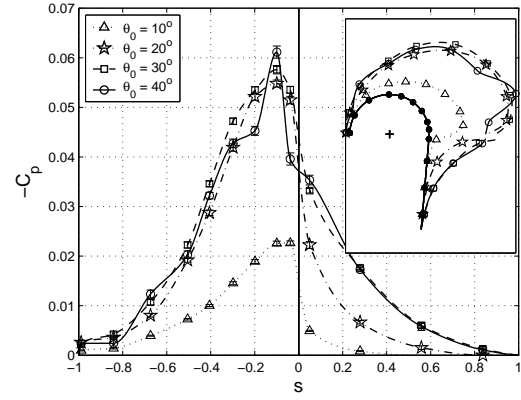
(h) Model LR13-D10-δ0.1-L31
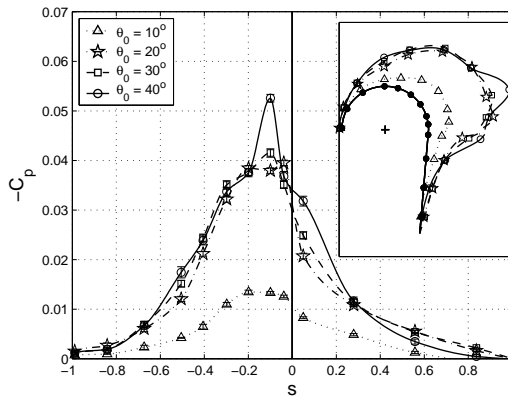
(i) Model LR13-D10-δ0.8-L31
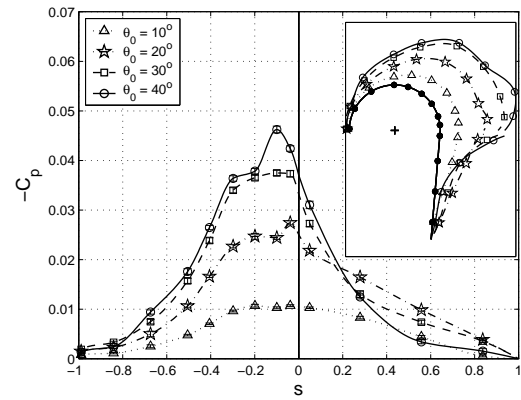
(j) Model LR13-D10-δ1.6-L31

Figure 3.22: Shroud surface pressure distributions in hover (contd.): LR13-D10 models
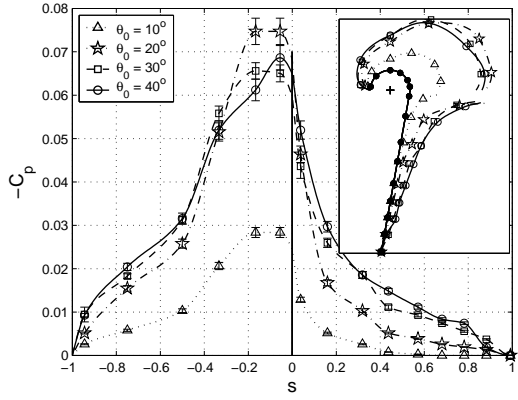
(k) Model LR09-D20-δ0.1
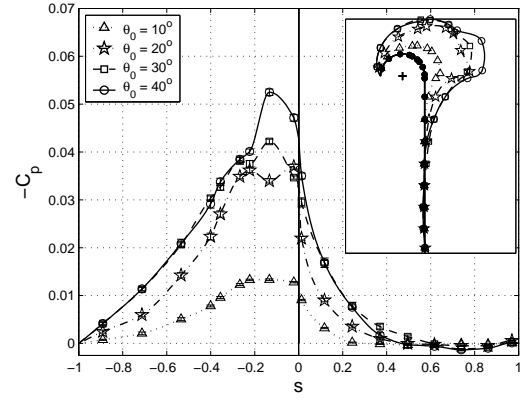
(l) Model LR09-D00-δ0.6
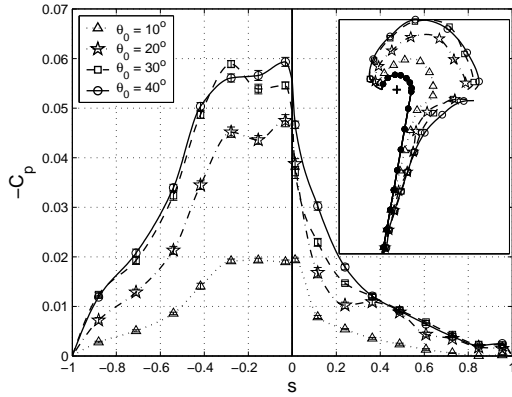
(m) Model LR06-D20-δ0.1
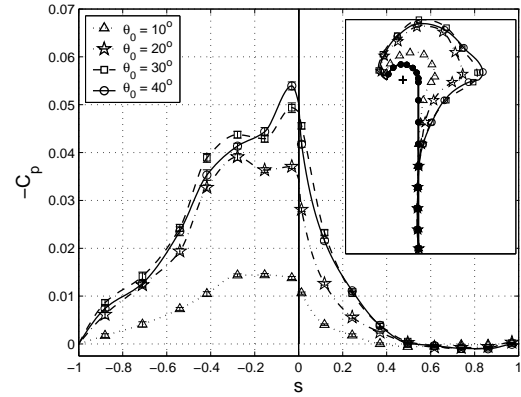
(n) Model LR06-D00-δ0.6

Figure 3.22: Shroud surface pressure distributions in hover (contd.): LR06 and LR09 models

each figure also contains an inset diagram that shows the distributions wrapped around a sectional, non-normalized view of the shroud's profile shape, along with the locations of the pressure taps on the shroud surface. In both representations, the two-dimensional and the 'unwrapped', the actual measured values are shown by the symbols, connected by piecewise cubic Hermite interpolating polynomials that were used to estimate the pressure values at the intermediate locations. These interpolated distributions were integrated over the length of the shroud profile (s = -1 to $+1$), and around the azimuth of the shroud ($\psi = 0°$–$360°$) to obtain the estimates of the shroud thrust, T_{shroud}. For the purpose of integration, the pressure at the boundary points — the oute edges of the diffuser and inlet lip — was assumed to be equal to ambient atmospheric pressure.

The most distinctive feature of all the pressure distributions is a region of very low pressures — a 'suction peak' — on the inner surface of the shroud inlets, just above the plane of the rotor disk and immediately preceding the rise in pressure through the rotor. All of the pressure profiles show an increase in suction from $\theta_{\text{lip}} = 180°$ to about $125°$ (s = -1.0 to -0.7), at which point the rate of increase decreases slightly. This decrease could, however, be an artifact of the imposed end-condition mentioned above. A steeper increase is then seen, to a suction peak at $\theta_{\text{lip}} = 50°$–$40°$, after which occurs a second leveling-off or slight drop, and then, except at a rotor collective of $10°$, a second, stronger suction peak just above the rotor plane, at $\theta_{\text{lip}} \approx 20°$–$0°$. In some cases, a distinction is not seen between these 'primary' and 'secondary' peaks, with the two merging into a single suction peak. However, the secondary peak is always distinctly seen at $\theta_0 = 40°$, for all the

shrouded-rotor models. This secondary peak on the inlet of a shrouded rotor has not been experimentally observed before; however, its existence has been predicted (Fig. 3.23) by the CFD analysis performed in 1993 by Rajagopalan and Keys [87]: Their analysis showed that because of the finite gap between the blade tips and the shroud wall, air flowing through this gap from the higher-pressure region below the rotor to the lower-pressure region above, opposite to the main flow direction, results in the formation of a small eddy — a rudimentary blade tip vortex, essentially — and that the high velocities of this vortical flow would create such a low-pressure region. Unfortunately, because of the location of the rotor at the shroud throat, the forces resulting from these high suction pressure act principally radially inwards, rather than in the axial direction, and therefore do not directly contribute much useful thrust. However, by suitably tailoring the shape of the shroud inlet profile in this region near the rotor blade tips, in such a way that the resulting forces are inclined more towards the axial direction, it may be possible to harness the potential of the strong secondary suction peak to produce even greater amounts of thrust. This may be a fruitful area for further research.

After the inlet suction peak(s), a rise in pressure occurs as the flow passes through the rotor, the increase being most abrupt at a rotor collective of 20°. In the diffusers, after the initial rapid increase in pressure below the rotor disk, pressure generally increases gradually to ambient levels at the diffuser exit. However, in the D00 diffusers (Figs. 3.22l, n), the wake expands to ambient pressure by about halfway through the diffuser, and then actually shows a very slight over-pressure before decreasing back again to ambient levels.
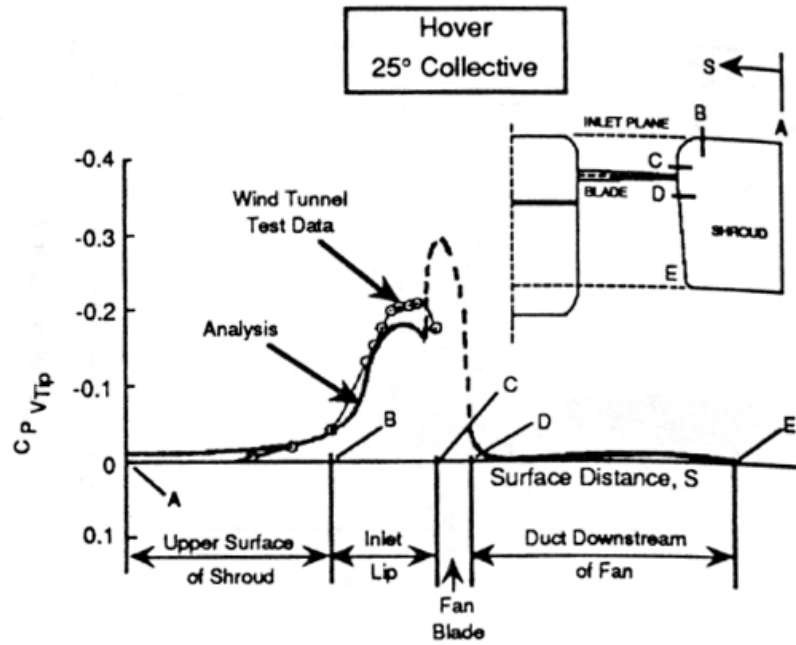
Figure 3.23: CFD prediction of secondary suction peak by Rajagopalan and Keys [87].

With increasing collective, the suction pressures increase over the entire inlet, the secondary peak becomes sharper and stronger, possibly corresponding to an increase in strength of the blade tip vortex, and the plateau region in between the peaks becomes smaller and less distinct. In most cases, the strength of the peak increases monotonically with increasing collective, with a large increase seen between $\theta_0 = 10°$ and $20°$, and smaller increases from $20°$ to $40°$. However, in some cases, the strength is seen to decrease from $\theta_0 = 20°$ to $30°$, and then increase slightly at $40°$. Diffuser suction pressures also increase as collective is increased from $10°$ to $30°$, with little change thereafter as θ_0 is increased to $40°$. The exceptions to this trend are the D10-L31 models with large blade tip clearances (Figs. 3.22i, j).

3.4.1.1 Inlet thrust distribution

Because of the dominant nature of the suction peak on the shroud pressure distributions, the inlet pressure distribution has a strong influence on the overall shroud thrust; it will be seen in the following section that the magnitude of the positive thrust from the inlet is four or more times the magnitude of the negative thrust from the diffuser. It is therefore worthwhile to analyze in more detail the characteristics of the inlet pressure and thrust distributions. It is immediately obvious that, because the normal vectors to the inlet surface do not all point in the thrust (axial) direction, the thrust distributions will not be the same as that of the inlet pressure distributions shown in Figures 3.22b–n. In addition, due to the compound curvature of the inlet, the outer portions of the two-dimensional inlet profile contribute greater amounts of area to the complete, three-dimensional inlet surface than do the inner portions, so that the amount of force produced by the outer portions of the inlet lip are greater than would be suggested by the pressure distributions. For this reason, the resultant two-dimensional, *sectional* force vector, F'_{inlet} (Figure 3.24), obtained by integration of the inlet pressure distribution over a single azimuthal section of the inlet[4], does not yield the value of the net inlet thrust when simply summed around the azimuth of the shroud inlet. In other words, $F_{\text{inlet}} \neq T_{\text{inlet}}$. Even though, due to the radial symmetry of the flow-field in hover, the summation results in the radial $(\cos(\angle F'_{\text{inlet}}))$ components of the sectional forces canceling out, leaving a three-dimensional force that is purely axial, still, the bias due to the outer portions of the inlet result in an effective axial force component of

---

[4]The prime denotes that this is a *two*-dimensional force.
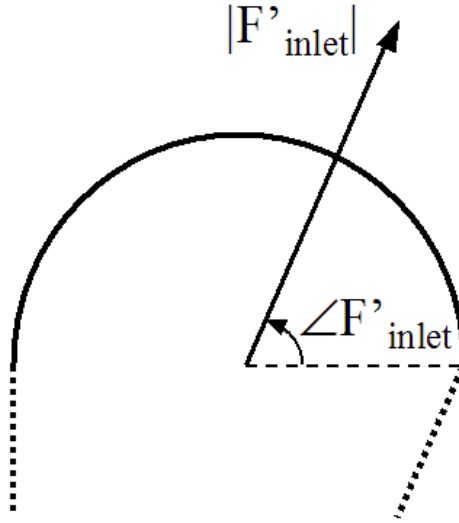
Figure 3.24: Sectional inlet resultant force vector

the sectional force that is greater than that given by $|F'_{\text{inlet}}| \cdot \sin(\angle F'_{\text{inlet}})$.

Thus, there are two ways of looking at the inlet thrust distribution: first, the two-dimensional distribution on a single, azimuthal section of the inlet, which can be represented by the magnitude and direction of the resultant sectional force vector, F'_{inlet}; and second, a 'three-dimensional' distribution that takes into consideration the additional area of the outer portions of the inlet when integrated around the shroud azimuth. Such a distribution is shown in Figure 3.25a, which plots the variation in the differential inlet thrust, $\mathrm{d}C_{T_{\text{inlet}}}/\mathrm{d}\theta_{\text{lip}}$, with inlet angular coordinate, θ_{lip}, for one of the models, LR13-D10-δ0.1, at four different rotor collectives. The relative magnitudes of the thrust distributions at the different collectives are similar to the relative magnitudes seen in the pressure distributions; therefore, in this figure, to better contrast the shapes of the distributions at the different collectives, the magnitudes are shown scaled to the total inlet thrust at the corresponding col-

(a) Variation in differential inlet thrust (b) Fractional contribution to total inlet thrust
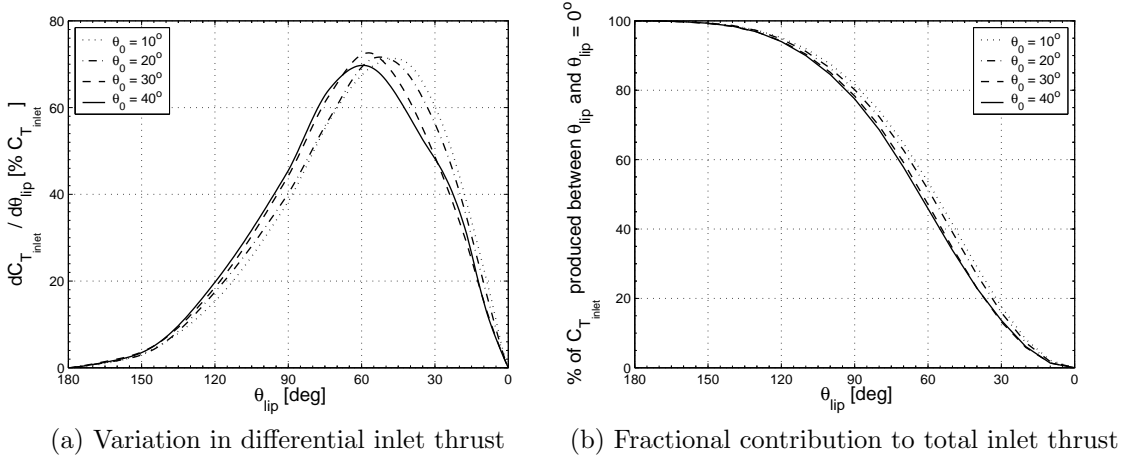
Figure 3.25: Inlet thrust distributions for model LR13-D10-δ0.1

lective. Comparing these distributions with those of the inlet pressures shown in Figure 3.22e, it can be seen that the peak thrust contribution occurs at $\theta_{\rm lip}$ between 45° and 60°, in contrast to the pressure distributions which peak at $\theta_{\rm lip}$ between 10° and 20°. As rotor collective is increased, the location of the peak thrust contribution moves outwards, to slightly higher values of $\theta_{\rm lip}$. The other shroud models showed similar distributions, and this trend was noticed, to varying amounts, in each of them.

Figure 3.25b plots the fraction of the total inlet thrust produced between $\theta_{\rm lip}$ = 0° and any other value of $\theta_{\rm lip}$. This graph shows that about 80% of the total inlet thrust is produced by the inner half of the inlet lip ($\theta_{\rm lip}$ = 0° to 90°). This suggests that the weight of the shroud can be reduced by reducing the stiffness of the structure forming the outer portion of the inlet lip, since it does not bear a substantial load. It is also seen that even though the location of the peak thrust shifts by approximately 15° as rotor collective is increased (Figure 3.25a), the extent of lip surface required for a given amount of inlet thrust changes by less than 10°

193

(Figure 3.25b).

3.4.2   Effects of changing shroud parameter values

The effects of varying the four shroud geometric parameters — δ_{tip}, r_{lip}, θ_{d} and L_{d} — on the pressure distributions and the consequent shroud forces are shown in Figures 3.26–3.29 and described in the following subsections. Just as for the performance analyses, multiple series of model comparisons are presented for each shroud parameter (Table 3.3). Each sub-figure shows the comparisons of the different models in a single series. The plots on the left-hand side of each figure show the two-dimensional (2-D) pressure distributions of the different models being compared, at four different collective angles. In these plots, unlike in the inset diagrams of Figures 3.22b–n, the different linear and angular dimensions of the different shrouds have been scaled to the same values, to enable easier comparison of the pressure profiles. The right-hand side of each figure shows graphs of the variations with rotor collective of shroud thrust ($C_{T_{\text{shroud}}}$), shroud inlet thrust ($C_{T_{\text{inlet}}}$), shroud diffuser thrust ($C_{T_{\text{diffuser}}}$), and the magnitude ($|C_{F'_{\text{inlet}}}|$) and direction ($\angle C_{F'_{\text{inlet}}}$) of the resultant sectional inlet force vector, for each of the different models in the series. Despite the slightly misleading nature of this quantity, discussed earlier, specifying the magnitude and direction of F'_{inlet} remains a useful technique for comparing the inlet thrust distributions of the different shroud models, and has therefore been included in these analyses.

From the figures, it can be seen that the force coefficients all generally increase

Table 3.3: Shrouded-rotor model comparison series for analyzing effects of the shroud geometric parameters on shroud pressure distributions

Model series for blade tip clearance	δ_{tip} values [$\%D_{\text{t}}$]
LR13-D20	0.09, 0.63, 0.82
LR13-D10	0.09, 0.63
LR13-D10-L31	0.09, 0.82, 1.57
Model series for inlet lip radius	r_{lip} values [$\%D_{\text{t}}$]
D20-δ0.1	6.48, 8.99, 13.1
D00-δ0.6	6.48, 8.99
Model series for diffuser included angle	θ_{d} values [°]
LR13-δ0.1	9.70, 20.22
LR13-δ0.6	9.70, 20.22
Model series for diffuser length	L_{d} values [$\%D_{\text{t}}$]
LR13-D10-δ0.1	31, 50, 72

in magnitude with increasing collective, up to around $\theta_0 = 30°$, and then level off or decrease at higher collectives, exhibiting a stall-like behavior. As would be expected, the variations in $|C_{F'_{\text{inlet}}}|$ and $C_{T_{\text{inlet}}}$ are very similar, and follow the trends of the inlet pressure distributions described earlier. $\angle C_{F'_{\text{inlet}}}$ generally increases with increasing collective, because of the increasing strength and merging of the two suction peaks, and has values mostly between $40°$ and $60°$. Note that this is 5–$12°$ lower than the location of the peak thrust contribution when 3-D effects are included — compare Figures 3.25a and 3.26b for model LR13-D10-δ0.1. The magnitudes of the diffuser thrust are at most only about 26% those of the inlet thrust, so the net shroud thrust more closely follows the trends of the inlet thrust, both with respect to rotor collective and with respect to changes in the shroud geometry.

3.4.2.1   Blade tip clearance

The effects of changing the blade tip clearance, δ_{tip}, are shown in Figure 3.26, with data available from three series of models: LR13-D10-L31, LR13-D10 and LR13-D20 (Table 3.3). From the measurements, increasing the tip clearance was seen to have the following effects:

(i) The suction pressures on the inlet lip decrease. This effect is generally more evident at $\theta_0 = 20°$ and $30°$ than at $10°$ and $40°$. Because of the drop in suction pressure, the magnitudes of $C_{F'_{\text{inlet}}}$, $C_{T_{\text{inlet}}}$ and $C_{T_{\text{shroud}}}$ decrease, the slopes of the initial part of the graphs of these coefficients with respect to θ_0 decrease, and the 'stall' behavior of these quantities changes from a 'sharper' stall to a
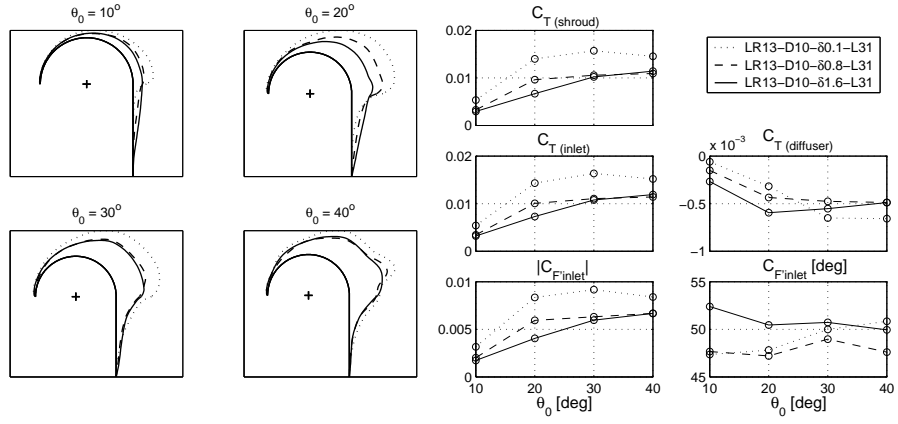
(a) Series LR13-D10-L31
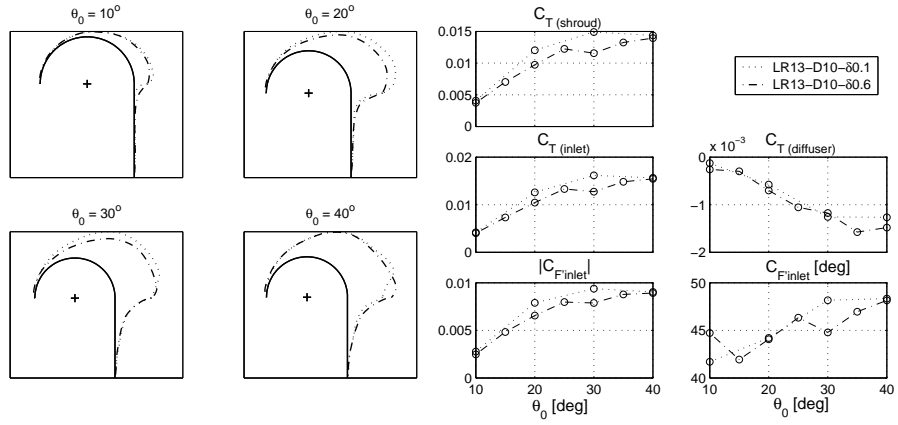
(b) Series LR13-D10
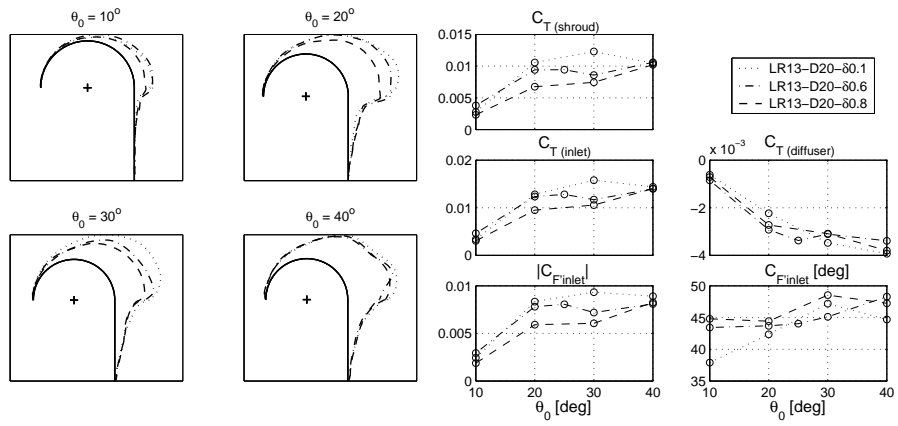
(c) Series LR13-D20

Figure 3.26: Effects of blade tip clearance on pressure distribution

more gentle one. At small tip clearances, the magnitudes of the forces increase up to a collective of about 30° and then decrease. At the larger tip clearances tested, the forces continue to increase over the full range of collectives, albeit with a lower slope. At the intermediate values of δ_{tip}, the forces decrease in magnitude at collectives between 20°–25°, after which the magnitude increases again from $\theta_0 = 30°$ to 40°.

(ii) The location of the secondary suction peak moves very gradually towards the rotor plane (to lower values of θ_{lip}). This is most clearly seen for the D10 models. The behavior of $\angle C_{F'_{\text{inlet}}}$ changes from increasing with increasing collective (with a stall pattern at higher collectives), to a more gentle increase, to remaining roughly constant with some fluctuations, to actually decreasing slightly.

(iii) Diffuser suction pressures and $|C_{T_{\text{diffuser}}}|$ increase at collectives of 10° and 20°. A crossover seems to take place near $\theta_0 = 30°$, so that the opposite trend is seen at the higher collectives. This effect of changing δ_{tip} is most pronounced in the D10-L31 models.

(iv) At collectives of 10° and 20°, the pressure jump through the rotor plane becomes less pronounced. This effect is not so consistent at the higher collectives.

3.4.2.2 Inlet lip radius

The effects of changing the inlet lip radius, r_{lip}, are shown in Figure 3.27, with data from two series of models: D00-δ0.6 and D20-δ0.1 (Table 3.3). From the
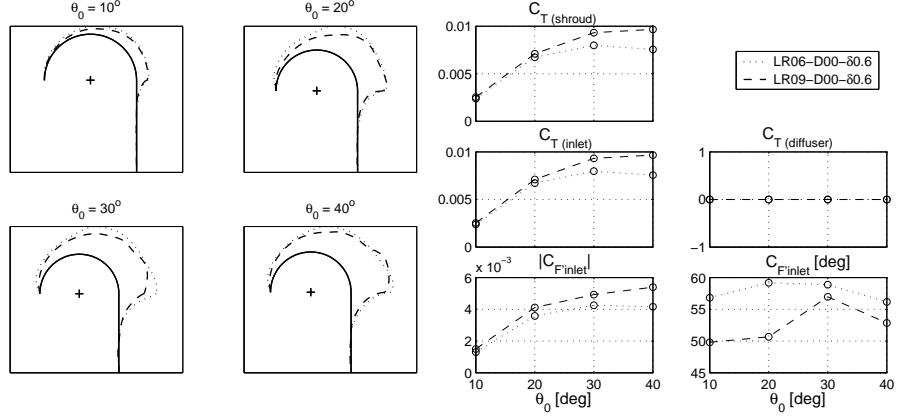
(a) Series D00-δ0.6
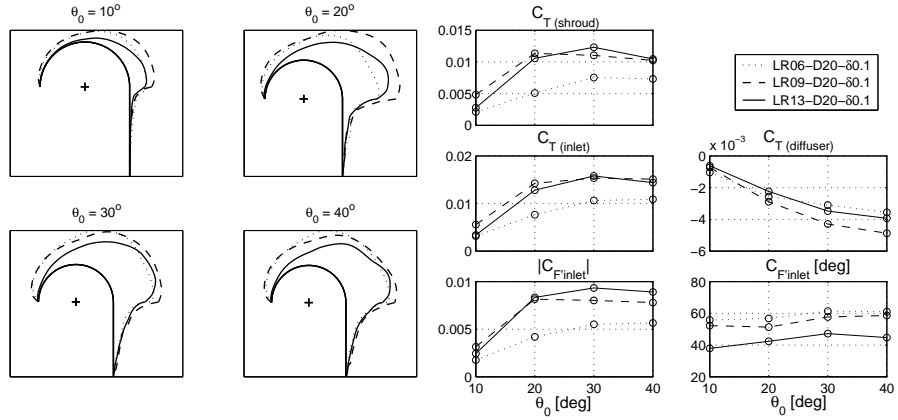
(b) Series D20-δ0.1

Figure 3.27: Effects of inlet lip radius on pressure distribution

measurements, increasing the lip radius was seen to have the following effects:

(i) The inlet pressure profile becomes less uniform and more skewed towards the inner portion of the inlet, generally decreasing over most of the inlet lip (θ_{lip} = 45°–180°) and increasing over only the innermost portion (θ_{lip} = 0°–45°), although a lot of small-scale variation is seen. However, the LR09 inlet has 46% more surface area than the LR06 inlet, and the LR13 inlet an additional 80% more, and this increase in total inlet surface area with increasing lip radius more than compensates for the loss in suction, resulting in a net increase in

$|C_{F'_{\text{inlet}}}|$.

(ii) The location of the secondary peak shows a very slight tendency to move further upstream away from the rotor plane, i.e., to larger values of θ_{lip}. However, the range of this movement is very small, within $\theta_{\text{lip}} = 0°$ to $30°$, so the increasing strength of the secondary peak, relative to the decreasing suction on the outer portions of the inlet, still causes $\angle C_{F'_{\text{inlet}}}$ to decrease, from $\sim 60°$ for the LR06 models to $\sim 45°$ for the LR13.

(iii) The inlet thrust is a function of both the magnitude and direction of F'_{inlet}, and is seen to increase from LR06 to LR09, and then decrease slightly from LR09 to LR13.

(iv) In the diffusers, too, the suction pressures generally decrease. In the D00-$\delta 0.6$ models, this has no effect on the net thrust because $\theta_{\text{d}} = 0°$, but in the D20-$\delta 0.1$ models it causes a reduction in $|C_{T_{\text{diffuser}}}|$.

(v) Except at $\theta_0 = 10°$, the net shroud thrust increases with increasing lip radius.

3.4.2.3 Diffuser angle

The effects of changing the diffuser included angle, θ_{d}, are shown in Figure 3.28, with data from two series of models: LR13-$\delta 0.1$ and LR13-$\delta 0.6$ (Table 3.3). From the measurements, the following observations were made:

(i) Although small-scale variations are seen in the inlet pressure distributions, changing the diffuser angle does not appear to significantly modify the inflow
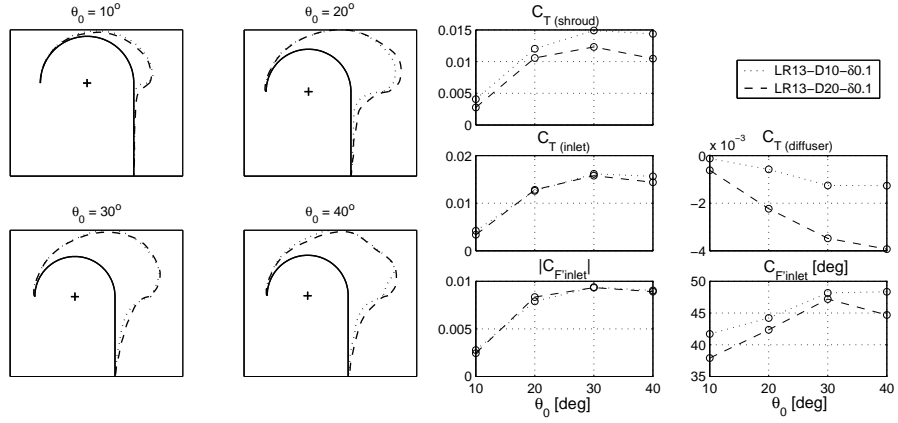
(a) Series LR13-δ0.1
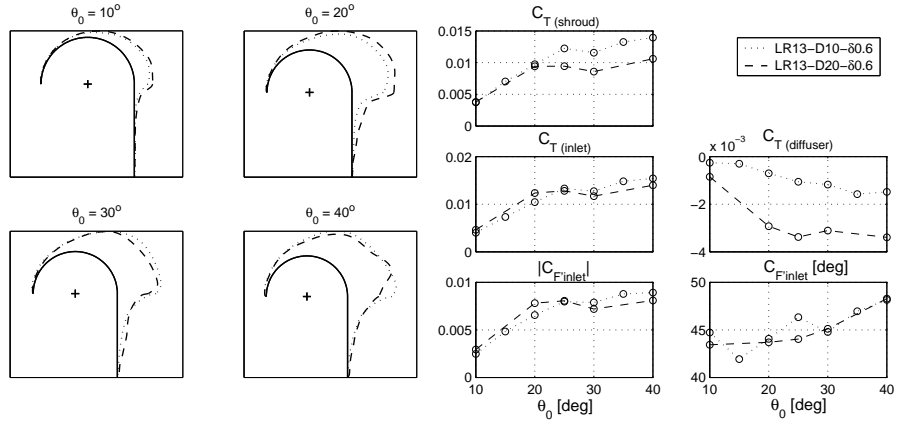
(b) Series LR13-δ0.6

Figure 3.28: Effects of diffuser included angle on pressure distribution

pattern of the shrouded rotors. Similarly, negligible effect is seen on the variations of $C_{F'_{\text{inlet}}}$ and $C_{T_{\text{inlet}}}$ with collective. Below $\theta_0 = 25°$, the D20 models show slightly higher forces, while above $25°$, the forces on the D10 models are higher; however, the differences are very small. These differences are slightly greater in the $\delta 0.6$ series than in the $\delta 0.1$ series.

(ii) For both series, $\angle C_{F'_{\text{inlet}}}$ lies around $45°$. In the $\delta 0.1$ series, $\angle C_{F'_{\text{inlet}}}$ is slightly higher for the D10 model than for the D20 model. In the $\delta 0.6$ series, apart from the fluctuations in the values for the D10 model, little difference is seen in the mean trends for the two models.

(iii) In the diffuser, on the other hand, the D20 models consistently show higher suction pressures. Because of this, and also because of the greater inclination of the their diffuser walls, the D20 models produce up to four times as much negative thrust from the diffuser as the D10 models.

(iv) The net effect is that the D10 models produce up to 25% to 40% more net shroud thrust than the D20 models, with the improvement seen mostly at collectives above $20°$.

3.4.2.4 Diffuser length

The effects of changing the diffuser length, L_{d}, are shown in Figure 3.29, with data from a single model series: the LR13-D10-$\delta 0.1$ models (Table 3.3). From the measurements, increasing the diffuser length was seen to have the following effects:
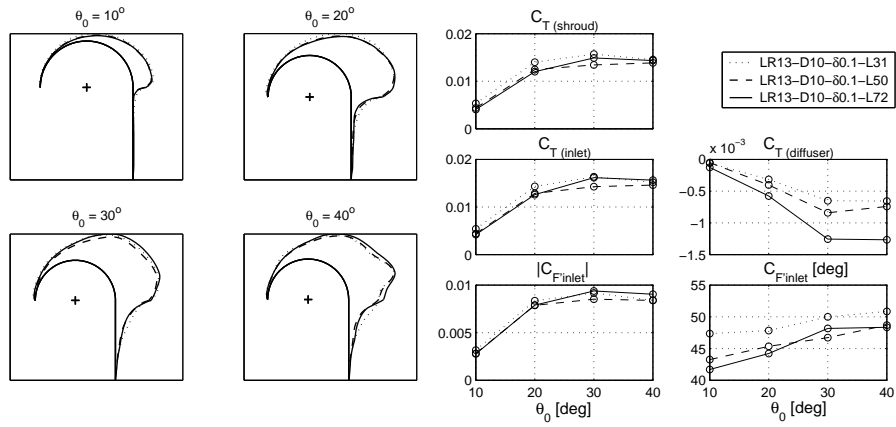
(a) Series LR13-D10-δ0.1
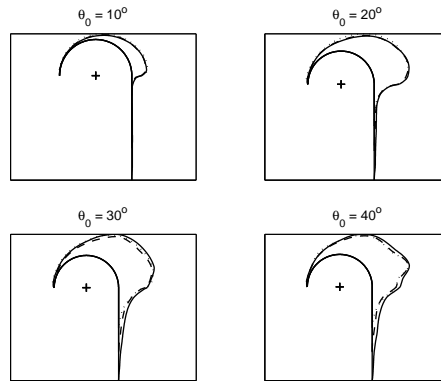
(b) Series LR13-D10-δ0.1, but with correct
scaling of diffuser lengths

Figure 3.29: Effects of diffuser length on pressure distribution

(i) No significant effects are seen on the inlet pressure distributions, and on the variations of $|C_{F'_{\text{inlet}}}|$, $C_{T_{\text{inlet}}}$ and $C_{T_{\text{shroud}}}$ with rotor collective. The magnitudes of the forces decrease slightly, more so from L31 to L50 than from L50 to L72, but the reduction is marginal. Similarly, $\angle C_{F'_{\text{inlet}}}$ decreases, but the overall decrease, while being more clear than the decrease in the forces, is still only by 5° or less.

(ii) When the diffuser pressure profiles are compared with all the diffusers scaled to the same length (Figure 3.29a), the shorter diffusers appear to expand the flow to ambient pressure more slowly, and so have higher suction pressures exerted on their surfaces. However, for this shroud parameter, this representation — with the diffusers all scaled to the same length — is misleading. When the pressure distributions are compared with the diffuser lengths shown in correct relation to each other (Figure 3.29b), it can be seen that the initial rate of expansion, immediately downstream of the rotor, is fairly independent of diffuser length. Further downstream from the rotor, though, the longer diffusers experience higher suction pressures. This, coupled with the larger surface area over which they act, causes $|C_{T_{\text{diffuser}}}|$ to increase significantly for the longer diffusers. However, since it is an order of magnitude smaller than the inlet thrust coefficient, the net shroud thrust is not much affected.

(a) Series D00-δ0.6

(b) Series D20-δ0.1
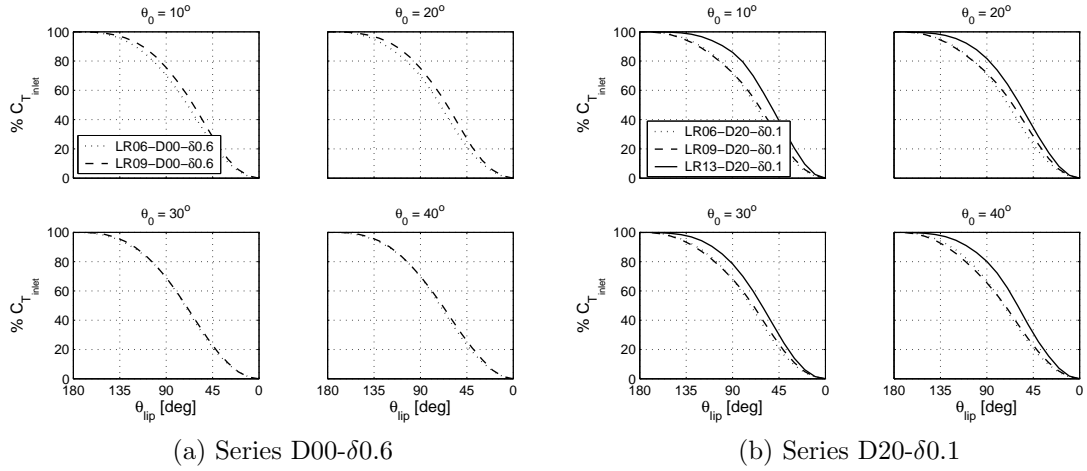
Figure 3.30: Effect of lip radius on inlet thrust distributions

3.4.2.5 Inlet thrust distribution

In contrast to the movement of the secondary suction peak, it was found that increasing the inlet lip radius caused the peak thrust location to move to lower values of θ_{lip} (Fig. 3.30). This implies that for shrouds with large inlet lip radii, a smaller extent of the inlet lip is required to produce a certain percentage of the maximum possible inlet thrust, while for shrouds with sharper inlet lips, the inlet needs to be extended to larger values of θ_{lip} to attain the same percentage of the maximum possible inlet thrust.

The effects of the other shroud parameters on the inlet thrust distribution were found to be negligible. Variations were seen between the distributions of the models with different tip clearances, but no consistent trends could be deduced. As diffuser length was increased, a smaller extent of the inlet lip was required for the same percentage of inlet thrust, just as for increasing lip radius, but the differences were minimal. When diffuser angle was changed, the LR13-δ0.6 models showed virtually

no change in the inlet thrust distribution, while the LR13-δ0.1 series showed that the D20 model required a smaller lip extent than the D10 model — but, again, by a very small amount.

3.5   Wake axial velocity measurements

This section discusses the measurements made of the axial flow velocities in the wakes of the open and shrouded rotors in hover. The velocity data are shown normalized by the ideal induced velocity at the rotor disk, v_i (Equation 1.1, page 16), while length dimensions have been normalized by the rotor radius, R.

3.5.1   General characteristics

For the open rotor, at a collective angle of 20°, the flow-field was mapped out to a depth (z) of 5 in ($1.6R$) below the plane of the rotor. This was also done for one of the shrouded rotors, model LR13-D10-δ0.6, at the same collective and to a similar depth below the diffuser exit plane. These measurements are shown in Figure 3.31, both in the form of two-dimensional maps of the entire wake, with superimposed dots indicating the locations at which the measurements were made, as well as in the form of radial profiles of the velocity at different axial stations. Limitations of the measurement apparatus prevented measurements from being made immediately below the plane of the rotor disk in the case of the shrouded rotor; however, the two sets of data do overlap between $z/R = 1.12$ and 1.60. Comparing the two sets of measurements within this range, it is readily apparent that the shroud is

very effective at improving the uniformity of the flow in the wake, which translates directly to lower induced power for the shrouded rotor, even though it is at a higher thrust coefficient than that of the open rotor (0.0211 vs. 0.0147). This improvement in uniformity is critical, considering the significant velocity deficit seen in the core region of the flow, caused by the lack of twist in the rotor blades and by the blockage and viscous losses at the rotor centerbody.[5]

By observing the inclination of the countour lines in the figures, it appears that the diameter of the shrouded rotor's wake remains fairly constant after exiting from the diffuser; this supports the fundamental assumption made in the momentum theory model that the flow is fully expanded at the diffuser exit plane. In contrast, the countours in the wake of the open rotor show the characteristic contraction that is expected for this configuration. However, when compared with the prediction — superimposed on the 2-D map — for the location of the wake boundary as given by the Landgrebe model, which is an empirical method that is commonly used for conventional, large-scale rotors [14, p. 450], these data seem to suggest that the wake of this micro-scale open rotor contracts significantly more than that of larger rotors. This hypothesis is supported by further comparisons, shown in Figure 3.32, of measurements in the wakes of hovering MAV-scale and conventional-scale rotors, using data from other researchers. Figure 3.32a shows the positions of the blade tip vortex cores at different wake ages, obtained by Hein and Chopra from flow-visualization experiments on a MAV-scale rotor [20], while Figure 3.32b shows data

---

[5]See also the flow visualization studies conducted by Hein and Chopra on a MAV-scale rotor in hover [20].
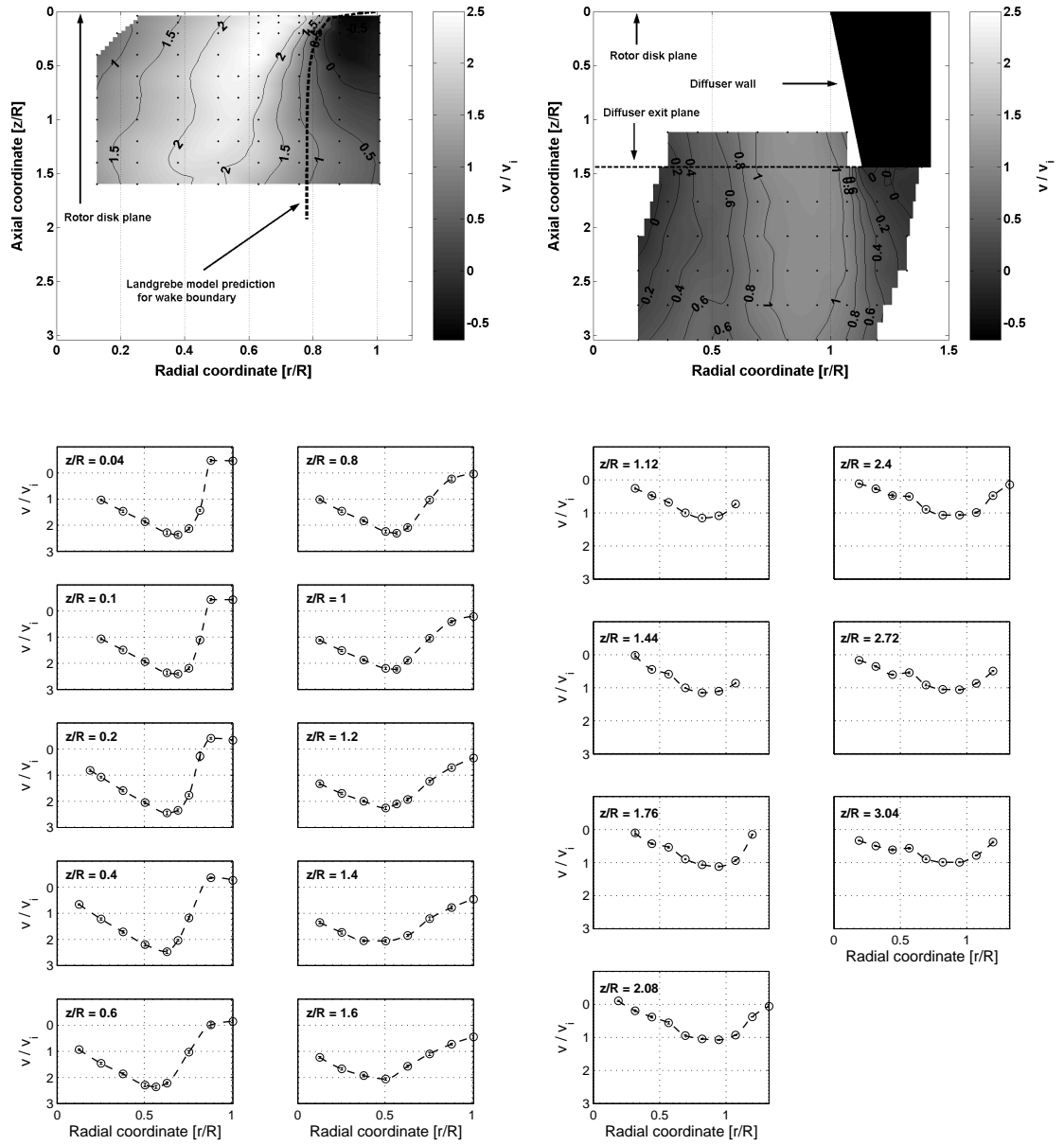
(a) Open rotor, $C_T = 0.0147$ (b) Shrouded-rotor LR13-D10-δ0.6, $C_T = 0.0211$

Figure 3.31: Rotor wake development at $\theta_0 = 20°$

from measurements by Bohorquez and Pines [168], mapping out the wake of another micro-rotor, similar to those done in this study. In both figures, the prediction by the Landgrebe wake-boundary model has been superimposed. Figure 3.32c shows a comparison of the wake profiles at different axial stations, obtained by interpolation from the data shown in Figure 3.31a, with measurements made by Boatright on a full-scale rotor [174]. All three comparisons indicate a greater contraction of the wake of the micro-scale rotors compared to that of larger ones.

Figure 3.31a also shows that, for the open rotor, the peak inflow velocity at the plane of the rotor disk takes place at a radial location of about $0.7R$, which is much further inboard compared to the inflow profiles of conventional-scale rotors. This suggests that the blade tip vortices of MAV-scale rotors have much larger cores than do conventional-scale rotors. The flow-visualization studies conducted on similarly-sized micro-rotors by Hein and Chopra [20] and by Ramasamy et al. [24, 171] resulted in similar observations.

For the remaining shrouded-rotor models in the LR13-D10 'family', wake velocity measurements were only made at the diffuser exit plane, but at additional rotor collective angles as well. Figure 3.33 shows these radial wake profiles (w/v_i) for four of the models, at collectives of 10°, 20°, 30° and 40°, along with the momentum-theory prediction, equal to $1/\sigma_\mathrm{d}$. It can be seen that with increasing collective, the wake profile becomes increasingly non-uniform, leading to increased induced power losses [14, p. 89]. In the case of the shortest-diffuser models (L31: Figs. 3.33a, b), the pitot-probe readings became negative at the higher collectives (30° and 40°), indicating large deviations in the flow direction away from the axial direction. A few

(a) Tip vortex trajectory, MAV-scale rotor: C_T = 0.0241, σ = 0.162, N_b = 2, no twist. Data from [20]

(b) Wake structure, MAV-scale rotor: C_T = 0.0157, σ = 0.110, N_b = 2, no twist, $\theta_0 = 15°$. Data from [168]

(c) Wake development: Comparison with data from tests on a large-scale rotor with $-4°$ of twist [174]
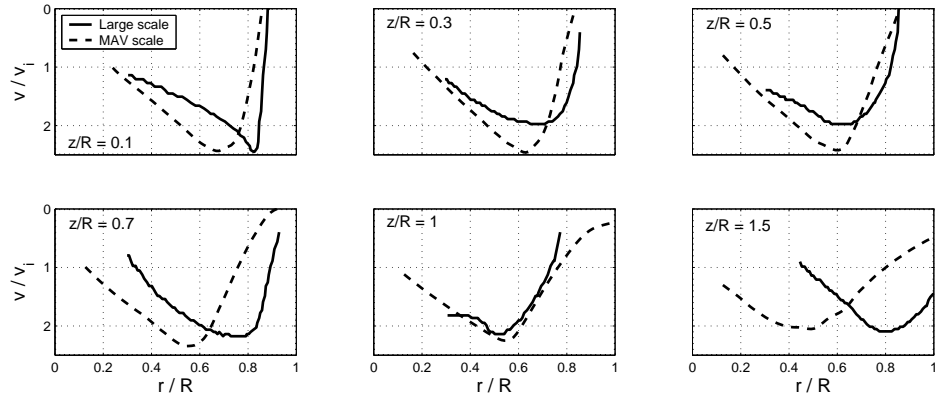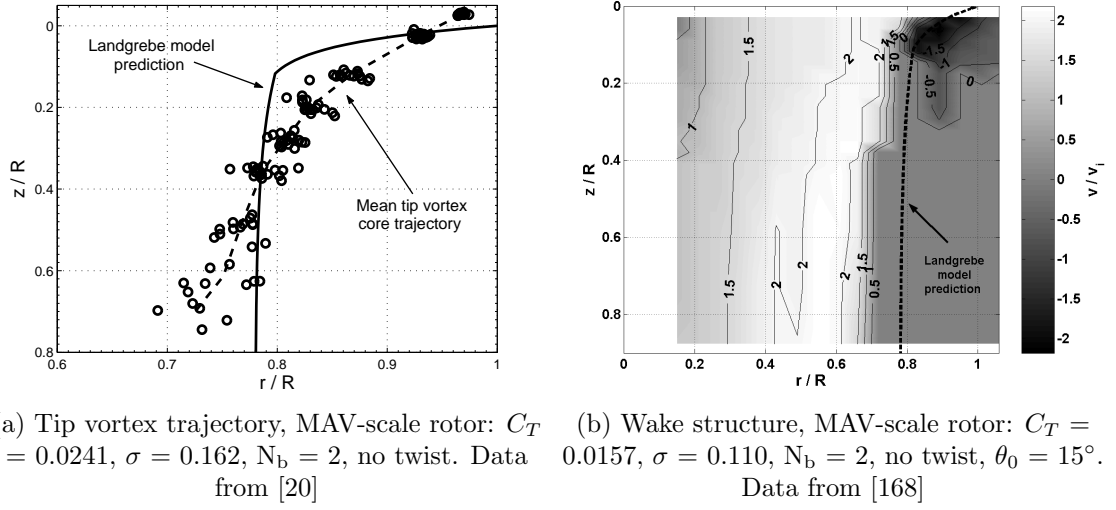
Figure 3.32: Comparison of rotor wake development of conventional-scale and MAV-scale rotors

(a) LR13-D10-δ0.8-L31

(b) LR13-D10-δ0.1-L31

(c) LR13-D10-δ0.1-L50

(d) LR13-D10-δ0.1-L72
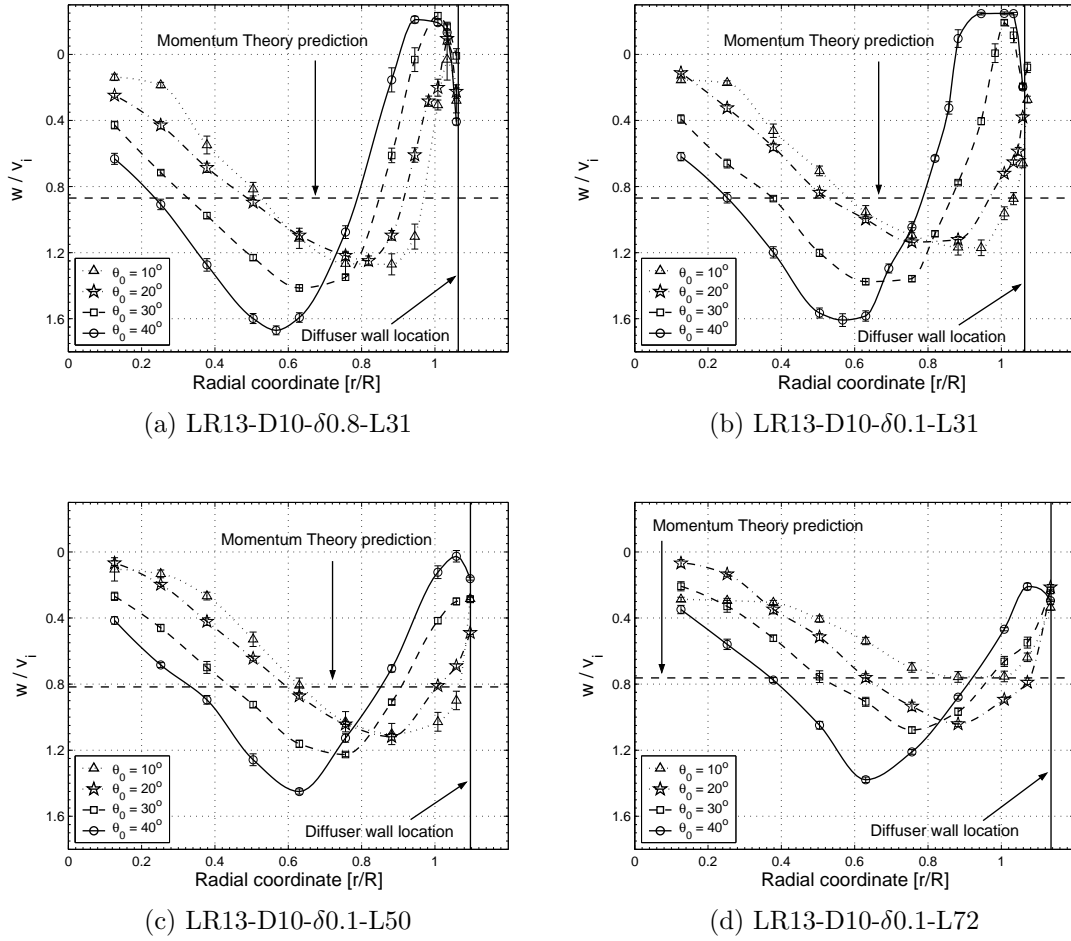
Figure 3.33: Wake profiles at diffuser exit plane of shrouded rotors

investigatory measurements were made with the pitot probe aligned in the tangential (azimuthal) direction, and these indicated the presence of large swirl velocities near the diffuser wall. These observations suggest that the rotor may have stalled at these higher collectives. The longer-diffuser models (L50, L72) also showed the trend of decreasing axial velocities near the shroud wall with increasing rotor collective, but in these cases the probe measurements did not become negative.

The radial variations in axial velocity can be integrated to obtain the value for an average velocity that produces the same mass flow through the diffuser exit

plane. These average values — again, normalized by v_i — are shown in Fig. 3.34a, and appear to be fairly close to the theoretical value of $1/\sigma_\mathrm{d}$. However, it is clear that the profiles are far from uniform, and the penalty of this non-uniformity on the induced power expenditure of the rotor can be quantified by integrating the radial distributions of axial kinetic *energy*, and dividing the result by the ideal power requirement of the shrouded rotor ($C_{P_i} = C_T^{3/2}/2\sqrt{\sigma_\mathrm{d}}$) to obtain an estimate for the induced power correction factor, κ. The effect of increasing collective on the estimates of κ thus obtained are shown in Fig. 3.34b. With the exception of the LR13-D10-δ0.1-L72 model, the lowest value of κ occurs at a rotor collective of 20°. At $\theta_0 = 10°$, the LR13-D10-δ0.1-L72 model shows a value of κ that is less than 1.0, which is not a physically realistic solution. The wake measurements for this model, at this collective, were therefore probably in error, a conclusion that is also suggested by the observation that the wake profile for this model at $\theta_0 = 10°$ does not show quite the same behavior shown by those of the other models at that collective angle (Figs. 3.33d and also 3.37a).

It should be noted that this derivation of the estimates for κ did not include measurements of the swirl velocity, and hence did not account for energy lost in imparting rotational momentum to the flow due to the rearward inclination of the lift vectors on the rotor blade elements. Even though a portion of the swirl in the wake is due to the profile drag of the blades, which would not be insignificant at low Reynolds numbers, still, shrouding a rotor has the effect of increasing the induced inflow angle (hence, the tilt of the lift vector) and reducing the aerodynamic angle of attack (hence, the profile drag) of the blade elements, compared to an open

(a) Average wake velocity   (b) Induced power correction factor
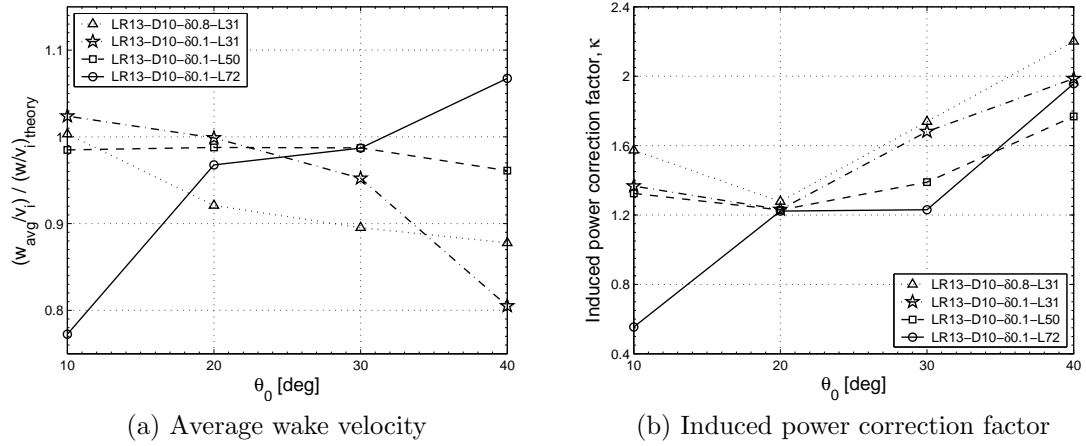
Figure 3.34: Effects of collective angle on induced power

rotor producing the same thrust (Eq. 3.1 on page 141). The true values of κ would therefore be somewhat higher than the values shown in these figures.

3.5.2   Effects of changing shroud parameter values

3.5.2.1   Blade tip clearance

Figure 3.35 shows the effect of changing blade tip clearance, δ_{tip}, on the wake profile at the diffuser exit plane of the shrouded rotors. Figures 3.35a–d show the wake profiles of the three LR13-D10-L31 models at each of four collective angles, while Figures 3.35e and 3.35f compare the exit wake profiles of the LR13-D10-L31 and LR13-D10-L72 models, at a collective of 20°, with the wake profile of the open rotor at the same collective and at the corresponding distance from the rotor plane ($z/R = 0.62$ and 1.44, respectively). It can be seen that increasing δ_{tip} causes the shrouded rotor's wake profile becomes less uniform, with increasing axial velocity deficit at the diffuser wall, and become more like that of the open rotor, with the

consequent increases in induced power losses and the induced power correction factor (Fig. 3.36b). The average wake velocity generally decreases (Fig. 3.36a), and the radial location of peak downwash moves inboard, possibly correlated with an increase in size of the tip vortex cores.

3.5.2.2   Diffuser length

Figure 3.37 shows the effect of increasing the expansion ratio by changing diffuser length, L_d, on the wake profile at the diffuser exit plane of the three LR13-D10-δ0.1 shrouded-rotor models. Figures 3.37a–d show the wake profiles of the models at each of four collective angles, while Figure 3.37e compares the exit wake profiles, at a collective of 20°, with the wake profiles of the open rotor at the same collective and at the corresponding distances from the rotor plane — $z/R = 0.62$, 1.00 and 1.44. From these figures, increasing diffuser length is seen to have two effects. The first is that the entire wake profile stretches radially outwards, corresponding to the increasing expansion of the wake. The second is that although the velocity deficit in the inner, core region of the wake increases, it gets reduced in the outer regions, at the diffuser wall. This is probably because, with the expansion of the flow, the higher-velocity flow at the mid-span locations of the wake energizes and entrains the flow at the diffuser walls. The net effect is that the induced power correction factor generally remains about the same (Fig. 3.38b). Although the peak downwash velocity decreases in magnitude, the average velocity also generally remains about the same (Fig. 3.38a). In contrast, in the case of the open rotor (Figure 3.37e),
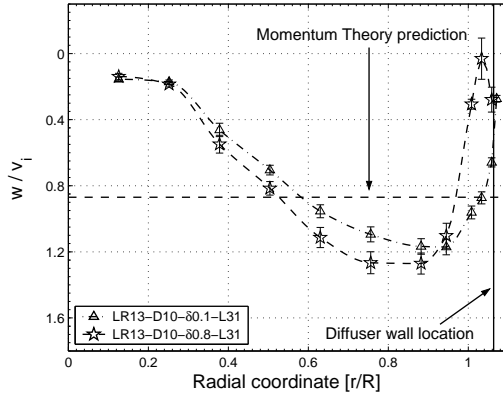
(a) Series LR13-D10-L31, $\theta_0 = 10°$
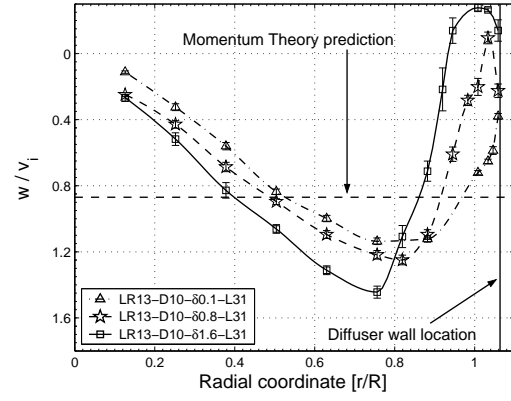
(b) Series LR13-D10-L31, $\theta_0 = 20°$
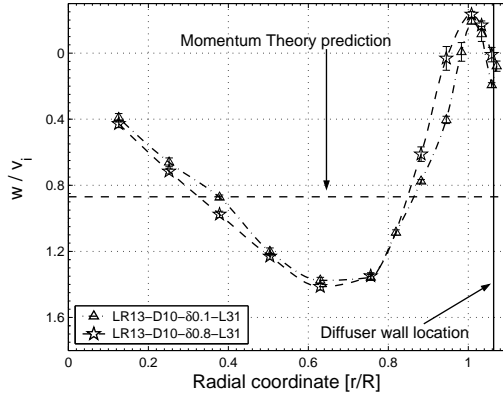
(c) Series LR13-D10-L31, $\theta_0 = 30°$
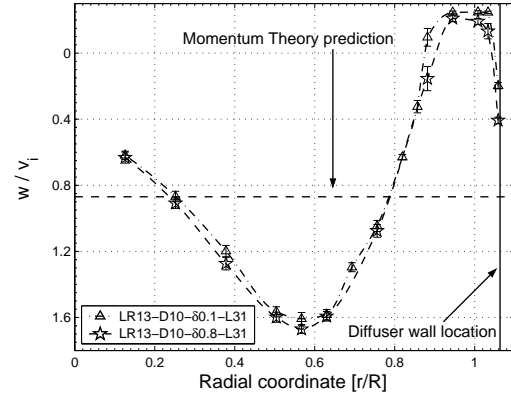
(d) Series LR13-D10-L31, $\theta_0 = 40°$
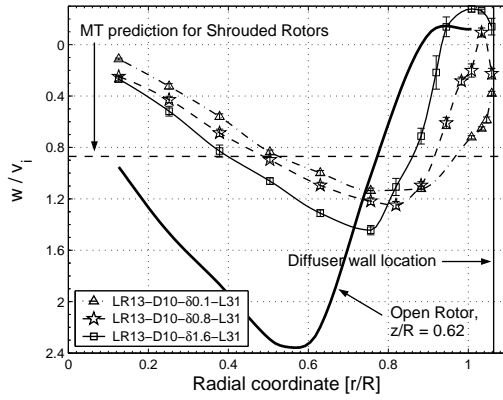
(e) Series LR13-D10-L31, $\theta_0 = 20°$, compared with open rotor
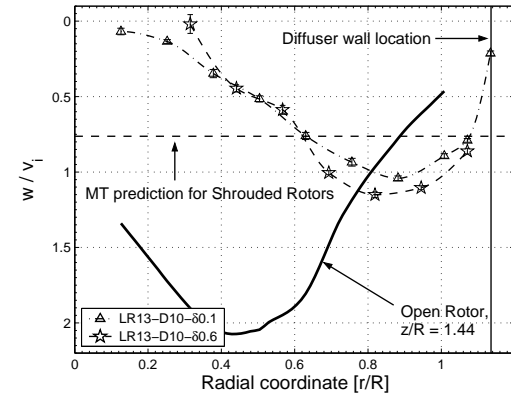
(f) Series LR13-D10-L72, $\theta_0 = 20°$, compared with open rotor

Figure 3.35: Effect of blade tip clearance on shrouded-rotor exit-plane wake profiles

(a) Average wake velocity   (b) Induced power correction factor
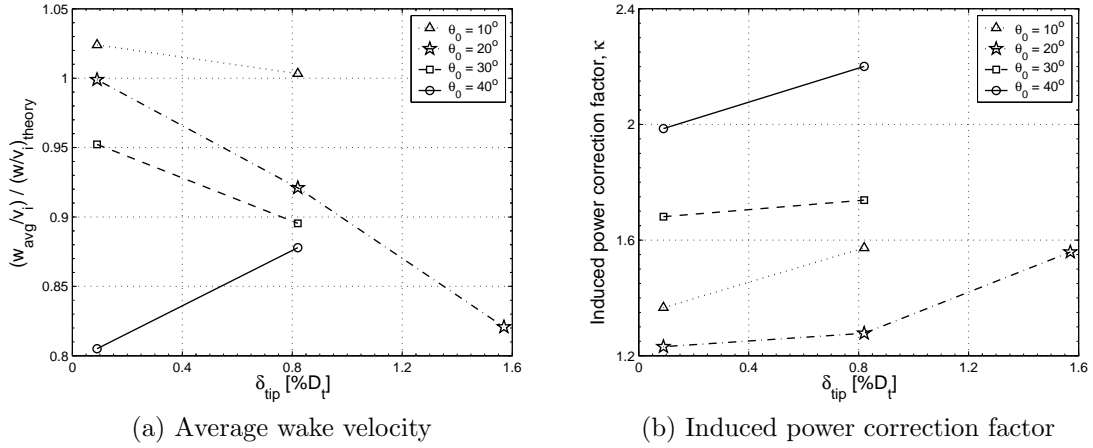
Figure 3.36: Effects of changing blade tip clearance on induced power

with increasing distance from the rotor plane, the radial location of peak downwash moves inboard, corresponding to the contraction of the wake, and while the profile also becomes more uniform in this case, it does so by the action of the higher-velocity mid-span flow entraining both the outer *and* the inner regions of the wake.
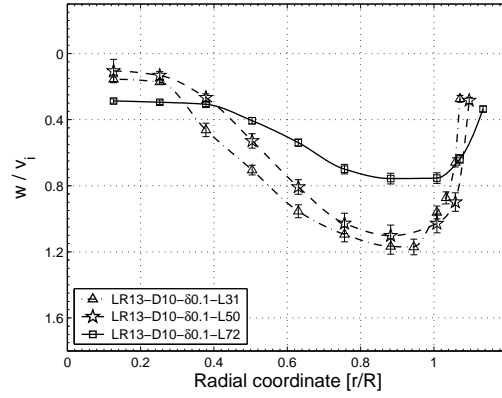
(a) Series LR13-D10-δ.1, $\theta_0 = 10°$
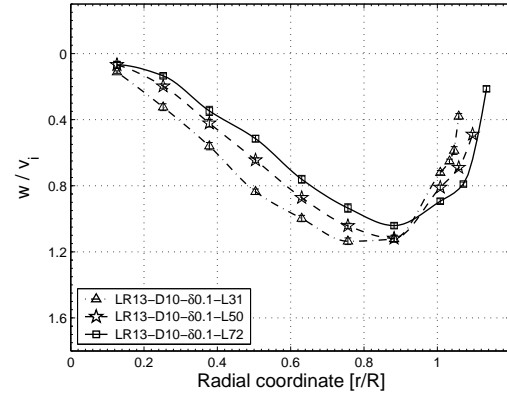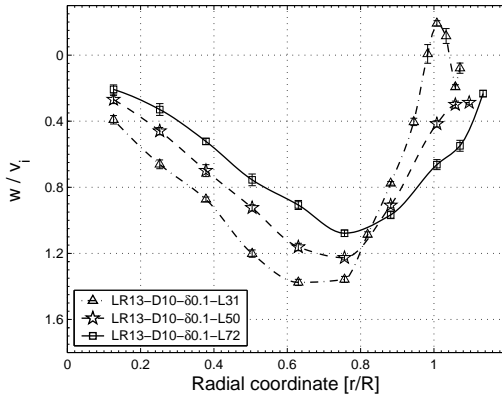
(b) Series LR13-D10-δ.1, $\theta_0 = 20°$

(c) Series LR13-D10-δ.1, $\theta_0 = 30°$
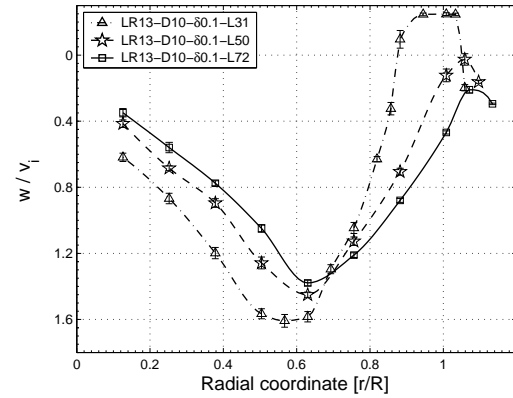
(d) Series LR13-D10-δ.1, $\theta_0 = 40°$
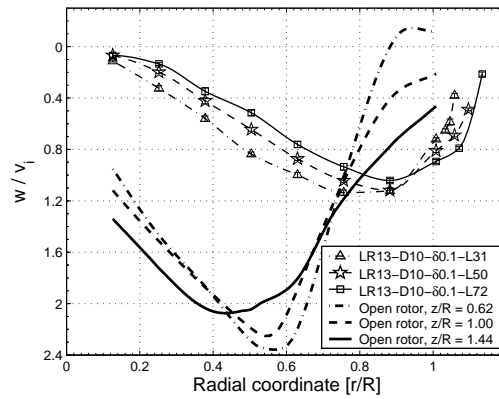
(e) Series LR13-D10-δ.1, $\theta_0 = 20°$, compared
with open rotor

Figure 3.37: Effect of diffuser length on shrouded-rotor exit-plane wake profiles

(a) Average wake velocity　　　　　(b) Induced power correction factor
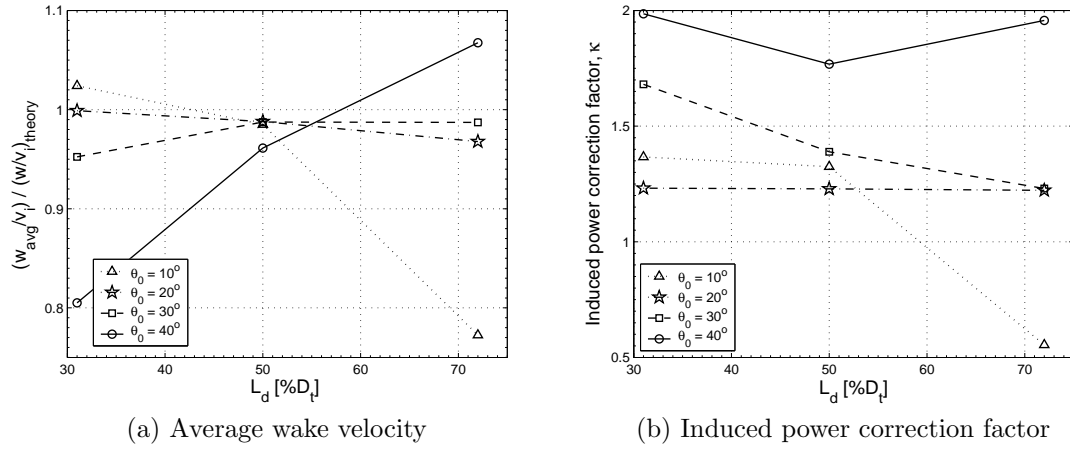
Figure 3.38: Effects of changing diffuser length on induced power

Chapter 4

Experimental Results: Wind-Tunnel Tests

4.1 Introduction

This chapter presents the measurements that were made in the translational-flight tests of the open rotor and the shrouded-rotor model LR13-D10-δ0.1-L31 at a rotor collective angle of 20°. With a shroud chord (equal to $r_{\text{lip}} + L_{\text{d}}$) of 44%$D_{\text{t}}$, this shrouded-rotor model falls under the category of what are known as "short-chord" shrouds. The data are presented in the form of the effects of changing free-stream velocity (airspeed) and angle of attack on the shroud surface pressure distribution and the on the seven performance variables: thrust, normal force, lift, drag, location of center of pressure, pitch moment and shaft power (Fig. 4.1). All quantities are presented in non-dimensional forms, either as aerodynamic coefficients or, in the case of the center-of-pressure location (x_{cp}), as normalized by the rotor radius (R). For presenting the effects of airspeed, a non-dimensional 'airspeed ratio' parameter, μ', has been used, defined as:

$$\mu' = v_\infty/\Omega R \tag{4.1}$$
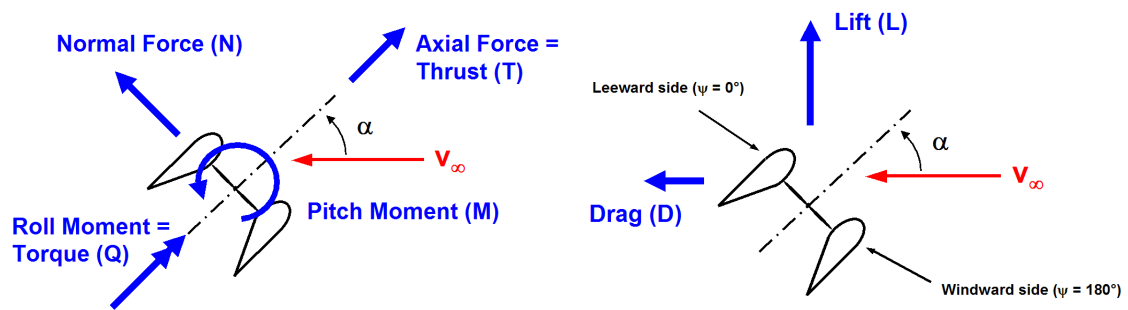
(a) Forces and moments
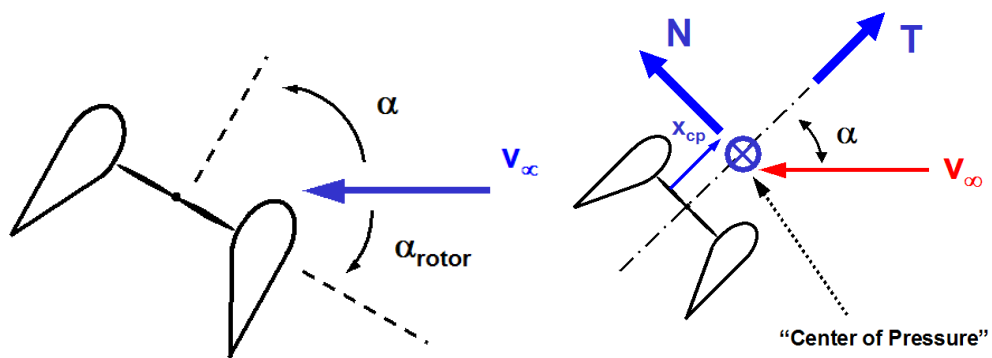
(b) Angle of attack

(c) Center of pressure

Figure 4.1: Translational flight: variable definitions

Table 4.1: Airspeed ratio (μ') values tested

Rotational speed	Blade tip speed	Wind tunnel speed		
		10 ft/s	15 ft/s	20 ft/s
2000 rpm	54.5 ft/s	0.18	0.28	0.37
3000 rpm	81.8 ft/s	0.12	0.18	0.24
4000 rpm	109.1 ft/s	0.09	0.14	0.18

This parameter differs from the conventional rotor advance ratio, μ, as follows:

$$\mu' = \mu / \cos(\alpha_{\mathrm{rotor}})$$

$$= \mu / \cos(90° - \alpha) \tag{4.2}$$

and from the conventional propeller advance ratio, J, by the constant factor $1/\pi$. At the higher angles of attack ($\alpha \approx 90°$), then, $\mu' \approx \mu$, and at $\alpha = 0°$, $\mu' = J/\pi$. The use of this parameter makes it convenient to present, on a single graph, the characteristics of the rotor at all angles of attack, from the 'propeller-mode' or climbing-flight condition ($\alpha = 0°$) to the edgewise-flight condition ($\alpha = 90°$), at all rotational speeds and airspeeds tested. In edgewise flow, the maximum value of μ' at which the models were tested was 0.37. In axial flow, the models were tested up to $\mu' = 0.28$ for the open rotor and 0.18 for the shrouded rotor, corresponding respectively to maximum propeller advance ratios of 0.88 and 0.57. Table 4.1 gives the values of μ' for each rotational speed and free-stream velocity tested.

4.2 Shroud surface pressure measurements

The pressure-distribution data are shown in Figures 4.3–4.5. The effect of changing airspeed on the pressure distributions is first shown in Figures 4.3a–d, at each of four angles of attack: 0°, 30°, 60° and 90°. These figures also include, for comparison, the pressure measurements taken on this model during the hover tests ($\mu' = 0$). The effects of changing angle of attack are then presented in Figures 4.5a–c, for each of the three airspeeds tested — 10, 15 and 20 ft/s, corresponding to airspeed ratios of 0.12, 0.18 and 0.24. In each figure, the measured values are shown by the symbols, joined by piecewise-cubic Hermite interpolating polynomials. The data for the windward side of the shroud ($\psi = 180°$) are shown on the left side of each figure, and the data for the leeward side ($\psi = 0°$) on the right side. The data are plotted in coefficient form (C_p) as functions of the non-dimensional distance coordinate, s, along the shroud surface. The s-coordinate system used in these plots is the same one used for the pressure-distribution plots in Chapter 3, and is shown again for convenience in Figure 4.2. Its origin lies at the blade passage region, where the inlet and diffuser surfaces meet. The coordinate s is positive for points below the rotor (the diffuser), and negative for points above the rotor (the inlet). Surface distances in the diffuser are normalized by the diffuser slant length, S, and in the inlet by the inlet lip circumference, $\pi \cdot r_{\text{lip}}$. Therefore, $s = 0$ at the rotor plane, $s = +1$ at the diffuser exit plane, and $s = -1$ at the outer edge of the inlet lip. The angular coordinate, θ_{lip}, is also convenient for locating points on the surface of the shroud inlet; $\theta_{\text{lip}} = 0°$ corresponds to the rotor plane and $\theta_{\text{lip}} = 180°$ corresponds to
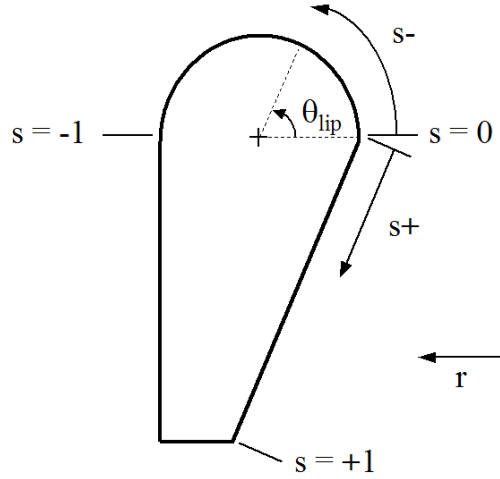
Figure 4.2: Coordinate system for pressure distribution plots

the outer edge of the inlet lip.

For better visualization of the actual shape of the pressure distributions, the data from Figures 4.3a–d are also plotted diagrammatically in a two-dimensional ('2-D') representation, superimposed on a sectional view of the shroud, as viewed from the $\psi = 270°$ azimuth, in Figures 4.4a–d. In these 2-D plots, the 'empty' symbols represent pressures lower than ambient atmospheric (suction), while the solid (filled) symbols represent pressures greater than ambient (over-pressure).

Figures 4.3a and 4.4a show the surface pressure measurements in the axial-flight condition ($\alpha = 0°$). Figure 4.3a shows the data plotted versus the non-dimensional surface coordinate s, while Figure 4.4a shows the two-dimensional representation of the pressure distributions. As expected for this flight condition, the pressure distributions are symmetric between $\psi = 180°$ and $\psi = 0°$. In hover ($\mu' = 0$), suction pressures ($C_p < 0$) are seen over the entire inner surface of the shroud, with the flow clearly expanding completely to ambient atmospheric pressure at the
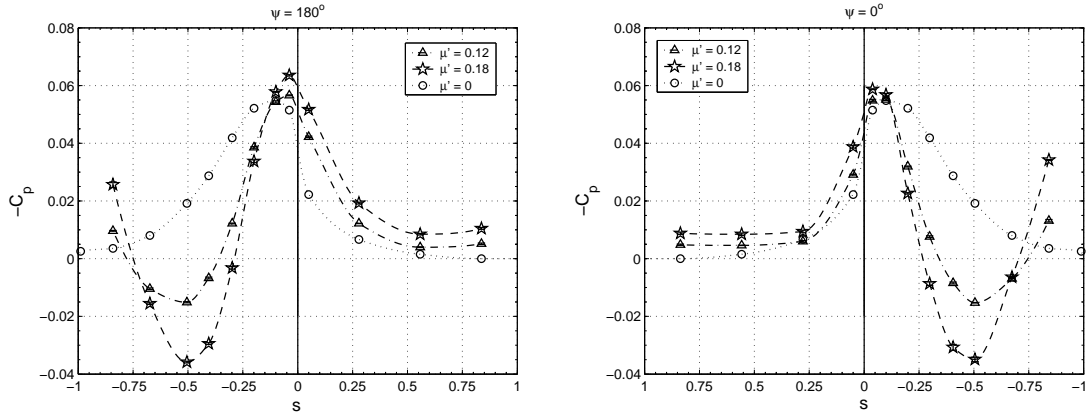
(a) $\alpha = 0°$(axial flow)
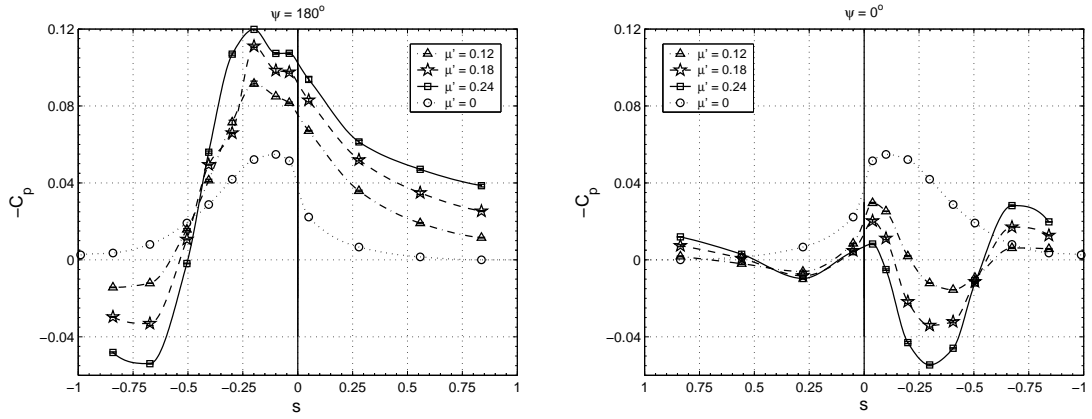
(b) $\alpha = 30°$
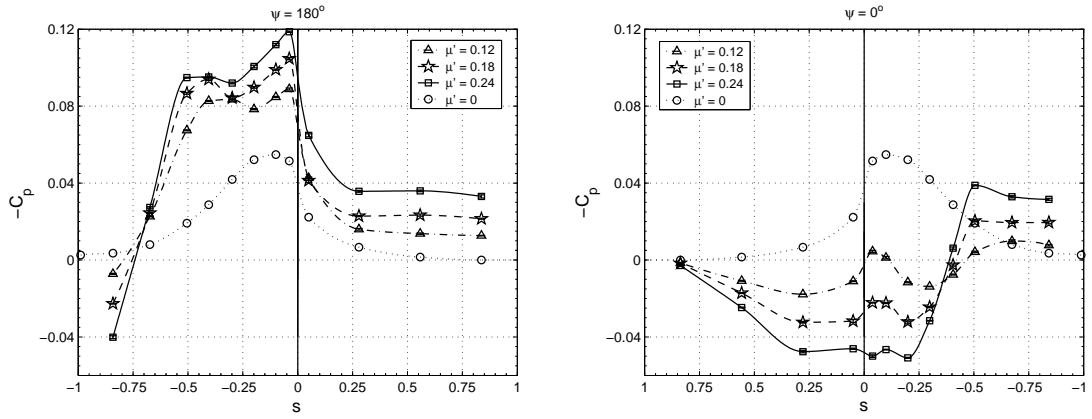
(c) $\alpha = 60°$

Figure 4.3: Effects of changing airspeed on pressure distributions, at fixed angle of attack
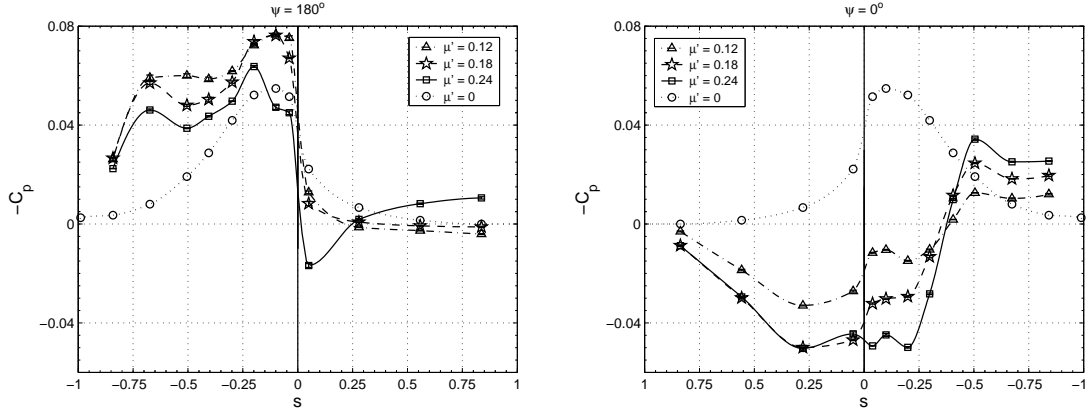
(d) $\alpha = 90°$ (edgewise flow)

Figure 4.3: Effects of changing airspeed on pressure distributions, at fixed angle of attack

diffuser exit plane ($s = 1$). The greatest suction is seen just slightly upstream of the blade passage region, and this is due to high-velocity air leaking through the gap between the blade tips and the shroud wall, from the higher-pressure region below the rotor to above it. The suction pressures over the shroud inlet are greater than those on the diffuser wall, and are the reason for the significant thrust contribution of the shroud in hovering flight.

In translational flight, due to the impingement of the free-stream air on the shroud, stagnation points are formed on the most forward portion of the shroud inlet ($s = -0.5$, $\theta_{\text{lip}} = 90°$), which faces directly into the oncoming flow. The stagnation points, which separate the internal and external flows over the shroud, lie at the center of regions of pressure greater than ambient. These over-pressure regions become stronger and larger as airspeed increases, and replace the suction pressures seen over the forward portions of inlet in hover. As will be seen in the performance data, this results in a severe reduction in the thrust produced by the
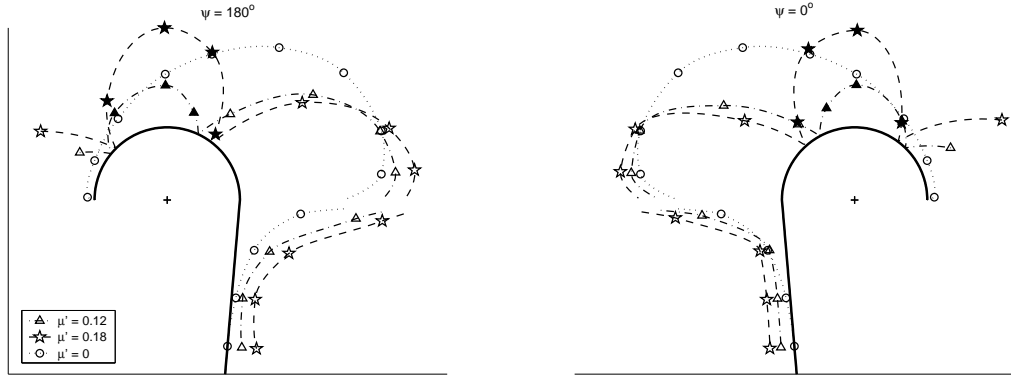
(a) $\alpha = 0°$(axial flow)
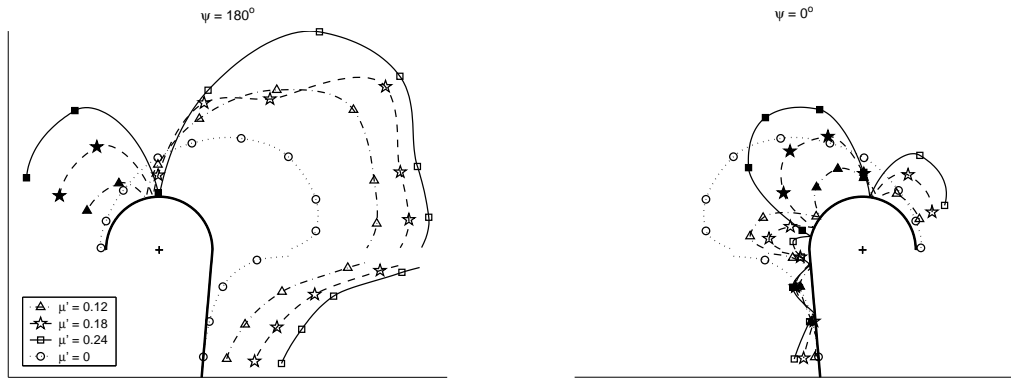
(b) $\alpha = 30°$
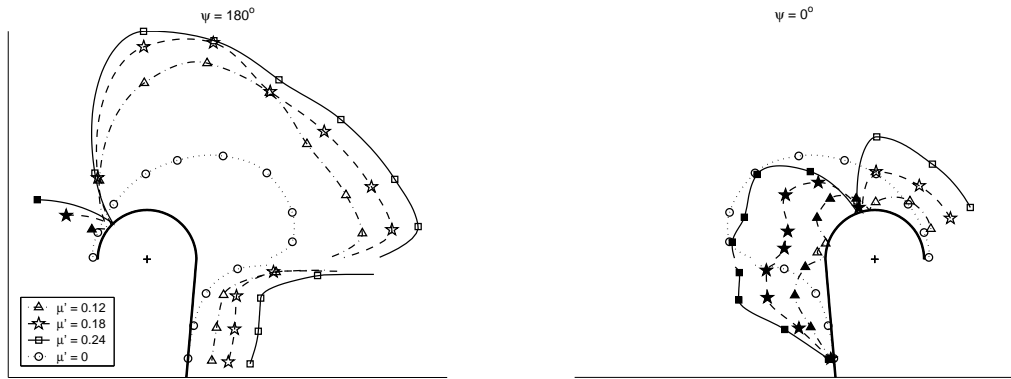
(c) $\alpha = 60°$

Figure 4.4: Effects of changing airspeed on pressure distributions, at fixed angle of attack: 2-D depictions

226
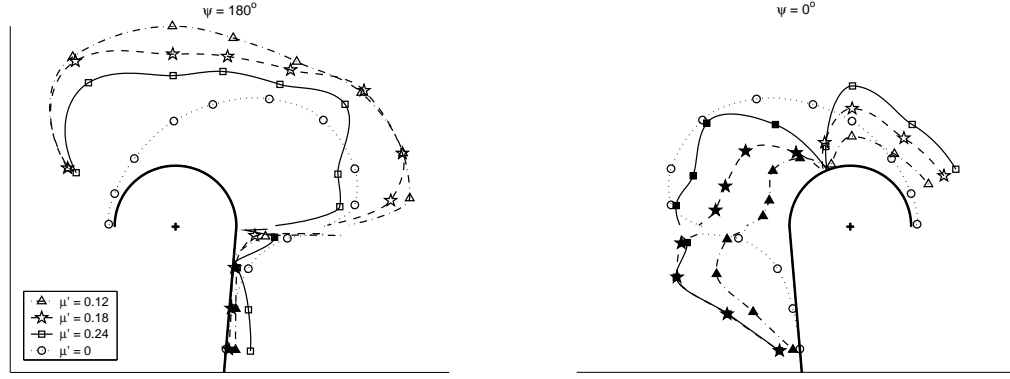
(d) $\alpha = 90°$ (edgewise flow)

Figure 4.4: Effects of changing airspeed on pressure distributions, at fixed angle of attack: 2-D depictions

shroud (Figure 4.6a). Suction pressures are still seen near the blade passage region, in the diffuser and on the outermost parts of the shroud inlet ($s < -0.7$) where the external flow accelerates past the outer surface of the shroud; however, these surfaces are inclined with their normal vectors pointing primarily radially inwards or outwards, and do not contribute much to the vehicle thrust.

As in hover, maximum suction is seen just above the blade passage region, at $s \approx -0.05$ ($\theta_{\text{lip}} \approx 10°$). With increasing airspeed, both suction and over-pressures increase in magnitude, and the location of the over-pressure region on the inlet moves slightly inwards. At the diffuser exit plane, the pressure approaches the ambient atmospheric value, but, unlike in hover, does not actually reach it. The difference increases with increasing airspeed, and indicates that further expansion of the rotor downwash occurs beyond the diffuser exit plane. Note that the assumption of complete expansion of the flow at the diffuser exit plane is the cornerstone of the simple Momentum Theory model for shrouded-rotor analysis. For short-chord
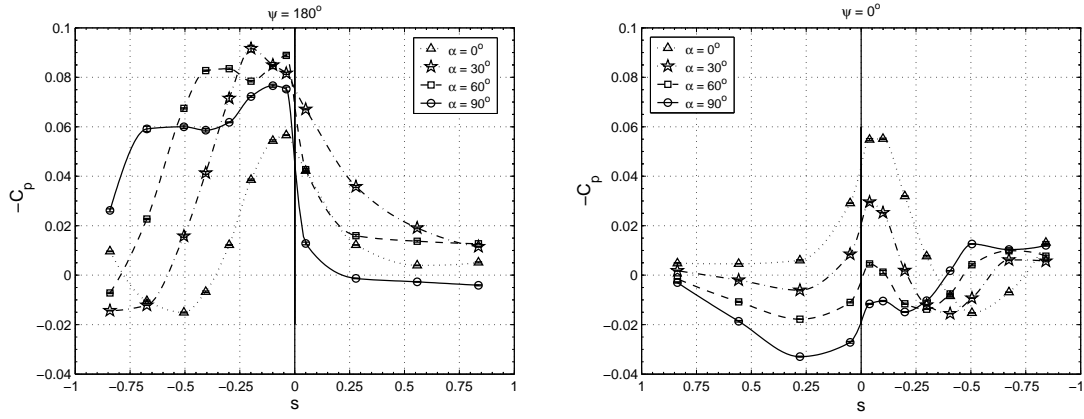
(a) $v_\infty = 10$ ft/s ($\mu' = 0.12$)
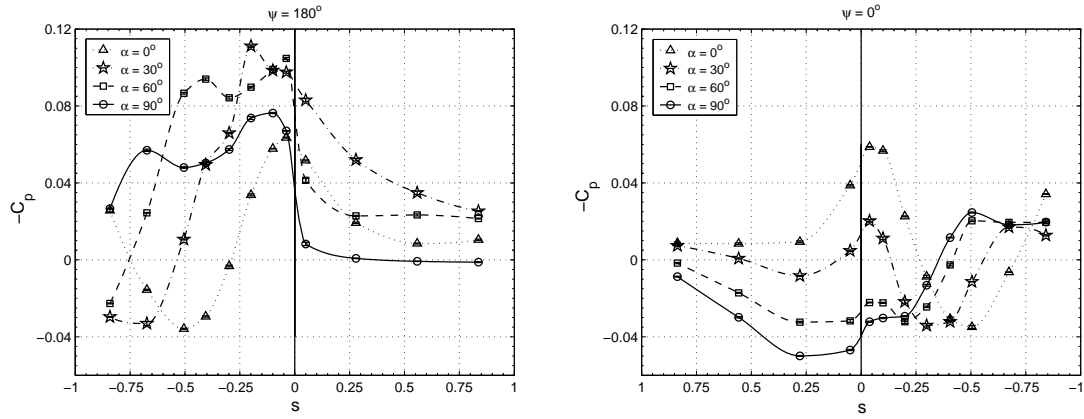
(b) $v_\infty = 15$ ft/s ($\mu' = 0.18$)
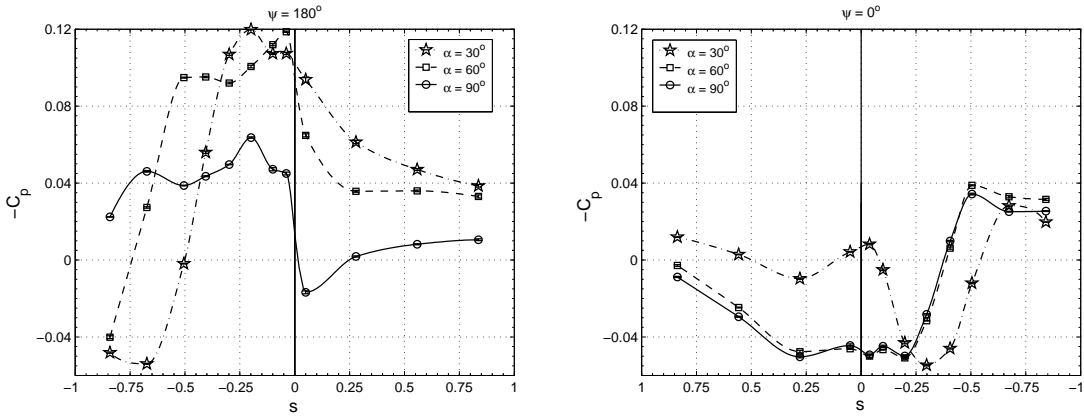
(c) $v_\infty = 20$ ft/s ($\mu' = 0.24$)

Figure 4.5: Effects of changing angle of attack on pressure distributions, at fixed airspeed

shrouds like the one tested in this investigation, the measurements show that such an assumption may not be valid.

When the angle of attack is increased to 30° (Figures 4.3b, 4.4b), the region of suction pressure expands on the windward side of the shroud ($\psi = 180°$) and shrinks on the downwind side ($\psi = 0°$), on both the inlet and diffuser surfaces. The stagnation points on the inlet lie at approximately $s = -0.67$ to -0.85 ($\theta_{lip} = 120°–153°$) on the windward side, and at approximately at $s = -0.3$ to -0.4 ($\theta_{lip} = 54°–72°$), which coincides with the direction of the oncoming free-stream flow. The stagnation points move inwards as the airspeed increases, indicating a decrease in the capture area of the rotor. The suction pressures on the windward side of the inlet are seen to be much greater than those in hover; this is probably due to the increased turning of the flow from the free-stream direction to the rotor axial direction. On the downwind side, suction is only seen in small regions near the blade tips, over the outermost portion of the inlet, and near the diffuser exit. Over-pressures are seen in the diffuser just below the rotor disk due to the pressure jump through the rotor. The extreme asymmetry of the pressure distribution, compared to the hover condition, results in a strong nose-up pitch moment on the shrouded rotor, as will be seen later when the performance measurements are discussed (Figures 4.11d, e, g). As in the axial-flow case, the magnitudes of the suction and over-pressures increase with increasing airspeed. At the diffuser exit plane, the flow approaches ambient pressure levels more closely on the downwind surface of the diffuser, while remaining considerably lower on the windward side. In general, suction pressures are seen on the surfaces of the shroud that are oriented away from the oncoming flow, while

overpressures are seen on the surfaces facing the flow. Similar pressure distributions would be expected on the outer surfaces of the shroud, where measurements were not made. This aspect of the pressure dissymmetry would manifest itself as a force on the vehicle perpendicular to the rotor axis (Figures 4.7c, e).

As the angle of attack is increased to 60° (Figures 4.3c, 4.4c) and 90° (edgewise flow, Figures 4.3d and 4.4d), the trends of increasing suction on the windward side of the shroud and increasing over-pressure on the downwind side are seen to continue. At these angles, no stagnation point is seen to lie within the range of pressure taps on the windward side. On the downwind side, the stagnation point lies between $s = -0.2$ and -0.3 ($\theta_{\text{lip}} = 36°$–$54°$) at $\alpha = 60°$, and near $s = -0.2$ at $\alpha = 90°$. At $\alpha = 90°$, suction pressures cover the entire windward surface of the inlet, just like in hover; however, the magnitude of these suction pressures are now much greater, and are spread more evenly over the entire surface instead of being concentrated near the rotor disk. Although large over-pressures are seen on the downwind side of the inlet, the net effect is to increase the thrust produced by the shroud over that produced in hover. Once again, this will be clearly seen in the performance data (Figure 4.6b). From $\alpha = 60°$ to $90°$, the trend of increasing magnitude in the surface pressures with increasing airspeed is seen to reverse over the windward side of the shroud inlet. Over the remaining regions of the shroud surface, however, the trend remains consistent.

The effect of changing angle of attack on the pressure distributions is more clearly illustrated in Figures 4.5a–c, at each of the three airspeeds tested. In each of the figures, the same trends are seen: with increasing angle of attack, the region

of suction pressures on the windward side of the inlet expands, while shrinking on the inner portion of the downwind side. The maximum suction on the windward side occurs between $\alpha = 30°$ and $60°$, and thereafter decreases in magnitude. In the diffuser, pressure increases with increasing angle of attack (i.e., decreasing suction or increasing over-pressure). On the windward side of the diffuser, the internal flow recovers most closely to ambient pressure at $\alpha = 90°$, while on the downwind side, the departure from ambient levels at the diffuser exit plane is approximately the same for all angles of attack. At $\psi = 180°$, the magnitude of the pressure jump through the rotor disk seems to be unaffected by the magnitude of the suction pressure above the rotor. At $\psi = 0°$, however, the magnitude of the pressure jump decreases with increasing airspeed and with increasing α, i.e., with increasing over-pressure above the rotor.

4.3   Performance measurements

The performance data are plotted in Figures 4.6–4.12 as functions of the airspeed ratio, μ', at constant angle of attack, for analyzing the effects of free-stream velocity, and as functions of α at constant airspeed ratio for analyzing the effects of angle of attack. In all the graphs, the data for 4000 rpm are shown by the solid (filled) symbols, those for 3000 rpm by the shaded-gray symbols, and those for 2000 rpm by the 'empty' symbols. When the coefficients are plotted versus μ', it was seen that, for a given angle of attack, the values are nearly independent of the rotor rotational speed, and vary close to quadratically or cubically with the airspeed ratio.

Therefore, to more easily discern the trends followed by the variables with changing airspeed, polynomial fits have been applied to the data for each angle of attack, and these are shown in the figures superimposed on the measured values. For the force coefficients (thrust, normal force, lift and drag), quadratic polynomials were found to fit the data well, while for the power coefficient, cubic polynomials gave the best fit. For the pitch moment coefficient, quadratic polynomials fit the data well at low angles of attack (Figures 4.11b, d). However, at the highest angles of attack ($\alpha \geq 75°$), cubic polynomials were required to match the data well (Figures 4.11c, e). For the location of the center of pressure, cubic polynomials generally gave the best fit (Figures 4.10b–c). As would be expected, the polynomial fits diverge widely beyond the limits of the measured data, in most cases, and cannot be considered as reliable estimates for extrapolation. When the coefficients are plotted versus α, no such polynomial variation can be assumed, so the measured values are shown connected by straight-line segments.

For each of the seven performance variables, the discussion of the measurements follows the following order: the effect of increasing airspeed on the open and shrouded rotors is compared, in the climb or axial-flow condition ($\alpha = 0°$) and the edgewise-flow condition ($\alpha = 90°$), then the effects of increasing airspeed at the other, intermediate angles of attack are discussed, and finally the effects of changing angle of attack at constant airspeed. In the figures showing the data for the shrouded rotor, the lines showing the trends for the open rotor have been superimposed for comparison of the shrouded and unshrouded cases.

4.3.1 Thrust

Figure 4.6a shows the thrust of the open and shrouded rotors in the axial-flow condition ($\alpha = 0°$). With increasing airspeed, the thrust of the open rotor decreases, as would be expected because of the increasing inflow while the rotor remains at fixed pitch, thereby reducing the blade section angles of attack. The shrouded rotor produces greater thrust than the open rotor in hover, but exhibits a much faster drop-off in thrust with increasing airspeed. By an airspeed ratio of about 0.075 ($J = 0.24$), the shrouded rotor's thrust has dropped below that of the open rotor. As was seen from the pressure data, a significant contribution to this reduction in thrust comes from the collapse of the suction forces on the shroud inlet and the increase in over-pressure with increasing airspeed. Essentially, the shroud behaves like a bluff body in the flow. As can be seen from Figures 2.1 (p. 108) and 2.5 (p. 119), the shroud model tested has a section profile that is not a streamlined airfoil-like shape. Flow separation off the trailing 'edge' of the diffuser may be causing substantial base drag on the model. This loss of shroud thrust, and the actual creation of additional drag by the shroud, is the most probably cause for the sharper reduction in thrust of the shrouded rotor, as compared to the open rotor.

Figure 4.6b shows the open and shrouded rotors compared in the edgewise-flow condition ($\alpha = 90°$). As airspeed increases, the in-plane component of the local velocity at the blades of the open rotor increases, leading to an increase in thrust. The thrust of the shrouded rotor also increases with increasing μ', but at a seemingly higher rate than that of the open rotor, so that the difference between the open-
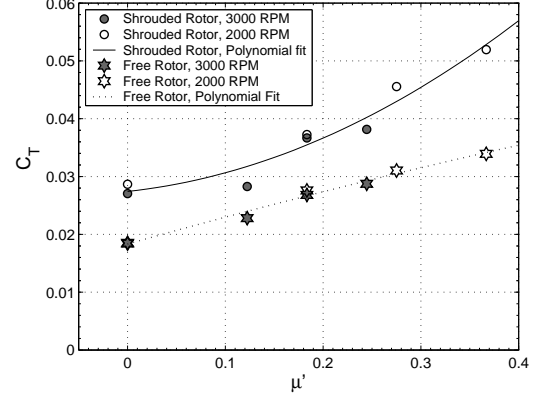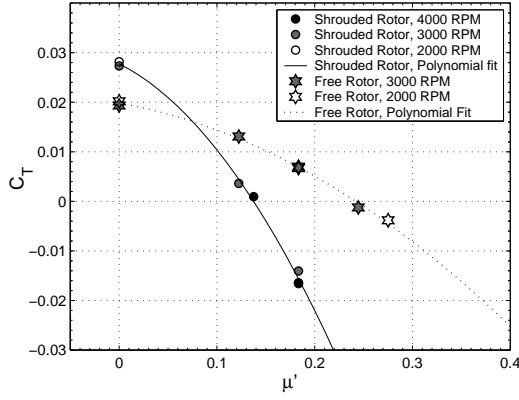
(a) Variation with airspeed: axial flow ($\alpha = 0°$) (b) Variation with airspeed: edgewise flow ($\alpha = 90°$)
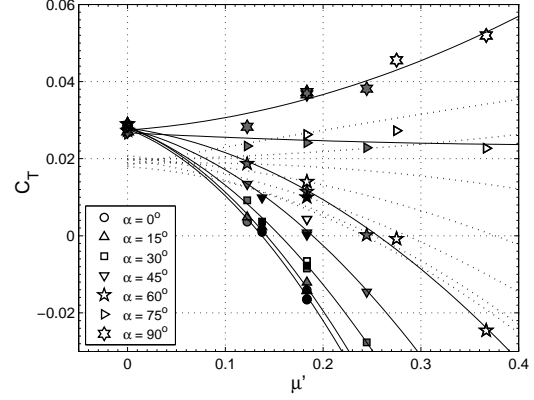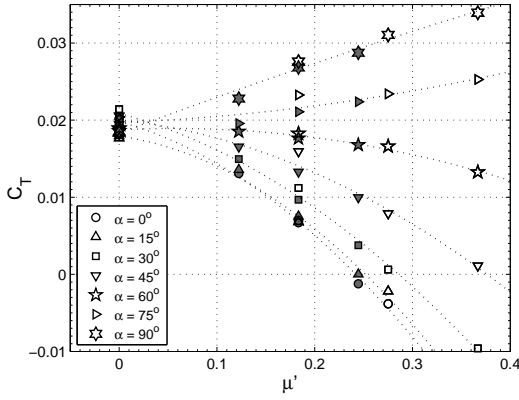
(c) Variation with airspeed: open rotor

(d) Variation with airspeed: shrouded rotor
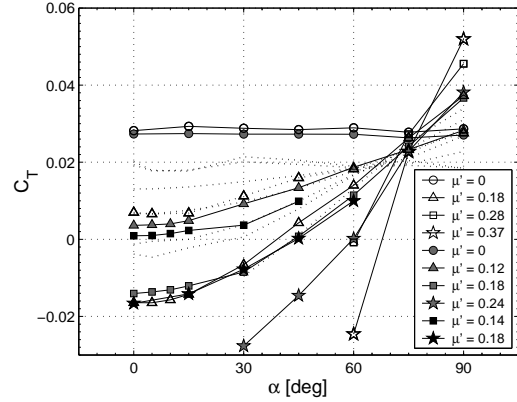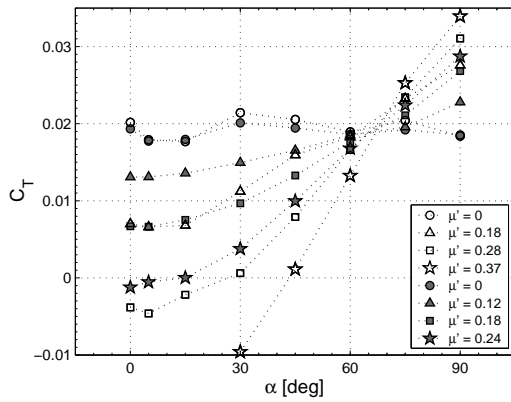
(e) Variation with angle of attack: open rotor

(f) Variation with angle of attack: shrouded rotor

Figure 4.6: Translational flight: variations in thrust

and shrouded-rotor thrusts actually increases with increasing airspeed ratio. This, as was mentioned earlier, is probably because of the greatly increased suction on the windward side of the shroud inlet.

Figure 4.6c shows the variation of thrust with airspeed for the open rotor at all angles of attack. It is seen that the change from decreasing thrust (with increasing μ') to increasing thrust occurs at an angle of attack between 60° and 75°. Figure 4.6d presents the data for the shrouded rotor in the same way, with the trendlines for the open rotor from Figure 4.6c superimposed for comparison. For the shrouded rotor, the change from decreasing to increasing thrust occurs at an angle of attack between 75° and 90°. This implies that at a certain value of α, which lies between 60° and 75° for the open rotor, and near 75° for the shrouded rotor, the thrust coefficient is independent of airspeed; this is confirmed in Figures 4.6e and 4.6f, which plot the thrust data for the open and shrouded rotors versus angle of attack, for the different airspeed ratios tested. These figures also illustrate how the thrust decreases as the rotor pitches forward from hover into the wind, with a more rapid drop-off as the speed of the relative wind increases. The shrouded rotor is seen to experience a more rapid drop-off than the open rotor, at the same airspeed ratio.

4.3.2   Normal force

The normal force is the force perpendicular to the thrust axis, in the body frame of reference. Figure 4.7a shows the effect of increasing airspeed on the normal force coefficient of the open and shrouded rotors in the edgewise-flow condition. For

both configurations, C_N increases with increasing airspeed, but much more so for the shrouded rotor. This is because of the substantial bluff-body drag of the shroud when broadside to the oncoming flow, and also due to the 'momentum drag' that arises from the turning of the flow from the free-stream direction to the rotor axial direction [125].

Figures 4.7b and 4.7c show the variation in C_N with μ' for the open and shrouded rotors at the other angles of attack, and Figures 4.7d and 4.7e cross-plot the data as functions of α for different airspeed ratios. At $\alpha = 0°$ (axial flight), the normal force is zero. It increases with increasing angle of attack, substantially more for the shrouded rotor than for the open rotor, before reaching a maximum at around $\alpha = 75°$ for the open rotor, and between $60°$ and $75°$ for the shrouded rotor, before decreasing again at $\alpha = 90°$ (edgewise flow). In general, the effect of changing α is more pronounced at higher μ', and for the shrouded rotor as compared to the open one.

4.3.3   Lift

Equation 2.1 (p. 118) shows that at low α, the lift coefficient is more greatly influenced by the variations in C_N, while at high α it is more strongly affected by the variations in C_T. At $\alpha = 0°$ (axial flight), $C_L = C_N = 0$, while at $\alpha = 90°$ (edgewise flow), $C_L = C_T$, and hence the variations of C_L with airspeed for the open and shrouded rotors are given by Figure 4.6b.

For the other angles of attack, Figures 4.8a and 4.8b show that, for both the
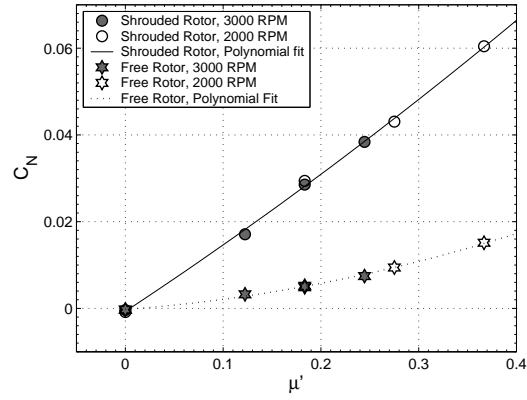
(a) Variation with airspeed: edgewise flow ($\alpha = 90°$)
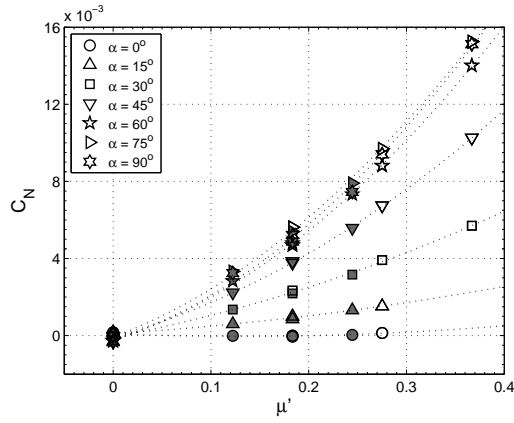
(b) Variation with airspeed: open rotor
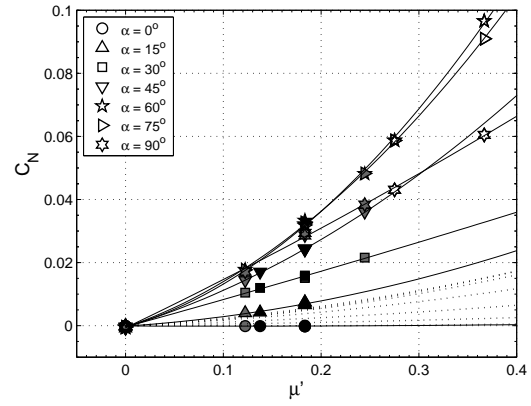
(c) Variation with airspeed: shrouded rotor

(d) Variation with angle of attack: open rotor
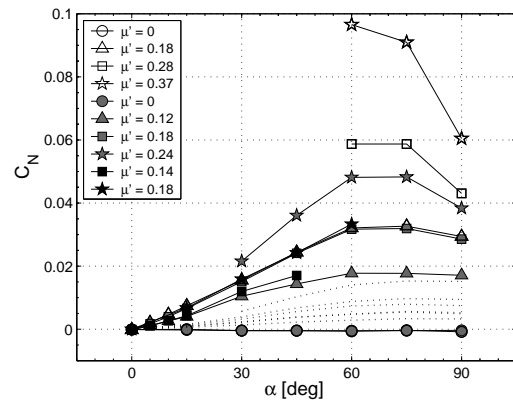
(e) Variation with angle of attack: shrouded rotor

Figure 4.7: Translational flight: variations in normal force
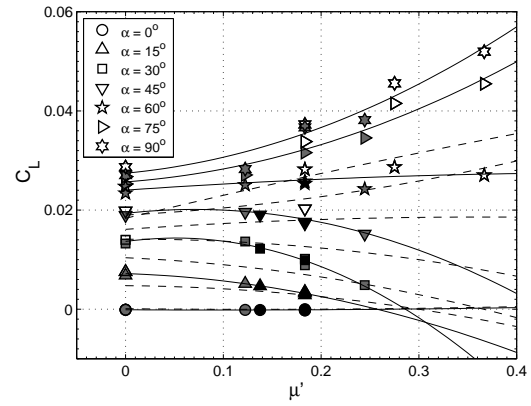
237

(a) Variation with airspeed: open rotor

(b) Variation with airspeed: shrouded rotor
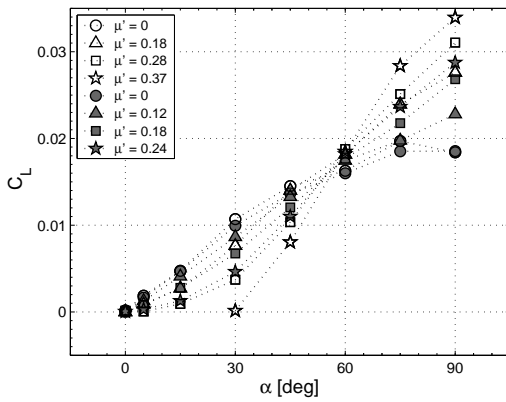
(c) Variation with angle of attack: open rotor
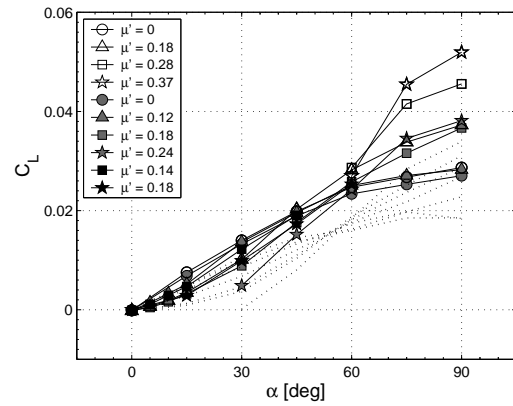
(d) Variation with angle of attack: shrouded rotor

Figure 4.8: Translational flight: variations in lift

shrouded and open rotors, C_L decreases with increasing μ' for $\alpha \leq 45°$, and increases with increasing μ' for $\alpha \geq 60°$. Figures 4.8c and 4.8d show that lift increases with increasing α at fixed airspeed, with more rapid rises as the airspeed is increased. At any given airspeed and angle of attack, the shrouded rotor produces more lift than the open rotor.

4.3.4   Drag

At $\alpha = 0°$ (axial flight), $C_D = $ -C_T, and the variations of drag coefficient with airspeed for the open and shrouded rotors can be inferred from Figure 4.6a. In climb, the shrouded rotor initially has lower drag because of its greater thrust, but as airspeed increases, its drag becomes far greater than that of the open rotor. At $\alpha = 90°$ (edgewise flow), $C_D = C_N$, and the comparison of the two configurations is given by Figure 4.7a. Figures 4.9b and 4.9d show that, at almost all flight conditions, the drag of the shrouded rotor is much higher than that of the open rotor.

Figures 4.9a and 4.9b show that, for both the open and shrouded rotors, C_D increases with increasing μ', more rapidly for the shrouded rotor, and also more rapidly as α is reduced. For the open rotor, this results in the minimum C_D for a given airspeed occurring at $\alpha = 0°$ for low μ', but at higher α for higher μ' (Figure 4.9c). For the shrouded rotor, at high α and high μ', the drag behavior is seen to change, from increasing with increasing α to decreasing with increasing α (Figure 4.9d). Although such behavior is unexpected for a shrouded rotor, wind-tunnel tests on annular airfoils [26, 55] have shown a similar maximum in drag
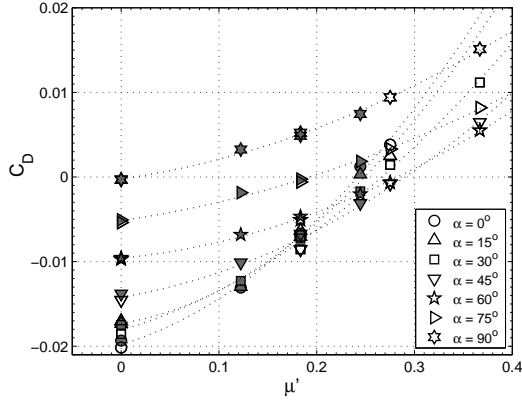
(a) Variation with airspeed: open rotor
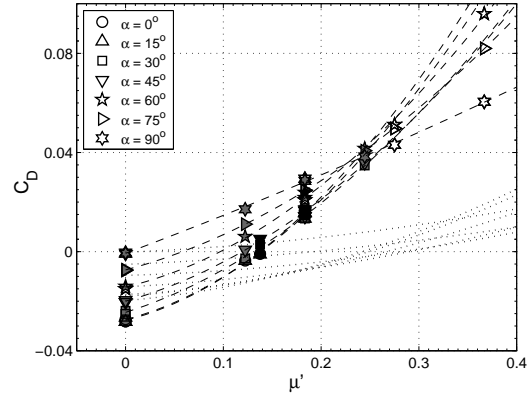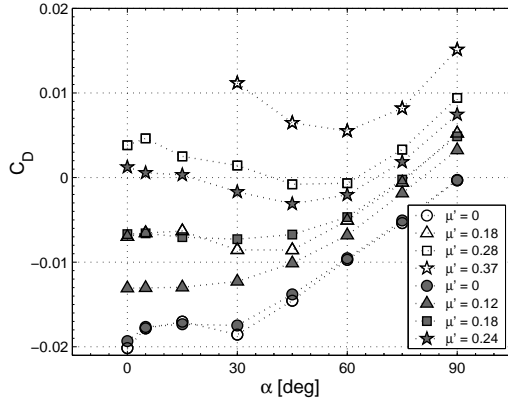
(b) Variation with airspeed: shrouded rotor

(c) Variation with angle of attack: open rotor

(d) Variation with angle of attack: shrouded rotor

Figure 4.9: Translational flight: variations in drag

coefficient at an angle of attack between 55° and 75° followed by a drop-off towards higher values of α. This suggests that the thrust of the model used in these tests might have been low enough that the annular-airfoil behavior of the shroud itself could be seen at the higher angles of attack.

4.3.5   Location of center of pressure

Figure 4.10a shows that, in the edgewise flow condition ($\alpha = 90°$), the center of pressure moves from above the rotor disk ($x_{\text{cp}}> 0$) to below it ($x_{\text{cp}}< 0$) with increasing airspeed. This, as is explained in Reference [125], is due to the greater increase in bluff-body drag, which scales with the square of the free-stream velocity, compared to the momentum drag, which increases linearly with v_∞. Figure 4.10a also shows that, at any given airspeed, the center of pressure of the shrouded rotor lies about $0.75R$ further above the corresponding location for the open rotor.

The decrease in x_{cp} with increasing airspeed is also seen at the other angles of attack, for both the open rotor (Figures 4.10b, c) and the shrouded rotor (Figures 4.10d, e). At fixed μ', with increasing α, x_{cp} shows a tendency to move slightly downstream for the open rotor, up to $\alpha \approx 30°$, before moving upstream again (Figure 4.10f). For all but the lowest airspeed ratios, the center of pressure lies below the rotor disk, which would lead to a nose-down pitch moment for the open rotor. For the shrouded rotor (Figure 4.10g), the center of pressure almost always lies above the plane of the rotor disk, leading to a nose-up pitch moment, and always moves upstream with increasing α.
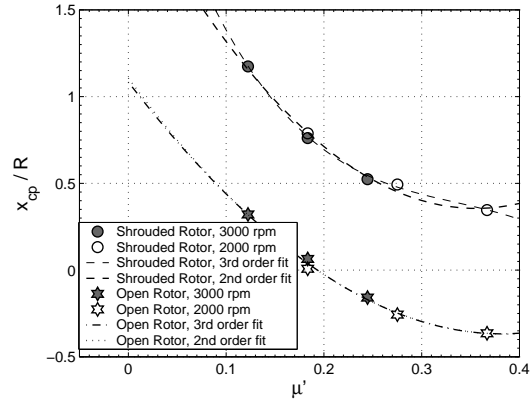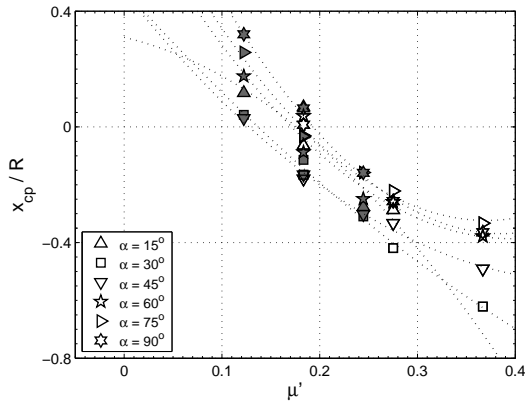
(a) Variation with airspeed: edgewise flow ($\alpha = 90°$)

(b) Variation with airspeed: open rotor, 2nd-order fit
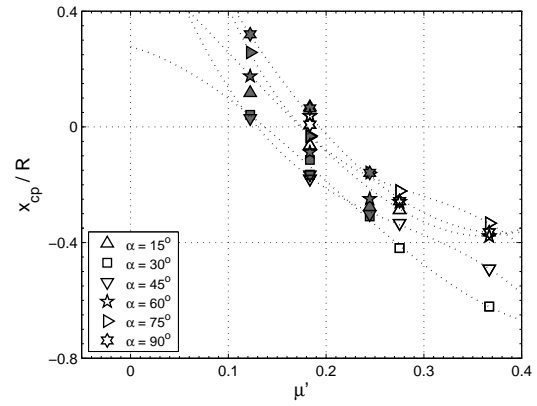
(c) Variation with airspeed: open rotor, 3rd-order fit
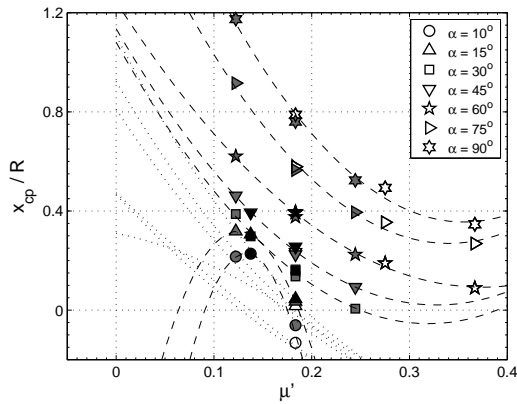
(d) Variation with airspeed: shrouded rotor, 2nd-order fit
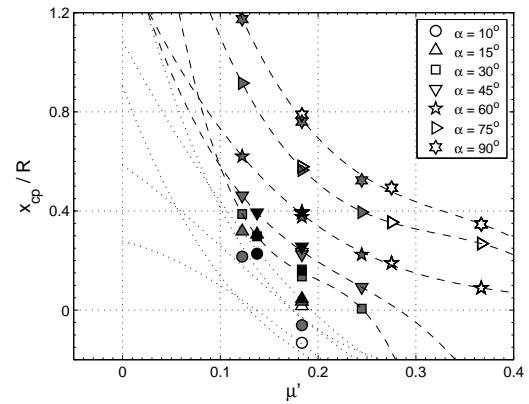
(e) Variation with airspeed: shrouded rotor, 3rd-order fit

Figure 4.10: Translational flight: variations in location of center of pressure

242

(f) Variation with angle of attack: open rotor

(g) Variation with angle of attack: shrouded rotor
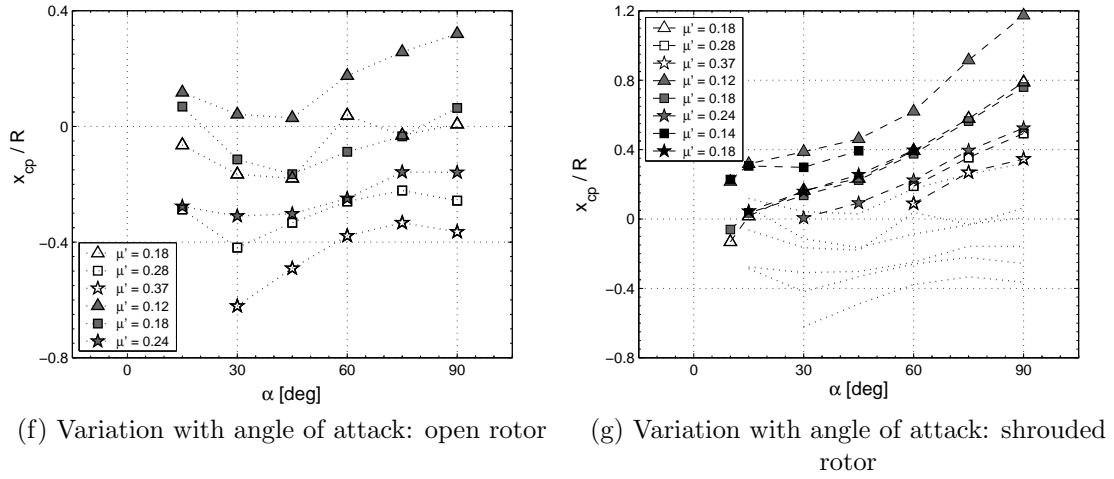
Figure 4.10: Translational flight: variations in location of center of pressure

4.3.6 Pitch moment

The pitch moment, calculated at the rotor hub, is the product of the normal force and the distance of the center of pressure from the plane of the rotor disk. Figure 4.11a compares the effect of increasing airspeed on C_M for the open and shrouded rotors, in the edgewise flow condition (in axial flow, $C_M = C_N = 0$). For the open rotor, as airspeed increases, there is initially a slight nose-up moment ($C_M > 0$), which eventually decreases and becomes a strong nose-down moment ($C_M < 0$). This is because, at fixed α, C_N increases with μ' while $x_{\rm cp}$ decreases from positive values to increasingly negative ones (Figures 26, 39), so the maximum product lies at some intermediate value of μ'. For the shrouded rotor, on the other hand, the increase in C_N is roughly matched by the decrease in $x_{\rm cp}$, which remains positive, so C_M rapidly increases to large positive values and remains roughly steady there as μ' is increased further. This very large nose-up pitch moment is what makes it difficult for a shrouded rotor to pitch forward into the wind to maintain hovering

243

position in a gust, and also to maintain a certain vehicle attitude to provide the required thrust for forward flight.

For the other angles of attack, Figures 4.11b–e show the variation in C_M with μ' for the open and shrouded rotors. For the open rotor, as α decreases, the initial nose-up moment becomes less strong, and C_M remains near zero for longer before becoming negative at higher airspeed ratios (Figures 4.11b, c). For the shrouded rotor, too, as α decreases, the maximum nose-up moment becomes less, and C_M starts to decrease back towards zero as μ' increases (Figures 4.11d, e).

At constant μ', C_M for the open rotor becomes increasingly negative with increasing α, at higher values of μ', but at lower μ' this trend starts to reverse and the pitch moment becomes nose-up again (Figure 4.11f). Equivalently, when the rotor in hover experiences a side-gust, at low gust velocities it will experience a small nose-up moment, while at high gust velocities, it will experience a large nose-down moment, which becomes less strong as the rotor pitches into the wind and α decreases. For the shrouded rotor (Figure 4.11g), C_M is seen to increase strongly with increasing α.

4.3.7 Power

Figure 4.12a compares the effect of increasing airspeed on the power consumption of the open and shrouded rotors in the climb condition ($\alpha = 0°$), while Figure 4.12b shows the open and shrouded rotors compared in the edgewise-flow condition ($\alpha = 90°$). In axial flow, at fixed collective, C_P for both configurations drops
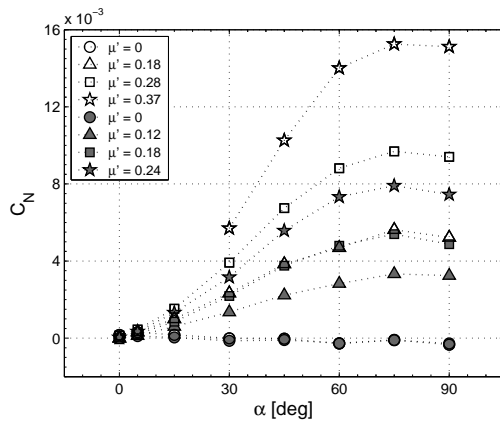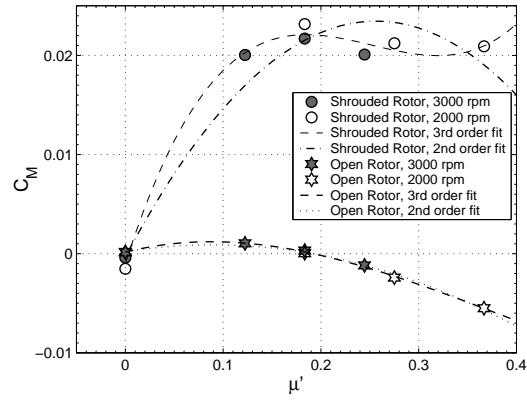
(a) Variation with airspeed: edgewise flow ($\alpha = 90°$)
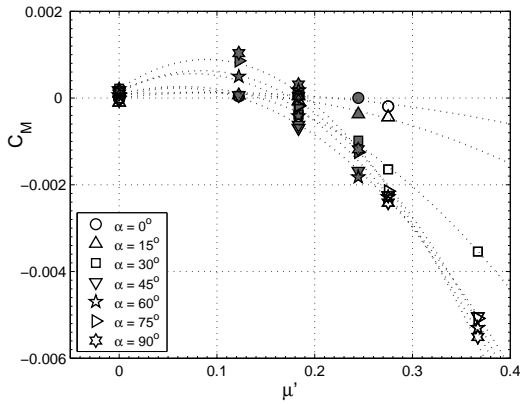
(b) Variation with airspeed: open rotor, 2nd-order fit
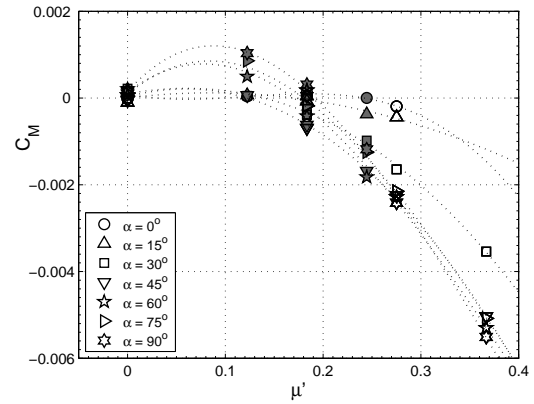
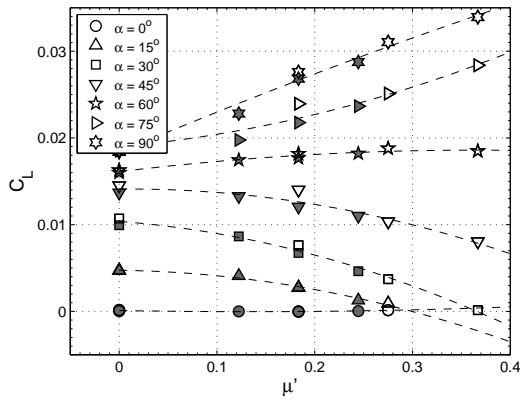(c) Variation with airspeed: open rotor, 3rd-order fit
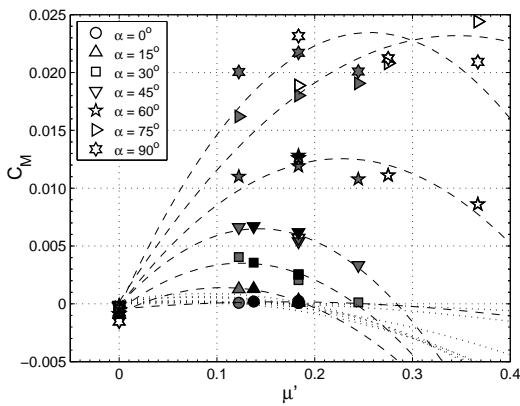
(d) Variation with airspeed: shrouded rotor, 2nd-order fit
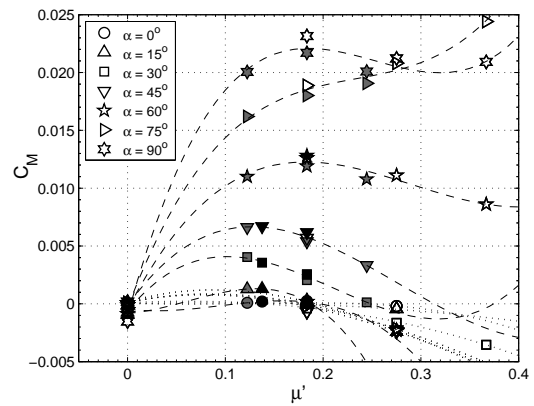
(e) Variation with airspeed: shrouded rotor, 3rd-order fit

Figure 4.11: Translational flight: variations in pitch moment

(f) Variation with angle of attack: open rotor

(g) Variation with angle of attack: shrouded rotor
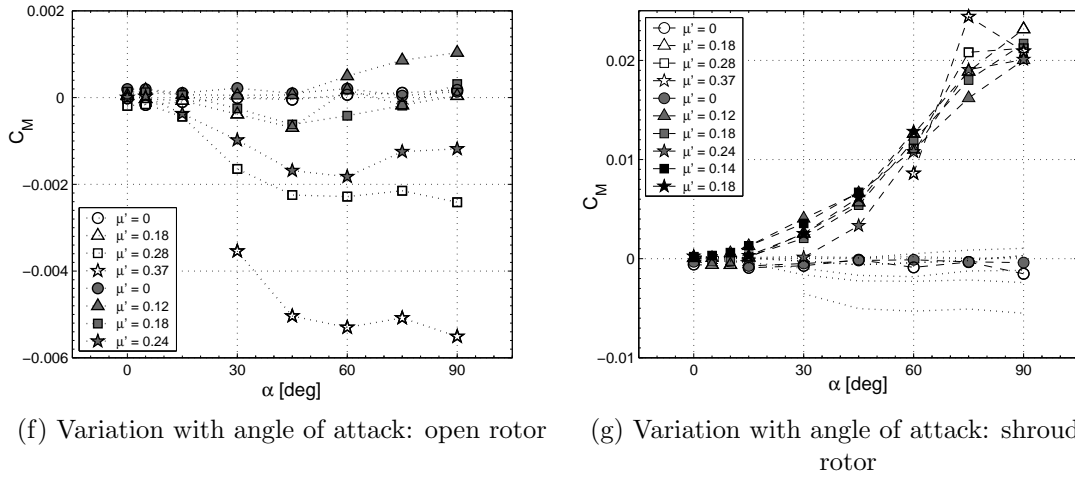
Figure 4.11: Translational flight: variations in pitch moment

rapidly with increasing μ'. In edgewise flow, the power consumption of the open rotor continuously increases with increasing airspeed, while that of the shrouded rotor remains constant up till about $\mu' = 0.3$, and then appears to decrease. In both cases, the shrouded rotor always consumes less power than the open rotor.

Figures 4.12c and 4.12d show the variations of C_P with increasing μ' for the other angles of attack. For the shrouded rotor, C_P decreases at higher rates as α is decreased. For the open rotor, similar behavior is seen: as α is decreased, C_P increases at lower rates with increasing μ', and then begins to decrease at higher rates. Figures 4.12e and 4.12f show the data as functions of angle of attack. Both open and shrouded rotors show an increase in power as α is increased, with the rate of increase being larger for higher values of μ'. However, the increase in C_P is much more rapid for the open rotor than for the shrouded rotor. Additionally, just as for the thrust coefficient, the power of the open rotor appears to be independent of airspeed at an angle of attack between 60° and 75°. For the shrouded rotor, the
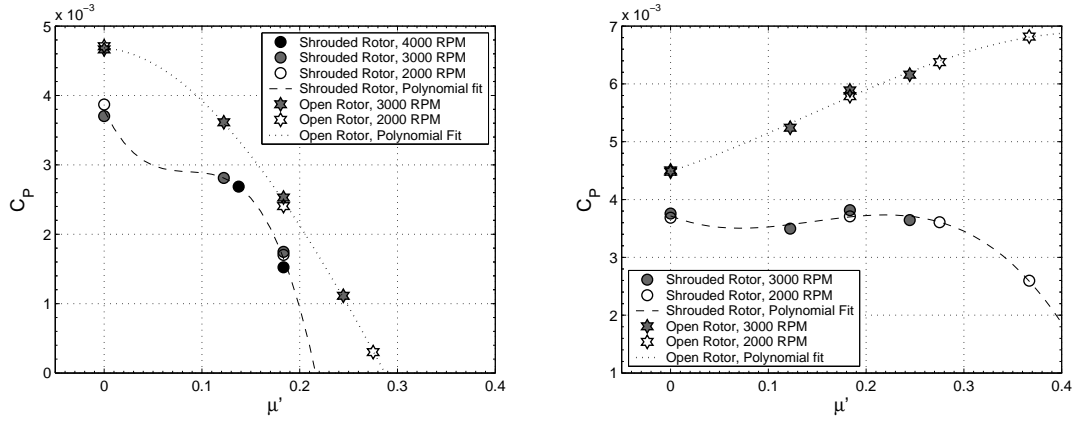
(a) Variation with airspeed: axial flow ($\alpha = 0°$) (b) Variation with airspeed: edgewise flow ($\alpha = 90°$)
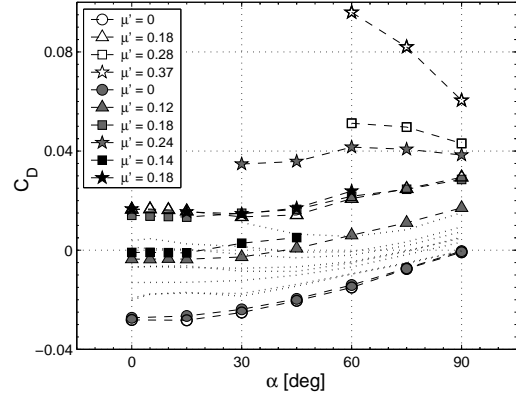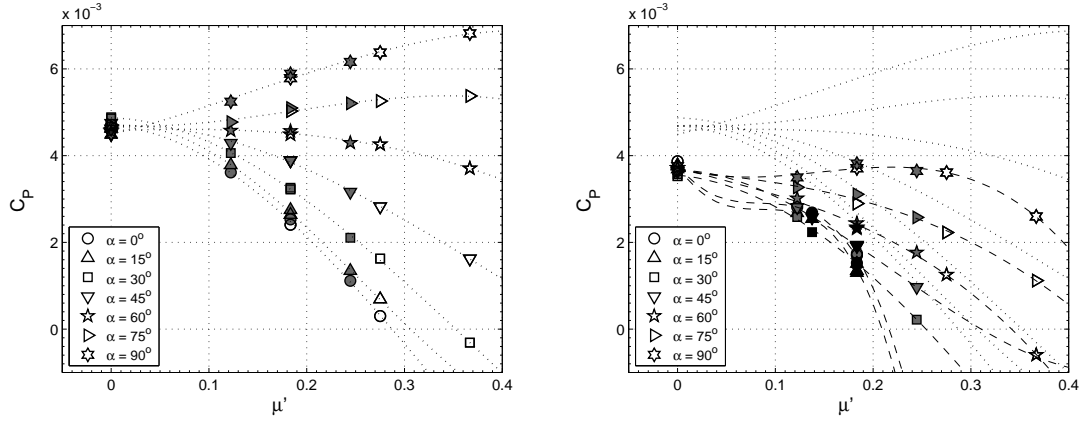
(c) Variation with airspeed: open rotor (d) Variation with airspeed: shrouded rotor
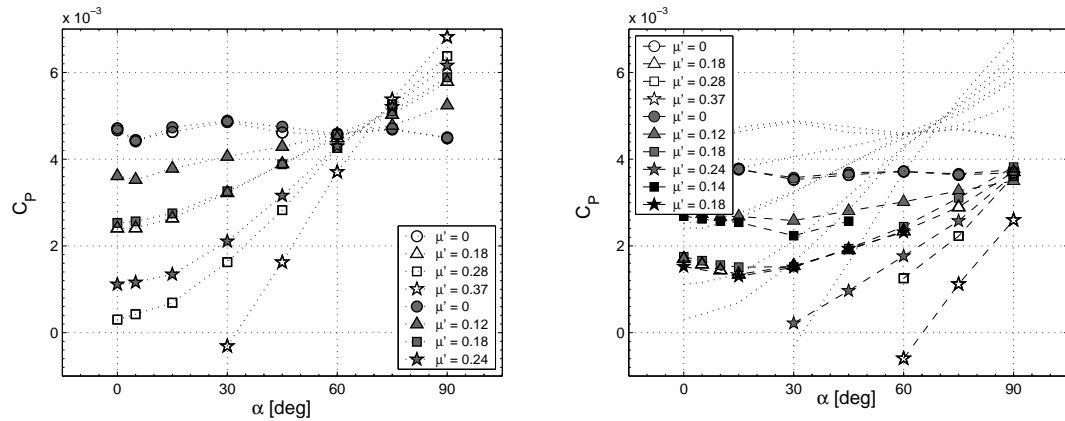
(e) Variation with angle of attack: open rotor (f) Variation with angle of attack: shrouded rotor

Figure 4.12: Translational flight: variations in power

data indicate that a similar independence from μ' occurs at $\alpha = 90°$.

Chapter 5

Vehicle Configuration Trade Studies

5.1   Introduction

The previous chapters have shown that, especially in the hovering-flight condition, significant improvements in performance are attainable by enclosing a MAV-scale rotor within a shroud. However, a serious drawback of the shrouded-rotor configuration is the the weight of the shroud itself, and it is imperative to take this factor into consideration when deciding between the open-rotor and the shrouded-rotor configurations during the design of a micro air vehicle. In addition, the addition of a shroud increases the size of the vehicle — with an LR13 shroud, for example, the outer diameter of the rotor tested in this investigation increased from 6.3 in to 9.6 in. A trade study should also therefore be conducted between using a shrouded rotor with a smaller rotor diameter versus using an open rotor with a larger rotor diameter. Based on the data that were acquired in this investigation, this chapter presents such trade studies to determine whether it is worthwhile to choose the shrouded-rotor configuration for the design of a MAV for missions consisting primarily of hovering and low-speed flight.

5.2   Shroud weights

In order to conduct these trade studies, estimates are needed for the weights of the shrouds. The weights of the shroud models used in this investigation — 260 g for the LR13-D10-L72, and 130 g for the LR13-D10-L31 shroud, for example — cannot be used, since the material for their fabrication was chosen from considerations of ease of manufacture and rapid-prototyping, and these weights are therefore not representative of the shroud on an actual flying MAV. Better estimates can be obtained from the weights of the shrouds used on the 'TiFlyer' shrouded-rotor MAVs tested and flown by Sirohi et al. [23] and Hrishikeshavan and Chopra [25]. Unlike the 'solid-block' shrouds used in this research, these shrouds had a 'shell' structure made from plies of carbon-fiber composite material (Graphite/Epoxy). From the geometry of these shrouds, the area density of the material/construction can be calculated, and applied to the geometries of the shrouds tested in this investigation. Two of these 'shell' shrouds were formed from continuous layers of carbon composite and had area densities of 0.51 kg/m^2 and 0.70 kg/m^2, the difference arising from the greater number of plies used to increase the stiffness of the second shroud.[1] Two other shrouds used a different construction method: that of stretching mylar or cellophane fabric over a carbon-composite frame, to obtain a stiff structure while reducing weight. These shrouds had area densities of 0.59 kg/m^2 and 0.16 kg/m^2, respectively. For the trade studies, the average of these different area-density values — 0.49 kg/m^2 — has been chosen as the representative value.

---

[1]The former shroud suffered from "severe vibration problems ... traced to the low stiffness of the [shroud] in an out-of-plane torsion mode" and consequent "interference with the rotor" [23].

5.3 Trade studies

The three trade studies described below have been conducted making use of the concept of the generalized figure of merit, $\mathrm{FM}^* = \mathrm{FM}\sqrt{\sigma_\mathrm{d}}$, which was introduced in Chapter 3 of this dissertation. Equation (3.3) (p. 145) from that chapter is repeated here, after manipulating it so as to directly express the generalized figure of merit in terms of the rotor diameter instead of the rotor disk area:

$$\mathrm{FM}^* = \frac{T^{3/2}}{P\sqrt{\pi\rho D_\mathrm{R}}} \tag{5.1}$$

Comparisons at stipulated values of thrust, power or rotor diameter can thus be readily obtained from the ratios of the FM^* values of different rotors, open or shrouded. As discussed in Chapter 3 and in Appendix B, the optimal operating point for any rotor is that at which it achieves its maximum value of FM^*, and the comparisons in these trade studies have been made for the different rotors operating at that point.

5.3.1 Shrouded vs. open, using the baseline 6.3-inch rotor

The first trade study compares the baseline, 6.3-inch-diameter open rotor tested in this investigation, which had a maximum FM^* of 0.177, against the baseline rotor when coupled with the LR13-D10-L50 shroud, which had a maximum FM^* of 0.470, the highest reached by any of the shrouds with this rotor. Based on a shroud area density of 0.49 kg/m^2, the weight of the shroud works out to be
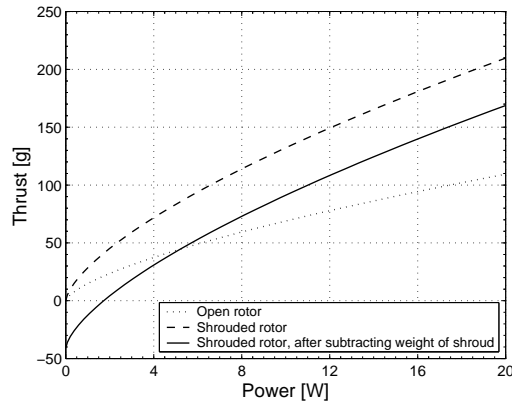
(a) Shrouded vs. open, using the baseline 6.3-inch rotor.
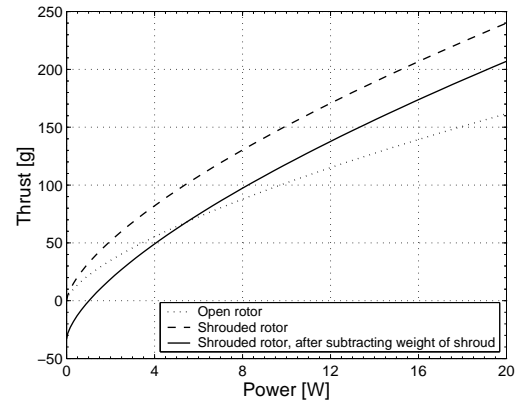
(b) Shrouded vs. open, using the cambered 6.3-inch rotor.
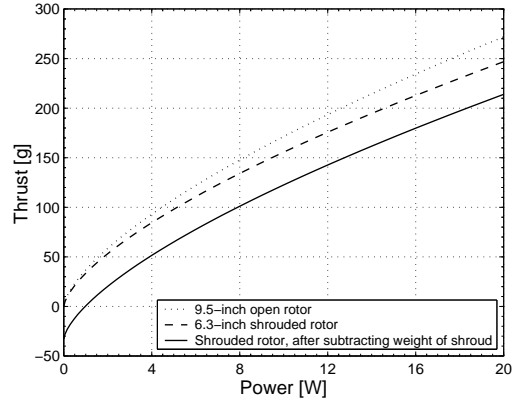
(c) 6.3-inch shrouded rotor vs. 9.5-inch open rotor.

Figure 5.1: Trade studies comparing open- and shrouded-rotor configurations for MAVs.

41 g. Figure 5.1a shows plots of the resulting thrust-power characteristics[2], calculated using Eq.(5.1), of the open rotor, the shrouded rotor, and the shrouded rotor after subtracting the weight of the shroud, to better illustrate the net gains from shrouding. It can be seen that for rotor system (including also the transmission, attitude control devices, electronics, batteries and support structures) + payload weights greater than approximately 45 g, the use of a shroud provides performance gains, either in the form of decreased power requirements for the same payload, or increased payload capacity at the same power.

5.3.2   Shrouded vs. open, using the cambered 6.3-inch rotor

The second trade study compares the more-efficient, cambered 6.3-inch-diameter open rotor, which had a maximum FM* of 0.318, against the cambered rotor when coupled with the LR13-D10-L31 shroud, which had a maximum FM* of 0.543. However, this shrouded-rotor model, as tested, had a blade tip clearance of $0.3\%D_\mathrm{t}$. Referring to the trends for the LR13-D10-L31 models given in Table 3.2 (p. 183), reducing the tip clearance to $0.1\%D_\mathrm{t}$ could possibly increase the maximum FM* of the shrouded rotor by $0.1\times$FM*$_\mathrm{OR,max}$, from 0.543 to 0.575. This higher value has therefore been considered instead, for this trade study. Based on a shroud area density of 0.49 kg/m^2, the weight of the shroud works out to be 33 g. As before, the thrust-power characteristics of the two configurations have been plotted, in Fig. 5.1b. With this rotor and this shroud, the benefits from shrouding are obtained at rotor

---

[2]These plots are similar in appearance to the C_T-versus-C_P rotor polars that were shown in Chapter 3; however, in a rotor polar, it is the collective angle that varies as a parameter along the curve, whereas in these figures shown here, the collective angle is constant (at the point for maximum FM*) and the rotor tip speed varies along the curve.

system + payload weights greater than approximately 70 g. As was realized earlier, in Chapter 3, the amount of benefit that is obtained with this, more efficient rotor is not as great as that obtained when the less efficient, baseline rotor is used.

5.3.3   6.3-inch shrouded rotor vs. 9.5-inch open rotor

The final trade study compares a shrouded rotor with a smaller rotor diameter against an open rotor with a larger rotor diameter. For the 9.5-inch-diameter open rotor, a FM^* value of 0.460 has been used, corresponding to the highest figure of merit of 0.65 achieved by an open rotor of this size [16], which utilized blades with camber as well as taper and twist. Similarly, for the smaller rotor, the highest value of FM that has been achieved at that size is 0.62 [20], corresponding to a FM^* value of 0.438. With the addition of a shroud to such a rotor, it can be expected that a generalized figure of merit of 0.60 could be attained. This value has therefore been used for the 6.3-inch-rotor-diameter shrouded rotor in this trade study. The thrust-power characteristics for these two configurations are shown in Fig. 5.1c. Based on these curves, it is clear that, from the standpoint of performance alone, for a given overall vehicle size limit, it is *always* preferrable to use a larger-diameter open rotor rather than a smaller-diameter shrouded rotor. In the end, however, it may be that, as in almost all other aircraft that have utilized shrouded rotors, it will be the safety benefits of the shroud, rather than the potential performance benefits, that will be the deciding reason for choosing this configuration over an open rotor.

Chapter 6

Concluding Remarks

Micro unmanned aerial vehicles (MAVs) have been predicted to be the next, emerging generation of aerospace systems, with many potential applications in both civilian and military missions. For hover-capable aircraft, reasons of improved safety, improved performance, and potentially lower noise emissions — compared to a traditional 'open'-rotor design — have led to the shrouded-rotor configurations becoming one of the most popular choices in the design of vertical take-off and landing (VTOL) MAVs. Although much work has been performed on larger-scale ducted propellers and shrouded rotors, there existed scarce data on the performance of shrouded rotors in the low-Reynolds-number regime of MAV-scale aircraft. In response to this dearth of reliable information, a systematic, experimental investigation has been conducted of the flight characteristics of MAV-scale aircraft of this configuration. The investigation had a two-fold goal: first, to investigate the improvements in performance that are achievable from using the shrouded-rotor configuration for micro air vehicles, and second, to aquire a body of experimental data that could be used for the validation of analytical, predictive tools, and as guidelines in the design of more efficient, more capable MAVs.

The first phase of the research consisted of an experimental investigation of the effects of varying the shroud profile shape on the hovering performance of MAV-

scale shrouded rotors, using seventeen models with a throat diameter (D_t) of 16 cm and with various values of diffuser expansion angle (θ_d), diffuser length (L_d), inlet lip radius (r_lip) and blade tip clearance (δ_tip). The values of these shrouded-rotor parameters that were tested were: from $0°$ to $20°$ for the diffuser angle, from 31% to $72\%D_\text{t}$ for the diffuser length, from 6.5% to $13\%D_\text{t}$ for the inlet lip radius, and from 0.1% to $1.6\%D_\text{t}$ for the blade tip clearance. Measurements were made of the thrust produced and mechanical power consumed, and, with the objective of obtaining a better understanding of the physics of the flow-field around this aircraft configuration, the distributions of pressure along the shroud surface and of the axial velocities in the wakes of the models. Integration of the shroud surface pressure distributions yielded an estimate of the fraction of the total thrust borne by the shroud itself, while integration of the wake velocity distributions yielded an estimate for the induced power losses of the shrouded rotors. The results of the various tests were compared to the predictions of the momentum-theory analytical model for a shrouded rotor.

This was followed by a wind-tunnel investigation — the second phase of the research — of the performance of the unshrouded ('open') rotor and of one of the shrouded-rotor models in translational flight. The fixed-collective, rigid-rotor models were tested at tunnel speeds of up to 20 ft/s, corresponding to a maximum airspeed ratio, $\mu' = v_\infty/\Omega R$, of 0.37 and angles of attack from $0°$ (axial climb or 'propeller mode') to $90°$ (hovering flight in a cross-wind). Measurements were made of thrust, shaft power, normal force, pitching moment and the pressure distribution over the shroud surface. The most noteworthy observations that resulted from these

investigations are summarized below.

6.1 Conclusions

6.1.1 Hover: Performance measurements

1. At rotor collectives above 10°, all shrouded-rotor models showed improvements in performance over the isolated ('open') rotor — that is, higher thrusts and lower power requirements. At the same power consumption, increases in thrust over the open rotor by up to 94% were observed, or, conversely, up to 49% reductions in power at the same thrust, for the condition where the open and shrouded rotors are required to have the same tip speed. If, instead, the rotor disk areas are required to be the same, then up to 90% increases in thrust at the same power are obtainable, or up to 62% reductions in power at the same thrust.

2. The performance improvements of the shrouded rotors over the open rotor obtained in these tests surpassed those predicted by momentum theory. This is because, in comparing the two configurations, the total power requirements of the rotors were considered, whereas momentum theory only considers the ideal power requirements. In other words, shrouding the rotors had the effect of reducing the non-ideal losses by a greater extent than the reductions in the ideal losses. This is an important benefit for MAV-scale rotors, which experience much greater profile-power losses than do larger-scale rotors.

3. Tests on a different micro-rotor, which had cambered blades and better open-rotor performance than the baseline rotor, revealed performance improvements from shrouding that, although also surpassing the predictions of momentum theory, were not nearly as remarkable as the improvements observed with the baseline rotor.

4. Within the range of values of the shrouded-rotor parameters tested, the optimal configuration was that with $\delta_{\text{tip}} = 0.1\%D_{\text{t}}$, $r_{\text{lip}} = 13\%D_{\text{t}}$, $\theta_{\text{d}} = 10°$ and $L_{\text{d}} = 50\%$ to $72\%D_{\text{t}}$. Increasing blade tip clearance, decreasing the inlet lip radius, decreasing the diffuser length and increasing or decreasing the diffuser angle from these optimum values led to degradations in performance. The improvement in performance with increasing expansion ratio (σ_{d}), as predicted by momentum theory, was seen to occur up to an expansion ratio of around 1.2. Increasing σ_{d} beyond this value, whether by increasing diffuser length or diffuser angle, caused performance to deteriorate. These trends are similar, qualitatively, to those seen in past research on larger-scale shrouded rotors.

5. The effects of changing any one of the four parameters (δ_{tip}, r_{lip}, θ_{d}, L_{d}) on the shrouded-rotors' performance became more pronounced as the other three parameters were changed to degrade the performance. It is therefore not possible to categorically state that any one particular parameter has a greater effect on performance than any other, since the amount of influence of any parameter depends on the values of the other parameters. The exception to this seems to be the lip radius, changes in which had almost same effect no

matter what the values of the other parameters are.

Thus, in general, it would seem that changing the value of any shroud parameter so as to improve performance results in less sensitivity of the performance to changes in any of the other parameters; similarly, improving the efficiency of the rotor itself would seem to result in less of a performance benefit from the presence of a shroud.

6. The traditional formulation of the figure of merit (FM) has been shown to be inappropriate for comparing the efficiencies of open and shrouded rotors of different expansion ratios. In its stead, an alternative, 'generalized' form of the figure of merit, equal to $\mathrm{FM} \cdot \sqrt{\sigma_d}$ or $C_T^{3/2}/2C_P$, has been proposed, which is applicable to any rotor, shrouded or open.

6.1.2   Hover: Flow-field measurements

1. Distinct primary and secondary suction-pressure peaks were seen on the shroud inlet; this phenomenon has been predicted by CFD analyses, but has not been previously seen experimentally. The stronger secondary peak occurs due to high-velocity vortical flow that forms at the gap between the blade tips and the shroud wall. Tailoring the inlet shape in this region such that the resulting suction forces are inclined more towards the axial direction can potentially result in significant thrust increases.

2. Up to 80% of the total inlet thrust was produced by the inner half of the inlet lips, which were semi-circular in profile. The outer portion of the lip bears

little load, and therefore can be constructed to be less stiff, resulting in weight savings.

3. The negative thrust from the diffuser had magnitudes up to only about one-fourth those of the positive thrust from the inlet, and therefore had less of an effect on the net shroud thrust. This implies that maintaining attached flow and favorable pressure distributions on the inlet would be more important than doing so in the diffuser.

4. With increasing collective, the ability of the shroud to successfully off-load the rotor decreased.

5. Increasing the blade tip clearance from $0.1\%D_t$ to $1.6\%D_t$ resulted in a reduction in inlet suction and the net shroud thrust.

6. Increasing the inlet lip radius from $6\%D_t$ to $13\%D_t$ reduced the strength of the inlet suction, but, because of the simultaneous increase in inlet surface area, resulted in a net increase in inlet and shroud thrust, and in greater off-loading of the rotor.

7. Increasing the diffuser expansion ratio increased the suction pressures in the diffuser, but had little effect on the inlet pressure distributions. For the same diffuser length, the 20-degree diffuser produced up to four times as much negative thrust as the 10-degree diffuser, with a consequent 20–30% reduction in net shroud thrust. The increase in length of the 10-degree diffuser from $31\%D_t$ to $72\%D_t$, on the other hand, while nearly doubling the negative thrust

from the diffuser, had little effect on the net shroud thrust.

8. The shrouds were effective in impoving the uniformity of the wake velocity distributions, compared to that of the open rotor, thus reducing both the ideal as well as the non-ideal components of the induced power expenditure. Reducing the blade tip clearance resulted in greater uniformity and therefore lower values of the induced power correction factor, κ. Increasing the expansion ratio by increasing the diffuser length, at fixed diffuser angle, did not have a significant effect on κ.

9. The diameter of the wake appeared to remain fairly constant after exiting the diffuser, thereby validating the fundamental assumption of the momentum theory model of a shrouded rotor: that the flow is fully expanded at the diffuser exit plane. However, because of the axial velocity deficit in the core of the wake due to the blockage from the centerbody, the actual achieved expansion will be less than expected. A smooth aft fairing for the centerbody is therefore of great importance.

10. The wake of the open rotor appeared to contract to a greater extent than that usually seen for conventional-scale rotors.

6.1.3 Translational flight

1. In axial flight ($\alpha = 0°$), the net thrust of the shrouded rotor was initially greater than that of the open rotor, but rapidly decreased to being lower than the open-rotor thrust as airspeed was increased, possibly because of the drag

of the shroud. The power consumption of both configurations also decreased with increasing airspeed, but that of the shrouded rotor always remained less than that of the open rotor.

2. In edgewise-flow conditions ($\alpha = 90°$), the thrust of both the open and shrouded rotors increased with increasing airspeed, with the thrust of the shrouded rotor always remaining higher than that of the open rotor. This was probably due to the large increases in suction pressure seen on the windward side of the shroud inlet. The power consumption of the open rotor increased with increasing airspeed, while that of the shrouded rotor remained roughly constant and then decreased. The normal force on the shrouded rotor increased much more rapidly with increasing airspeed than did that of the open rotor, again probably because of the drag of the shroud. The location of the center of pressure at which the normal force acts generally moved from above the plane of the rotor disk to below it, for both configurations. However, for the shrouded rotor, the center of pressure always lay approximately $0.75R$ further above the location for the open rotor. Both of these factors contributed to much larger nose-up pitching moments for the shrouded rotor than for the open rotor. The physical basis of these pitching moments was clearly seen in the extreme asymmetry of the flow-field, with large suction pressures on the windward side of the shroud inlet and large over-pressures on the leeward side.

3. At an angle of attack between $60°$ and $75°$ for the open rotor, and between $75°$ and $90°$ for the shrouded rotor, the data indicate that the thrust and power

coefficients of the rotors are independent of the free-stream velocity. At higher angles of attack, C_T and C_P increased with increasing airspeed, while at lower angles they decreased with increasing μ'.

4. The normal force coefficient displayed a stall-like behavior with increasing angle of attack, with a maximum value near $\alpha = 75°$. The location of the center of pressure generally moved from below the rotor plane to above the rotor plane as α increased. The resultant effect was an increase in nose-up pitch moment or a decrease in nose-down moment with increasing α.

5. In general, the addition of the shroud caused the effects of changing airspeed or angle of attack on the rotor forces and moments to become stronger. The variations in power consumption were an exception to this rule.

6. Polynomial curve-fits showed the force and power coefficients to vary with the square and cube, respectively, of airspeed ratio. The variations of the location of the center of pressure and of the pitch moment coefficients were best approximated with cubic polynomials.

7. At high tunnel speeds and high angles of attack, the shrouded rotor displayed a decrease in drag coefficient with increasing α that is characteristic of annular airfoils. This was possibly due to the relatively low thrust of the shrouded-rotor model tested.

8. The pressure in the rotor wake at the diffuser exit plane more closely approaches ambient atmospheric levels on the downwind side of the diffuser,

compared to the windward side. At high airspeeds and at low angles of attack (near-axial flow), the static pressure at the diffuser exit remains significantly lower than ambient, indicating that further expansion of the wake takes place beyond the diffuser. This observation challenges the validity of the fundamental assumption of the momentum-theory model for shrouded rotors, namely, that the flow has fully expanded at the diffuser exit.

6.2 Contributions to state of the art

The contributions of this research to the state of the art lie in the value of the extensive, systematic body of experimental data that has been generated, comprising both performance as well as flow-field measurements. The latter, especially, have been instrumental in providing a better understanding of the physics of the flow around a MAV-scale shrouded rotor. Unlike most previous research programs, this data set contains valuable measurements of the *mechanical* power consumption of the shrouded-rotor models, clarification of the effects of increasing power input by increasing rotor collective rather than by increasing tip speed, data on the effects of interference (or coupling) between the various shrouded-rotor parameters, and comparisons with the performance of the open rotor over a collective range that spans its entire operating envelope, thereby enabling comparisons of the open and shrouded rotors at their respective points of optimal operation, for a true estimate of the benefits that can be obtained from shrouding. The research program demonstrated that significant improvements in performance can be obtained by shrouding

a rotor at the MAV scale; however, the amount of improvement becomes less when the rotor itself is designed to be more efficient. In either case, though, the measured improvements were greater than those predicted by momentum theory, due both to substantial reductions in the rotor profile drag as well as increases in the uniformity of the wake profiles — non-ideal power losses that are not considered by the momentum theory. This is a significant result, since the predictions of momentum theory are usually considered to be upper limits of attainable performance. The measurements of the shroud surface pressure distributions and wake axial velocity distributions provide physical explanations for the performance variations; a notable contribution of the pressure measurements is the first known experimental demonstration of the secondary suction peak on the inlet of the shroud, which has, so far, only been predicted by CFD analyses. The changes in the pressure distributions with changing airspeed and angle of attack in translational flight clearly illustrated the sources of the high drag and nose-up pitch moment exerted on the shroud in this flight condition, and also the reason for the increased thrust of the shrouded rotor in edgewise flight. Finally, a new standard metric, the 'generalized figure of merit,' has been proposed for correctly comparing the performances of open and shrouded rotors of different expansion ratios.

In the end, however, the air-vehicle design trade studies that were performed showed that, due to the due to the increases in weight and aircraft size that result from the incorporation of a shroud, the performance benefits that would be obtained for an actual aircraft might only be marginal, and that the *safety* benefits of a shroud might be the principal reason for choosing this configuration rather than

a conventional open-rotor design. Still, the results of this research program are useful in that they show how the shroud should be designed so as to minimize any detrimental consequences of incorporating a shroud, and indeed, how to obtain the best possible performance if other design requirements result in the choice of the shrouded-rotor configuration.

6.3   Recommendations for future work

There are several avenues along which research could be conducted to extend and improve upon the knowledge gained from this present investigation. The most obvious would be to test a greater number of values of each of the different shrouded-rotor parameters; in the hover tests, although data were obtained from multiple series of models, each series had a maximum of three values of any of the parameters of interest — this is not sufficient for obtaining a true understanding of the effects of varying those parameters on performance, and where the performance limits lie. This is especially true in the case of the diffuser parameters — the diffuser length and expansion angle — for which the data showed that an extreme point lay somewhere within the range of values tested. As was done for the 10-degree diffuser, the 20-degree diffuser model should be cut into sections to obtain a shorter diffuser with the same expansion ratio as the longest 10-degree diffuser; this would yield valuable information on the relative effects of expansion angle and expansion ratio. Such a test was planned in this investigation, but was not carried out due to time limitations. A follow-up investigation to this would be to test the effects of

varying the values of the shroud parameters on the translational-flight performance of shrouded rotors. For those tests, it would also be worthwhile to measure the pressure distributions over the external surfaces of the shrouds. In addition, for the translational-flight tests, shrouds with tapered diffuser-exit 'trailing edges' should be tested, to avoid the separation drag that is sure to have occurred on the models that were tested in this investigation. These tests should also be conducted with a rotor that has been optimized for the low-Reynolds-number flight regime, with blades that incorporate taper and twist, and with thin, cambered airfoils with sharpened leading and trailing edges.

Another research avenue that could be pursued is the performance of coaxial, contra-rotating rotors when shrouded. Although most current shrouded-rotor UAVs use vanes in the downwash of the rotor for yaw control and to nullify the reaction torque of the rotor, it is possible that use of coaxial rotors, as were used in the Sikorsky Cypher aircraft, could result in aircraft with greater capabilities and better flight characteristics. For further innovation, a study of different inlet lip profile shapes should be conducted, not remaining restricted to simple semi-circular lips, with one goal being to harness the potential of the inlet suction-pressure peaks for greater thrust production. Measurements should be made of the inflow velocity distributions, to supplement those that have been made in the wakes of the rotors, and thus to obtain a better understanding of the flow conditions at the rotor disk.

Finally, efforts should be made to develop techniques for predicting the performance of shrouded-rotor MAVs, to relieve the amount of experimental testing that would otherwise need to be conducted. This research direction would, of course,

rely heavily upon computational-fluid-dynamic (CFD) methods, but a fair amount of insight can also be obtained by the more elementary potential-flow and blade-element methods. For the latter, a model for the effect of the blade tip clearance on the aerodynamics is essential, as well as reliable data on the performance of the blade airfoils at these low Reynolds numbers.

Appendix A

Theoretical Derivations

This appendix provides the detailed derivations of the theoretical model used for predicting the performance of a shrouded rotor. The Momentum Theory model for the hover and climb (axial-flight) conditions is first given, followed by the Combined Blade-Element-Momentum Theory ('BEMT') model for the hover condition. The derivations shown here have been presented for the principal purpose of comparing the aerodynamics of open and shrouded rotors. For a more in-depth analysis and discussion of the aerodynamics of an open rotor, a standard textbook such as Ref. [14] is recommended.

A.1   Momentum Theory

The 'simple' Momentum Theory model of a rotor is based on the conservation laws of fluid dynamics, and uses the simplifying assumptions of inviscid, incompressible, steady, and quasi-one-dimensional flow. The rotor is assumed to impart only axial momentum to the flow, i.e., there is no swirl in the wake. Additionally, in the case of a shrouded rotor, the flow is assumed to have expanded back to ambient atmospheric pressure at the diffuser exit plane.
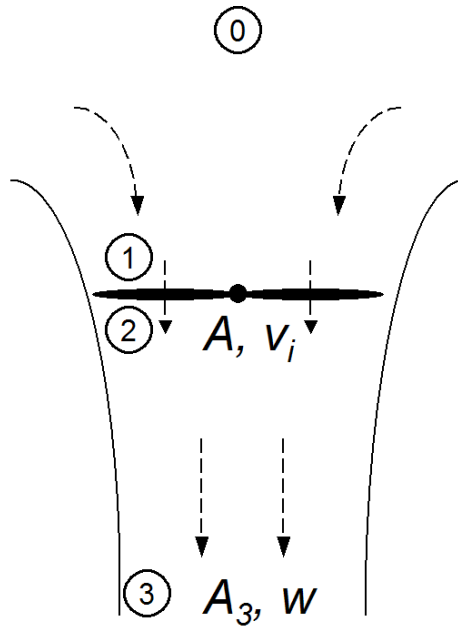
(a) Open rotor
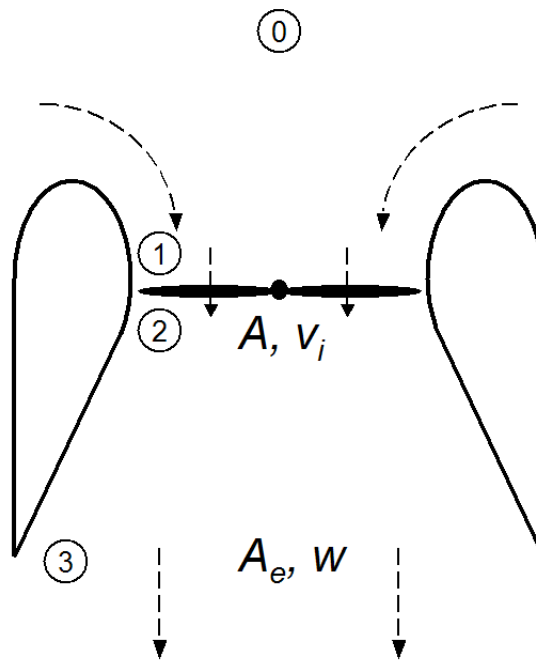
(b) Shrouded rotor

Figure A.1: Flow-field models for open and shrouded rotors in hover.

A.1.1 Hover

Figure A.1 shows the flow-fields of an open (unshrouded) and a shrouded rotor in the hovering-flight condition. Station 0 represents the free-stream, infinitely upstream of the rotor. Stations 1 and 2, respectively, lie just above and below the plane of the rotor disk. Station 3 is at the exit plane of the shroud's diffuser or the far wake, infinitely downstream, of an open rotor. The following identities and definitions therefore arise:

$$\text{Velocities:} \quad v_0 = 0$$

$$v_1 = v_2 = v_i$$

$$v_3 = w$$

$$\text{Areas:} \quad A_1 = A_2 = A$$

$$A_3 = A_e = \sigma_{\mathrm{d}} A$$

$$\text{Pressures:} \quad p_0 = p_3 = p_{atm}$$

$$\Delta p = p_2 - p_1$$

A.1.1.1 Open rotor

In the case of an open rotor ('OR'), the development of the model is as follows:

$$\text{Conservation of Mass:} \quad \dot{m} = \rho A v_i \tag{A.1}$$

$$\text{Conservation of Momentum:} \quad T_{OR} = \dot{m}(v_3 - v_0) = \dot{m}w \tag{A.2}$$

$$\text{Conservation of Energy:} \quad P_{i_{OR}} = KE_3 - KE_0 = \frac{1}{2}\dot{m}w^2 \tag{A.3}$$

$$\text{Actuator-disk model of the rotor:} \quad T_{OR} = \Delta p A \tag{A.4}$$

$$P_{i_{OR}} = T_{OR} v_i \qquad \text{(A.5)}$$

Actuator-disk model of rotor and Conservation of Energy (application of the Bernoulli equation between stations 0 and 1, and between stations 2 and 3):

$$
\begin{aligned}
p_0 + \frac{1}{2}\rho v_0^2 &= p_1 + \frac{1}{2}\rho v_1^2 \\
p_2 + \frac{1}{2}\rho v_2^2 &= p_3 + \frac{1}{2}\rho v_3^2
\end{aligned}
$$

$$\Rightarrow \Delta p = \frac{1}{2}\rho w^2 \qquad \text{(A.6)}$$

By combining either equations A.2, A.3 and A.5, or equations A.1, A.2, A.4 and A.6, the relation between the induced velocity at the rotor disk plane and in the far wake is obtained:

$$w = 2v_i \qquad \text{(A.7)}$$

Together with equation A.2, this gives

$$v_i = \sqrt{\frac{T_{OR}}{2\rho A}} \qquad \text{(A.8)}$$

and from either equation A.3 or A.5

$$P_{i_{OR}} = \frac{T_{OR}^{3/2}}{\sqrt{2\rho A}} \qquad \text{(A.9)}$$

A.1.1.2 Shrouded rotor

In the case of a shrouded rotor ('SR'), the development is as follows:

$$\text{Conservation of Mass:} \qquad \dot{m} = \rho A v_i = \rho A_e w \qquad\qquad \text{(A.10)}$$

$$\Rightarrow \quad w = \frac{v_i}{\sigma_\mathrm{d}} \qquad\qquad \text{(A.11)}$$

$$\text{Conservation of Momentum:} \qquad T_{total} = \dot{m} w = \rho A \frac{v_i^2}{\sigma_\mathrm{d}} \qquad\qquad \text{(A.12)}$$

$$\Rightarrow \quad v_i = \sqrt{\frac{\sigma_\mathrm{d} T_{total}}{\rho A}} \qquad\qquad \text{(A.13)}$$

$$\text{Conservation of Energy:} \qquad P_i = \frac{1}{2}\dot{m} w^2 = \frac{1}{2}\rho A \frac{v_i^3}{\sigma_\mathrm{d}^2} \qquad\qquad \text{(A.14)}$$

$$\Rightarrow \quad P_i = \frac{T_{total}^{3/2}}{\sqrt{4\sigma_\mathrm{d}\rho A}} \qquad\qquad \text{(A.15)}$$

Thus, the relation A.11 has replaced the result A.7 derived for the open rotor, and the actuator-disk model of the rotor was not required in order to derive expressions for the induced velocity (eq. A.13) and induced power (eq. A.15).

The actuator-disk model is only required to derive expressions for the the thrust provided by the rotor alone:

$$T_{rotor} \;=\; \Delta p \cdot A \ \text{or} \ \frac{P_i}{v_i} = \frac{1}{2}\rho A w^2 \qquad\qquad \text{(A.16)}$$

$$\Rightarrow \frac{T_{rotor}}{T_{total}} \;=\; \frac{1/2\rho A w^2}{(\rho A v_i)w} = \frac{1}{2\sigma_\mathrm{d}} \qquad\qquad \text{(A.17)}$$

In non-dimensional coefficient form, the various quantities are expressed as

follows:

$$C_{T_{total}} = \frac{T_{total}}{\rho A(\Omega R)^2}$$

$$C_{T_{rotor}} = \frac{T_{rotor}}{\rho A(\Omega R)^2} = \frac{1}{2\sigma_{\mathrm{d}}}C_{T_{total}}$$

$$\lambda_i = \frac{v_i}{\Omega R} \quad = \sqrt{\sigma_{\mathrm{d}}\,C_{T_{total}}} \tag{A.18}$$

$$= \sigma_{\mathrm{d}}\sqrt{2\,C_{T_{rotor}}}$$

$$C_{P_i} = \frac{P_i}{\rho A(\Omega R)^3} \quad = \frac{C_{T_{total}}^{3/2}}{2\sqrt{\sigma_{\mathrm{d}}}} \tag{A.19}$$

$$= \sqrt{2}\,\sigma_{\mathrm{d}}\,C_{T_{rotor}}^{3/2}$$

$$= \lambda_i\,C_{T_{rotor}}$$

For the shrouded rotor, $T_{\mathrm{total}} \equiv T_{\mathrm{SR}}$. In the case of an open rotor, $T_{\mathrm{rotor}} = T_{\mathrm{total}} \equiv T_{\mathrm{OR}}$, so, from equation A.17, $\sigma_{\mathrm{d}} = 1/2$, which is exactly the value of the 'expansion' that momentum theory predicts for an open rotor (eq. A.7). Equations A.10–A.17, as well as the coefficient forms of the quantities shown above, therefore apply equally to both shrouded and unshrouded (open) rotors, with the effective value of $1/2$ being used for the expansion ratio in the case of an open rotor.

The contribution to the total shrouded-rotor thrust provided by the diffuser alone can be found by applying the conservation laws to a control volume consisting of the fluid within the diffuser only. The control volume is therefore bounded by the diffuser walls, the rotor disk plane and the diffuser exit plane. Applying the momentum equation and summing the forces in the z-direction, where $+z$ is an axial coordinate in the direction of the flow (opposite to the direction of positive

thrust on the rotor), we have:

$$\sum F_z = \sum v_z (\rho \vec{A} \cdot \vec{v})$$

$$\Rightarrow F_{diff} + p_2 A_2 - p_3 A_3 = -v_2 \rho A_2 v_2 + v_3 \rho A_3 v_3$$

where F_{diff} is the force exerted by the diffuser on the control volume

$$\Rightarrow F_{diff} + p_2 A - p_{atm} \sigma_\mathrm{d} A = -\rho A v_i^2 + \rho \sigma_\mathrm{d} A \frac{v_i^2}{\sigma_\mathrm{d}^2}$$

$$\Rightarrow F_{diff} = \rho A v_i^2 \left(\frac{1}{\sigma_\mathrm{d}} - 1 \right) + A(\sigma_\mathrm{d}\, p_{atm} - p_2) \tag{A.20}$$

Applying the Bernoulli equation (conservation of energy):

$$p_2 + \frac{1}{2}\rho v_2^2 = p_3 + \frac{1}{2}\rho v_3^2$$

$$= p_{atm} + \frac{1}{2}\rho \frac{v_i^2}{\sigma_\mathrm{d}^2}$$

$$\Rightarrow p_2 = p_{atm} + \frac{1}{2}\rho v_i^2 \left(\frac{1}{\sigma_\mathrm{d}^2} - 1 \right) \tag{A.21}$$

Substituting eq. A.21 into eq. A.20 and simplifying, we obtain:

$$F_{diff} = -\frac{\rho A v_i^2 (\sigma_\mathrm{d} - 1)^2}{2\sigma_\mathrm{d}^2} + A(\sigma_\mathrm{d} - 1)p_{atm} \tag{A.22}$$

Note that $-F_{diff}$ is the force exerted by the control volume on the diffuser, in the $+z$ direction. Therefore, the *thrust* (which is in the $-z$ direction) on the diffuser due to the control volume is equal to $-(-F_{diff})$. The *net* thrust on the diffuser is equal to

the sum of the forces (in the $-z$ direction) due to both the internal control volume and the external atmosphere. This latter quantity is equal to $-p_{atm}(A_3 - A_2) = -p_{atm}A(\sigma_\mathrm{d} - 1)$. Adding this to F_{diff} from eq. A.22, we have:

$$\text{Net thrust on diffuser} = T_{diff} = -\frac{\rho A v_i^2 (\sigma_\mathrm{d} - 1)^2}{2\sigma_\mathrm{d}^2}$$

Making use of eq. A.12, we obtain the final result:

$$\frac{T_{diffuser}}{T_{total}} = -\frac{(\sigma_\mathrm{d} - 1)^2}{2\sigma_\mathrm{d}} \tag{A.23}$$

Given expressions for the thrust fractions from the rotor (eq. A.17) and the diffuser (eq. A.23), the thrust fraction from the inlet is directly obtained:

$$\frac{T_{inlet}}{T_{total}} = 1 - \frac{T_{rotor}}{T_{total}} - \frac{T_{diffuser}}{T_{total}}$$
$$= \frac{\sigma_\mathrm{d}}{2} \tag{A.24}$$

From eq. A.17, the thrust-sharing between the shroud and the rotor is:

$$\frac{T_{shroud}}{T_{rotor}} = \frac{1 - \frac{1}{2\sigma_\mathrm{d}}}{\frac{1}{2\sigma_\mathrm{d}}} = (2\sigma_\mathrm{d} - 1) \tag{A.25}$$

which shows that as the expansion ratio is increased, the shroud increasingly off-loads the rotor.

A.1.1.3 Comparisons of shrouded-rotor and open-rotor performance

Expressions A.9 and A.15 describe the relationship between four fundamental characteristics of open or shrouded rotors: thrust, power requirement, rotor disk area and (effective) expansion ratio. By taking the ratio of these expressions:

$$\frac{P_{i_{SR}}}{P_{i_{OR}}} = \frac{1}{\sqrt{2\sigma_\mathrm{d}}} \left(\frac{T_{SR}}{T_{OR}}\right)^{3/2} \left(\frac{A_{OR}}{A_{SR}}\right)^{1/2} \tag{A.26}$$

comparisons can be made between the characteristics of open and shrouded rotors, as a function of the shrouded rotor's expansion ratio. By holding any two variables fixed between the two configurations, the behavior of the other variables can be analysed. For example, if the open and shrouded rotors are compared, subject to the condition that they have the same rotor disk area ($A_\mathrm{SR} = A_\mathrm{OR}$) and consume the same amount of (ideal) power ($P_\mathrm{SR} = P_\mathrm{OR}$), then the following relations result:

$$\begin{aligned}
\frac{T_{SR}}{T_{OR}} &= (2\sigma_\mathrm{d})^{1/3} \\
\frac{T_{rotor}}{T_{OR}} &= \frac{1}{(2\sigma_\mathrm{d})^{2/3}} \\
\frac{v_{i_{SR}}}{v_{i_{OR}}} &= \frac{\dot{m}_{SR}}{\dot{m}_{OR}} = (2\sigma_\mathrm{d})^{2/3} \\
\frac{w_{SR}}{w_{OR}} &= \frac{1}{(2\sigma_\mathrm{d})^{1/3}}
\end{aligned} \tag{A.27}$$

Similarly, if the configurations are compared when they are producing the same total amount of thrust ($T_\mathrm{SR} = T_\mathrm{OR}$) and are of the same disk area, then:

$$\frac{P_{i_{SR}}}{P_{i_{OR}}} = \frac{1}{\sqrt{2\sigma_\mathrm{d}}}$$

$$\frac{T_{rotor}}{T_{OR}} = \frac{1}{2\sigma_d}$$

$$\frac{v_{i_{SR}}}{v_{i_{OR}}} = \frac{\dot{m}_{SR}}{\dot{m}_{OR}} = \sqrt{2\sigma_d}$$

$$\frac{w_{SR}}{w_{OR}} = \frac{1}{\sqrt{2\sigma_d}} \tag{A.28}$$

If the configurations are compared when they are producing the same total amount of thrust and are consuming the same amount of ideal power, then:

$$\frac{A_{SR}}{A_{OR}} = \frac{1}{2\sigma_d} \qquad \Rightarrow \qquad \frac{D_{SR}}{D_{OR}} = \frac{1}{\sqrt{2\sigma_d}}$$

$$\frac{T_{rotor}}{T_{OR}} = \frac{1}{2\sigma_d}$$

$$\frac{v_{i_{SR}}}{v_{i_{OR}}} = 2\sigma_d$$

$$\frac{\dot{m}_{SR}}{\dot{m}_{OR}} = 1$$

$$\frac{w_{SR}}{w_{OR}} = 1 \tag{A.29}$$

And, if the configurations are compared when the *rotors* are producing the same amount of thrust $(\mathrm{T_{rotor}} = \mathrm{T_{OR}})$ and are of the same disk area, then:

$$\frac{T_{SR}}{T_{OR}} = 2\sigma_d$$

$$\frac{P_{i_{SR}}}{P_{i_{OR}}} = 2\sigma_d$$

$$\frac{v_{i_{SR}}}{v_{i_{OR}}} = \frac{\dot{m}_{SR}}{\dot{m}_{OR}} = 2\sigma_d$$

$$\frac{w_{SR}}{w_{OR}} = 1 \tag{A.30}$$

A.1.1.4 Pressure distributions

The momentum-theory model can be used to obtain a prediction of the variations in air pressure through the flow-field of an open or shrouded rotor. For a hovering rotor, the total pressure upstream of the rotor is equal to ambient atmospheric pressure (p_{atm}), while downstream of the rotor it is equal to the sum of atmospheric pressure and the disk loading ($\text{DL} = T_{\text{rotor}}/A_{\text{rotor}} \approx T_{\text{rotor}}/A_{\text{throat}}$). Expressing the pressures in terms of the pressure coefficient, C_p, the following development is obtained. Upstream of the rotor, or at the shroud inlet:

$$p = p_{\text{total}} - q = p_{\text{atm}} - \frac{1}{2}\rho v^2 \tag{A.31}$$

$$
\begin{aligned}
-C_p &= \frac{p_{\text{atm}} - p}{q_{\text{tip}}} \\
&= \frac{\frac{1}{2}\rho v^2}{\frac{1}{2}\rho v_{\text{tip}}^2} \\
&= \left(\frac{v}{v_{\text{tip}}}\right)^2 \\
&= \left(\frac{v_i}{v_{\text{tip}}}\right)^2 \cdot \left(\frac{v}{v_i}\right)^2 \\
&= \lambda_i^2 \cdot \left(\frac{v}{v_i}\right)^2 \\
&= (\sigma_{\text{d}} C_T) \cdot \left(\frac{v}{v_i}\right)^2
\end{aligned}
\tag{A.32}
$$

where v is the flow velocity at any given axial station in the flow. Downstream of the rotor, or in the diffuser of a shroud, the development is similar:

$$p = p_{\text{total}} - q = p_{\text{atm}} + \text{DL} - \frac{1}{2}\rho v^2 \tag{A.33}$$

$$
\begin{aligned}
-C_p &= \frac{p_{\text{atm}} - p}{q_{\text{tip}}} \\
&= \frac{\frac{1}{2}\rho v^2 - \text{DL}}{\frac{1}{2}\rho v_{\text{tip}}^2} \\
&= \left(\frac{v}{v_{\text{tip}}}\right)^2 - \frac{\text{DL}}{q_{\text{tip}}} \\
&= \left(\frac{v_i}{v_{\text{tip}}}\right)^2 \cdot \left(\frac{v}{v_i}\right)^2 - \frac{T_{\text{rotor}}/A_{\text{throat}}}{\frac{1}{2}\rho v_{\text{tip}}^2} \\
&= \lambda_i^2 \cdot \left(\frac{v}{v_i}\right)^2 - 2C_{T_{\text{rotor}}} \\
&= (\sigma_{\text{d}} C_T) \cdot \left(\frac{v}{v_i}\right)^2 - \frac{2C_T}{2\sigma_{\text{d}}} \\
&= (\sigma_{\text{d}} C_T) \cdot \left[\left(\frac{v}{v_i}\right)^2 - \frac{1}{\sigma_{\text{d}}^2}\right]
\end{aligned}
\tag{A.34}
$$

By mass conservation, $v/v_i = A_{\text{throat}}/A$, where A is the cross-sectional area of the flow-field at the corresponding axial station. Therefore, expressions are needed for the shape of the flow-field boundary as a function of distance from the plane of the rotor disk. For an open rotor ($\sigma_{\text{d}} = 1/2$), the geometry of the wake, downstream of the rotor, can be estimated using a model such as the Landgrebe wake model [14, p. 450] — this was done for Fig. 1.8c on page 19, repeated here as Fig. A.2 for convenience. In this figure, the pressure variation upstream of the open rotor was obtained by assuming that the cross-sectional area of the upstream flow varied 'linearly' from infinity to the area of the rotor disk, i.e., that v/v_i varied linearly from 0 to 1.

For a shrouded rotor, the geometry of the wake is defined by the shape of the diffuser. For a conical diffuser, $A_{\text{throat}}/A = (R/r)^2$, where R is the radius of the shroud throat and r is the radius at any axial station. For such a diffuser, r can be
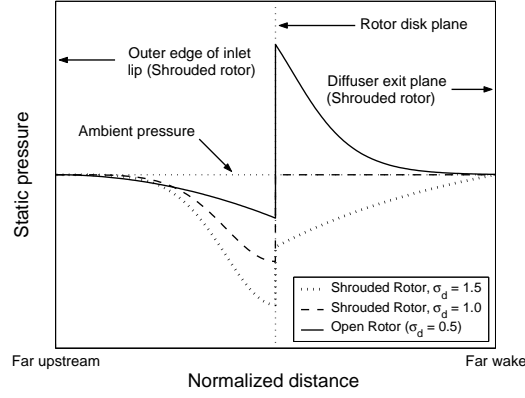
Figure A.2: Variations in pressure in the hover flow-fields of open and shrouded rotors, at the same thrust coefficient.

expressed as:

$$r = R + z \cdot (R_e - R) \tag{A.35}$$

where $R_e = \sqrt{\sigma_\mathrm{d}}R$ is the radius of the diffuser exit and z is a normalized axial coordinate that varies linearly from 0 at the rotor disk plane to 1 at the diffuser exit plane (Fig. A.3b). Using this expression, the velocity — or area — ratio, downstream of the rotor, is given by:

$$\frac{v}{v_i} = \frac{A_\mathrm{throat}}{A} = \frac{1}{[1 + z(\sqrt{\sigma_\mathrm{d}} - 1)]^2} \tag{A.36}$$

For the inlet, the inflow geometry can be defined using the 'sphere-cap' model proposed by Dyer [123], illustrated in Fig. A.3. A sphere cap is the surface obtained when a spherical shell is intersected by a plane, and the portion of the shell above that plane (the 'base plane') is considered (Fig. A.3a). The base plane may lie either above or below the center of the sphere. Applied to an inlet flow model, a sphere cap is used to represent a potential surface, normal to which are the streamlines of

(a) Sphere cap geometry.

(b) Sphere cap geometry applied to shroud inlet.
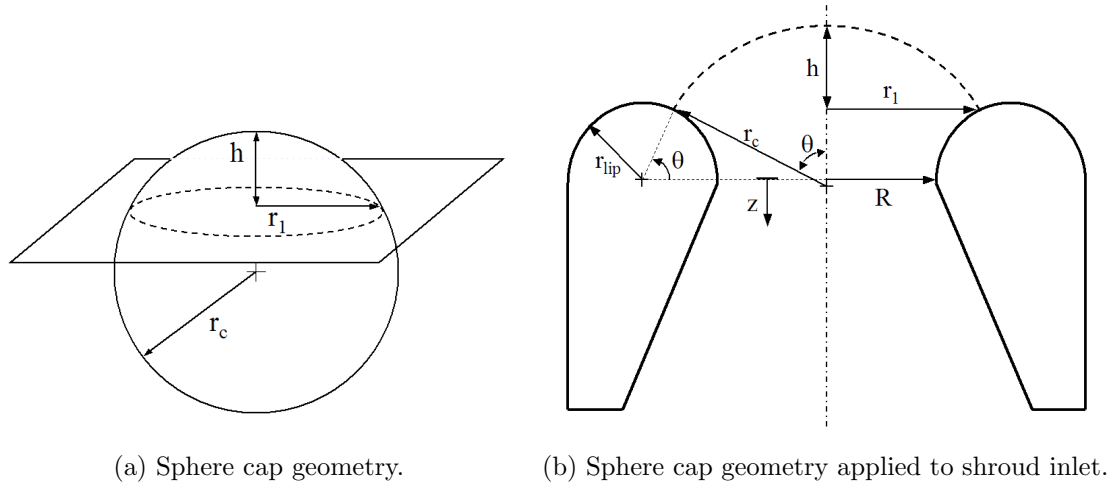
Figure A.3: Sphere-cap model for inlet flow geometry of a shrouded rotor.

the flow. The sphere caps, shown in cross-section by the dashed line in Fig. A.3b, are centered on the shroud axis and intersect the inlet lip surface at right angles. The line of intersection is a circle that represents the base plane of the sphere cap. The surface area of a sphere cap is given by the equation:

$$A_{\text{cap}} = 2\pi r_C h = \pi(r_1^2 + h^2) \tag{A.37}$$

where r_C is the radius of the sphere, h is the height of the sphere cap, and r_1 is the radius of the base circle. Applied to a shroud inlet, r_1 and h are given by:

$$r_1 = r_C \sin\theta = R + r_{\text{lip}}(1 - \cos\theta) \tag{A.38}$$

$$h = r_C(1 - \cos\theta) = \frac{r_1}{\sin\theta}(1 - \cos\theta) \tag{A.39}$$

where θ is an inlet angular coordinate that varies from $0°$ at the throat to $180°$ at the outer edge of the inlet lip. Using these expressions, the velocity and area ratios,

282

upstream of the rotor, are given by:

$$\frac{v}{v_i} = \frac{A_{\text{throat}}}{A_{\text{cap}}} = \frac{1}{\left[1 + \frac{r_{\text{lip}}}{R}(1 - \cos\theta)\right]^2 \cdot \left[1 + \left(\frac{1 - \cos\theta}{\sin\theta}\right)^2\right]} \qquad (A.40)$$

Equations (A.40) and (A.36) can now be substituted into Eqs. (A.32) and (A.34), respectively, to obtain the pressure distributions over the inlet and diffuser surfaces of a shroud, as a function of the inlet lip radius, diffuser expansion ratio and thrust coefficient. Figure A.4 shows such predictions of pressure distributions, while Fig. A.5 compares these theoretical predictions with the experimentally measured distributions for shrouded-rotor models LR06-D00-δ0.6 and LR13-D20-δ0.8. In Figure A.5, the theoretical distributions were generated using the experimentally-measured values of C_T for the shrouded rotors at the different rotor collectives. It can be seen that the theoretical model qualitatively captures the general shape of the pressure distributions quite well, but under-predicts the strength of the suction peak on the inlet lip. The prediction is a little closer to the experimental values in the case of the model with the larger tip clearance (Fig. A.5b); this correlates well with the observation, described in Chapter 3, that decreasing the tip clearance causes an increase in the inlet suction. It is therefore quite probable that incorporating a theoretical model for the effect of the tip clearance on the pressure distributions would improve the predictions.

Finally, the values of the pressure just above and below the plane of the rotor disk (stations 1 and 2 in Fig. A.1) are obtained by setting $v = v_i$ in Eqs. (A.32) and
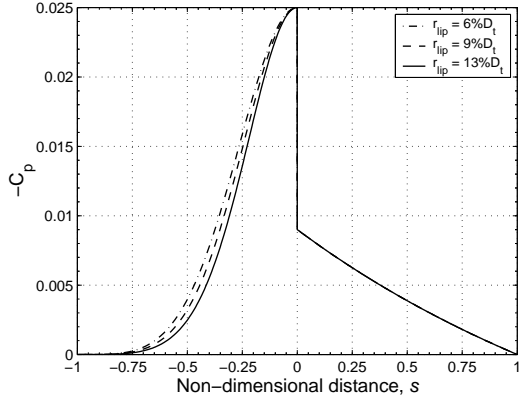
(a) Effect of inlet lip radius; $C_T = 0.02$, $\sigma_{\mathrm{d}}=$ 1.25.
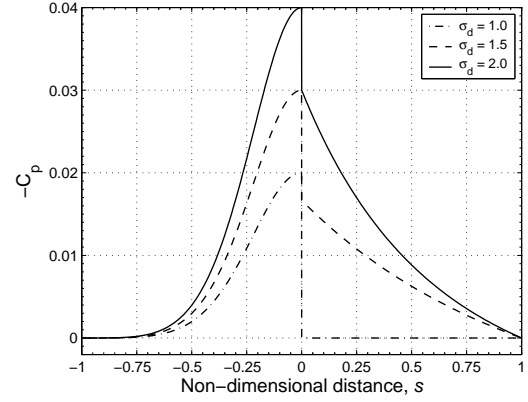
(b) Effect of diffuser expansion ratio; $C_T = 0.02$, $r_{\mathrm{lip}}= 13\%D_{\mathrm{t}}$.
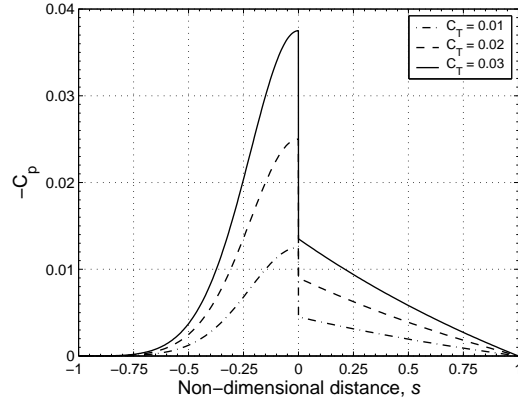
(c) Effect of thrust coefficient; $r_{\mathrm{lip}}= 13\%D_{\mathrm{t}}$, $\sigma_{\mathrm{d}}=$ 1.25.

Figure A.4: Theoretical predictions of shrouded-rotor surface pressure distributions.

(a) Model LR06-D00-δ0.6.

(b) Model LR13-D20-δ0.8.
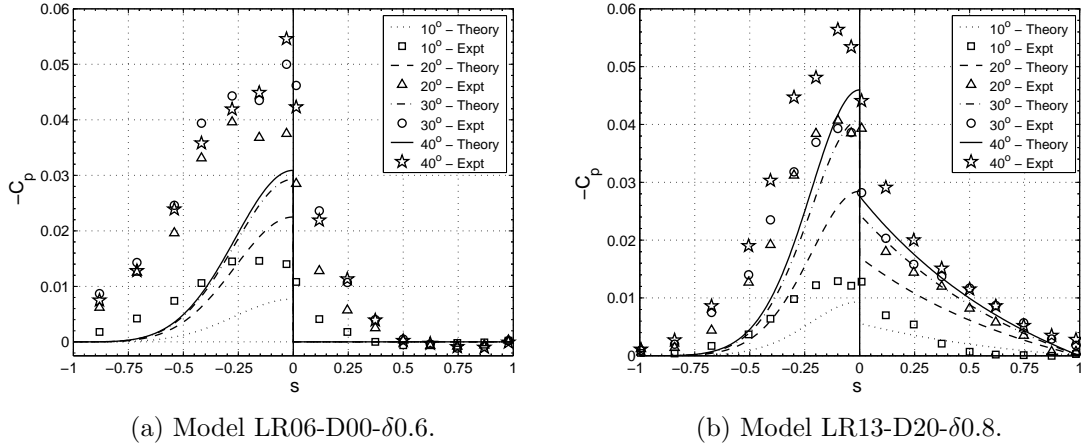
Figure A.5: Shroud surface pressure distributions: comparison of theory with experimental measurements.

(A.34), to obtain:

$$p_1 = p_{\text{atm}} - \text{DL} \cdot (\sigma_{\text{d}}^2) \tag{A.41}$$

$$p_2 = p_{\text{atm}} - \text{DL} \cdot (\sigma_{\text{d}}^2 - 1) \tag{A.42}$$

Substituting the value of $1/2$ for σ_{d} in these equations results in the familiar expressions $(p_{\text{atm}} - \text{DL}/4)$ and $(p_{\text{atm}} + 3\text{DL}/4)$, respectively, for an open rotor. Figure A.6 shows the effect of increasing the expansion ratio on the (suction) pressures at the rotor disk plane, above and below the rotor disk, at fixed total thrust. The decreasing distance between the two lines illustrates the reduction in thrust borne by the rotor itself (T_{rotor}) with increasing σ_{d}.
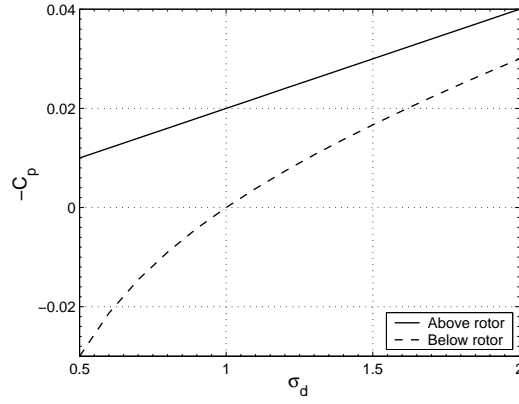
Figure A.6: Effect of expansion ratio on pressures at the rotor disk plane; $C_T = 0.02$.

A.1.2 Climb (Axial Flight)

The development of the climb model parallels that for the hover condition, with the difference that the velocities at the different stations in Fig. A.1 are now incremented by the climb velocity, V_c:

$$v_0 = V_c$$

$$v_1 = v_2 = V_c + v_i$$

$$v_3 = V_c + w \tag{A.43}$$

Therefore, for an open rotor:

$$\text{Conservation of mass:} \quad \dot{m} = \rho A (V_c + v_i) \tag{A.44}$$

$$\text{Conservation of momentum:} \quad T_{\text{OR}} = \dot{m}(v_3 - v_0) = \dot{m}w \tag{A.45}$$

$$\text{Conservation of energy:} \quad P_{i_{\text{OR}}} = \frac{1}{2}\dot{m}(V_c + w)^2 - \frac{1}{2}\dot{m}V_c^2 \tag{A.46}$$

$$= \frac{1}{2}\dot{m}w(w + 2V_c)$$

286

$$\text{Actuator-disk model:} \quad P_{i_{\mathrm{OR}}} = T_{\mathrm{OR}}(V_{\mathrm{c}} + v_{\mathrm{i}}) \tag{A.47}$$

Solving Eqs. (A.45), (A.46) and (A.47) yields:

$$w = 2v_{\mathrm{i}} \tag{A.48}$$

which is the same result as for the hover condition. Using this result with Eqs. (A.44) and (A.45) yields the formula for the ideal induced velocity at the rotor disk:

$$\frac{v_{\mathrm{i}}}{v_{\mathrm{h}}} = -\frac{V_{\mathrm{c}}}{2v_{\mathrm{h}}} + \sqrt{\left(\frac{V_{\mathrm{c}}}{2v_{\mathrm{h}}}\right)^2 + 1} \tag{A.49}$$

where $v_{\mathrm{h}} = \sqrt{T_{\mathrm{OR}}/2\rho A}$ is the ideal induced velocity at the rotor in the hover condition (cf. Eq. (A.8)). Note that the 'effective' expansion ratio for the open rotor is no longer equal to $1/2$, as it was in hover, and is now given by:

$$\sigma_{\mathrm{d}} = \frac{A_3}{A} = \frac{V_{\mathrm{c}} + v_{\mathrm{i}}}{V_{\mathrm{c}} + w} = \frac{V_{\mathrm{c}} + v_{\mathrm{i}}}{V_{\mathrm{c}} + 2v_{\mathrm{i}}} \tag{A.50}$$

which has a value between $1/2$ and close to 1.0, depending on the climb velocity.

On the other hand, for a shrouded rotor, the expansion ratio is fixed by the geometry of the diffuser, and is forced to remain the same (equal to A_e/A) at all climb velocities — assuming complete expansion at the diffuser exit plane. For a shrouded rotor, therefore:

$$\text{Conservation of mass:} \quad \dot{m} = \rho A(V_{\mathrm{c}} + v_{\mathrm{i}}) = \rho A_e(V_{\mathrm{c}} + w) \tag{A.51}$$

$$\Rightarrow w = \frac{V_{\mathrm{c}} + v_{\mathrm{i}}}{\sigma_{\mathrm{d}}} - V_{\mathrm{c}} \tag{A.52}$$

$$\text{Conservation of momentum:} \quad T_{\mathrm{total}} = \dot{m}w \tag{A.53}$$

Solving these equations, and using the result $v_{\mathrm{h}} = \sqrt{\sigma_{\mathrm{d}} T_{\mathrm{total}}/\rho A}$, yields the formula for the ideal induced velocity:

$$\frac{v_{\mathrm{i}}}{v_{\mathrm{h}}} = \frac{V_{\mathrm{c}}}{2v_{\mathrm{h}}}(\sigma_{\mathrm{d}} - 2) + \sqrt{\left(\frac{\sigma_{\mathrm{d}} V_{\mathrm{c}}}{2v_{\mathrm{h}}}\right)^2 + 1} \tag{A.54}$$

The division of thrust between the rotor and the shroud is found, once again, by using the actuator-disk model of the rotor:

$$T_{\mathrm{rotor}} = \Delta p \cdot A = (p_2 - p_2) \cdot A$$

Applying the Bernoulli equation between stations 0 and 1, and between stations 2 and 3:

$$p_0 + \frac{1}{2}\rho V_{\mathrm{c}}^2 = p_1 + \frac{1}{2}\rho(V_{\mathrm{c}} + v_{\mathrm{i}})^2$$

$$p_2 + \frac{1}{2}\rho(V_{\mathrm{c}} + v_{\mathrm{i}})^2 = p_3 + \frac{1}{2}\rho(V_{\mathrm{c}} + w)^2$$

Solving these yields, for the pressure jump across the rotor:

$$p_2 - p_1 = \frac{1}{2}\rho(V_{\mathrm{c}} + w)^2 - \frac{1}{2}\rho V_{\mathrm{c}}^2$$

$$= \rho w(w/2 + V_{\mathrm{c}}) \tag{A.55}$$

288

Using Eqs. (A.52) and (A.53), the rotor thrust fraction is therefore given by:

$$\begin{aligned}
\frac{T_{\text{rotor}}}{T_{\text{total}}} &= \frac{(p_2 - p_1)A}{\dot{m}w} \\
&= \frac{V_{\text{c}} + w/2}{V_{\text{c}} + v_{\text{i}}} \\
&= \frac{v_{\text{i}} + V_{\text{c}}(\sigma_{\text{d}} + 1)}{2\sigma_{\text{d}}(v_{\text{i}} + V_{\text{c}})}
\end{aligned} \tag{A.56}$$

Thus, even though the total thrust is constant in a steady (unaccelerated) climb, the rotor thrust is not, but depends on the climb velocity. The change in rotor thrust from the hover condition is readily obtained as:

$$\begin{aligned}
\frac{(T_{\text{rotor}})_{\text{c}}}{(T_{\text{rotor}})_{\text{h}}} &= \frac{(T_{\text{rotor}}/T_{\text{total}})_{\text{c}}}{(T_{\text{rotor}}/T_{\text{total}})_{\text{h}}} \\
&= \frac{v_{\text{i}} + V_{\text{c}}(\sigma_{\text{d}} + 1)}{v_{\text{i}} + V_{\text{c}}}
\end{aligned} \tag{A.57}$$

The (ideal) power required to climb, P_{c}, is given by the product of the rotor thrust and the velocity of the air through the rotor:

$$\begin{aligned}
P_{\text{c}} &= (T_{\text{rotor}})_{\text{c}} \cdot (v_{\text{i}} + V_{\text{c}}) \\
&= (T_{\text{rotor}})_{\text{h}} \cdot \left[v_{\text{i}} + V_{\text{c}}(\sigma_{\text{d}} + 1) \right] \qquad \text{(By Eq. (A.57))}
\end{aligned}$$

Denoting $P_{\text{h}} = (T_{\text{rotor}})_{\text{h}} \cdot v_{\text{h}} = T_{\text{total}}^{3/2}/\sqrt{4\sigma_{\text{d}}\rho A}$ (cf. Eq. (A.15)) as the ideal power required in hover, the climb power can be expressed as:

$$\begin{aligned}
\frac{P_{\text{c}}}{P_{\text{h}}} &= \frac{v_{\text{i}} + V_{\text{c}}(\sigma_{\text{d}} + 1)}{v_{\text{h}}} \\
&= \left(3\sigma_{\text{d}} \frac{V_{\text{c}}}{2v_{\text{h}}} \right) + \sqrt{\left(\frac{\sigma_{\text{d}} V_{\text{c}}}{2v_{\text{h}}} \right)^2 + 1}
\end{aligned} \tag{A.58}$$

For an open rotor, the rotor thrust is equal to the total thrust and is constant. The climb power is therefore given simply by:

$$\frac{P_c}{P_h} = \frac{v_i + V_c}{v_h}$$

$$= \frac{V_c}{2v_h} + \sqrt{\left(\frac{V_c}{2v_h}\right)^2 + 1} \qquad (A.59)$$

Equations (A.54), (A.54), (A.58) and (A.59) have been plotted in Fig. A.7 as functions of the climb velocity ratio, V_c/v_h, for an open rotor and for different values of the expansion ratio for a shrouded rotor. Although it might seem, from these figures, that the shrouded rotors have a severe power penalty compared to the open rotor, these representations are misleading, because the open and shrouded rotors have different values of v_h and P_h. These figures only serve to illustrate the forms of the equations, but cannot be used for comparing the different configurations. Figure A.8 therefore shows a true comparison of the power requirements of the configurations when they are producing the same total thrust and have the same disk area, using Eq. (A.28). The ordinate shows the ratio of the shrouded-rotor and open-rotor power requirements, while the abscissa shows the climb velocity normalized by the ideal induced velocity of the open rotor in hover.[1] It can be clearly seen that shrouding the rotor provides power savings up to a climb velocity nearly equal to $v_{h_{OR}}$, and increasing the expansion ratio increases the velocity up to which these savings are obtained. At much higher climb velocities, however, shrouding results in a power penalty, and lower expansion ratios are preferable, as

[1]I.e., the figure shows $(P_c/P_h)_{SR}/(P_c/P_h)_{OR} \times (P_h)_{SR}/(P_h)_{OR}$ plotted versus $(V_c/v_h)_{SR} \times (v_h)_{SR}/(v_h)_{OR}$.

(a) Ideal induced velocity.　　　　　　　(b) Ideal power.
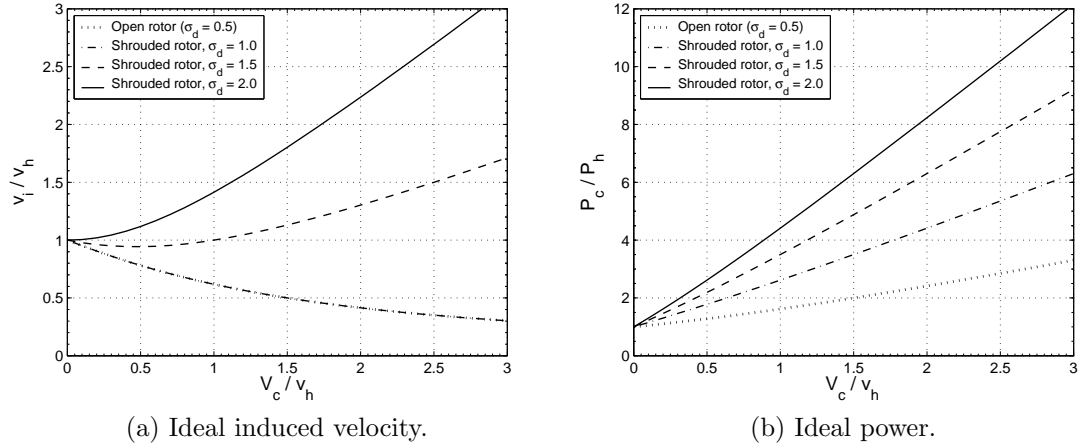
Figure A.7: Predicted variations in ideal induced velocity and power in climb, for open and shrouded rotors.
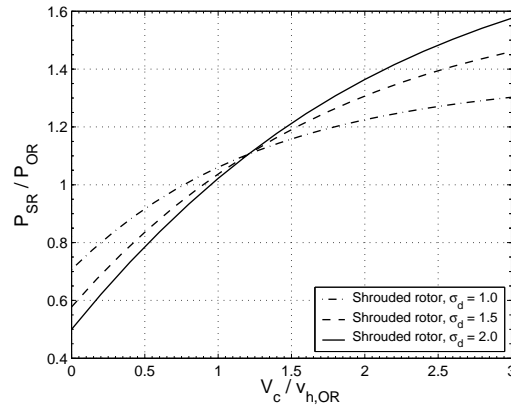
Figure A.8: Comparison of open and shrouded rotor power requirements in climb.

would be expected. In addition, since these analyses do not consider the additional thrust that would be required to overcome the drag of the shroud, the true penalties of shrouding would be even greater.

Finally, as in the previous sections, the equations derived here for shrouded rotors represent a general case; by substituting the expression in Eq. (A.50) for the expansion ratio, the equations reduce to the special case of an open rotor, and by substituting $V_c = 0$, they reduce to the special case of the hover condition.

A.2 Combined Blade-Element-Momentum Theory (Hover)

The Momentum Theory model of a rotor, with its various simplifying assumptions and idealized conditions, is useful for predicting the upper performance limits of a rotor and for gaining a broad understanding of the relationships between the top-level rotor parameters: thrust, power, the size of the rotor, and the size of the wake. For more realistic analysis and design, however, theoretical models with greater degrees of refinement and detail are necessary. The Combined Blade-Element-Momentum-Theory (BEMT) model is one such: it allows for modeling of the effects of the discrete number of rotor blades, of the aerodynamic characteristics of the airfoil sections used for the blades, and of the geometry of the blades themselves, i.e., of radial variations in chord length (blade 'taper'), pitch angle (blade 'twist') and airfoil section. The model is thus able to predict the effects of the profile drag of the blades and of a non-uniform inflow distribution. One remaining assumption is that the two-dimensional ('2-D') aerodynamic characteristics of the individual airfoil sections are not affected by those of the neighboring sections. In effect, BEMT is essentially Lifting-Line theory applied to a rotating wing.

In the BEMT model, the azimuthally discrete nature of the rotor is accounted for by a parameter called the solidity ratio (σ), equal to the total planform area of all the blades divided by the area of the rotor disk:

$$\sigma = \frac{N_b c R}{\pi R^2} = \frac{N_b c}{\pi R} \tag{A.60}$$

and by a parameter called the Prandtl Tip-Loss Factor (F). The spanwise variation

in the geometry of the blades is modeled by dividing the rotor disk into concentric

annuli, and equating the change in axial momentum flux of the air passing through

each annulus with the sum of the differential thrust forces acting on all the blade

elements within that annulus. Since the total change in momentum flux of the air

passing through the shrouded rotor, equal to $\dot{m}w$, is due to both the rotor thrust

as well as the shroud thrust, the change in momentum flux due only to the rotor

thrust is obtained from Eq. (A.17):

$$T_{\text{rotor}} = \frac{1}{2\sigma_{\text{d}}}T_{\text{total}} = \frac{1}{2\sigma_{\text{d}}}(\dot{m}w) = \dot{m}\left(\frac{v_{\text{i}}}{2\sigma_{\text{d}}^2}\right) \tag{A.61}$$

where $w = v_{\text{i}}/\sigma_{\text{d}}$ is the Δv — the additional flow velocity in the far wake compared

to the freestream — due to the total thrust of the rotor-shroud system, while $v_{\text{i}}/2\sigma_{\text{d}}^2$

is the Δv due to the rotor thrust only. The thrust on a single annular section of the

(shrouded) rotor is therefore given by:

$$\begin{aligned} \mathrm{d}T_{\text{annulus}}(r) &= \mathrm{d}\dot{m}(r) \cdot \Delta v(r) \cdot F(r) \\ &= \left(\rho \cdot \mathrm{d}A(r) \cdot v_{\text{i}}(r)\right) \cdot \left(\frac{v_{\text{i}}(r)}{2\sigma_{\text{d}}^2}\right) \cdot F(r) \end{aligned} \tag{A.62}$$

or, in non-dimensionalized coefficient form:

$$\mathrm{d}C_{T_{\text{annulus}}}(r) = r \cdot \mathrm{d}r \cdot \frac{\lambda^2(r)}{\sigma_{\text{d}}^2} \cdot F(r) \tag{A.63}$$

where $\lambda = v_{\text{i}}/R$ is the (induced) inflow ratio. The Prandtl tip-loss correction factor

for an open rotor, $F(r)$, should be replaced with the equivalent Goodman correction factor [141] or the Prandtl-Shaidakov factor used in the analytical model presented by Bourtsev and Selemenev [92], both of which were discussed in Section 1.4.4.1 of this dissertation.

In Ref. [175, p. 323, Eq. 6.49], a different formulation for the differential rotor thrust coefficient is given:

$$\mathrm{d}C_{T_{\text{annulus}}}(r) = r \cdot \mathrm{d}r \cdot \frac{2\lambda^2(r)}{\sigma_{\text{d}}} \tag{A.64}$$

This latter expression would seem to have been obtained by multiplying the rotor thrust fraction, $T_{\text{rotor}}/T_{\text{total}}$, by the expression for the differential (total) thrust coefficient of an *open* rotor:

$$\mathrm{d}C_{T_{\text{annulus,OR}}} = \frac{1}{\rho \, A \, v_{\text{tip}}^2} \times \left[\left(\rho \cdot 2\pi y \mathrm{d}y \cdot v_{\text{i}}(y) \right) \cdot \left(2v_{\text{i}}(y) \right) \right]$$

$$= 4\lambda^2(r) \cdot r \cdot \mathrm{d}r \tag{A.65}$$

where $2v_{\text{i}}$ is the Δv corresponding to the (total) thrust on an open rotor. The formulation in Eq. (A.64) therefore cannot be correct, and that of Eq. (A.63) must be used.

From the blade-element model, the differential rotor thrust coefficient is obtained from the vector summation of the lift and drag acting on an airfoil section:

$$\mathrm{d}T_{\text{annulus}}(r) = N_{\text{b}} \times \left(\mathrm{d}L(r) \cdot \cos(\phi(r)) - \mathrm{d}D(r) \cdot \sin(\phi(r)) \right) \tag{A.66}$$

$$\Rightarrow \mathrm{d}C_{T_\mathrm{annulus}}(r) = \frac{1}{2}\sigma(r) \cdot r \cdot \sqrt{\lambda^2(r) + r^2} \cdot \left(c_l(r) - c_d(r)\frac{\lambda(r)}{r}\right) \cdot \mathrm{d}r \qquad \text{(A.67)}$$

Equating the expressions in Eqs. (A.63) and (A.67) yields a 4$^\text{th}$-order equation in λ, which is easily solved with a computer. If the inflow is assumed to be small, compared to the rotational (tangential) velocity of the blade element ($v_\mathrm{i} \ll \Omega y$, i.e., $\lambda^2 \ll r^2$), then a quadratic in λ is obtained, with the solution given by:

$$\lambda = \frac{\sigma\,\sigma_\mathrm{d}^2\,c_d}{4F}\left[-1 + \sqrt{1 + \frac{8F\,r\,c_l}{\sigma\,\sigma_\mathrm{d}^2\,c_d^2}}\right] \qquad \text{(A.68)}$$

where all terms except the expansion ratio (σ_d) are functions of the radial coordinate, r. These equations must be iteratively solved, as they involve c_l and c_d, which are — in general — non-linear functions of angle of attack, which in turn is dependent on the inflow ratio. If the further assumptions are made that c_l is a linear function of α (i.e., in the pre-stall range) and that c_d is a constant:

$$c_l = a \cdot (\alpha - \alpha_0) = a \cdot (\theta - \phi - \alpha_0) \qquad \text{(A.69)}$$

$$c_d = c_{d_0} \qquad \text{(A.70)}$$

then a closed-form, analytic expression for λ is obtained:

$$\lambda = \frac{\sigma\,\sigma_\mathrm{d}^2\,(c_{d_0} + a)}{4F}\left[-1 + \sqrt{1 + \frac{8F\,r\,a\,(\theta - \alpha_0)}{\sigma\,\sigma_\mathrm{d}^2\,(c_{d_0} + a)^2}}\right] \qquad \text{(A.71)}$$

which reduces to the familiar expression for the inflow ratio of an open rotor:

$$\lambda = \frac{\sigma\, a}{16F}\left[-1 + \sqrt{1 + \frac{32F\, r\, (\theta - \alpha_0)}{\sigma\, a}}\right] \tag{A.72}$$

when $\sigma_{\mathrm{d}} = 1/2$ and c_d is ignored $(c_d \ll c_l)$.

Appendix B

Measures of Rotor Efficiency

B.1   Introduction

The designer of a rotor is ultimately interested in minimizing the amount of power required to generate a specified amount of thrust, or, equivalently, maximizing the amount of thrust that can be generated with a given amount of power. Efficiency parameters are therefore key to determining the optimal operating state of a rotor and to comparing the performances of different rotor designs. A fair amount of confusion exists, however, regarding the best way to describe the efficiency of a *hovering* rotor. Although the direct ratio of thrust to power — also known as the Power Loading[1] (PL) — gives an immediately appreciable idea of the power penalty of a system, it is dimensional in nature, having dimensions of 1/velocity, and therefore non-dimensional quantities are sought which would be independent of the scale of the system. For a fluid-dynamic propulsive device operating at a freestream velocity, v_0, and producing a thrust, T, efficiency (η) is traditionally expressed as the ratio of the 'useful' propulsive power, $T \cdot v_0 = \dot{m}(v_f - v_0) \cdot v_0$, to the total input power, this being equal to the change in kinetic energy of the fluid, $\frac{1}{2}\dot{m}(v_f^2 - v_0^2)$, where v_f is the final velocity of the fluid in the wake of the propulsor. This ratio simplifies to the expression $2v_0/(v_0 + v_f)$, which implies an

---

[1]In some of the literature, this term has also been used to instead refer to the ratio of the input power to propeller disk area.

efficiency of zero in hover ($v_0 = 0$). Since this result is obviously not physical, a different formulation is required for the special case of zero translational velocity. In the field of helicopter aerodynamics, the traditional wisdom has been to consider the maximum figure of merit as the benchmark of a rotor's efficiency; however, arguments have also been made for considering the point of maximum C_T/C_P — the ratio of the thrust and power coefficients — as that for optimum performance [14, p. 53],[24]. In this appendix, it will be shown that both of these measures deserve consideration, but that, depending on the constraints faced in the design of a rotor, one or the other will assume greater importance. In the special case of rotary-wing micro air vehicles (MAVs), which are usually operated with varying rotor tip speeds, it will be shown that the figure of merit is preferrable to the C_T/C_P ratio as criterion for determining the optimum operating state of an open rotor and for comparing the performances of different rotors. However, in the case of the shrouded-rotor configuration, the use of the figure of merit for comparing the performances of configurations with different diffuser expansion ratios can result in misleading conclusions. For this configuration, a generalized form of the figure of merit is proposed, which is equally applicable to the specific case of an open rotor as well.

B.2   Figure of Merit

The Figure of Merit (FM), also known as the static thrust efficiency, is the ratio of the ideal — i.e., minimum possible — amount of power required to produce

a given thrust, to the actual amount required by the propulsor:

$$\text{FM} = \frac{\text{ideal power}}{\text{actual power}} = \frac{P_i}{P}$$

$$= \frac{\text{ideal power}}{\text{induced power} + \text{profile power}} = \frac{P_i}{\kappa P_i + P_o} \tag{B.1}$$

where P_i, the ideal power, is a function of the thust and the disk loading $(\text{DL} = T/A)$ of the rotor:

$$P_i = T \times \sqrt{\frac{\text{DL}}{2\rho}} = \frac{T^{3/2}}{\sqrt{2\rho A}} \tag{B.2}$$

By normalizing the power quantities by the rotor disk area and tip speed, the figure of merit can be expressed in terms of non-dimensional coefficients:

$$\text{FM} = \frac{C_{P_i}}{C_P} = \frac{C_{P_i}}{\kappa C_{P_i} + C_{P_o}} \tag{B.3}$$

$$= \frac{C_T^{3/2}/\sqrt{2}}{C_P} \tag{B.4}$$

where, for a given rotor, all terms are now solely functions of the collective angle (see Fig. B.3a on page 308, for example). Similar to the propulsive efficiency, this formulation informs that $(100 \times \text{FM})\%$ of the total input power is converted into useful thrust. The figure of merit therefore quantifies the additional power required — $(\frac{1}{\text{FM}} - 1)$ times the ideal power — to overcome losses due to the non-ideal characteristics of the flow: blade profile drag losses due to the viscosity of the fluid, represented by the profile power term (P_o, C_{P_o}), and losses due to non-uniform inflow distributions and to rotational momentum imparted to the wake, represented by the induced power correction factor, κ.

The relation between the figure of merit and the power loading is given by:

$$\text{PL} = \frac{T}{P} = \frac{T}{P_i} \times \text{FM}$$

$$= \sqrt{\frac{2\rho}{\text{DL}}} \times \text{FM} \tag{B.5}$$

where $T/P_\text{i} = \sqrt{2\rho/\text{DL}}$ is the ideal, or maximum possible, power loading for a given disk loading. The variation in power loading with disk loading, as given by this equation, is plotted in Fig. B.1 for different values of FM. Thus, for a high value of power loading, Eq. (B.5) indicates that the figure of merit should be high and the disk loading should be low. The equation also shows that if two different rotors have the same thrust and area — in other words, the same disk loading — then their (total) power requirements are inversely proportional to their figures of merit. Just as the propulsive efficiency, η, is used to compare the performances of different propellers at the same advance ratio ($J = v_\infty/nD$), the figures of merit of different hovering rotors are only meaningfully compared when the rotors are at the same disk loading [14, p. 47]. The reason for this can be seen from the following example arguments:

1. If two rotors are producing the same thrust but have different disk areas, then the rotor with the smaller area (higher disk loading) will have a greater ideal-power requirement. If, additionally, the two rotors happen to have the same non-ideal loss characteristics (κ, P_o), then, by Equation B.1, the higher-disk-loading rotor will have a higher figure of merit, thereby giving the misleading conclusion that it is the more efficient rotor, even though it actually consumes
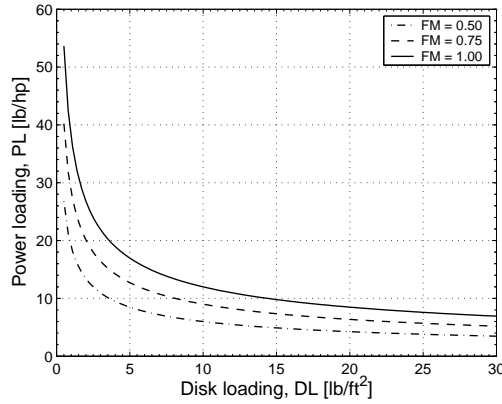
Figure B.1: Variation of power loading with disk loading for different values of figure of merit (sea-level standard atmosphere).

a greater total amount of power for the same thrust.

2. If a given rotor (fixed disk area) is operated at a higher tip speed but at the same collective angle, and hence at the same thrust and power coefficients, the thrust (proportional to v_{tip}^2) and disk loading will be higher, but the power loading will be lower, since the power is proportional to v_{tip}^3, even though the figure of merit is the same.

At the most fundamental level, though, this constraint on the usefulness of the figure of merit as a comparative measure can be understood by recognizing, from Eq. (B.5) and Fig. B.1, that the power loading is a function of FM only when the disk loading is constant.

According to this constraint, therefore, the efficiency of rotors should be expressed by plotting the variation in their figures of merit as a function of disk loading. However, for a single rotor, this would result in a family of curves with different curves for different tip speeds, and with rotor collective as a parameter that

changes along any given curve.[2] The curves would be identical, except that they would be expanded further 'sideways' along the x-axis for increasing values of v_{tip}. By normalizing the abscissa values — the disk loading — by the square of the tip speed (and by the air density), the variation in FM can be plotted versus the thrust coefficient, C_T, and expressed as a single characteristic curve for a given rotor. The restriction on comparing figures of merit at the same disk loading implies that it *is* permissible to compare them at different thrust coefficients, or at different values of ideal power, since it possible for rotors to have different values of C_T or P_i while having the same disk loading. A question that naturally arises, then, is: if two rotors have the same (maximum) value of FM, but at different values of C_T, then is one better than the other? The answer is "no — not necessarily." For the same desired thrust, and with the same restriction on disk area (therefore, the same disk loading), the two rotors will have the same power requirement (Eq. (B.5)); the only difference will be that the rotor with the higher C_T will allow for a lower tip speed, which, depending on other design considerations, may or may not be desirable.

B.3 C_T/C_P

Although the figure of merit is undoubtedly a useful concept, it is arguably a level of abstraction away from the more direct and intuitively appealing thrust:power ratio. A parameter that retains this appeal, while also having the desired attribute

---

[2]The data could also be plotted as a family of curves with different curves for different collectives, and with tip speed as the parameter that changes along a curve. However, since FM is constant for a given collective, this method would result in a collection of straight lines parallel to the x-axis, and would be of little use.

of being non-dimensional, is the ratio of the thrust and power coefficients: C_T/C_P.
The relation of this quantity to the power loading is given by:

$$\text{PL} = \frac{T}{P} = \frac{1}{v_{tip}} \times \frac{C_T}{C_P} \tag{B.6}$$

and, by using Equation B.4, to the figure of merit by:

$$\frac{C_T}{C_P} = \frac{\text{FM}}{\sqrt{C_T/2}} \tag{B.7}$$

Therefore, by this formulation, a high power loading is obtained by having a low tip speed and a high value of C_T/C_P. Following the method[3] shown by Leishman [14, p. 53], differentiating the ratio:

$$\frac{P}{T} = v_{tip}\frac{C_P}{C_T} = v_{tip}\left(\kappa\sqrt{\frac{C_T}{2}} + \frac{C_{P_o}}{C_T}\right) \tag{B.8}$$

with respect to C_T, while holding the tip speed constant, reveals the maximum value of C_T/C_P (minimum C_P/C_T) to lie at a thrust coefficient equal to $2(C_{P_o}/\kappa)^{2/3}$. Experimental data illustrating these results can be seen in Fig. B.2, which shows plots of power loading versus disk loading taken from Refs. [16] and [20]. The figures show families of curves, with each curve for a different tip speed. Within each curve, the maximum power loading occurs at the rotor collective angle for maximum C_T/C_P. Plotting the same data in non-dimensional form, as C_T/C_P

---

[3]This analysis is predicated on the assumption — which is reasonable when the blades are operating at small angles of attack — that C_{P_o} remains approximately constant with rotor collective.
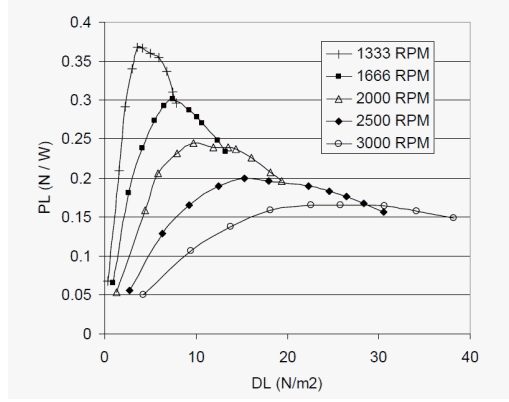
(a) Data from Bohorquez and Pines [16] (b) Data from Hein and Chopra [20]
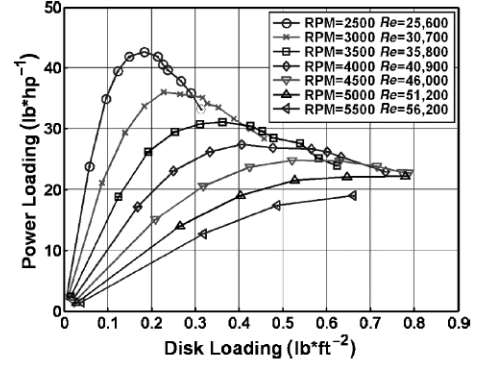
Figure B.2: Experimental data showing variation of power loading with disk loading for MAV-scale rotors. (1 N/W = 168 lb/hp, 1 lb/ft^2 = 47.9 N/m^2)

versus C_T, would cause all the curves in each figure to collapse to a single line that would completely characterize that rotor for any tip speed.

B.4   Comparison of FM and C_T/C_P

In the section describing the figure of merit, it was stated that the requirements for high power loading were a high figure of merit and a low disk loading. In the next section, describing the C_T/C_P ratio, it was found that a low tip speed is necessary for obtaining a high power loading. These requirements can be combined by solving Eqs. (B.6) and (B.7) to obtain:

$$\mathrm{PL} = \frac{T}{P} = \frac{1}{v_{tip}} \times \frac{\mathrm{FM}}{\sqrt{C_T/2}} \tag{B.9}$$

However, these requirements are contradictory: disk loading is reduced by lowering the thrust [coefficient], while the highest figures of merit are obtained at the higher values of C_T. In addition, for any given thrust, the tip speed is minimized by

304

increasing C_T. The optimal operating state of a rotor must therefore lie at some intermediate value of thrust coefficient — or collective angle, since the various non-dimensional coefficients and ratios are functions of rotor collective only — which maximizes the product of these terms. At the collective for maximum C_T/C_P, inserting the corresponding value of C_T into Eqs. (B.4) and (B.3) shows that the figure of merit has a value of $2/3\kappa$. In comparison, depending on the value of C_{P_o}, the maximum FM achievable by a rotor is closer to $1/\kappa$, and occurs at a higher collective angle. (This can also be intuitively seen from the fact that the figure of merit is proportional to $C_T^{3/2}/C_P$.) The question therefore arises as to which is the optimal operating state (collective) of a rotor: that for maximum C_T/C_P, or that for maximum FM; and indeed, which of these two parameters is the better, or 'correct' measure of efficiency for comparing different rotors. It can be immediately recognized from Eq. (B.6) that, for a given rotor, if the collective is changed from that for maximum C_T/C_P, then, although C_T/C_P has decreased, the same power loading can be achieved by reducing the tip speed. As a further example, it can be seen from the curves shown in Fig. B.2 that, at a fixed thrust (disk loading), the required power can be reduced (PL increased) by reducing the tip speed *and* simultaneously increasing the rotor collective to compensate.

It is now clear that, with tip speed being allowed to vary, the collective for maximum T/P at a given thrust is higher than that for maximum C_T/C_P. With v_{tip} now being expressed as $\sqrt{T/\rho A C_T}$, the right-hand-side of Eq. (B.8) becomes $\sqrt{T/2\rho A}\cdot(\kappa+C_{P_o}/C_{P_i})$, or $\sqrt{T/2\rho A}\cdot(1/\text{FM})$, which is the same as Eq. (B.5). For a given thrust and constrained rotor disk area, therefore, maximizing the power load-

ing (minimizing P/T) is equivalent to maximizing the figure of merit. Under these circumstances, a rotor should be operated at the thrust coefficient corresponding to maximum FM, and the tip speed adjusted to produce the desired thrust. Conversely, if constraints exist on the choice of tip speed — for example, due to considerations of noise, autorotational capability, rotor dynamic stability, advancing-blade compressibility or retreating-blade stall — then, in this case, the rotor should be operated at the thrust coefficient corresponding to maximum C_T/C_P, and the disk area adjusted to produce the desired thrust.

The same conditions apply whether for comparing different operating states (collectives) of the same rotor, or for comparing the performances of different rotors. If the tip speed is constrained, the maximum values of C_T/C_P should be compared in order to determine the better rotor for the application, while if disk area is constrained, the maximum values of FM should be compared.[4] In rotary-wing MAVs, for reasons of mechanical simplicity, rotor thrust is typically varied by adjusting rotational speed rather than by changing collective; also, by definition, a restriction exists on the maximum size of these vehicles. Therefore, for this class of vehicles, it would be the figure of merit that is more important as an efficiency parameter.

In most situations, however, constraints exist on both tip speed as well as on

---

[4]In the latter case, the requirement for equal disk loading is automatically fulfilled, since both thrust and area are the same for both rotors. An analogous requirement for comparing C_T/C_P would be equality of tip speed. If two rotors have the same disk loading and power loading, and hence the same figure of merit, but are operated at different thrust coefficients to produce the desired thrust (i.e., different tip speeds), then Eq. (B.7) shows that they would have different values of C_T/C_P; using C_T/C_P as the measure of efficiency in this case would give misleading results. Similarly, if two rotors have the same value of C_T/C_P, but at different thrust coefficients, then the rotor with the higher C_T will produce the same thrust at a lower tip speed, and have a higher power loading and lower power requirement (Eq. (B.6)).

the rotor disk area. In these cases, the optimal operating point of a rotor may lie at a collective that is neither that for maximum C_T/C_P nor that for maximum FM, but, instead, somewhere in between. If the constraint on tip speed is more severe than that on disk area, then the the optimal operating point will be closer to that for maximum C_T/C_P; if vice versa, then that for maximum FM. In general, however, in such cases, the best method for choosing the operating point would be to simply plot the required power for a desired thrust on a *3*-axis plot as a function of both tip speed and disk area, and directly examine the region within the constraint boundaries for the minimum power requirement. As an example, this procedure has been carried out using the experimental data for the MAV-scale open rotor tested in this study, and is illustrated in Fig. B.3. Figure B.3a shows the experimental values of C_T, C_P, C_T/C_P and FM as functions of rotor collective angle, showing that maximum C_T/C_P is achieved at $\theta_0 = 10°$, while maximum FM is achieved at $\theta_0 = 20°$. By interpolating in between these measured values, the 3-axis carpet plots shown in Figs. B.3b–d were obtained — these show, respectively, the rotor collective, thrust coefficient and input power that are required in order to produce a desired thrust of 40 g, depending on the choice of rotor diameter and tip speed. Superimposed on these plots are contour lines of constant collective which indicate the locations of operation at maximum C_T/C_P and maximum FM. Figure B.3e reproduces the plot of required power from Fig. B.3d, but in the form of 2-dimensional contour plot. It clearly illustrates how, at a fixed tip speed, operating at the point of maximum C_T/C_P results in the lowest power requirement, while at fixed rotor diameter, it is the point of maximum FM that results in the lowest power requirement.
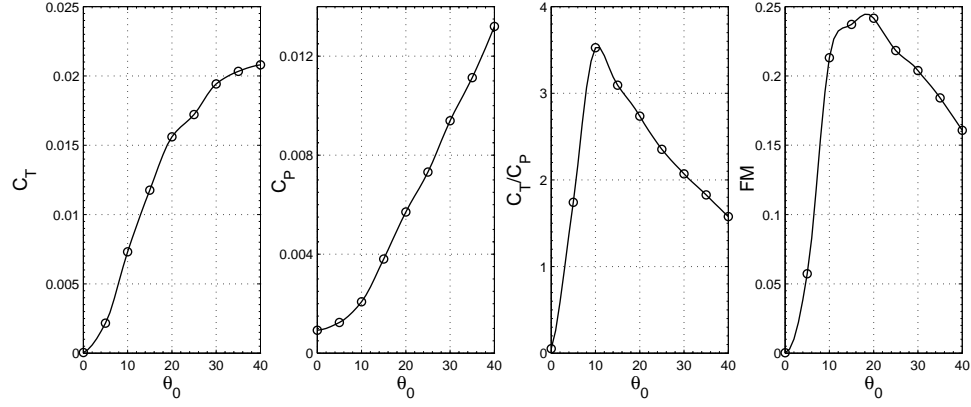
(a) Rotor source data
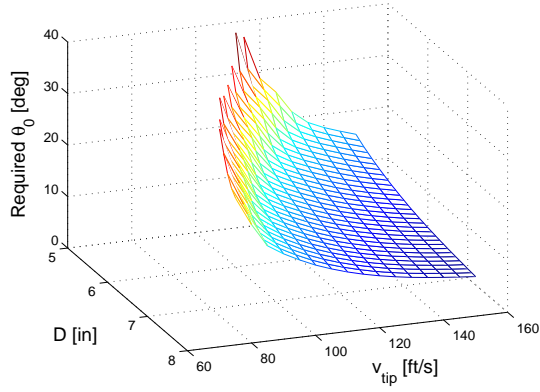
(b) Required collective
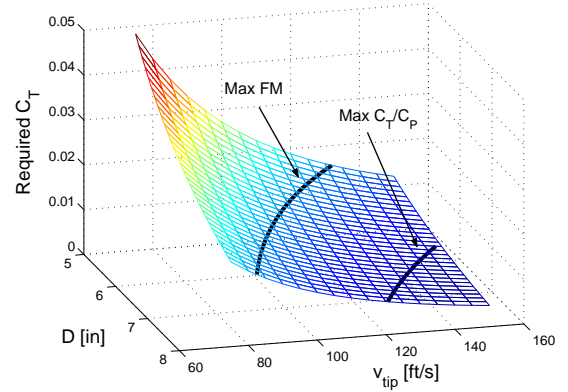
(c) Required thrust coefficient
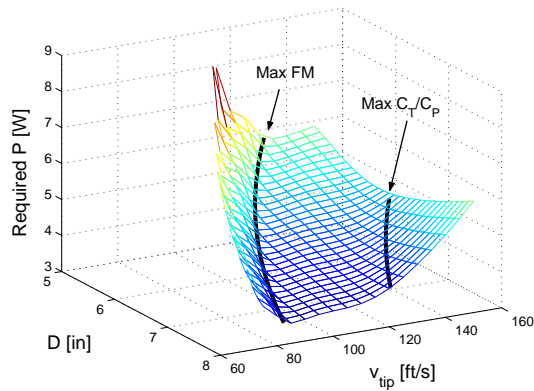
(d) Required power
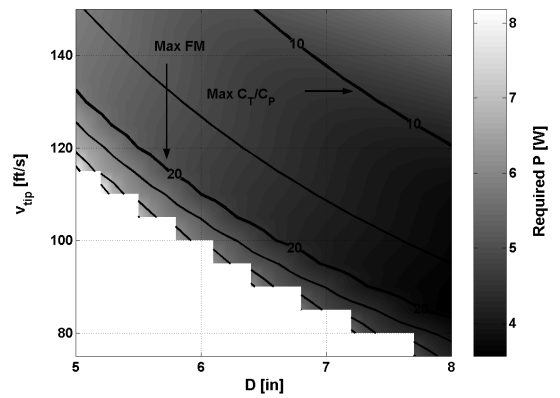
(e) Required power

Figure B.3: Values of collective angle, thrust coefficient, and power required to produce a desired thrust of 40 g, as functions of rotor diameter and tip speed

B.5 Shrouded rotors

The preceding discussions have dealt with the special case of an 'open' or 'free' rotor, for which, in hover, the wake is allowed to naturally contract to a final cross-sectional area equal to one-half that of the rotor disk. In the case of a shrouded rotor, for which the development of the wake is dictated by the geometry of the shroud, the ideal power requirement is now additionally a function of the expansion ratio of the shroud's diffuser, σ_{d}. In this, more general case[5], the ideal power is given by:

$$P_{\mathrm{i}} = T_{\mathrm{rotor}} \times v_{\mathrm{i}} = \frac{T}{2\sigma_{\mathrm{d}}} \times \sqrt{\frac{\sigma_{\mathrm{d}}T}{\rho A}} = \frac{T^{3/2}}{\sqrt{4\sigma_{\mathrm{d}}\rho A}} \tag{B.10}$$

$$C_{P_i} = C_{T_{\mathrm{rotor}}} \times \lambda_i = \frac{T}{2\sigma_{\mathrm{d}}} \times \sqrt{\sigma_{\mathrm{d}}C_T} = \frac{C_T^{3/2}}{2\sqrt{\sigma_{\mathrm{d}}}} \tag{B.11}$$

where T is the *total* thrust of the system, equal to $T_{\mathrm{rotor}} + T_{\mathrm{shroud}}$. Equation (B.6), relating the power loading and the C_T/C_P ratio, still holds for the case of a shrouded rotor, so this measure of efficiency retains its importance for cases where contraints exist on the choice of rotor tip speed, just as for an open rotor. However, when it is the disk area that is constrained, use of the traditional formulation of the figure of merit (Eq. (B.1)) can lead to incorrect conclusions. From Eq. (B.10) it can be seen that, at fixed total thrust and rotor disk area, if the expansion ratio is increased, then the ideal power requirement decreases. Since the rotor is being off-loaded — i.e., the rotor itself is producing less thrust — the blade section airfoils would be

---

[5]These equations derived here also hold for the special case of an open rotor, with the effective value of 1/2 for the expansion ratio.

operating at lower angles of attack, and therefore it can be expected that the profile power losses would decrease as well. If the proportional decrease in the profile power is the same as that for the ideal power, then the figure of merit is unchanged. On the other hand, if the assumption is made, as it is often done in first-order analyses, that the profile power is independent of the blade angle, and therefore remains the same, then the decrease in ideal power would cause FM to decrease as well. In either case, however, it is obvious that the total power requirement has decreased, and the power loading increased. Therefore, while the figure of merit remains an appropriate measure of efficiency for comparing different operating states of the same rotor-shroud combination, or of different rotors within the same shroud, it cannot be the correct means for comparing configurations with different expansion ratios. Direct comparison of the rotor polars, that is, plots of C_P versus C_T, would accurately enable such a comparison; however, this representation has the limitation of not being able to indicate the location on the characteristic curve for optimal operation of the rotor (i.e., the point of maximum FM). Thus, some other measure of efficiency is required, which incorporates all the benefits of each of these methods, for the case of constrained disk area.

Equation (B.10) can be re-arranged to show that the relation $P_i = T \times \sqrt{\mathrm{DL}/2\rho}$ also holds for a shrouded rotor (cf. Eq. (B.2)), where DL, the disk loading, is equal to $T_{\mathrm{rotor}}/\mathrm{A} = T/2\sigma_{\mathrm{d}}A$. With FM still defined as P_i/P, the relationship between FM and power loading remains that given by Eq. (B.5), repeated below for convenience:

$$\frac{T}{P} = \sqrt{\frac{2\rho}{\mathrm{DL}}} \times \mathrm{FM} \tag{B.12}$$

However, for a given *total* thrust and constrained disk area, the disk loadings of different rotors are now not the same if they have different [effective] values of σ_{d}. Consequently, the power requirements would not be inversely proportional to the figures of merit. On the other hand, expanding Eq. (B.12) results in the formulation:

$$\frac{T}{P} = \sqrt{\frac{4\sigma_{\mathrm{d}}\rho A}{T}} \times \mathrm{FM} \tag{B.13}$$

$$= \sqrt{\frac{4\rho A}{T}} \times \mathrm{FM}\sqrt{\sigma_{\mathrm{d}}} \tag{B.14}$$

which shows that, at fixed total thrust and disk area, power is inversely proportional to the product $\mathrm{FM} \cdot \sqrt{\sigma_{\mathrm{d}}}$, which can therefore be referred to as a 'generalized' figure of merit. At fixed *power* and disk area, manipulation of the same equation shows that the thrust that would be produced is directly proportional to $(\mathrm{FM}\sqrt{\sigma_{\mathrm{d}}})^{2/3}$. A graph of $\mathrm{FM} \cdot \sqrt{\sigma_{\mathrm{d}}}$ versus C_T would therefore perform the same role as that of the traditional FM-vs.-C_T graph for an open rotor, while *also* allowing for valid comparisons of the performances of configurations with different expansion ratios.[6] Using Eq. (B.6), the relation between the generalized FM and C_T/C_P is:

$$\frac{C_T}{C_P} = \frac{2}{\sqrt{C_T}} \times \mathrm{FM}\sqrt{\sigma_{\mathrm{d}}} \tag{B.15}$$

while its relation to the power loading is as given above in Eq. (B.14).

---

[6]Note that the product $\mathrm{FM}\sqrt{\sigma_{\mathrm{d}}}$ is equal to $C_T^{3/2}/2C_P$, so plotting a graph of this 'generalized' figure of merit is nothing more than plotting the variation in $C_T^{3/2}/C_P$, which is applicable to *any* rotor configuration. Strikingly, this parameter has the same form as the ratios $c_l^{3/2}/c_d$ and $C_L^{3/2}/C_D$ which are used to determine the angle of attack for minimum power consumption (maximum endurance) of airfoils and fixed-wing aircraft, respectively.

Bibliography

[1] Hundley, R. O., and Gritton, E. C., "Future Technology-Driven Revolutions in Military Operations: Results of a Workshop," RAND National Defense Research Institute DB-110-ARPA, Santa Monica, CA, 1994 Defense Technical Information Center (DTIC) Accession Number ADA285478.

[2] McMichael, J. M., and Francis, USAF (Ret.), C. M. S., "Micro Air Vehicles Toward a New Dimension in Flight," *U.S. Department of Defense Weapons Systems Technology Information Analysis Center (WSTIAC) Newsletter*, Vol. 1, No. 1–3, Jan–Jul 2000 Originally published online at http://www.darpa.mil/tto/MAV/mav_auvsi.html, Aug. 7, 1997.

[3] Wilson, III, S. B., "Micro Air Vehicles (MAV)," Presentation at the AIAA Student Chapter meeting at the University of Maryland, College Park, Oct 19, 2000 Presentation prepared Dec 14, 1999.

[4] Grasmeyer, J. M., and Keennon, M. T., "Development of the Black Widow Micro Air Vehicle," 39th AIAA Aerospace Sciences Meeting and Exhibit, Reno, NV, Jan 8–11, 2001, no. AIAA-2001-127.

[5] Tarascio, M. J., and Chopra, I., "Design and Development of a Thrust Augmented Entomopter: An Advanced Flapping Wing Micro Hovering Air Vehicle," American Helicopter Society 59th Annual Forum Proceedings, Phoenix, AZ, May 6–8, 2003.

[6] Singh, B., *Dynamics And Aeroelasticity Of Hover Capable Flapping Wings: Experiments And Analysis* PhD thesis, University of Maryland, College Park, Department of Aerospace Engineering, 2006.

[7] Vogel, S., *Life in Moving Fluids: The Physical Biology of Flow*, 2nd ed., Princeton University Press, Princeton, NJ, 1994.

[8] Lowson, M. V., "Aerodynamics of Aerofoils at Low Reynolds Numbers," 14th International Unmanned Air Vehicle Systems Conference, Bristol, United Kingdom, Apr 12–14, 1999, no. 35, University of Bristol, Cranfield College of Aeronautics and Royal Aeronautical Society.

[9] Tennekes, H., *The Simple Science of Flight: From Insects to Jumbo Jets* The MIT Press, Cambridge, MA, 1997.

[10] Azuma, A., *The Biokinetics of Flying and Swimming* Springer-Verlag, Tokyo, Japan, 1992.

[11] Taylor, J. W. R., *Jane's All the World's Aircraft - 2000/2001* Jane's Publishing Company, London, U.K., 2000.

[12] Bohorquez, F., *Rotor Hover Performance And System Design Of An Efficient Coaxial Rotary Wing Micro Air Vehicle* PhD thesis, University of Maryland, College Park, Department of Aerospace Engineering, 2007.

[13] Jacobs, E. N., and Sherman, A., "Airfoil Section Characteristics as Affected by Variations of the Reynolds Number," NACA Report No. 586, Langley Memorial Aeronautical Laboratory, Langley Field, VA, Jun. 24, 1936.

[14] Leishman, J. G., *Principles of Helicopter Aerodynamics*, 1st ed., Cambridge Aerospace Series. Cambridge University Press, New York, NY, 2000.

[15] Prouty, R. W., *Helicopter Performance, Stability, and Control* Krieger Publishing Company, Malabar, FL, 1995.

[16] Bohorquez, F., and Pines, D., "Rotor and Airfoil Design for Efficient Rotary Wing Micro Air Vehicles," American Helicopter Society 61st Annual Forum Proceedings, Grapevine, TX, Jun 1–3, 2005.

[17] Samuel, P., Sirohi, J., Rudd, L., Pines, D., and Perel, R., "Design and Analysis of a Micro Coaxial Rotorcraft," American Helicopter Society Vertical Lift Aircraft Design Conference, San Francisco, CA, Jan 19–21, 2000.

[18] Young, L., Aiken, E., Johnson, J., Andrews, J., R., D., and J., K., "New Concepts and Perspectives on Micro-Rotorcraft and Small Autonomous Rotary-Wing Vehicles," 20th AIAA Applied Aerodynamics Conference, St. Louis, MO, Jun 24–27, 2002.

[19] Bohorquez, F., "Hover Performance of Rotor Blades at Low Reynolds Numbers for Rotary Wing Micro Air Vehicles: An Experimental Study," American Helicopter Society 59th Annual Forum Proceedings, Phoenix, AZ, May 6–8, 2003.

[20] Hein, B. R., and Chopra, I., "Hover Performance of a Micro Air Vehicle: Rotors at Low Reynolds Number," *Journal of the American Helicopter Society*, Vol. 52, No. 3, Jul 2007, pp. 254–262.

[23] Sirohi, J., Tishchenko, M., and Chopra, I., "Design and Testing of a Micro-Aerial Vehicle with a Single Rotor and Turning Vanes," American Helicopter Society 61st Annual Forum Proceedings, Grapevine, TX, Jun 1–3, 2005.

[25] Hrishikeshavan, V., and Chopra, I., "Design and Testing of a Shrouded Rotor Micro Air Vehicle with Anti-torque Vanes," American Helicopter Society 64th Annual Forum Proceedings, Montreal, Canada, Apr 29 – May 1, 2008.

[22] Bohorquez, F., Samuel, P., Sirohi, J., Pines, D., Rudd, L., and Perel, R., "Design, Analysis and Hover Performance of a Rotary Wing Micro Air Vehicle," *Journal of the American Helicopter Society*, Vol. 48, No. 2, Apr 2003, pp. 80–90.

[24] Ramasamy, M., Johnson, B., and Leishman, J. G., "Toward Understanding the Aerodynamic Efficiency of a Hovering Micro-Rotor," AHS International Specialists' Meeting on Unmanned Rotorcraft: Design, Control and Testing, Chandler, AZ, Jan 23–25, 2007.

[21] Hein, B., "Rotor Blade Optimization Studies for MAVs Operating at Low Reynolds Number," AIAA Mid-Atlantic Region I Student Conference, College Park, MD, Apr. 11–12, 2003.

[26] Fletcher, H. S., "Experimental Investigation of Lift, Drag and Pitching Moment of Five Annular Airfoils," NACA TN 4117, Langley Memorial Aeronautical Laboratory, Langley Field, VA, Oct 1957.

[27] Lipera, L., "Micro Craft Ducted Air Vehicle," AHS/AIAA/RaeS/SAE International Powered Lift Conference, Arlington, VA, Oct 30–Nov 1 2000.

[28] Mouille, R., "The "Fenestron," Shrouded Tail Rotor of the SA.341 Gazelle," *Journal of the American Helicopter Society*, Vol. 15, No. 4, Oct 1970, pp. 31–37.

[29] Mouille, R., and d'Ambra, F., "The "Fenestron" A Shrouded Tail Rotor Concept for Helicopters," American Helicopter Society 42nd Annual Forum Proceedings, Washington, D.C., Jun 2–5, 1986, pp. 597–606.

[30] Vuillet, A., "Operational Advantages and Power Efficiency of the Fenestron as Compared to a Conventional Tail Rotor," *Vertiflite*, Vol. 35, No. 5, Jul/Aug 1989, pp. 24–29.

[31] Clemmons, M. G., "Antitorque Safety and the RAH-66 Fantail," American Helicopter Society 48th Annual Forum Proceedings, Washington, D.C., Jun 3–5, 1992, pp. 169–175.

[33] Basset, P.-M., and Brocard, M., "A Fenestron Model for Improving the Helicopter Yaw Dynamics Flight Simulation," 30th European Rotorcraft Forum, Marseilles, France, Sep 14–16, 2004.

[32] Niwa, Y., "The Development of the New Observation Helicopter (XOH-1)," AHS International 54th Annual Forum Proceedings, Washington, D.C., May 20–22, 1998, pp. 1285–1297.

[34] Fleming, J., Jones, T., Lusardi, J., Gelhausen, P., and Enns, D., "Improved Control of Ducted Fan UAVs in Crosswind Turbulence," AHS 4th Decennial Specialists' Conference on Aeromechanics, San Francisco, CA, Jan 21–23, 2004.

[35] Weir, R. J., "Aerodynamic Design Considerations for a Free-Flying Ducted Propeller," AIAA Atmospheric Flight Mechanics Conference, Minneapolis, MN, Aug 1988, no. AIAA-88-4377, pp. 420–431.

[36] Kuhn, R. E., "Review of Basic Principles of V/STOL Aerodynamics," NASA Conference on V/STOL Aircraft, Langley Field, VA, Nov 17–18, 1960, Langley Research Center, pp. 1–17.

[37] Hamel, G., "Aeroplane," US Patent No. 1,463,694, Jul 31, 1923 Application filed Apr 4, 1922; Serial No. 549,576.

[38] Kort, L., "Combined Device of a Ship's Propeller Enclosed by a Nozzle," US Patent No. 2,030,375, Feb 11, 1936 Application filed Sep 7, 1933; In Germany Jul 25, 1933; Serial No. 688,505.

[39] Stipa, L., "Experiments with Intubed Propellers," NACA TM 655, Jan 30, 1932 Translated from L'Aerotecnica (Rome), pp. 923-953, Aug 1931.

[40] Stipa, L., "Stipa Monoplane with Venturi Fuselage," NACA TM 753, Washington, DC, Sep 1934 Translated from Rivista Aeronautica, Vol. IX, No. 7, pp. 13–37, Jul 1933.

[41] van Manen, J. D., and van Oossanen, P., *Principles of Naval Architecture, Second Revision*, 3rd ed.,, Vol. II: Resistance, Propulsion and Vibration The Society of Naval Architects and Marine Engineers (SNAME), Jersey City, NJ, 1988, Ch. VI, Section 9: Ducted Propellers, pp. 213–225.

[42] Thurston, S., and Amsler, R. C., "Review of Marine Propellers and Ducted Propeller Propulsive Devices," *Journal of Aircraft*, Vol. 3, No. 3, May–Jun 1966, pp. 255–261.

[43] Kruger, W., "On Wind Tunnel Tests and Computations Concerning the Problem of Shrouded Propellers," NACA TM 1202, Feb 1949 Translation of ZWB Forschungsbericht Nr. 1949, Aerodynamischen Versuchsanstalt (AVA), Göttingen, Germany, Jan 21, 1944.

[44] Kuchemann, D., "Concerning the Flow About Ring-Shaped Cowlings of Finite Thickness, Part I," NACA TM 1325, Jan 1952 Translation of ZWB Forschungsbericht Nr. 1235, Jun 13, 1940.

[45] Kuchemann, D., and Weber, J., "Concerning the Flow About Ring-Shaped Cowlings, Part II: Annular Bodies of Infinite Length with Circulation for Smooth Entrance," NACA TM 1326, Nov 1951 Translation of ZWB Forschungsbericht Nr. 1236/2, Nov 11, 1940.

[46] Kuchemann, D., and Weber, J., "Concerning the Flow About Ring-Shaped Cowlings Part VI: Further Measurements on Inlet Devices," NACA TM 1327, Dec 1951 Translation of ZWB Forschungsbericht Nr. 1236/6, Mar 30, 1942.

[47] Kuchemann, D., and Weber, J., "Concerning the Flow About Ring-Shaped Cowlings, Part VIII: Further Measurements on Annular Profiles," NACA TM 1328, Feb 1952 Translation of ZWB Forschungsbericht Nr. 1236/8, Mar 25, 1943.

[48] Kuchemann, D., and Weber, J., "Concerning he Flow About Ring-Shaped Cowlings, Part IX: The Influence of Oblique Oncoming Flow on the Incremental Velocities and Air Forces at the Front Part of Circular Cowls," NACA TM 1329, Feb 1952 Translation of ZWB Forschungsbericht Nr. 1236/9, Jun 10, 1943.

[49] Kuchemann, D., and Weber, J., "Concerning the Flow About Ring-Shaped Cowlings, Part XII: Two New Classes of Circular Cowls," NACA TM 1360, Oct 1953 Translation of ZWB Untersuchen und Mitteilungen Nr. 3111.

[50] Kuchemann, D., "Concerning the Flow About Ring-Shaped Cowlings, Part XIII: The Influence of a Projecting Hub," NACA TM 1361, Oct 1953 Translation of ZWB Untersuchen und Mitteilungen Nr. 3144.

[51] Kuchemann, D., and Weber, J., *Aerodynamics of Propulsion*, 1st ed., McGraw-Hill Publications in Aeronautical Science. McGraw-Hill Book Company, Inc., New York, NY, 1953, Ch. 6: The ducted propeller, pp. 125–139.

[52] Platt, Jr., R. J., "Static Tests of a Shrouded and an Unshrouded Propeller," NACA RM L7H25, Langley Memorial Aeronautical Laboratory, Langley Field, VA, Feb 9 1948.

[53] Fairchild, J. E., Batra, N. N., and Stewart, R. L., "Influence of Design Parameters on Fan-in-Fin Static Performance," American Helicopter Society 29th Annual National Forum, May 1973.

[54] Sacks, A. H., and Burnell, J. A., "Ducted Propellers — A Critical Review of the State of the Art," In *Progress in Aeronautical Sciences*, A. Ferri, D. Kuchemann, and L. H. G. Sterne, Eds., Vol. 3. Pergammon Press, The Macmillan Company, New York, NY, 1962, Ch. Part 2, pp. 85–135.

[55] Parlett, L. P., "Aerodynamic Characteristics of a Small-Scale Shrouded Propeller at Angles of Attack from 0° to 90°," NACA TN 3547, Langley Memorial Aeronautical Laboratory, Langley Field, VA, Nov 1955.

[56] Ham, N. D., and Moser, H. H., "Preliminary Investigation of a Ducted Fan in Lifting Flight," *Journal of the American Helicopter Society*, Vol. 3, No. 3, Jul 1958, pp. 17–29.

[57] Taylor, R. T., "Experimental Investigation of the Effects of Some Shroud Design Variables on the Static Thrust Characteristics of a Small-Scale Shrouded Propeller Submerged in a Wing," NACA TN 4126, Langley Memorial Aeronautical Laboratory, Langley Field, VA, Jan 1958.

[58] Moser, H. H., "Some Effects of the Shroud on the Forward Flight Performance of the Lifting Fan," *Journal of the American Helicopter Society*, Vol. 4, No. 2, Apr 1959, pp. 39–44.

[59] Nelson, N. E., "The Ducted Fan in VTOL Aircraft Design," *Journal of the American Helicopter Society*, Vol. 4, No. 1, Jan 1959, pp. 53–56.

[60] Parlett, L. P., "Stability and Control Characteristics of a Small-scale Model of an Aerial Vehicle Supported by Two Ducted Fans," NASA TN D-920, Langley Research Center, Langley Field, VA, Jul 1961.

[61] Yaggy, P. F., and Goodson, K. W., "Aerodynamics of a Tilting Ducted Fan Configuration," NASA TN D-785, Ames Research Center, Moffett Field, CA and Langley Research Center, Langley, VA, Mar 1961.

[62] Yaggy, P. F., and Mort, K. W., "A Wind-Tunnel Investigation of a 4-Foot-Diameter Ducted Fan Mounted on the Tip of a Semispan Wing," NASA TN D-776, Ames Research Center, March 1961.

[63] Goodson, K. W., and Grunwald, K. J., "Aerodynamic Characteristics of a Powered Semispan Tilting-Shrouded-Propeller VTOL Model in Hovering and Transition Flight," NASA TN D-981, Langley Research Center, Jan 1, 1962.

[64] Grunwald, K. J., and Goodson, K. W., "Aerodynamic Loads on an Isolated Shrouded-Propeller Configuration for Angles of Attack from $-10°$ to $110°$," NASA TN D-995, Langley Research Center, Jan 1, 1962.

[65] Grunwald, K. J., and Goodson, K. W., "Division of Aerodynamic Loads on a Semispan Tilting Ducted-Propeller Model in Hovering and Transition Flight," NASA TN D-1257, Langley Research Center, May 1, 1962.

[66] Mort, K. W., and Yaggy, P. F., "Aerodynamic Characteristics of a 4-Foot-Diameter Ducted Fan Mounted on the Tip of a Semispan Wing," NASA TN D-1301, Ames Research Center, Apr 1, 1962.

[67] Kelley, H. L., and Champine, R. A., "Flight Operating Problems and Aerodynamic Performance Characteristics of a Fixed-Wing, Tilt-Duct, VTOL Research Aircraft," NASA TN D-1802, Langley Research Center, Jul 1, 1963.

[68] Mort, K. W., "Performance Characteristics of a 4-Foot-Diameter Ducted Fan at Zero Angle of Attack for Several Fan Blade Angles," NASA D-3122, Ames Research Center, Moffett Field, CA, Dec 1965.

[69] Newsom, Jr., W. A., "Aerodynamic Characteristics of Four-Duct Tandem VTOL-Aircraft Configurations," NASA TN D-1481, Langley Research Center, Langley Station, Hampton, VA, Jan 1963.

[70] Paxhia, V. B., and Sing, E. Y., "The X-22A Design Development," 1st AIAA Annual Meeting, Washington, D.C., Jun 29 – Jul 2, 1964, no. AIAA-64-282, American Institute of Aeronautics and Astronautics.

[71] Maki, R. L., and Giulianetti, D. J., "Aerodynamic Stability and Control of Ducted-Propeller Aircraft," Conference on V/STOL and STOL Aircraft, Ames Research Center, Moffett Field, CA, Apr 1966, no. 9 in NASA-SP-116, NASA, pp. 115–128.

[72] Mort, K. W., "Summary of Large-Scale Tests of Ducted Fans," Conference on V/STOL and STOL Aircraft, Ames Research Center, Moffett Field, CA, Apr 1966, no. 8 in NASA-SP-116, NASA, pp. 97–113.

[73] Spreemann, K. P., "Wind-Tunnel Investigation of Longitudinal Aerodynamic Characteristics of a Powered Four-Duct-Propeller VTOL Model in Transition," NASA TN D-3192, Langley Research Center, Langley Station, Hampton, VA, Apr 1966.

[74] Giulianetti, D. J., Biggers, J. C., and Maki, R. P., "Longitudinal Aerodynamic Characteristics in Ground Effect of a Large-Scale, V/STOL Model with Four Tilting Ducted Fans Arranged in a Dual Tandem Configuration," NASA NASA TN-D-4218, Ames Research Center, Moffett Field, CA, Oct 1967.

[75] Mort, K. W., and Gamse, B., "A Wind-Tunnel Investigation of a 7-Foot-Diameter Ducted Propeller," NASA TN D-4142, Ames Research Center, Moffett Field, CA, Aug 1967.

[76] Rhodes, W. B., "Initial Military Flight Tests of the X-22A VSTOL Research Aircraft," *Journal of Aircraft*, Vol. 7, No. 2, Mar–Apr 1970, pp. 169–174.

[77] Thompson, J. F., and Roberts, S. C., "Shrouded propeller research at Mississippi State University leading to application of the United States Army XV-11A," Proceedings of the CAL/USAAVLABS Symposium on Aerodynamic Problems Associated with V/STOL Aircraft, Vol II: Propulsion and Interference Aerodynamics, Buffalo, NY, Jun 1966, Vol. 2.

[78] Lazareff, M., "Aerodynamics of Shrouded Propellers," The Aerodynamics of V/STOL Aircraft, AGARD-VKI Lecture Series, AGARDograph 126, Rhode-Saint-Genese, Belgium, May 13–17, 1968, P. E. Colin and J. Williams, Eds., no. D, AGARD and Von Karman Institute, pp. 237–289.

[79] Mouille, R., "Ten years of Aerospatiale experience with the Fenestron and conventional tail rotor," American Helicopter Society 35th Annual Forum, May 1979, no. Preprint No. 79-58.

[80] Andrews, III, J. R., Riley, Jr., R. G., and Rahnke, C., "Design and Testing of a Ducted Tail Rotor Concept Demonstrator for a Model 222U Helicopter," Twenty-Second European Rotorcraft Forum, Brighton, U.K., Sep 16–19, 1996, no. Paper No. 4.

[81] Riley, Jr., R. G., "Effects of Uneven Blade Spacing on Ducted Tail Rotor Acoustics," American Helicopter Society 52nd Annual Forum Proceedings, Washington, D.C., Jun 4–6, 1996, pp. 1–12.

[82] Lemont, H. E., "Ringfin Augmentation Effects," American Helicopter Society 38th Annual Forum Proceedings, Anaheim, CA, May 4–7, 1982, pp. 451–460.

[83] Harr, H. K., Hollifield, P. J., and Smith, R. P., "Flight investigation of Bell Model 206 ring fin," American Helicopter Society 41st Annual Forum Proceedings, Fort Worth, TX, May 15–17, 1985, pp. 327–337.

[84] Clark, D. R., "Aerodynamic Design Rationale for the Fan-in-Fin on the S-67 Helicopter," American Helicopter Society 31st Annual National Forum, Washington, D.C., May 13–15, 1975, no. Preprint No. 904.

[87] Rajagopalan, R. G., and Keys, C. N., "Detailed Aerodynamic Design of the RAH-66 FANTAIL$^{\text{TM}}$ Using CFD," American Helicopter Society 49th Annual Forum Proceedings, St. Louis, MO, May 19–21, 1993, pp. 1193–1206.

[85] Keys, C., Sheffler, M., Weiner, S., and Heminway, R., "LH Wind Tunnel Testing: Key to Advanced Aerodynamic Design," American Helicopter Society 47th Annual Forum Proceedings, Phoenix, AZ, May 6–8, 1991, pp. 77–87.

[86] Wright, G. P., Driscoll, J. T., and Nickerson, Jr., J. D., "Handling Qualities of the H-76 FANTAIL TM Demonstrator," American Helicopter Society 47th Annual Forum Proceedings, 1991, pp. 123–135.

[88] Kothmann, B. D., and Ingle, S. J., "RAH-66 Comanche Linear Aeroservoelastic Stability Analysis: Model Improvements and Flight Test Correlation," AHS International 54th Annual Forum Proceedings, Washington, D.C., May 20–22, 1998, pp. 620–643.

[89] Alpman, E., Long, L. N., and Kothmann, B. D., "Toward a Better Understanding of Ducted Rotor Antitorque and Directional Control in Forward Flight," American Helicopter Society 59th Annual Forum Proceedings, Phoenix, AZ, May 6–8, 2003.

[90] Alpman, E., Long, L. N., and Kothmann, B. D., "Understanding Ducted-Rotor Antitorque and Directional Control Characteristics Part I: Steady-State Simulation," *Journal of Aircraft*, Vol. 41, No. 5, Sep–Oct 2004, pp. 1042–1053.

[91] Alpman, E., Long, L. N., and Kothmann, B. D., "Understanding Ducted-Rotor Antitorque and Directional Control Characteristics Part II: Unsteady Simulations," *Journal of Aircraft*, Vol. 41, No. 6, Nov–Dec 2004, pp. 1370–1378.

[92] Bourtsev, B. N., and Selemenev, Serguei, V., "Fan-in-fin Performance at Hover Computational Method," 26th European Rotorcraft Forum, The Hague, Netherlands, Sep 26–29, 2000, no. Paper No. 10.

[93] Vuillet, A., and Morelli, F., "New Aerodynamic Design of the Fenestron for Improved Performance," Twelfth European Rotorcraft Forum, Garmisch-Partenkirchen, Federal Republic of Germany, Sep 22–25, 1986, no. Paper No. 8.

[94] Fleming, J., Jones, T., Gelhausen, P., and Enns, D., "Improving Control System Effectivenss for Ducted Fan VTOL UAVs Operating in Crosswinds," 2nd AIAA "Unmanned Unlimited" Systems, Technologies and Operations — Aerospace, San Diego, CA, Sep 15–18, 2003, no. AIAA-2003-6514.

[95] "Airborne Remotely Operated Device (1982-1988)," World-Wide Web document, http://www.spawar.navy.mil/robots/air/arod/arod.html, Dec 10, 1999.

[96] Murphy, D. W., and Bott, J. P., "On the Lookout: The Air Mobile Ground Security and Surveillance System (AMGSSS) Has Arrived," *Unmanned Systems*, Vol. 13, No. 4, Fall 1995.

[97] Cycon, J. P., "Decoding the Cypher UAV," *Vertiflite*, Vol. 36, No. 6, Nov/Dec 1990, pp. 56–58.

[98] Cycon, J. P., "Sikorsky Aircraft UAV Program," *Vertiflite*, Vol. 38, No. 3, May/Jun 1992, pp. 26–30.

[99] Thornberg, C. A., and Cycon, J. P., "Sikorsky Aircraft's Unmanned Aerial Vehicle, Cypher: System Description and Program Accomplishments," American Helicopter Society 51st Annual Forum Proceedings, Fort Worth, TX, May 9–11, 1995, pp. 804–811.

[100] Walsh, D., and Cycon, J. P., "The Sikorsky Cypher(R) UAV: A Multi-Purpose Platform with Demonstrated Mission Flexibility," AHS International 54th Annual Forum Proceedings, Washington, D.C., May 20–22, 1998, pp. 1410–1418.

[101] Murphy, D. W., Bott, J. P., Cycon, J. P., Bryan, W. D., Coleman, J. L., Gage, D. W., Marsh, W. C., Martin, B. F., Nguyen, H. G., and Schneider, R., "Air-Mobile Ground Surveillance and Security System (AMGSSS) Project Summary Report," Naval Command, Control and Ocean Surveillance Center (NCCOSC), RDT&E Division NRaD TD 2914, San Diego, CA, Sep 1996.

[102] "Multipurpose Security and Surveillance Mission Platform (1992-1998)," World-Wide Web document, http://www.spawar.navy.mil/robots/air/amgsss/mssmp.html, May 21, 2002.

[103] Cycon, J. P., Rosen, K. M., and Whyte, A. C., "Unmanned Flight Vehicle Including Counter Rotating Rotors Positioned Within a Toroidal Shroud and Operable to Provide All Required Vehicle Flight Controls," US Patent No. 5,152,478, Oct 6, 1992 Filed May 18, 1990.

[104] Cycon, J. P., Millea, V. F., Kohlhepp, F. W., and Hansen, B. D., "Drive Train Assembly for a Rotor Assembly Having Ducted, Coaxial Counter-Rotating Rotors," US Patent No. 5,226,350, Jul 13, 1993 Filed Jun 22, 1992.

[105] Cycon, J. P., Kohlhepp, F. W., and Millea, V. F., "Coaxial Transmission/Center Hub Subassembly for a Rotor Assembly Having Ducted, Coaxial Counter-Rotating Rotors," US Patent No. 5,351,913, Oct 4, 1994 Filed Jun 22, 1992.

[106] Cycon, J. P., Furnes, K. M., Kohlhepp, F. W., Darrell, M. D., and Sandy, D. F., "Toroidal Fuselage Structure for Unmanned Aerial Vehicles Having Ducted, Coaxial, Counter-Rotating Rotors," US Patent No. 5,277,380, Jan 11, 1994 Filed Jun 22, 1992.

[107] Cycon, J. P., DeWitt, C. W., and Scott, M. W., "Unmanned Multi-Mode Vertical Take Off and Landing Aircraft," US Patent No. Des. 418,805, Jan 11, 2000 Filed Nov 24, 1998.

[108] Cycon, J. P., Scott, M. W., and DeWitt, C. W., "Method of Reducing a Nose-Up Pitching Moment on a Ducted Unmanned Aerial Vehicle," US Patent No. US 6,170,778 B1, Jan 9, 2001 Filed Apr 22, 1999.

[109] Cycon, J. P., Scott, M. W., and DeWitt, C. W., "Unmanned Aerial Vehicle with Counter-Rotating Ducted Rotors and Shrouded Pusher-Prop," US Patent No. US 6,270,038 B1, Aug 7, 2001 Filed Apr 22, 1999.

[110] McGonigle, K. P., Ferraro, J., and Cycon, J. P., "Unmanned VTOL Ground Surveillance Vehicle," US Patent No. 5,575,438, Nov 19, 1996 Filed May 9, 1994.

[111] Ebbert, M. D., Gustin, R. G., Horbett, E. G., Edwards, J. J., and Adcock, C. L., "Unmanned Vertical Take-off and Landing, Horizontal Cruise, Air Vehicle," US Patent No. 5,295,643, Mar 22, 1994 Filed Dec 28, 1992.

[112] Lipera, L., Colbourne, J. D., Tischler, M. B., Mansur, M. H., Rotkowitz, M. C., and Patangui, P., "The Micro Craft iSTAR Micro Air Vehicle: Control System Design and Testing," American Helicopter Society 57th Annual Forum Proceedings, Washington, D.C., May 9–11, 2001.

[113] Wilson, III, S. B., and Schnepf, S., "Ground Loiter for OAVs and MAVs," American Helicopter Society 58th Annual Forum Proceedings, Montreal, Canada, Jun 11–13, 2002.

[114] Black, D. M., Wainauski, H. S., and Rohrbach, C., "Shrouded Propellers — A Comprehensive Performance Study," AIAA 5th Annual Meeting and Technology Display, Philadelphia, PA, Oct 21–24, 1968, no. AIAA-68-994, AIAA.

[115] Ahn, J., "Parametric Design of a Ducted Fan System in Forward Flight and Static Conditions," AHS International Specialists' Meeting on Unmanned Rotorcraft: Design, Control and Testing, Chandler, AZ, Jan 18–20, 2005.

[116] Kriebel, A. R., and Mendehall, M. R., "Predicted and Measured Performance of Two Full-Scale Ducted Propellers," Proceedings of the CAL/USAAVLABS Symposium on Aerodynamic Problems Associated with V/STOL Aircraft, Vol II: Propulsion and Interference Aerodynamics, Buffalo, NY, Jun 1966, Vol. 2.

[117] Martin, P., and Tung, C., "Performance and Flowfield Measurements on a 10-inch Ducted Rotor VTOL UAV," American Helicopter Society 60th Annual Forum Proceedings, Baltimore, MD, Jun 7–10, 2004.

[118] Bell, E. B., "Test of a Single-Stage Axial-Flow Fan," NACA Report No. 729, Langley Memorial Aeronautical Laboratory, Langley Field, VA, Sep 22 1941.

[119] Hubbard, H. H., "Sound Measurements for Five Shrouded Propellers at Static Conditions," NACA TN 2024, Langley Memorial Aeronautical Laboratory, Langley Field, VA, Apr 1950.

[120] Nygaard, T. A., Dimanlig, A. C., and Meadowcroft, E. T., "Application of a Momentum Source Model to the RAH-66 Comanche FANTAIL," AHS 4th Decennial Specialists' Conference on Aeromechanics, San Francisco, CA, Jan 21–23, 2004.

[121] Lee, H. D., Kwon, O. J., and Joo, J., "Aerodynamic Performance Analysis of a Helicopter Shrouded Tail Rotor Using an Unstructured Mesh Flow Solver," 5th Asian Computational Fluid Dynamics, Busan, Korea, Oct 27–30, 2003, no. Paper No. 8.

[122] Gupta, N., and Plump, J., "Design of a VTOL Micro Air Vehicle that Incorporates Counter-Rotating, Reversible Thrust Propellers," AUVSI Unmanned Systems Conference, Baltimore, MD, Jul 31 – Aug 2, 2001.

[123] Dyer, K. G., *Aerodynamic Study of a Small, Ducted VTOL Aerial Vehicle* PhD thesis, Massachusetts Institute of Technology, Department of Aeronautics and Astronautics, Cambridge, MA, Jun 2002.

[124] Martin, P. B., and Boxwell, D. A., "Design, Analysis and Experiments on a 10-inch Ducted Rotor VTOL UAV," AHS International Specialists' Meeting on Unmanned Rotorcraft: Design, Control and Testing, Chandler, AZ, Jan 18–20, 2005.

[125] Graf, W., Fleming, J., and Gelhausen, P., "Ducted Fan Aerodynamics in Forward Flight," AHS International Specialists' Meeting on Unmanned Rotorcraft: Design, Control and Testing, Chandler, AZ, Jan 18–20, 2005.

[126] Kondor, S., Amitay, M., Parekh, D., Fung, P., and Glezer, A., "Active Flow Control Application on a Mini Ducted Fan Uav," No. AIAA-2001-2440, AIAA.

[127] Kondor, S., and Heiges, M., "Active Flow Control for Control of Ducted Rotor Systems," Proceedings of the 39th AIAA Aerospace Sciences Meeting & Exhibit, Reno, NV, Jan 8–11, 2001, no. AIAA-2001-0117.

[128] Fung, P. H., and Amitay, M., "Control of a Miniducted-Fan Unmanned Aerial Vehicle Using Active Flow Control," *Journal of Aircraft*, Vol. 39, No. 4, Jul–Aug 2002, pp. 561–571.

[129] Plump, J. M., and Gupta, N. R., "Vertical Takeoff and Landing Aerial Vehicle," US Patent No. 6,691,949 B2, Feb 17, 2004 Application filed Jul 8, 2002.

[130] Moller, P. S., "Robotic or Remotely Controlled Flying Platform," US Patent No. 4,795,111, Jan 3, 1989 Application filed Feb 17, 1987.

[131] Moller, P. S., "Stabilizing Control Apparatus for Robotic or Remotely Controlled Flying Platform," US Patent No. US 6,450,445 B1, Sep 17, 2002 Filed Dec 10, 1999.

[132] Kelly, Mark, W., "Large-Scale Wind-Tunnel Studies of Several Vtol Types," NASA Conference on V/STOL Aircraft, Langley Field, VA, Nov 17–18, 1960, Langley Research Center, pp. 35–48.

[133] Milla, J. H., and Blick, E. F., "Lift and Drag Characteristics of a Biannular Wing Airplane," *Journal of Aircraft*, Vol. 3, No. 6, Nov–Dec 1966, pp. 586–587.

[134] Abrego, A. I., and Bulaga, R. W., "Performance Study of a Ducted Fan System," American Helicopter Society Aerodynamics, Acoustics, and Test and Evaluation Technical Specialists' Meeting, San Francisco, CA, Jan 23–25, 2002.

[135] Kriebel, A. R., "Theoretical Stabiity Derivatives for a Ducted Propeller," *Journal of Aircraft*, Vol. 1, No. 4, Jul–Aug 1964, pp. 203–210.

[136] Mendenhall, M. R., and Spangler, S. B., "Theoretical Study of Ducted Fan Performance," NASA CR 1494, Jan 1, 1970.

[137] Mendenhall, M. R., and Spangler, S. B., "A Computer Program for the Prediction of Ducted Fan Performance," NASA CR 1495, Feb 1, 1970.

[138] Sheehy, T. W., "Computer Aided Shrouded Propeller Design," Proceedings of the AIAA 9th Annual Meeting and Technical Display, 1973, no. AIAA-73-54, AIAA.

[139] Gray, R. B., and Wright, T., "A Vortex Wake Model for Optimum Heavily Loaded Ducted Fans," *Journal of Aircraft*, Vol. 7, No. 2, Mar–Apr 1970, pp. 152–158.

[140] McCormick, Jr., B. W., *Aerodynamics of V/STOL Flight* Aerodynamic Press, New York, NY, 1976.

[141] Goodman, T. R., "The Tip Correction for Wind-Tunnel Tests of Propellers," *Journal of the Aeronautical Sciences*, Vol. 23, No. 12, Dec 1956, pp. 1094–1098.

[142] Gibson, I. S., "Theoretical Studies of Tip Clearance and Radial Variation of Blade Loading on the Operation of Ducted Fans and Propellers," *Journal of Mechanical Engineering Science*, Vol. 16, No. 6, 1974, pp. 367–376.

[143] de Campos, J. F., "A Three-Dimensional Theory for the Design Problem of Propeller Ducts in a Shear Flow," Eighteenth Symposium on Naval Hydrodynamics, 1991, National Academy of Sciences, pp. 645–665.

[144] Page, G. S., "Design and Analysis of Single and Dual Rotation Ducted Fans," Proceedings of the AIAA 34th Aerospace Sciences Meeting and Exhibit, Reno, NV, Jan 15–18, 1996, no. AIAA-96-0677.

[145] Guerrero, I., Londenberg, K., Gelhausen, P., and Myklebust, A., "A Powered Lift Aerodynamic Analysis for the Design of Ducted Fan UAVs," 2nd AIAA "Unmanned Unlimited" Systems, Technologies and Operations — Aerospace, San Diego, CA, Sep 15–18, 2003, no. AIAA-2003-6567.

[146] Quackenbush, T. R., Wachspress, D. A., Boschitsch, A. H., and Solomon, C. L., "Aeromechanical Analysis Tools for Design and Simulation of VTOL UAV Systems," American Helicopter Society 60th Annual Forum Proceedings, Baltimore, MD, Jun 7–10, 2004.

[147] Rajagopalan, R. G., and Zhaoxing, Z., "Performance and Flow Field of a Ducted Propeller," AIAA/ASME/SAE/ASEE 25th Joint Propulsion Conference, Monterey, CA, Jul 10–12, 1989, no. AIAA-89-2673.

[148] Alpman, E., and Long, L. N., "Unsteady RAH-66 Comanche Flowfield Simulations Including Fan-in-fin," 16th AIAA Computational Fluid Dynamics Conference, Orlando, FL, Jun 23–26, 2003, no. AIAA-2003-4231.

[149] Ruzicka, G. C., Strawn, R. C., and Meadowcroft, E. T., "Discrete Blade CFD Analysis of Ducted Tail Fan Flow," 42nd AIAA Aerospace Sciences Meeting and Exhibit, Reno, NV, Jan 5–8, 2004, no. AIAA-2004-48.

[150] Ruzicka, G. C., Strawn, R. C., and Meadowcroft, E. T., "Discrete-Blade, Navier-Stokes Computational Fluid Dynamics Analysis of Ducted-Fan Flow," *Journal of Aircraft*, Vol. 42, No. 5, Sep–Oct 2005, pp. 1109–1117.

[151] Ahn, J., and Lee, K., "Performance Prediction and Design of a Ducted Fan System," 40th AIAA/ASME/SAE/ASEE Joint Propulsion Conference and Exhibit, Fort Lauderdale, FL, Jul 11–14, 2004, no. AIAA-2004-4196.

[152] Drela, M., and Giles, M. B., "ISES - A Two-Dimensional Viscous Aerodynamic Design and Analysis Code," 25th AIAA Aerospace Sciences Meeting, Jan 12–15, 1987, no. AIAA 1987-424.

[153] Srivastava, R., Reddy, T. S. R., and Stefko, G. L., "A Numerical Aeroelastic Stability Analysis of a Ducted-Fan Configuration," Proceedings of the 32nd AIAA/ASME/SAE/ASEE Joint Propulsion Conference and Exhibit, Buena Vista, FL, Jul 1–3, 1996, no. AIAA-96-2671.

[154] Keith, Jr., T. G., and Srivastava, R., "Final Technical Report for Euler/Navier-Stokes Solvers Applied to Ducted Fan Configurations," University of Toledo NASA CR 97-112953, Toledo, OH, Dec 1997.

[155] Srivastava, R., and Reddy, T. S. R., "Application of Three Flutter Analysis Methods to a Ducted-Fan Configuration," AIAA.

[156] Elena, L., and Schiestel, R., "Turbulence Modeling of Rotating Confined Flows," International Journal of Heat and Fluid Flow, Vol. 17, No. 3, Jun 1996, pp. 283–289.

[157] Randriamampianina, A., Elena, L., Fontaine, J. P., and Schiestel, R., "Numerical Prediction of Laminar, Transitional and Turbulent Flows in Shrouded Rotor-Stator Systems," Physics of Fluids, Vol. 9, No. 6, Jun 1997, pp. 1696–1713.

[158] Drischler, J. A., "Analytic Studies of Sound Pressures Inside the Duct of Ducted Propellers," NASA TN D-6345, Langley Research Center, Sep 1, 1971.

[159] Fricke, W., Bissell, J. R., Bamberg, W. T., and Martina, C. K., "Analytical and Experimental Studies of Sound Pressures on Ducted Propellers," Bell Aerosystems Company NASA-CR-66270; Report No. 9500-950001, Dec 1, 1966 NASA Contract NASW-1217.

[160] Gearhart, W. S., "Tip Clearance Cavitation in Shrouded Underwater Propulsors," Journal of Aircraft, Vol. 3, No. 2, Mar–Apr 1966, pp. 185–192.

[161] Oweis, G. F., and Ceccio, S. L., "Instantaneous and Time-Averaged Flow-Fields of Multiple Vortices in the Tip Region of a Ducted Propulsor," Experiments in Fluids, Vol. 38, Mar 24, 2005, pp. 615–636.

[162] Oweis, G. F., Fry, D., Chesnakas, C. J., Jessup, S. D., and Ceccio, S. L., "Development of a Tip-Leakage Flow — Part 1: The Flow Over a Range of Reynolds Numbers," Journal of Fluids Engineering, Vol. 128, No. 4, Jul 2006, pp. 751–764.

[163] Oweis, G. F., Fry, D., Chesnakas, C. J., Jessup, S. D., and Ceccio, S. L., "Development of a Tip-Leakage Flow — Part 2: Comparison Between the

Ducted and Un-ducted Rotor," *Journal of Fluids Engineering*, Vol. 128, No. 4, Jul 2006, pp. 765–773.

[164] Avanzini, G., D'Angelo, S., and de Matteis, G., "Performance and Stability of a Ducted-Fan Uninhabited Aerial Vehicle," Proceedings of the 39th AIAA Aerospace Sciences Meeting & Exhibit, Reno, NV, Jan 8–11, 2001, no. AIAA-2001-0844.

[165] Avanzini, G., de Matteis, G., and Fresta, F., "Robust Multivariable Control of a Shrouded-Fan Uninhabited Aerial Vehicle," AIAA Atmospheric Flight Mechanics Conference and Exhibit, Monterey, CA, Aug 5–8, 2002.

[166] Avanzini, G., D'Angelo, S., and de Matteis, G., "Performance and Stability of Ducted-Fan Uninhabited Aerial Vehicle Model," *Journal of Aircraft*, Vol. 40, No. 1, Jan-Feb 2003, pp. 86–93.

[167] Salluce, D. N., "Comprehensive System Identification of Ducted Fan UAVs," Master's thesis, California Polytechnic State University, San Luis Obispo, CA, Jan 2004.

[168] Bohorquez, F., and Pines, D., "Hover Performance and Swashplate Design of a Coaxial Rotary Wing Micro Air Vehicle," American Helicopter Society 60th Annual Forum Proceedings, Baltimore, MD, Jun 7–10, 2004.

[169] Bohorquez, F., and Pines, D., "Rotor Design for Efficient Rotary Wing Micro Air Vehicles," AHS International Specialists Meeting on Unmanned Rotorcraft: Design, Control and Testing,, Chandler, AZ, Jan 18–20, 2005.

[170] Hein, B., and Chopra, I., "Hover Performance of a Micro Air Vehicle: Rotors at Low Reynolds Number," AHS International Specialists' Meeting on Unmanned Rotorcraft: Design, Control and Testing, Chandler, AZ, Jan 18–20, 2005.

[171] Ramasamy, M., Leishman, J. G., and Lee, T. E., "Flow Field of a Rotating-Wing Micro Air Vehicle," American Helicopter Society 62nd Annual Forum Proceedings, Phoenix, AZ, May 9–11, 2006.

[172] Schroeder, E. J., "Low Reynolds Number Flow Validation Using Computational Fluid Dynamics With Application To Micro Air Vehicles," Master's thesis, University of Maryland, College Park, College Park, MD, 2005.

[173] Schroeder, E. J., and Baeder, J. D., "Using Computational Fluid Dynamics for Micro-Air Vehicle Airfoil Validation and Prediction," 23rd AIAA Applied Aerodynamics Conference, Toronto, Canada, Jun 6–9, 2005, no. AIAA-2005-4841.

[174] Boatwright "Measurements of Velocity Components in the Wake of a Full-Scale Helicopter Rotor in Hover," USAAMRDL TR 72-33, 1972 In Prouty,

R. W., *Helicopter Performance, Stability, and Control* , Krieger Publishing Company, Malabar, FL, 1995, p.40.

[175] Leishman, J. G., *Principles of Helicopter Aerodynamics*, 2nd ed., Cambridge Aerospace Series. Cambridge University Press, New York, NY, 2006.

[176] Armutcuoglu, O., Kavsaoglu, M. S., and Tekinalp, O., "Tilt Duct Vertical Takeoff and Landing Uninhabited Aerial Vehicle Concept Design Study," *Journal of Aircraft*, Vol. 41, No. 2, Mar–Apr 2004, pp. 215–223.

[177] Behun, M., Rom, F. E., and Hensley, R. V., "Evaluation of a Ducted-Fan Power Plant Designed for High Output and Good Cruise Fuel Economy," NACA RM E50E01, Lewis Flight Propulsion Laboratory, Cleveland, OH, Oct 17, 1950.

[178] Brocard, J. M. R., "Aircraft," US Patent No. 3,128,062, Apr 7 1964 Filed Feb 19, 1962; In France, Jul 19, 1961; Serial No. 174,314.

[179] Campbell, J. P., "Development of V/STOL Aircraft 1950 to 1970," *Journal of the American Helicopter Society*, Vol. 24, No. Special V/STOL Aircraft Issue, Jun 1979, pp. 7–16.

[180] Corson, Jr., B. W., "The Aerodynamics of a Wind-Tunnel Fan," NACA Report No. 820, Langley Memorial Aeronautical Laboratory, Langley Field, VA, Aug. 1941.

[181] Drela, M., and Youngren, H., "Axisymmetric Analysis and Design of Ducted Rotors," Jan 30, 2005.

[182] Gilmore, A. W., and Grahame, W. E., "Research Studies on a Ducted Fan Equipped with Turning Vanes," *Journal of the American Helicopter Society*, Vol. 4, No. 4, Oct 1959, pp. 11–21.

[183] Gruzling, J., "Propeller Shroud," US Patent No. 4,789,302, Dec 6, 1988 Application filed Feb 6, 1987.

[184] Kort, L., "Combined Propelling and Steering Device for Screw Propelled Ships," US Patent No. 2,139,594, Dec 6, 1938 Application filed Jun 25, 1937; In Germany Feb 8, 1936; Serial No. 150,398.

[185] Lindenbaum, B., and Blake, W., "The VZ-9 "Avrocar"," *Vertiflite*, Vol. 44, No. 2, Spring 1998.

[186] Milde, Jr., K. F., Pruszenski, Jr., A. S., and Wagner, J., "A Safe and Fuel-Efficient VTOL "Personal Aircraft"," American Helicopter Society 59th Annual Forum Proceedings, Phoenix, AZ, May 6–8, 2003.

[187] Okan, A., Tekinalp, O., and Kavsaoglu, M. S., "Flight Control of a Tilt-Duct Vtol Uav," Proceedings of the AIAA 1st Technical Conference and Workshop on Unmanned Aerospace Vehicles, Portsmouth, VA, May 20–23, 2002, no. AIAA-2002-3466.

[188] Perl, W., and Tucker, M., "A General Representation for Axial-Flow Fans and Turbines," NACA Report No. 814, Langley Memorial Aeronautical Laboratory, Langley Field, VA, May 4 1945.

[189] de Piolenc, F. M., and Wright, Jr., G. E., "Ducted Fan Design, Volume 1," 522 E. Vine, 213, West Covina, CA 91790, USA., 2001.

[190] Sato, T., and Engeda, A., "Design and Performance Analysis of Ducted Fans for Micro UAV Applications," AHS International Specialists' Meeting on Unmanned Rotorcraft: Design, Control and Testing, Chandler, AZ, Jan 18–20, 2005.

[191] Van Weelden, S. D., Smith, D. E., and Mullins, Jr., B. R., "Preliminary Design of a Ducted Fan Propulsion System for General Aviation Aircraft," Proceedings of the AIAA 34th Aerospace Sciences Meeting and Exhibit, Reno, NV, Jan 15–18, 1996, no. AIAA-96-0376.

[192] Wallis, A. M., Denton, J. D., and Demargne, A. A. J., "The Control of Shroud Leakage Flows to Reduce Aerodynamic Losses in a Low Aspect Ratio, Shrouded Axial Flow Turbine," *Transactions of the ASME*, Vol. 123, Apr 2001, pp. 334–341 Presented at the 45th International Gas Turbine and Aeroengine Congress and Exhibition, Munich, Germany, May 811, 2000. International Gas Turbine Institute Paper No. 2000-GT-475.

[193] Xu, G.-H., and Wang, S.-C., "Effects of the Shroud on Aerodynamic Performance in Helicopter Shrouded Tail Rotor System," *Aircraft Engineering and Aerospace Technology*, Vol. 73, No. 6, 2001, pp. 568–572.